Journal of Applied Mathematics

Modeling and Control of Complex Dynamic Systems 2013

Guest Editors: Zhiwei Gao, Dexing Kong, Chuanhou Gao, and Michael Chen

Modeling and Control of Complex Dynamic Systems 2013

Journal of Applied Mathematics

Modeling and Control of Complex Dynamic Systems 2013

Guest Editors: Zhiwei Gao, Dexing Kong, Chuanhou Gao, and Michael Chen

Copyright © 2013 Hindawi Publishing Corporation. All rights reserved.

This is a special issue published in "Journal of Applied Mathematics." All articles are open access articles distributed under the Creative Commons Attribution License, which permits unrestricted use, distribution, and reproduction in any medium, provided the original work is properly cited.

Editorial Board

Saeid Abbasbandy, Iran
Mina B. Abd-El-Malek, Egypt
Mohamed A. Abdou, Egypt
Subhas Abel, India
Mostafa Adimy, France
Carlos J. S. Alves, Portugal
Mohamad Alwash, USA
Igor Andrianov, Germany
Sabri Arik, Turkey
Francis T.K. Au, Hong Kong
Olivier Bahn, Canada
Roberto Barrio, Spain
Alfredo Bellen, Italy
Jafar Biazar, Iran
Hester Bijl, The Netherlands
Anjan Biswas, Saudi Arabia
Stephane P.A. Bordas, USA
James Robert Buchanan, USA
Alberto Cabada, Spain
Xiao Chuan Cai, USA
Jinde Cao, China
Alexandre Carvalho, Brazil
Song Cen, China
Qianshun S. Chang, China
Tai-Ping Chang, Taiwan
Shih-sen Chang, China
Rushan Chen, China
Xinfu Chen, USA
Ke Chen, UK
Eric Cheng, Hong Kong
Francisco Chiclana, UK
Jen-Tzung Chien, Taiwan
C. S. Chien, Taiwan
Han H. Choi, Republic of Korea
Tin-Tai Chow, China
M. S. H. Chowdhury, Malaysia
Carlos Conca, Chile
Vitor Costa, Portugal
Livija Cveticanin, Serbia
Eric de Sturler, USA
Orazio Descalzi, Chile
Kai Diethelm, Germany
Vit Dolejsi, Czech Republic
Bo-Qing Dong, China
Magdy A. Ezzat, Egypt
Meng Fan, China
Ya Ping Fang, China
Antonio J. M. Ferreira, Portugal
Michel Fliess, France
M. A. Fontelos, Spain
Huijun Gao, China
Bernard J. Geurts, The Netherlands
Jamshid Ghaboussi, USA
Pablo González-Vera, Spain
Laurent Gosse, Italy
K. S. Govinder, South Africa
Jose L. Gracia, Spain
Yuantong Gu, Australia
Zhihong GUAN, China
Nicola Guglielmi, Italy
Frederico G. Guimarães, Brazil
Vijay Gupta, India
Bo Han, China
Maoan Han, China
Pierre Hansen, Canada
Ferenc Hartung, Hungary
Xiaoqiao He, Hong Kong
Luis Javier Herrera, Spain
J. Hoenderkamp, The Netherlands
Ying Hu, France
Ning Hu, Japan
Zhilong L. Huang, China
Kazufumi Ito, USA
Takeshi Iwamoto, Japan
George Jaiani, Georgia
Zhongxiao Jia, China
Tarun Kant, India
Ido Kanter, Israel
Abdul Hamid Kara, South Africa
Hamid Reza Karimi, Norway
Jae-Wook Kim, UK
Jong Hae Kim, Republic of Korea
Kazutake Komori, Japan
Fanrong Kong, USA
Vadim . Krysko, Russia
Jin L. Kuang, Singapore
Miroslaw Lachowicz, Poland
Hak-Keung Lam, UK
Tak-Wah Lam, Hong Kong
PGL Leach, Cyprus
Yongkun Li, China
Wan-Tong Li, China
J. Liang, China
Ching-Jong Liao, Taiwan
Chong Lin, China
Mingzhu Liu, China
Chein-Shan Liu, Taiwan
Kang Liu, USA
Yansheng Liu, China
Fawang Liu, Australia
Shutian Liu, China
Zhijun Liu, China
Julián López-Gómez, Spain
Shiping Lu, China
Gert Lube, Germany
Nazim Idrisoglu Mahmudov, Turkey
Oluwole Daniel Makinde, South Africa
Francisco J. Marcellán, Spain
Guiomar Martín-Herrán, Spain
Nicola Mastronardi, Italy
Michael McAleer, The Netherlands
Stephane Metens, France
Michael Meylan, Australia
Alain Miranville, France
Ram N. Mohapatra, USA
Jaime E. Munoz Rivera, Brazil
Javier Murillo, Spain
Roberto Natalini, Italy
Srinivasan Natesan, India
Jiri Nedoma, Czech Republic
Jianlei Niu, Hong Kong
Roger Ohayon, France
Javier Oliver, Spain
Donal O'Regan, Ireland
Martin Ostoja-Starzewski, USA
Turgut Öziş, Turkey
Claudio Padra, Argentina
Reinaldo Martinez Palhares, Brazil
Francesco Pellicano, Italy
Juan Manuel Peña, Spain
Ricardo Perera, Spain
Malgorzata Peszynska, USA
James F. Peters, Canada
Mark A. Petersen, South Africa
Miodrag Petkovic, Serbia

Vu Ngoc Phat, Vietnam
Andrew Pickering, Spain
Hector Pomares, Spain
Maurizio Porfiri, USA
Mario Primicerio, Italy
Morteza Rafei, The Netherlands
Roberto Renò, Italy
Jacek Rokicki, Poland
Dirk Roose, Belgium
Carla Roque, Portugal
Debasish Roy, India
Samir H. Saker, Egypt
Marcelo A. Savi, Brazil
Wolfgang Schmidt, Germany
Eckart Schnack, Germany
Mehmet Sezer, Turkey
Naseer Shahzad, Saudi Arabia
Fatemeh Shakeri, Iran
Jian Hua Shen, China
Hui-Shen Shen, China
Fernando Simões, Portugal
Theodore E. Simos, Greece
Abdel-Maksoud A. Soliman, Egypt
Xinyu Song, China
Qiankun Song, China
Yuri N. Sotskov, Belarus
Peter J. C. Spreij, The Netherlands
Niclas Strömberg, Sweden
Ray KL Su, Hong Kong
Jitao Sun, China
Wenyu Sun, China
XianHua Tang, China
Alexander Timokha, Norway
Mariano Torrisi, Italy
Jung-Fa Tsai, Taiwan
Ch Tsitouras, Greece
Kuppalapalle Vajravelu, USA
Alvaro Valencia, Chile
Erik Van Vleck, USA
Ezio Venturino, Italy
Jesus Vigo-Aguiar, Spain
Michael N. Vrahatis, Greece
Baolin Wang, China
Mingxin Wang, China
Qing-Wen Wang, China
Guangchen Wang, China
Junjie Wei, China
Li Weili, China
Martin Weiser, Germany
Frank Werner, Germany
Shanhe Wu, China
Dongmei Xiao, China
Gongnan Xie, China
Yuesheng Xu, USA
Suh-Yuh Yang, Taiwan
Bo Yu, China
Jinyun Yuan, Brazil
Alejandro Zarzo, Spain
Guisheng Zhai, Japan
Jianming Zhan, China
Zhihua Zhang, China
Jingxin Zhang, Australia
Shan Zhao, USA
Chongbin Zhao, Australia
Renat Zhdanov, USA
Hongping Zhu, China

Contents

Modeling and Control of Complex Dynamic Systems 2013, Zhiwei Gao, Dexing Kong, Chuanhou Gao, and Michael Chen
Volume 2013, Article ID 151372, 3 pages

Distributed Adaptive Synchronization for Complex Dynamical Networks with Uncertain Nonlinear Neutral-Type Coupling, Shi Miao and Li Junmin
Volume 2013, Article ID 548375, 12 pages

H_∞ **Formation Control and Obstacle Avoidance for Hybrid Multi-Agent Systems**, Dong Xue, Jing Yao, and Jun Wang
Volume 2013, Article ID 123072, 11 pages

Dynamic Modeling and Control of Electromechanical Coupling for Mechanical Elastic Energy Storage System, Yang Yu and Zengqiang Mi
Volume 2013, Article ID 603063, 11 pages

PDE Modeling of a Microfluidic Thermal Process for Genetic Analysis Application, Reza Banaei Khosroushahi, Horacio J. Marquez, Jose Martinez-Quijada, and Christopher J. Backhouse
Volume 2013, Article ID 767853, 12 pages

Block Empirical Likelihood for Longitudinal Single-Index Varying-Coefficient Model, Yunquan Song, Ling Jian, and Lu Lin
Volume 2013, Article ID 792196, 10 pages

Adaptive Synchronization of Complex Dynamical Networks with State Predictor, Yuntao Shi, Bo Liu, and Xiao Han
Volume 2013, Article ID 394137, 8 pages

An Irregular Flight Scheduling Model and Algorithm under the Uncertainty Theory, Deyi Mou and Wanlin Zhao
Volume 2013, Article ID 361926, 8 pages

Dynamics Control of the Complex Systems via Nondifferentiability, Carmen Nejneru, Anca Nicuţă, Boris Constantin, Liliana Rozemarie Manea, Mirela Teodorescu, and Maricel Agop
Volume 2013, Article ID 137056, 12 pages

Modeling and Analysis of Epidemic Diffusion with Population Migration, Ming Liu and Yihong Xiao
Volume 2013, Article ID 583648, 8 pages

A New Type of Distributed Parameter Control Systems: Two-Point Boundary Value Problems for Infinite-Dimensional Dynamical Systems, De-Xing Kong and Fa Wu
Volume 2013, Article ID 454857, 3 pages

Multiangle Social Network Recommendation Algorithms and Similarity Network Evaluation, Jinyu Hu, Zhiwei Gao, and Weisen Pan
Volume 2013, Article ID 248084, 8 pages

Optimal Combination of EEFs for the Model Reduction of Nonlinear Partial Differential Equations, Jun Shuai and Xuli Han
Volume 2013, Article ID 347248, 6 pages

Analysis of Average Shortest-Path Length of Scale-Free Network, Guoyong Mao and Ning Zhang
Volume 2013, Article ID 865643, 5 pages

A Data-Based Approach for Modeling and Analysis of Vehicle Collision by LPV-ARMAX Models, Qiugang Lu, Hamid Reza Karimi, and Kjell Gunnar Robbersmyr
Volume 2013, Article ID 452391, 9 pages

Hindawi Publishing Corporation
Journal of Applied Mathematics
Volume 2013, Article ID 151372, 3 pages
http://dx.doi.org/10.1155/2013/151372

Editorial

Modeling and Control of Complex Dynamic Systems 2013

Zhiwei Gao,[1] Dexing Kong,[2] Chuanhou Gao,[2] and Michael Chen[3]

[1] *Faculty of Engineering and Environment, Northumbria University, Newcastle upon Tyne NE1 8ST, UK*
[2] *Department of Mathematics, Zhejiang University, Hang Zhou 310027, China*
[3] *Department of Mechanical Engineering, The University of Hong Kong, Hong Kong*

Correspondence should be addressed to Zhiwei Gao; zhiwei.gao@northumbria.ac.uk

Received 28 October 2013; Accepted 28 October 2013

Copyright © 2013 Zhiwei Gao et al. This is an open access article distributed under the Creative Commons Attribution License, which permits unrestricted use, distribution, and reproduction in any medium, provided the original work is properly cited.

1. Introduction

The concept of complex dynamic systems arises in many research fields and practical applications, which can be found anywhere such as in the areas of energy generation and distribution, ecosystems, health delivery, safety and security systems, telecommunications, transportation networks, biomedical systems, and the rapidly emerging research topics seeking to be understood and analyzed. A complex process may be characterized by a system with environmental uncertainties, communication time delay, stochastic perturbation, hybrid dynamics, distributed dynamics, chaotic dynamics, and systems with collective behavior. As a result, modeling and control of a complex system are interesting but challenging. Following the great success of the special issue last year [1], the guest editorial team is pleased to organize the second special issue for "Modelling and Control for Complex Dynamic Systems."

This special issue aims to provide a platform for researchers to discuss various mathematical methods and techniques for modeling and control of complex dynamic systems and to identify critical issues and challenges for future investigation in this field. The special issue received 56 submissions, and 14 papers are selected after a strict peer review procedure, indicating an acceptance rate at 25%.

2. Modeling of Complex Dynamic Systems

Partial differential equations can be used to describe infinite-dimensional dynamics of a complex process. In the paper by Khosroushahi et al. the infinite-dimensional dynamics of a prototype micro-fluidic thermal process is investigated for genetic analysis purposes. Compared with conventional lumped modeling approaches, the infinite-dimensional dynamic model is more effective to be used to develop a precise control framework to meet the very tight performance requirements. The equations of the dynamic models are solved analytically and the proposed models are validated by a known experimentally verified model. The model framework can be used for designing a precise tracking controller applicable to the selected Lab-on-a-Chip device.

Model reduction is a technique to reduce model dimensions particularly for a high-dimensional system. It is noted that, for certain types of nonlinear partial differential equations, some neglectful modes could be crucial in the modeling although they only represent a tiny amount of energy. In the work by J. Shuai and X. Han, an optimal EEF (empirical eigenfunction) method is proposed for model reduction of nonlinear partial differential equations, which is based on the basis function transformation from the initial EEFs. The present model reduction method can generate a lower-dimensional dynamic model but keep dynamical information of neglectful modes, leading to a more precise model for the partial differential equations. The effectiveness and feasibility for model reduction are verified by simulated results.

Recently, uncertainty theory has attracted attention on the modeling of complex problems. For instance, flight scheduling, practically for the case with irregular flights, is a real-time optimization problem. Due to the uncertainty of the problem and insufficiency of the data in the decision-making procedure, the traditional modeling tool (such as probability theory) becomes invalid. In the paper by D. Mou

and W. Zhao, the uncertainty theory is applied to develop an uncertain programming model with constraints. In the model, the total delay minutes of passengers are considered as the optimization objective by reassigning fleets in response to the irregular flights with the constraints in available resources and estimated cost of airlines. The model and algorithms are demonstrated and illustrated by a numerical example.

Ordinary differential equations are an alternative for modeling. In the work by M. Liu and Y. Xiao an improved Susceptible-Infected-Susceptible (SIS) epidemic diffusion model with population migration between two cities is modeled. The global stability conditions are discussed for both disease-free equilibrium and endemic equilibrium. Unequal migration rates are taken into account and only susceptible individuals can migrate between the two cities, which form the main feature of the proposed model. In terms of numerical simulation results, the stability of the epidemic diffusion system is demonstrated.

Data-driven method is a powerful tool for modelling of a dynamic system. In the paper by Q. Lu et al. a mathematical model of vehicle crash, namely, LPV-ARMAX model, is established by using data-driven techniques to simulate the car-to-pole collision with different initial impact velocities. The parameters of the LPV-ARMAX model are assumed to have dependence on the initial impact velocities, and the LPV-ARMAX model is comparatively simple and applicable to predict the responses of new collision situations different from the ones used for identification. Moreover, the high fidelity of the LPV-ARMAX model is demonstrated by using real test data.

Varying-coefficient modeling method is useful to describe a dynamic process. In the paper by Y. Song et al. the block empirical likelihood procedure is employed to establish a longitudinal single-index varying coefficient model with the capability of accommodating within-group correlations. In comparison with normal approximations, the proposed method does not need a consistent estimator for the asymptotic covariance matrix, indicating an easier way to conduct inference for parametric components of the model. The proposed modeling methods are demonstrated by numerical simulations.

3. Control of Complex Dynamic Systems

Dynamics control of a complex system is interesting but challenging. In the work by C. Nejneru et al. a novel approach is addressed for the control of complex systems dynamics using nondifferentiability of the movement curves in a complex system. The standard properties of the complex system such as emergence, self-organisation, and adaptability can be controlled through the non-differentiability of the motion curves of the subsystems that constitute the complex system.

Electromechanical coupling for mechanical elastic energy storage forms a complex system. In the work by Y. Yu and Z. Mi the modeling and control of the complex electromechanical system are both investigated. The theory of direct feedback linearization is applied to decouple the nonlinear dynamic model and convert the developed model from nonlinear to linear. Optimal control theory is then utilized to achieve speed tracking control for the linearized systems. The simulation results have demonstrated the feasibility and efficiency of the proposed model and control algorithms by evaluating three scenarios.

Control and obstacle avoidance for hybrid multiagent systems is an interesting topic. In the paper by D. Xue et al., an H1 formation method is proposed to handle a group of agents navigating in either a free or an obstacle-laden environment with changing formation subject to internal or external events. The disturbed situation and the attenuation level of the obstacle avoidance can be characterized by the formation information and its H1 formation norm, respectively. Simulation results show that the proposed formation algorithms can effectively avoid penetration into obstacles while accomplishing the prespecified global objective.

Two-point boundary value problems for infinite-dimensional dynamical systems were first introduced by Kong in 2010 (see pages 121-122 in [2]). This kind of problems is an emerging topic to solve the distributed parameter control systems. The survey paper contributed by D. X. Kong and E. Wu, describes a new type of distributed parameter control systems related to two-point boundary value problems for infinite-dimensional dynamical systems and reviews the results which have been obtained so far. Furthermore, some unresolved questions are proposed which aim to stimulate further researches in this interesting topic.

In the paper by M. Shi and J. Li, distributed adaptive synchronization control of complex dynamical networks with nonlinearly derivative coupling is investigated. An effective distributed adaptive technique is addressed to eliminate the effect of time-varying parameters and synchronize the considered network with a given trajectory in the sense of square error norm. The applicability and feasibility of the approach are illustrated by an example.

The work, contributed by Y. Shi et al., dealt with adaptive synchronization problem of complex dynamical networks with nonlinear dynamics. By using Lyapunov method and local adaptive strategy, it is shown that the network can synchronize with the synchronous states. Moreover, the convergent speed of complex dynamical networks can be increased via designing a state predictor. The results are finally demonstrated and illustrated by numerical simulations.

4. Computing/Evaluating Algorithms for Complex Networks

The computation of the average shortest-path length for a large scale-free network needs much memory space and computing time. In the work by G. Mao and N. Zhang, the relationship between the computing time of a single-source shortest-path length of node and the features of nodes are investigated. A native array and multimap representation of the network are addressed to reduce the memory consumption of the network. A simplified load-balancing model is applied to a network of tens of millions of nodes. By using

experiments, it is shown that the model proposed can be used to effectively solve the load-imbalance problem of a large scale-free network.

In the work by J. Hu et al., multi-angle social network recommendation algorithms are addressed and the similarity network evaluation method is proposed. The six algorithms for multi-angle social network recommendations are investigated and evaluated. Compared with the traditional recall/precision method, the similarity network evaluation method has an advantage of the effectiveness, visualization, and simple procedure for use. The comparisons of the six algorithms are finally discussed, leading to explicit comments on the algorithms.

5. Conclusion

The 14 selected papers can roughly be categorized into modeling of complex systems, control of complex systems, and computing/evaluating algorithms of complex networks, which can reflect recent progresses in the research fields on complex dynamic systems to some broadness and deepness. We hope this special issue will further stimulate the researches of complex dynamic systems from a variety of academic societies and industrial communities.

Acknowledgments

Firstly, sincere thanks are addressed to all the authors who responded to the call of the special issue. Secondly, the guest editor team is deeply indebted to the volunteer contributions from the reviewers, whose crucial and valuable comments lay a foundation of the successful selection of the 14 interesting papers.

Zhiwei Gao
Dexing Kong
Chuanhou Gao
Michael Chen

References

[1] Z. Gao, D. Kong, and C. Gao, "Modeling and control of complex dynamic systems: applied mathematical aspects," *Journal of Applied Mathematics*, vol. 2012, Article ID 869792, 5 pages, 2012.

[2] D. X. Kong, *Partial Differential Equations*, Higher Education Press, Beijing, China, 2010, (Chinese).

Hindawi Publishing Corporation
Journal of Applied Mathematics
Volume 2013, Article ID 548375, 12 pages
http://dx.doi.org/10.1155/2013/548375

Research Article

Distributed Adaptive Synchronization for Complex Dynamical Networks with Uncertain Nonlinear Neutral-Type Coupling

Shi Miao and Li Junmin

Department of Mathematics, Xidian University, Xi'an 710071, China

Correspondence should be addressed to Li Junmin; jmli@mail.xidian.edu.cn

Received 10 July 2013; Revised 23 August 2013; Accepted 28 August 2013

Academic Editor: Zhiwei Gao

Copyright © 2013 S. Miao and L. Junmin. This is an open access article distributed under the Creative Commons Attribution License, which permits unrestricted use, distribution, and reproduction in any medium, provided the original work is properly cited.

Distributed adaptive synchronization control for complex dynamical networks with nonlinear derivative coupling is proposed. The distributed adaptive strategies are constituted by directed connections among nodes. By means of the parameters separation, the nonlinear functions can be transformed into the linearly form. Then effective distributed adaptive techniques are designed to eliminate the effect of time-varying parameters and made the considered network synchronize a given trajectory in the sense of square error norm. Furthermore, the coupling matrix is not assumed to be symmetric or irreducible. An example shows the applicability and feasibility of the approach.

1. Introduction

A complex network is a large set of interconnected nodes, where the nodes represent individuals in the graph and the edges represent the connections among them, such as climate system [1], biological neural networks [2], human brain system [3]. Many natural and man-made systems can be modeled and characterized by complex networks successfully [4]. Such systems may be characterized by a system with uncertainties, time delays, nonlinearity, neutral properties, hybrid dynamics, distributed dynamics and chaotic dynamics.

Synchronization phenomena has been found in different forms in complex networks, such as fireflies in the forest, description of hearts, and routing messages in the internet. Thus synchronization is one of meaningful issues in dynamical characteristics of the complex dynamical networks. A considerable number of papers on this topic have appeared (see [5–7] and references therein.)

Recently, various control techniques have been reported to achieve networks synchronization (see [4, 8–16] and references therein) Some control schemes [8–13] were based on a solution of the homogenous system, in which it may be difficult to obtain the state information of an isolated node. Consequently, utilizing the information from neighborhood to realize the network synchronization is more reasonable. Paper [17] introduced the concept of control topology to describe the whole controller structure. In [18], based on local information of node dynamics, an effective distributed adaptive strategy was designed to tune the coupling weights of a network. A considerable number of controlled synchronization techniques have been derived for complex dynamic networks based on the assumption which is the coupled nodes of CDN with the same dynamics (see the above papers and the references therein). In reality, complex networks are more likely to have different nodes for different dynamics. For example, in a multi-robot system, the robots can have distinct dynamic structures or different parameters. Recently, special attention has been focused on the synchronization of complex dynamical networks with nonidentical nodes [19–22]. Paper [20] investigated the synchronization problem of a complex network with nonidentical nodes via open-loop controllers. The paper [22] considered nonlinearly coupled networks with non-identical nodes and designed pinning control to obtain synchronization criteria. On the other hand, many real-world network systems' structure will change over time and contain unknown parameters. Very recently, some papers studied complex networks with

unknown time-varying coupling strength [23–26]. In these results, non-identical nodes were not considered. Only in [21], the time-varying complex network with non-identical nodes was investigated, and a criterion of global bounded synchronization of the maximum state deviation between nodes was developed.

In other aspects, new complex networks models are proposed to reflect the complexity from the network structure. Thus, the problem of neutral-type couplings has also been widely investigated [27–31]. However, in the above studies, only linear derivative coupling is considered. More recently, [32] studied the synchronization in a class of dynamical networks with distributed delays and nonlinear derivative coupling. Considering the preceding discussion, non-identical nodes complex dynamic network with nonlinear derivative coupling, and time-varying coupling strength is not concerned yet.

Inspired by the aforementioned results, the problem of adaptive synchronization is studied for complex dynamical networks with non-identical nodes, nonlinearly derivative couplings, and unknown time-varying coupling strength. A prominent feature of this network is that its complexity originates not only from the nonlinear dynamics of the nodes, but also from the complex coupling strength. The difficulty in dealing with the nonlinearly derivative couplings with unknown time-varying parameters is solved by using the parameter separation method. The distributed adaptive learning laws of periodically time-varying and constant parameters and the distributed adaptive controllers are constructed to guarantee that the system is asymptotically stable and that all closed loop signals are bounded.

The remainder of the paper is organized as follows. The problem statement and preliminaries are given in Section 2. Section 3 gives the main results and proofs. In Section 4, an illustrative example is provided to verify the theoretical results. Finally, conclusion is given.

2. Problem Statement and Preliminaries

The complex dynamical network is described as

$$\begin{aligned}\dot{x}_i(t) = f_i(x_i(t)) + \sum_{J=1}^{N} a_{ij}\Gamma g\left(x_j(t), \varphi_i(t)\right) \\ + \sum_{j=1}^{N} b_{ij}\Gamma k\left(\dot{x}_j(t), \beta_i(t)\right), \quad i = 1, 2, \ldots, N,\end{aligned} \tag{1}$$

where $x_i(t) = [x_{i1}(t), x_{i2}(t), \ldots, x_{in}(t)]^T \in R^n$ is the state vector of the ith node, $f_i(\cdot) : R^n \to R^n$ is a vector-valued continuous function, and $g(\cdot,\cdot)$, $k(\cdot,\cdot) : R^n \times R \to R^n$ are unknown continuous nonlinear vector-valued functions, $\varphi_i(t)$, $\beta_i(t)$ represent the unknown time-varying functions, the inner-coupling matrix $\Gamma = \mathrm{diag}(\gamma_1, \ldots, \gamma_n)$ is positive definite. $A = (a_{ij})_{N\times N}$ and $B = (b_{ij})_{N\times N}$ are the coupling configuration matrices, which satisfying $\sum_{j=1}^{N} a_{ij} = \sum_{j=1}^{N} b_{ij} = 0$ and defined as follows: if there is a connection between node i and node j $(i \neq j)$, then $a_{ij} > 0$, $b_{ij} > 0$, otherwise, $a_{ij} = b_{ij} = 0$.

Remark 1. It should be pointed out that the nonlinear derivative couplings consist of more information in CDN than the linear derivative couplings in [28], the challenge problem in (1) is due to the uncertain nonlinear neutral-type coupling $\sum_{j=1}^{N} b_{ij}\Gamma k(\dot{x}_j(t), \beta_i(t))$. For the unknown parameter $\beta_i(t)$ and the nonlinear function $k(\dot{x}_j(t), \beta_i(t))$, in this paper, we shall overcome the obstacle though the domination technique and the parameters separation principle. Under later assumption, we can "separate" the parameters from the nonlinear function.

Define synchronization error as

$$e_i(t) = x_i(t) - s(t), \quad i = 1, 2, \ldots, N, \tag{2}$$

where $s(t) \in R^n$ is a solution of the dynamics of the isolated node to which all $x_i(t)$ are expected to synchronize.

Then, (1) is said to be asymptotic synchronization in the L_T^2 norm sense if

$$\lim_{t\to\infty} \int_{t-T}^{t} \left\|e_i(\tau)\right\|^2 d\tau = 0, \quad i = 1, 2, \ldots, N \tag{3}$$

and the system (1) is said to be globally asymptotically synchronized onto state $s(t)$ if

$$\lim_{t\to\infty} e_i(t) = 0, \quad i = 1, 2, \ldots, N. \tag{4}$$

To achieve the control objective in (3) and (4), we need an adaptive control strategy to nodes in network (1). Then, the controlled network is given by

$$\begin{aligned}\dot{x}_i(t) = f_i(x_i(t)) + \sum_{j=1}^{N} a_{ij}\Gamma g\left(x_j(t), \varphi_i(t)\right) \\ + \sum_{j=1}^{N} b_{ij}\Gamma k\left(\dot{x}_j(t), \beta_i(t)\right) \\ + u_i(t), \quad i = 1, 2, \ldots, N,\end{aligned} \tag{5}$$

where $u_i(t) = [u_{i1}(t), u_{i2}(t), \ldots, u_{in}(t)]^T \in R^n$, $i = 1, 2, \ldots, N$, are the adaptive controllers to be designed. Since the row sum of coupling matrix is zero, it is easily obtained that $\sum_{j=1}^{N} a_{ij}\Gamma g(s(t), \varphi_i(t)) = \sum_{j=1}^{N} b_{ij}\Gamma k(\dot{s}(t), \beta_i(t)) = 0$, which implies the dynamical error equations as

$$\begin{aligned}\dot{e}_i(t) = \dot{x}_i(t) - \dot{s}(t) = f_i(x_i(t)) \\ + \sum_{j=1}^{N} a_{ij}\Gamma\left(g\left(x_j(t), \varphi_i(t)\right) - g\left(s(t), \varphi_i(t)\right)\right) \\ + \sum_{j=1}^{N} b_{ij}\Gamma\left(k\left(\dot{x}_j(t), \beta_i(t)\right) - k\left(\dot{s}(t), \beta_i(t)\right)\right) \\ - \dot{s}(t) + u_i(t).\end{aligned} \tag{6}$$

Our objective is to design a distributed adaptive control law $u_i(t)$ so as to obtain the convergence of the synchronization errors.

In order to derive the main results, the following assumptions and lemmas are introduced.

Assumption 2 (Lipschits condition). For the system (1), there exist positive constants $l_i > 0$, $i = 1, \ldots, N$ such that

$$\left\| f_i(x) - f_i(y) \right\| \le l_i \left\| x - y \right\|, \quad \forall x, y \in R^n, \ 1 \le i \le N. \tag{7}$$

Remark 3. For many well-known systems, such as Lorenz's system, Chen's system, and Lü's system, the above condition is satisfied.

Assumption 4 (see [33]). For the unknown continuous functions $g(\cdot,\cdot)$, $k(\cdot,\cdot)$, the following inequality holds:

$$\begin{aligned} &\left\| g(x_j(t), \varphi_i(t)) - g(s(t), \varphi_i(t)) \right\|^2 \\ &\quad \le \left\| x_j(t) - s(t) \right\|^2 h\left(x_j(t), s(t)\right) \lambda\left(\varphi_i(t)\right), \\ &\left| k\left(\dot{x}_j(t), \beta_i(t)\right) - k\left(\dot{s}(t), \beta_i(t)\right) \right| \\ &\quad \le M\left(\beta_i(t)\right) \left| \dot{x}_j(t) - \dot{s}(t) \right| \triangleq M_i(t) \left| \dot{e}_j(t) \right|, \end{aligned} \tag{8}$$

where $h(\cdot,\cdot)$ is an known nonnegative continuous function $\lambda(\cdot)$ is a unknown nonnegative continuous function, $M(\cdot)$ or $M_i(\cdot)$ is an $n \times n$ unknown nonnegative continuous function matrix.

Remark 5. It is well known that the estimation of unknown nonlinear parameters in the systems is a difficult problem. In this paper, we separate the unknown parameters from the nonlinear function in (8), according to the separation principle in [33]; thus, Assumption 4 is reasonable and easily obtained. By using Assumption 4, we are able to solve the synchronization problem for a class of nonlinearly parameterized systems with nonlinear derivative couplings.

Assumption 6. In the given networks in (1), $\varphi_i(t)$, $\beta_i(t)$ are unknown time-varying periodic functions with a known period T.

From Assumption 6, it is easy to see that $\lambda(\varphi_i(t))$ and each element in $M_i(t)$ are periodic functions with the same period T. Suppose

$$\lambda\left(\varphi_i(t)\right) = \phi_i(t) + \theta_i, \tag{9}$$

where $\phi_i(t)$ is an unknown continuous periodic function with a known period T and θ_i is an unknown constant parameter.

Assumption 7. In network (1), the inner coupling matrix Γ and $h(\cdot,\cdot)$ satisfies

$$\begin{aligned} &\max\left(\|\Gamma\|, \max\left(|\gamma_i|\right)\right) \le \gamma, \quad h\left(x_i(t), s(t)\right) < H, \\ &\qquad\qquad\qquad\qquad i = 1, 2, \ldots, N, \end{aligned} \tag{10}$$

where γ, H are positive constants.

Assumption 8. Assume that the state and the state derivative of system (1) are measurable.

Remark 9. This assumption is necessary to design controller and adaptive laws. Assumption 8 seems to be restrictive. The observer for state derivative will be considered in the near future.

Lemma 10 (Young's inequality). *For vectors $x, y \in R^n$, and any positive constant c, the following matrix inequality holds:*

$$x^T y \le c x^T x + \frac{1}{4c} y^T y. \tag{11}$$

Lemma 11. *For any vectors $x, y \in R^n$, according to the properties of matrix trace, the following equality holds:*

$$x^T y = \operatorname{tr}\left(y x^T\right) = \operatorname{tr}\left(x y^T\right). \tag{12}$$

Lemma 12 (Barbalat's Lemma [34]). *If $e(t) \in L_2$ and $\dot{e}(t) \in L_\infty$, then $\lim_{t\to\infty} e(t) = 0$, where $L_2 = \{x \mid x : [0,\infty) \to R, (\int_0^\infty |x(t)|^2)^{1/2} < \infty\}$ and $L_\infty = \{x \mid x : [0,\infty) \to R, \sup_{t\ge 0}|x(t)| < \infty\}$.*

Lemma 13. *For a positive constant T, if $\forall t \ge 0$, $f(t)$ is a continuous function and $\int_{t-T}^{t} f(\tau)\, d\tau$ exists and is bounded with M. Then, $f(t)$ is bounded.*

Proof. In fact, if $f(t)$ is unbounded, we can get $\forall N > 0$, $\exists \tau \in [t-T, t]$, $f(\tau) > N$. As $f(t)$ is continuous function, according to the properties of the continuous functions, we have $\exists \varepsilon > 0$ $\forall k \in [\tau-\varepsilon, \tau+\varepsilon] \subset [t-T, t]$, $f(k) > N$; then $\int_{t-T}^{t} f(\tau)\, d\tau \ge \int_{\tau-\varepsilon}^{\tau+\varepsilon} f(\tau)\, dt \ge 2\varepsilon N$. We can choose $N = (M/2\varepsilon) + 1$; then $\int_{t-T}^{t} f(\tau)\, d\tau > M$; this is a contradiction with the assumption. The proof is completed. □

3. Adaptive Synchronization of the Complex Dynamical Networks

In this section, distributed adaptive controller and distributed adaptive laws are designed to control the given system to synchronize the given trajectory $s(t)$, and the synchronization process is proved.

Considering the controlled networks, we design the controller by

$$\begin{aligned} u_i(t) &= \dot{s}(t) - f_i(s(t)) \\ &\quad - \gamma H e_i(t) \sum_{j=1}^{N} a_{ji}^2 \left(\widehat{\phi}_j(t) + \widehat{\theta}_j(t)\right) \\ &\quad - \gamma \sum_{j=1}^{N} \left|b_{ij}\right| \operatorname*{diag}_{1\le j\le N}\left(\operatorname{sign}\left(e_{ij}(t)\right)\right) \widehat{M}_i(t) \left|\dot{e}_j(t)\right|, \end{aligned} \tag{13}$$

where γ, H satisfy condition (10), N is the node number, and $\widehat{\phi}_i(t)$, and $\widehat{\theta}_i(t)$, are $\widehat{M}_i(t)$ used to estimate $\phi_i(t)$, θ_i, $M_i(t)$. $|\dot{e}_j(t)| = (|\dot{e}_{j1}(t)|, \ldots, |\dot{e}_{jn}(t)|)^T$.

The constant parameter distributed update law is designed as follows:

$$\dot{\widehat{\theta}}_i(t) = r_i \sum_{j=1}^{N} a_{ij}^2 e_j^T(t)\, e_j(t) \tag{14}$$

and the time-varying distributed periodic adaptive learning laws as

$$\widehat{\phi}_i(t) = \begin{cases} 0, & t \in [-T, 0) \\ q_{i0}(t) \sum_{j=1}^{N} a_{ij}^2 e_j^T(t) e_j(t), & t \in [0, T) \\ \widehat{\phi}_i(t-T) + q_i \sum_{j=1}^{N} a_{ij}^2 e_j^T(t) e_j(t), & t \in [T, +\infty), \end{cases} \tag{15}$$

$$\widehat{M}_i(t) = \begin{cases} 0, & t \in [-T, 0) \\ f_{i0}(t) \sum_{j=1}^{N} \left|b_{ij}\right| \left|e_i(t)\right| \left|\dot{e}_j^T(t)\right|, & t \in [0, T) \\ \widehat{M}_i(t-T) + f_i \sum_{j=1}^{N} \left|b_{ij}\right| \left|e_i(t)\right| \left|\dot{e}_j^T(t)\right|, & t \in [T, +\infty), \end{cases} \tag{16}$$

where r_i, q_i, and f_i are positive constants and $q_{i0}(t)$, $f_{i0}(t)$ are continuous and strictly increasing nonnegative functions satisfying $q_{i0}(0) = 0$, $q_{i0}(T) = q_i$, and $f_{i0}(0) = 0$, $f_{i0}(T) = f_i$ which ensure that $\widehat{\phi}_i(t)$, $\widehat{M}_i(t)$ are continuous in $t = iT$, $i = 1, 2, \ldots, N$, $|e_j(t)| = (|e_{j1}(t)|, \ldots, |e_{jn}(t)|)^T$.

The following theorem will give a sufficient condition for the controlled network in (5) to be asymptotical synchronization.

Theorem 14. *Under Assumptions 2–7, the control law* (13) *with the adaptive learning laws* (14)–(16) *guarantees the controlled networks in* (5) *achieve asymptotic synchronization in the L_T^2 norm sense. All closed-loop signals are bounded. Furthermore, if $k(\cdot,\cdot)$ is bounded function, we can obtain globally asymptotical synchronization.*

Proof. Define a Lyapunov-Krasovskii-like function as follows:

$$\begin{aligned} V(t) = {} & \frac{1}{2}\sum_{i=1}^{N} e_i^T e_i + \frac{\gamma H}{2}\sum_{i=1}^{N}\int_{t-T}^{t} q_i^{-1}\widetilde{\phi}_i^2(\tau)\, d\tau \\ & + \frac{\gamma H}{2}\sum_{i=1}^{N} r_i^{-1}\left(\widetilde{\theta}_i(t) + L\right)^2 \\ & + \frac{\gamma}{2}\sum_{i=1}^{N}\int_{t-T}^{t} f_i^{-1}\operatorname{tr}\left(\widetilde{M}_i(\tau)\widetilde{M}_i^T(\tau)\right) d\tau, \\ & t \in [0, \infty), \end{aligned} \tag{17}$$

where $\widetilde{\phi}_i(t) = \phi_i(t) - \widehat{\phi}_i(t)$, $\widetilde{\theta}_i(t) = \theta_i - \widehat{\theta}_i(t)$, $\widetilde{M}_i(t) = M_i(t) - \widehat{M}_i(t)$, and L is a sufficiently large positive constant which will be determined later.

It should be noted that we define $\phi_i(t) = \phi_i(0)$, $M_i(t) = M_i(0)$ $t \in [-T, 0)$; then, from the adaptive laws (15) and (16), we get

$$\begin{aligned} \widetilde{\phi}_i^2(t-T) &= \phi_i^2(t-T) = \phi_i^2(0), \\ \widetilde{M}_i(t-T)\widetilde{M}_i^T(t-T) &= M_i(t-T)M_i^T(t-T) \\ &= M_i(0)M_i^T(0), \quad t \in [0, T]. \end{aligned} \tag{18}$$

Firstly, the finiteness property of $V(t)$ for the period $[0, T)$ is given.

Consider the system (6) and the proposed control laws (14)–(16); it can be seen that the right-hand side of (6) is continuous with respect to all arguments. According to the existence theorem of differential equation, (6) has unique solution in the interval $[0, T_1) \subset [0, T)$ with $0 < T_1 \leq T$. This can guarantee the boundedness of $V(t)$ over $[0, T_1)$. Therefore, we need only focus in the interval $[T_1, T)$.

The derivative of $V(t)$ with respect to time is given by

$$\begin{aligned} \dot{V}(t) = {} & \sum_{i=1}^{N} e_i^T(t)\dot{e}_i(t) \\ & + \frac{\gamma H}{2}\sum_{i=1}^{N}\left[q_i^{-1}\widetilde{\phi}_i^2(t) - q_i^{-1}\widetilde{\phi}_i^2(t-T)\right] \\ & + \gamma H\sum_{i=1}^{N} r_i^{-1}\left(\widetilde{\theta}_i(t) + L\right)\dot{\widetilde{\theta}}_i(t) \\ & + \frac{\gamma}{2}\sum_{i=1}^{N}\left[f_i^{-1}\operatorname{tr}\left(\widetilde{M}_i(t)\widetilde{M}_i^T(t)\right)\right. \\ & \left. - f_i^{-1}\operatorname{tr}\left(\widetilde{M}_i(t-T)\widetilde{M}_i^T(t-T)\right)\right]. \end{aligned} \tag{19}$$

Let us introduce some notations as

$$\begin{aligned} & f_i(x_i(t)) - f_i(s(t)) = \Phi, \\ & g\left(x_j(t), \varphi_i(t)\right) - g\left(s(t), \varphi_i(t)\right) = \Lambda, \\ & k\left(\dot{x}_j(t), \beta_i(t)\right) - k\left(\dot{s}_j(t), \beta_i(t)\right) = K. \end{aligned} \tag{20}$$

From (6) and (13), the first term on the right hand side of (19) satisfies

$$\begin{aligned} & \sum_{i=1}^{N} e_i^T(t)\dot{e}_i(t) \\ & = \sum_{i=1}^{N} e_i^T(t)\left[f_i(x_i(t)) + \sum_{j=1}^{N} a_{ij}\Gamma\Lambda\right. \\ & \qquad \left. + \sum_{j=1}^{N} b_{ij}\Gamma K - \dot{s}(t) + u_i(t)\right] \\ & = \sum_{i=1}^{N}\left(e_i^T\Phi + \sum_{j=1}^{N} a_{ij}e_i^T\Gamma\Lambda\right. \\ & \qquad + \sum_{j=1}^{N} b_{ij}e_i^T\Gamma K - \gamma H\sum_{j=1}^{N} a_{ji}^2\left(\widehat{\phi}_j(t) + \widehat{\theta}_j(t)\right)e_i^T e_i \\ & \qquad \left. -\gamma\sum_{j=1}^{N}\left|b_{ij}\right|\left|e_i^T(t)\right|\widehat{M}_i(t)\left|\dot{e}_j(t)\right|\right). \end{aligned} \tag{21}$$

According to Assumptions 2–7 and Lemma 10, from the above equation, we get

$$\begin{aligned}
&\sum_{i=1}^{N} e_i^T(t)\,\dot{e}_i(t)\\
&\quad\le \sum_{i=1}^{N}\Bigg[ce_i^Te_i+\frac{1}{4c}\phi^T\phi\\
&\qquad+\sum_{j=1}^{N}\left(de_i^Te_i+\frac{1}{4d}a_{ij}^2\Lambda^T\Gamma^T\Gamma\Lambda\right)\\
&\qquad+\gamma\sum_{j=1}^{N}\left|b_{ij}\right|\left|e_i^T\right||K|\\
&\qquad-\gamma H\sum_{j=1}^{N}a_{ji}^2\left(\widehat{\phi}_j(t)+\widehat{\theta}_j(t)\right)e_i^Te_i\\
&\qquad-\gamma\sum_{j=1}^{N}\left|b_{ij}\right|\left|e_i^T(t)\right|\widehat{M}_i(t)\left|\dot{e}_j(t)\right|\Bigg]\\
&\quad\le \sum_{i=1}^{N}\Bigg[\left(c+\frac{l_i^2}{4c}\right)e_i^Te_i+Nde_i^Te_i\\
&\qquad+\sum_{j=1}^{N}a_{ij}^2\left(\phi_i(t)+\theta_i\right)\frac{H\gamma^2}{4d}e_j^Te_j\\
&\qquad+\gamma\sum_{j=1}^{N}\left|b_{ij}\right|\left|e_i^T(t)\right|M_i(t)\left|\dot{e}_j(t)\right|\\
&\qquad-\gamma H\sum_{j=1}^{N}a_{ji}^2\left(\widehat{\phi}_j(t)+\widehat{\theta}_j(t)\right)e_i^Te_i\\
&\qquad-\gamma\sum_{j=1}^{N}\left|b_{ij}\right|\left|e_i^T(t)\right|\widehat{M}_i(t)\left|\dot{e}_j(t)\right|\Bigg],
\end{aligned}\tag{22}$$

where c, d are positive constants. Choosing $c=1/2$, $d=\gamma/4$, and according to Lemma 11, we have

$$\begin{aligned}
&\sum_{i=1}^{N} e_i^T(t)\,\dot{e}_i(t)\\
&\quad\le \sum_{i=1}^{N}\Bigg[\left(\frac{l_i}{2}+\frac{1}{2}+\frac{N\gamma}{4}\right.\\
&\qquad\left.+\gamma H\sum_{j=1}^{N}a_{ji}^2\left(\widetilde{\phi}_j(t)+\widetilde{\theta}_j(t)\right)\right)e_i^Te_i\\
&\qquad+\gamma\sum_{j=1}^{N}\left|b_{ij}\right|\left|e_i^T(t)\right|\widetilde{M}_i(t)\left|\dot{e}_j(t)\right|\Bigg]\\
&\quad= \sum_{i=1}^{N}\Bigg[\left(\frac{l_i}{2}+\frac{1}{2}+\frac{N\gamma}{4}\right.\\
&\qquad\left.+\gamma H\sum_{j=1}^{N}a_{ji}^2\left(\widetilde{\phi}_j(t)+\widetilde{\theta}_j(t)\right)\right)e_i^Te_i\\
&\qquad+\gamma\,\mathrm{tr}\left(\sum_{j=1}^{N}\left|b_{ij}\right|\widetilde{M}_i(t)\left|\dot{e}_j(t)\right|\left|e_i^T(t)\right|\right)\Bigg]\\
&\quad= \sum_{i=1}^{N}\Bigg[\left(\frac{l_i}{2}+\frac{1}{2}+\frac{N\gamma}{4}\right.\\
&\qquad\left.+\sum_{j=1}^{N}a_{ji}^2\gamma H\left(\widetilde{\phi}_j(t)+\widetilde{\theta}_j(t)\right)\right)e_i^Te_i\\
&\qquad+\gamma\,\mathrm{tr}\left(\sum_{j=1}^{N}\left|b_{ij}\right|\left|e_i(t)\right|\left|\dot{e}_j^T(t)\right|\widetilde{M}_i^T(t)\right)\Bigg].
\end{aligned}\tag{23}$$

Applying (14), the third term on the right-hand side of (19) satisfies

$$\begin{aligned}
&\gamma H\sum_{i=1}^{N}r_i^{-1}\left(\widetilde{\theta}_i(t)+L\right)\dot{\widetilde{\theta}}_i(t)\\
&\quad=-\gamma H\sum_{i=1}^{N}\left(\widetilde{\theta}_i(t)+L\right)\sum_{j=1}^{N}a_{ij}^2e_j^Te_j.
\end{aligned}\tag{24}$$

Let us focus on the second and fourth terms on the right-hand side of (19). In the interval $[T_1,T)$, since $q_{i0}(t)$, $f_{i0}(t)$ are continuous and strictly increasing functions, $q_i^{-1}\le q_{i0}^{-1}(t)<\infty$, $f_i^{-1}\le f_{i0}^{-1}(t)<\infty$ are ensured, we obtain

$$\begin{aligned}
&\frac{\gamma H}{2}\sum_{i=1}^{N}\left[q_i^{-1}\widetilde{\phi}_i^2(t)-q_i^{-1}\widetilde{\phi}_i^2(t-T)\right]\\
&\quad=\frac{\gamma H}{2}\sum_{i=1}^{N}\left[q_i^{-1}\widetilde{\phi}_i^2(t)-q_i^{-1}\widetilde{\phi}_i^2(0)\right]\\
&\quad\le\frac{\gamma H}{2}\sum_{i=1}^{N}q_{i0}^{-1}\widetilde{\phi}_i^2(t)\\
&\quad=\frac{\gamma H}{2}\sum_{i=1}^{N}q_{i0}^{-1}\left[\phi_i^2(t)+2\widehat{\phi}_i^2(t)\right.\\
&\qquad\left.-2\phi_i(t)\,\widehat{\phi}_i(t)-\widehat{\phi}_i^2(t)\right]\\
&\quad\le\frac{\gamma H}{2}\sum_{i=1}^{N}q_{i0}^{-1}\left[\phi_i^2(t)+2\widehat{\phi}_i^2(t)\right.\\
&\qquad\left.-2\phi_i(t)\,\widehat{\phi}_i(t)\right]\\
&\quad=\frac{\gamma H}{2}\sum_{i=1}^{N}q_{i0}^{-1}\phi_i^2(t)-\gamma H\sum_{i=1}^{N}\sum_{j=1}^{N}a_{ij}^2\widetilde{\phi}_i(t)\,e_j^Te_j.
\end{aligned}\tag{25}$$

According to Lemma 11, we can get

$$\begin{aligned}
&\operatorname{tr}\left(\widetilde{M}_i(t)\,\widetilde{M}_i^T(t)\right)\\
&\quad=\operatorname{tr}\left[\left(M_i-\widehat{M}_i(t)\right)\left(M_i-\widehat{M}_i(t)\right)^T\right]\\
&\quad=\operatorname{tr}\left(M_iM_i^T-M_i\widehat{M}_i^T-\widehat{M}_iM_i^T+\widehat{M}_i\widehat{M}_i^T\right)\\
&\quad=\operatorname{tr}\left(M_iM_i^T+2\widehat{M}_i\widehat{M}_i^T-M_i\widehat{M}_i^T-\widehat{M}_iM_i^T-\widehat{M}_i\widehat{M}_i^T\right)\\
&\quad\le\operatorname{tr}\left(M_iM_i^T+2\widehat{M}_i\widehat{M}_i^T-M_i\widehat{M}_i^T-\widehat{M}_iM_i^T\right)\\
&\quad=\operatorname{tr}\left(M_iM_i^T\right)+2\operatorname{tr}\left(\widehat{M}_i\widehat{M}_i^T-M_i\widehat{M}_i^T\right)\\
&\quad=\operatorname{tr}\left(M_iM_i^T\right)-2\operatorname{tr}\left(\widehat{M}_i\widehat{M}_i^T\right).
\end{aligned}\tag{26}$$

Then from (26), the last term on the right-hand side of (19) satisfies

$$\begin{aligned}
&\frac{\gamma}{2}\sum_{i=1}^{N}\left[f_i^{-1}\operatorname{tr}\left(\widetilde{M}_i(t)\,\widetilde{M}_i^T(t)\right)\right.\\
&\qquad\left.-f_i^{-1}\operatorname{tr}\left(\widetilde{M}_i(t-T)\,\widetilde{M}_i^T(t-T)\right)\right]\\
&\quad\le\frac{\gamma}{2}\sum_{i=1}^{N}f_i^{-1}\operatorname{tr}\left(\widetilde{M}_i(t)\,\widetilde{M}_i^T(t)\right)\\
&\quad\le\frac{\gamma}{2}\sum_{i=1}^{N}f_{i0}^{-1}\left[\operatorname{tr}\left(M_iM_i^T\right)-2\operatorname{tr}\left(\widehat{M}_i\widehat{M}_i^T\right)\right]\\
&\quad=\frac{\gamma}{2}\sum_{i=1}^{N}f_{i0}^{-1}\operatorname{tr}\left(M_iM_i^T\right)-\gamma\sum_{i=1}^{N}\operatorname{tr}\left(f_{i0}^{-1}\widehat{M}_i\widehat{M}_i^T\right)\\
&\quad=\frac{\gamma}{2}\sum_{i=1}^{N}f_{i0}^{-1}\operatorname{tr}\left(M_iM_i^T\right)\\
&\qquad-\gamma\sum_{i=1}^{N}\operatorname{tr}\left(\sum_{j=1}^{N}\left|b_{ij}\right|\left|e_i(t)\right|\left|\dot{e}_j^T(t)\right|\widetilde{M}_i^T(t)\right).
\end{aligned}\tag{27}$$

Substituting (23)–(27) into (19) we obtain

$$\begin{aligned}
\dot{V}(t)\le&\sum_{i=1}^{N}\left(\frac{l_i}{2}+\frac{1}{2}+\frac{N\gamma}{4}-L\sum_{j=1}^{N}a_{ji}^2\right)e_i^Te_i\\
&+\frac{\gamma H}{2}\sum_{i=1}^{N}q_{i0}^{-1}(t)\,\phi_i^2(t)+\frac{\gamma}{2}\sum_{i=1}^{N}f_{i0}^{-1}\operatorname{tr}\left(M_iM_i^T\right)
\end{aligned}\tag{28}$$

It is obvious that there exist sufficiently large positive constants L such that

$$\frac{1}{2}+\frac{1}{2}l_i^2+\frac{N\gamma}{4}-L\sum_{j=1}^{N}a_{ji}^2<0,\quad i=1,\ldots,N.\tag{29}$$

According to (28) we have

$$\begin{aligned}
\dot{V}(t)\le&\frac{\gamma H}{2}\sum_{i=1}^{N}q_{i0}^{-1}(t)\,\phi_i^2(t)+\frac{\gamma}{2}\sum_{i=1}^{N}f_{i0}^{-1}\operatorname{tr}\left(M_iM_i^T\right),\\
&t\in\left[T_1,T\right).
\end{aligned}\tag{30}$$

For $\forall t\in[T_1,T)$, since $\phi_i(t)$ is continuous and periodic and every element in matrix $M_i(\cdot)$ is continuous function, the boundedness of them can be obtained. The boundedness of $\phi_i(t)$ and $\operatorname{tr}(M_iM_i^T)$ leads to the boundedness of $\dot{V}(t)$. That is, $V(t)$ is bounded in $[0,T)$. For $V(T_1)$ is bounded, the finiteness of $V(t)$ is obvious by using integral technique, $\forall t\in[0,T)$.

Next step, the asymptotical convergence of $e(t)$ is proved.

According to (17), $\forall t\ge T$, we can get

$$\begin{aligned}
\Delta V(t)=&V(t)-V(t-T)\\
=&-\frac{1}{2}\sum_{i=1}^{N}e_i^T(t)\,e_i(t)\\
&-\frac{1}{2}\sum_{i=1}^{N}e_i^T(t-T)\,e_i(t-T)\\
&+\frac{\gamma H}{2}\sum_{i=1}^{N}r_i^{-1}\left(\widetilde{\theta}_i(t)+L\right)^2\\
&-\frac{\gamma H}{2}\sum_{i=1}^{N}r_i^{-1}\left(\widetilde{\theta}_i(t-T)+L\right)^2\\
&+\frac{\gamma H}{2}\sum_{i=1}^{N}\int_{t-T}^{t}\left[q_i^{-1}\widetilde{\phi}_i^2(\tau)-q_i^{-1}\widetilde{\phi}_i^2(\tau-T)\right]d\tau\\
&+\frac{\gamma}{2}\sum_{i=1}^{N}\int_{t-T}^{t}f_i^{-1}\left[\operatorname{tr}\left(\widetilde{M}_i(\tau)\,\widetilde{M}_i^T(\tau)\right)\right.\\
&\qquad\left.-\operatorname{tr}\left(\widetilde{M}_i(\tau-T)\,\widetilde{M}_i^T(\tau-T)\right)\right]d\tau.
\end{aligned}\tag{31}$$

With Newton-Leibniz's formula, the first two terms on the right-hand side of (31) satisfied

$$\begin{aligned}
&\frac{1}{2}\sum_{i=1}^{N}e_i^T(t)\,e_i(t)-\frac{1}{2}\sum_{i=1}^{N}e_i^T(t-T)\,e_i(t-T)\\
&\quad=\sum_{i=1}^{N}\int_{t-T}^{t}e_i^T(\tau)\,\dot{e}_i(\tau)\,d\tau\\
&\quad\le\sum_{i=1}^{N}\int_{t-T}^{t}\left(\frac{1}{2}+\frac{1}{2}l_i^2+\frac{N\gamma}{4}\right)e_i^T(\tau)\,e_i(\tau)\,d\tau\\
&\qquad+\sum_{i=1}^{N}\sum_{j=1}^{N}\int_{t-T}^{t}a_{ji}^2\gamma He_i^T(\tau)\,e_i(\tau)\left(\widetilde{\phi}_j(\tau)+\widetilde{\theta}_j(\tau)\right)d\tau\\
&\qquad+\sum_{i=1}^{N}\int_{t-T}^{t}\left|b_{ij}\right|\gamma\operatorname{tr}\left(\sum_{j=1}^{N}\left|e_i(\tau)\right|\left|\dot{e}_j^T(\tau)\right|\widetilde{M}_i^T(\tau)\right)d\tau.
\end{aligned}\tag{32}$$

Using the algebraic relation

$$\begin{aligned}&(a-b)^T G(a-b)-(a-c)^T G(a-c)\\&\quad=(c-b)^T G[2(a-b)+(b-c)],\end{aligned}\tag{33}$$

where $a, b, c \in R^p$, $G \in R^{p\times p}$.

After choosing $G = 1$, $a = \phi_i(\tau)$, $b = \hat{\phi}(\tau)$, $a-b = \tilde{\phi}_i(\tau)$, $\phi_i(\tau) = \phi_i(\tau - T)$, $c = \hat{\phi}_i(\tau - T)$, and $a - c = \tilde{\phi}_i(\tau - T)$, we can get

$$\begin{aligned}&\frac{\gamma H}{2}\sum_{i=1}^{N} q_i^{-1}\tilde{\phi}_i^2(\tau)-\frac{\gamma H}{2}\sum_{i=1}^{N} q_i^{-1}\tilde{\phi}_i^2(\tau-T)\\&\quad=\frac{\gamma H}{2}\sum_{i=1}^{N} q_i^{-1}\left[2\tilde{\phi}_i(\tau)+\hat{\phi}_i(\tau)-\hat{\phi}_i(\tau-T)\right]\\&\qquad\times\left[\hat{\phi}_i(\tau-T)-\hat{\phi}_i(\tau)\right]\\&\quad=-\gamma H\sum_{i=1}^{N}\left(\tilde{\phi}_i(\tau)+\frac{1}{2}q_i\sum_{j=1}^{N} a_{ij}^2 e_j^T e_j\right)\sum_{k=1}^{N} a_{ik}^2 e_k^T e_k.\end{aligned}\tag{34}$$

From Lemma 11, we have

$$\begin{aligned}&\mathrm{tr}\left(\widetilde{M}_i(\tau)\widetilde{M}_i^T(\tau)\right)-\mathrm{tr}\left(\widetilde{M}_i(\tau-T)\widetilde{M}_i^T(\tau-T)\right)\\&\quad=\mathrm{tr}\left(\widetilde{M}_i(\tau)\widetilde{M}_i^T(\tau)-\widetilde{M}_i(\tau-T)\widetilde{M}_i^T(\tau)\right.\\&\qquad\left.+\widetilde{M}_i(\tau-T)\widetilde{M}_i^T(\tau)-\widetilde{M}_i(\tau-T)\widetilde{M}_i^T(\tau-T)\right)\\&\quad=\mathrm{tr}\left(\left[\widetilde{M}_i(\tau)-\widetilde{M}_i(\tau-T)\right]\widetilde{M}_i^T(\tau)\right.\\&\qquad\left.+\widetilde{M}_i(\tau-T)\left[\widetilde{M}_i^T(\tau)-\widetilde{M}_i^T(\tau-T)\right]\right)\\&\quad=\mathrm{tr}\left(\left[\widetilde{M}_i(\tau)-\widetilde{M}_i(\tau-T)\right]\left[\widetilde{M}_i^T(\tau)+\widetilde{M}_i^T(\tau-T)\right]\right)\\&\quad=\mathrm{tr}\left(\left[\widetilde{M}_i(\tau)-\widetilde{M}_i(\tau-T)\right]\right.\\&\qquad\left.\times\left[2\widetilde{M}_i^T(\tau)+\widetilde{M}_i^T(\tau-T)-\widetilde{M}_i^T(\tau)\right]\right).\end{aligned}\tag{35}$$

According to (34) and (35), the last two terms on the right-hand side of (31) satisfy

$$\begin{aligned}&\frac{\gamma H}{2}\sum_{i=1}^{N}\int_{t-T}^{t}\left[q_i^{-1}\tilde{\phi}_i^2(\tau)-q_i^{-1}\tilde{\phi}_i^2(\tau-T)\right]d\tau\\&\quad=-\gamma H\sum_{i=1}^{N}\int_{t-T}^{t}\left[\tilde{\phi}_i(\tau)+\frac{1}{2}q_i\sum_{j=1}^{N} a_{ij}^2 e_j^T e_j\right]\\&\qquad\times\sum_{k=1}^{N} a_{ik}^2 e_k^T e_k d\tau,\end{aligned}\tag{36}$$

$$\begin{aligned}&\frac{\gamma}{2}\sum_{i=1}^{N}\int_{t-T}^{t} f_i^{-1}\\&\qquad\times\left[\mathrm{tr}\left(\widetilde{M}_i(\tau)\widetilde{M}_i^T(\tau)\right)\right.\\&\qquad\left.-\mathrm{tr}\left(\widetilde{M}_i(\tau-T)\widetilde{M}_i^T(\tau-T)\right)\right]d\tau\\&\quad=\frac{\gamma}{2}\sum_{i=1}^{N}\int_{t-T}^{t} f_i^{-1}\\&\qquad\times\mathrm{tr}\left[\left(f_i\sum_{j=1}^{N}\left|b_{ij}\right|\left|e_i\right|\left|\dot{e}_j^T\right|\right)\right.\\&\qquad\left.\times\left(2\widetilde{M}_i^T(\tau)-\left(f_i\sum_{j=1}^{N}\left|b_{ij}\right|\left|e_i\right|\left|\dot{e}_j^T\right|\right)^T\right)\right]d\tau\\&\quad=-\gamma\sum_{i=1}^{N}\int_{t-T}^{t}\mathrm{tr}\left(\sum_{j=1}^{N}\left|b_{ij}\right|\left|e_i\right|\left|\dot{e}_j^T\right|\widetilde{M}_i^T(\tau)\right)d\tau\\&\qquad-\frac{\gamma}{2}\sum_{i=1}^{N}\int_{t-T}^{t}\sum_{i=1}^{N} f_i\,\mathrm{tr}\left[\left(\sum_{j=1}^{N}\left|b_{ij}\right|\left|e_i\right|\left|\dot{e}_j^T\right|\right)\right.\\&\qquad\left.\times\left(\sum_{j=1}^{N}\left|b_{ij}\right|\left|e_i\right|\left|\dot{e}_j^T\right|\right)^T\right]d\tau.\end{aligned}\tag{37}$$

The other terms of right-hand side of (31) can be simplified as follows:

$$\begin{aligned}&\frac{\gamma H}{2}\sum_{i=1}^{N} r_i^{-1}\left(\tilde{\theta}_i(t)+L\right)^2-\frac{\gamma H}{2}\sum_{i=1}^{N} r_i^{-1}\left(\tilde{\theta}_i(t-T)+L\right)^2\\&\quad=\gamma H\sum_{i=1}^{N}\int_{t-T}^{t} r_i^{-1}\left(\tilde{\theta}_i(\tau)+L\right)\dot{\tilde{\theta}}_i(\tau)\,d\tau\\&\quad=-\gamma H\sum_{i=1}^{N}\int_{t-T}^{t}\left(\tilde{\theta}_i(\tau)+L\right)\sum_{j=1}^{N} a_{ij}^2 e_j^T(\tau)e_j(\tau)\,d\tau.\end{aligned}\tag{38}$$

Substituting (32) and (36)–(38) into (31), we can attain

$$\Delta V(t)\le\sum_{i=1}^{N}\int_{t-T}^{t}\left(\frac{1}{2}+\frac{1}{2}l_i^2+\frac{N\gamma}{4}-L\sum_{j=1}^{N} a_{ji}^2\right)e_i^T(\tau)e_i(\tau)\,d\tau.\tag{39}$$

Choosing $1/2 + (1/2)l_i^2 + N\gamma/4 - L\sum_{j=1}^{N} a_{ji}^2 < 0$, $i = 1, \ldots, N$, we can obtain

$$\Delta V(t) < 0.\tag{40}$$

For any $t \in [lT, (l+1)T]$, $l = 1, 2, \ldots$, and denoting $t_0 = t - lT$, $t_0 \in [0, T)$, we have

$$V(t) = V(t_0)+\sum_{j=0}^{l-1}\Delta V(t-jT).\tag{41}$$

Considering $t_0 \in [0,T)$ and the positive of $V(t)$, according to (41), we obtain

$$V(t) < \max_{t_0\in[0,T)} V(t_0) - \sum_{j=0}^{l-1}\sum_{i=1}^{N}\int_{t-(j+1)T}^{t-jT}\left(L\sum_{j=1}^{N}a_{ji}^2 - \frac{1}{2} - \frac{1}{2}l_i^2 - \frac{N\gamma}{4}\right) \times e_i^T(\tau)\,e_i(\tau)\,d\tau. \quad (42)$$

Since $V(t_0)$ is bounded in the interval $[0,T)$, according to the convergence theorem of the sum of series and (42), the error $e(t)$ converges to zero asymptotically in L_T^2 norm. That is to say, we have

$$\lim_{t\to\infty}\int_{t-T}^{t} e_i^T(\tau)\,e_i(\tau)\,d\tau = 0. \quad (43)$$

Finally, we prove that all the closed-loop signals are bounded. Considering $\forall t \in [T,\infty)$, the derivative of $V(t)$ is

$$\begin{aligned}\dot V(t) &= \sum_{i=1}^{N} e_i^T(t)\,\dot e_i(t) + \frac{\gamma H}{2}\sum_{i=1}^{N} q_i^{-1}\widetilde{\phi}_i^2(t) \\ &\quad - \frac{\gamma H}{2}\sum_{i=1}^{N} q_i^{-1}\widetilde{\phi}_i^2(t-T) \\ &\quad + \gamma H\sum_{i=1}^{N} r_i^{-1}\left(\widetilde{\theta}_i(t)+L\right)\dot{\widetilde{\theta}}_i(t) \\ &\quad + \frac{\gamma}{2}f_i^{-1}\left[\operatorname{tr}\left(\widetilde{M}_i(t)\,\widetilde{M}_i^T(t)\right)\right. \\ &\qquad \left. - \operatorname{tr}\left(\widetilde{M}_i(t-T)\,\widetilde{M}_i^T(t-T)\right)\right] \\ &\le -\frac{\gamma H}{2}\sum_{i=1}^{N} q_i\left(\sum_{j=1}^{N} a_{ij}^2 e_j^T e_j\right)^2 \\ &\quad - \sum_{i=1}^{N}\left(L\sum_{j=1}^{N}a_{ji}^2 - \frac{1}{2} - \frac{1}{2}l_i^2 - \frac{N\gamma}{4}\right)e_i^T e_i \\ &\quad - \frac{\gamma}{2}\sum_{i=1}^{N} f_i \operatorname{tr}\left[\left(\sum_{j=1}^{N}\left|b_{ij}\right|\left|e_i\right|\left|\dot e_j^T\right|\right)\right. \\ &\qquad \left.\times\left(\sum_{j=1}^{N}\left|b_{ij}\right|\left|e_i\right|\left|\dot e_j^T\right|\right)^T\right]. \end{aligned} \quad (44)$$

Having the two sides of (44) integration, one can obtain

$$\begin{aligned}V(t) &\le V(T) - \frac{\gamma H}{2}\sum_{i=1}^{N}\int_T^t q_i\left(\sum_{j=1}^{N}a_{ij}^2 e_j^T e_j\right)^2 d\tau \\ &\quad - \sum_{i=1}^{N}\int_T^t\left(L\sum_{j=1}^{N}a_{ji}^2 - \frac{1}{2} - \frac{1}{2}l_i^2 - \frac{N\gamma}{4}\right)e_i^T e_i d\tau \\ &\quad - \frac{\gamma}{2}\sum_{i=1}^{N} f_i\int_{t-T}^{t}\operatorname{tr}\left[\left(\sum_{j=1}^{N}\left|b_{ij}\right|\left|e_i\right|\left|\dot e_j^T\right|\right)\right. \\ &\qquad \left.\times\left(\sum_{j=1}^{N}\left|b_{ij}\right|\left|e_i\right|\left|\dot e_j^T\right|\right)^T\right]d\tau. \end{aligned} \quad (45)$$

Choosing $(L > 1/2 + ((1/2)l_i^2) + N\gamma/4)/\sum_{j=1}^{N} a_{ji}^2$, $i = 1,\ldots,N$, we have

$$V(t) < V(T). \quad (46)$$

From the boundedness of $V(t)$ and (17), we can conclude that e_i, $\int_{t-T}^{t}\widetilde{\phi}_i^2(\tau)d\tau$, $\widetilde{\theta}_i(t)$ For θ_i is constant and $\int_{t-T}^{t}\operatorname{tr}(\widetilde{M}_i(\tau)\widetilde{M}_i^T(\tau))d\tau$ are all bounded., it implies the boundedness of $\widehat{\theta}_i(t)$. According to Lemma 13 and the continuity of $\widetilde{\phi}_i(t)$ and $\widetilde{M}_i(t)$, the boundedness of $\widetilde{\phi}_i(t)$ and $\widetilde{M}_i(t)$ are obviously obtained. As $\phi_i(t)$ is a continuous periodic function and $M_i(t)$ is continuous periodic matrix, we can get that $\widehat{\phi}_i(t)$, $\widehat{M}_i(t)$ are bounded. According to (1), the boundedness of the control input $u_i(t)$ is obtained. Since $e_i(t)$ is bounded, the boundedness of $x_i(t)$ is received. The proof is completed. □

It is worth mentioning that when $k(\cdot,\cdot)$ is bounded function, the boundedness of $\dot e_i(t)$ can be easy to get. Then, from Lemma 12 we can obtain the error globally asymptotical synchronization.

4. Simulation Example

To demonstrate the theoretical result obtained in Section 3, the following dynamical network with six non-identical nodes is considered:

$$\begin{aligned}\dot x_i(t) &= f_i(x_i(t)) \\ &\quad + \sum_{j=1}^{N} a_{ij}\Gamma\exp\left(-\varphi_i(t)\begin{pmatrix}x_{j1}^2(t)\\ x_{j2}^2(t)\\ x_{j3}^2(t)\end{pmatrix}\right) \\ &\quad + \sum_{j=1}^{N} b_{ij}\Gamma\left(\exp\begin{pmatrix}\sin(2\pi t)\\ \sin(2\pi t)\\ \sin(2\pi t)\end{pmatrix}\right. \\ &\qquad \left. - \begin{pmatrix}0.1\cos\left(\dot x_{j1}(t)\right)\sin(2\pi t)\\ 0.1\cos\left(\dot x_{j2}(t)\right)\sin(2\pi t)\\ 0.1\cos\left(\dot x_{j3}(t)\right)\sin(2\pi t)\end{pmatrix}\right) \\ &\quad + u_i(t), \quad i = 1,\ldots,6, \end{aligned} \quad (47)$$

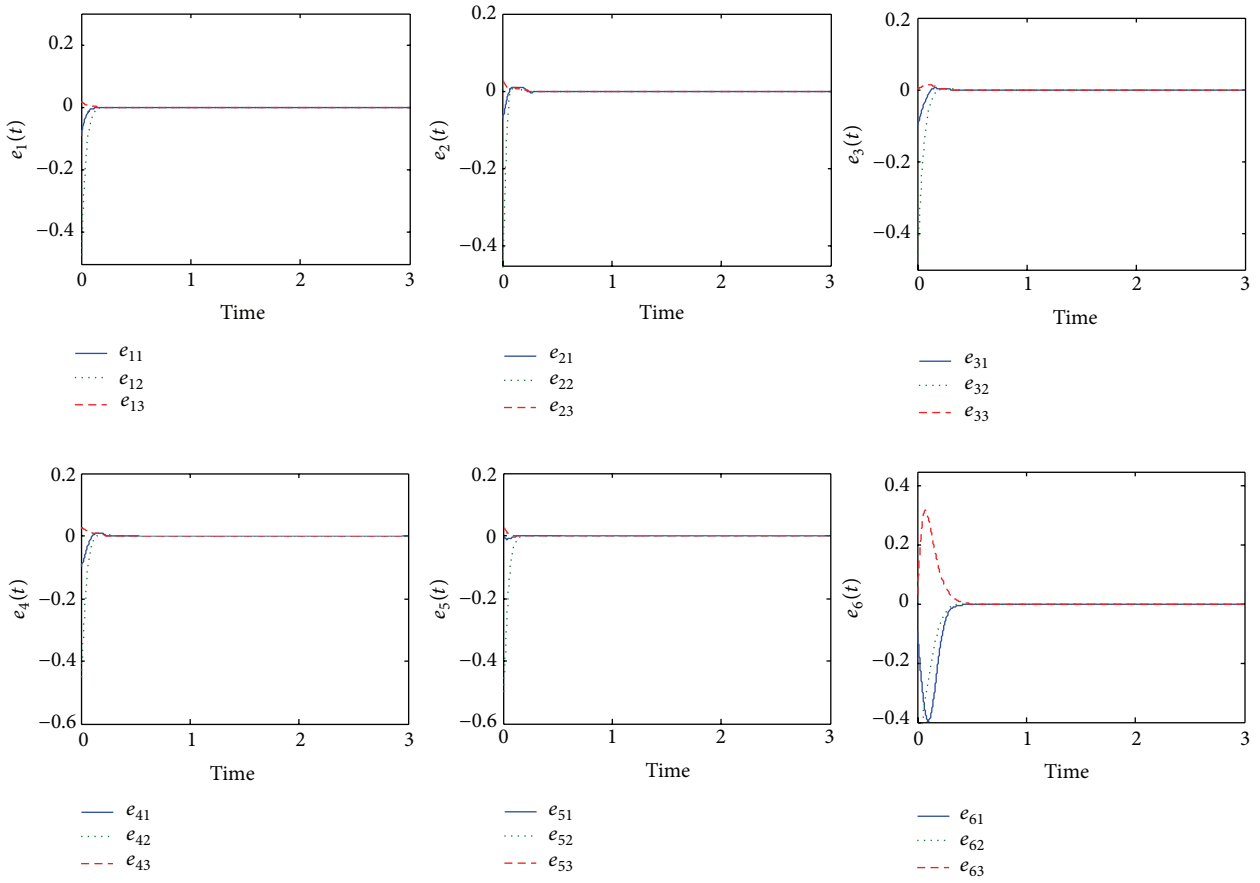

FIGURE 1: The evaluations of synchronization errors $e_i(t)$, $i = 1, \ldots, 6$.

where

$$f_1(x_1) = \begin{pmatrix} -2.5x_{11} + 0.3x_{12} + 0.9x_{13} + 3x_{13}^2 \\ 0.6x_{11} - 2.6x_{12} + 3x_{12}^2 + x_{13} \\ -2.8x_{11} + \sin x_{11} \cos x_{12} - 2.2x_{13} \end{pmatrix},$$

$$f_2(x_2) = \begin{pmatrix} -2.5x_{21} + x_{22} + x_{21}x_{22} + x_{23} \\ 0.5x_{21} - 0.8x_{22} - \sin x_{22} + x_{23} - x_{23}^2 \\ -2x_{21} - 0.8x_{23} - 0.5 \sin(2x_{23}) \end{pmatrix},$$

$$f_3(x_3) = \begin{pmatrix} -2.5x_{31} + x_{31} \sin x_{31} + x_{32} + 1.4x_{33} \\ 0.5x_{31} - 2.5x_{32} + x_{33} \\ -2x_{31} + x_{32}x_{33} - 0.6x_{33} - x_{33} \cos x_{33} \end{pmatrix},$$

$$f_4(x_4) = \begin{pmatrix} -2.5x_{41} + 1.5x_{42} + 1.5x_{43} \\ x_{41} - 2.5x_{42} + x_{42}^2 + 1.5x_{43} + x_{43}^2 \\ -2x_{41} + x_{41}x_{43} - 2.5x_{43} \end{pmatrix},$$

$$f_5(x_5) = \begin{pmatrix} -2.1x_{51} + 0.5x_{51}^2 + 1.4x_{52} + x_{53} \\ 0.9x_{51} - 2.1x_{52} + x_{52}x_{53} + x_{53} \\ -2x_{51} + 0.4x_{52} - 2.1x_{53} \end{pmatrix},$$

$$f_6(x_6) = \begin{pmatrix} -3.2x_{61} + 10x_{62} + 2.95\left(|x_{61} + 1| - |x_{61} - 1|\right) \\ x_{61} - x_{62} + x_{63} \\ -14.7x_{62} \end{pmatrix},$$

$$\Gamma = \begin{bmatrix} 1 & 0 & 0 \\ 0 & 1 & 0 \\ 0 & 0 & 1 \end{bmatrix},$$

$$A = \begin{bmatrix} -3 & 0 & 2 & 1 & 0 & 0 \\ 2 & -5 & 0 & 0 & 2 & 1 \\ 0 & 3 & -4 & 0 & 0 & 1 \\ 1 & 1 & 0 & -5 & 2 & 1 \\ 0 & 0 & 1 & 3 & -4 & 0 \\ 0 & 1 & 1 & 1 & 0 & -3 \end{bmatrix},$$

$$B = \begin{bmatrix} -3 & 2 & 0 & 1 & 0 & 0 \\ 0 & -3 & 0 & 0 & 1 & 2 \\ 0 & 1 & -3 & 2 & 0 & 0 \\ 1 & 0 & 2 & -4 & 0 & 1 \\ 0 & 0 & 1 & 1 & -2 & 0 \\ 2 & 0 & 0 & 0 & 1 & -3 \end{bmatrix}. \quad (48)$$

Nonlinearly parameterized function satisfies

$$\left\| \exp\left(-\varphi_i(t) \begin{pmatrix} x_{j1}^2(t) \\ x_{j2}^2(t) \\ x_{j3}^2(t) \end{pmatrix}\right) - \exp\left(-\varphi_i(t) \begin{pmatrix} s^2(t) \\ s^2(t) \\ s^2(t) \end{pmatrix}\right) \right\|^2$$
$$\leq \left\| e_j(t) \right\|^2 2\varphi_i(t) \exp(-1),$$

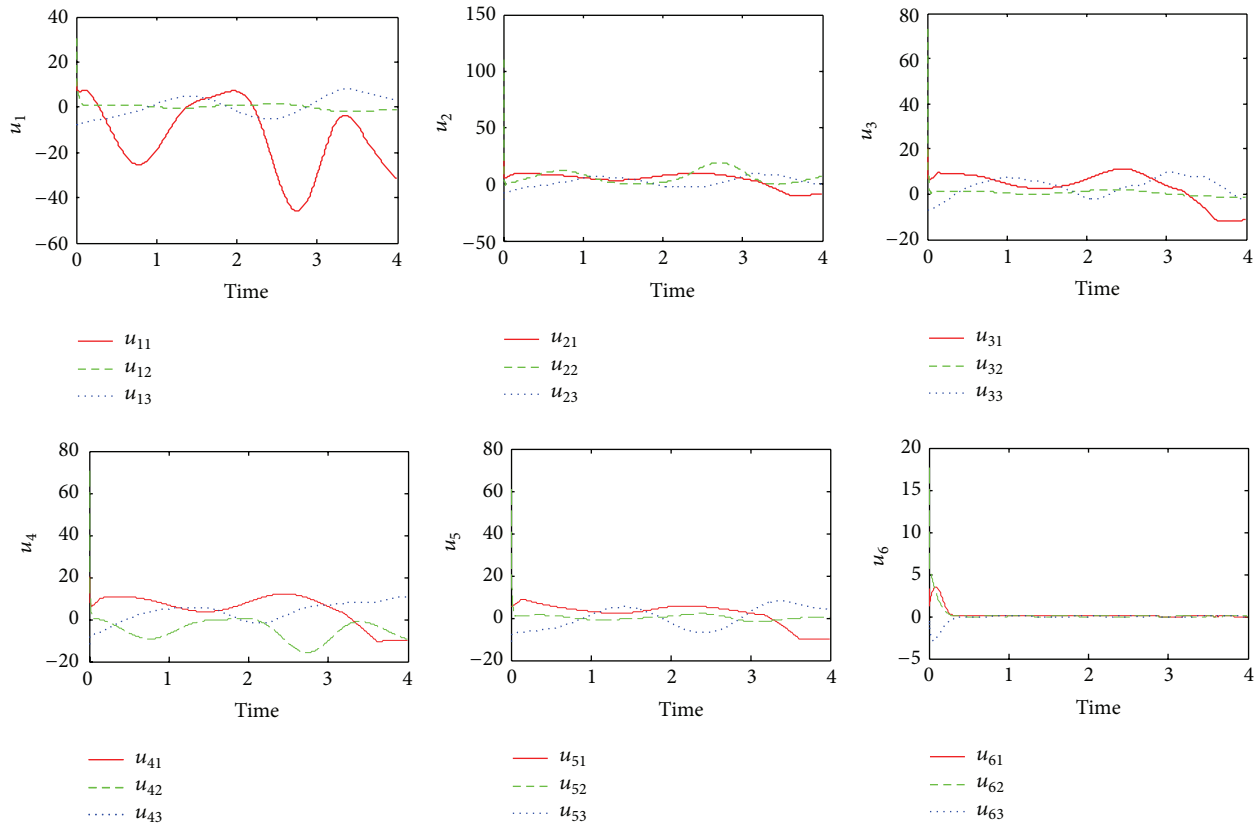

FIGURE 2: The curve of control $u_i(t)$ with $i = 1, \ldots, 6$.

$$\left\| \left(\exp \begin{pmatrix} \sin(2\pi t) \\ \sin(2\pi t) \\ \sin(2\pi t) \end{pmatrix} - \begin{pmatrix} 0.1\cos\left(\dot{x}_{j1}(t)\right)\sin(2\pi t) \\ 0.1\cos\left(\dot{x}_{j2}(t)\right)\sin(2\pi t) \\ 0.1\cos\left(\dot{x}_{j3}(t)\right)\sin(2\pi t) \end{pmatrix} \right) - \left(\exp \begin{pmatrix} \sin(2\pi t) \\ \sin(2\pi t) \\ \sin(2\pi t) \end{pmatrix} + \begin{pmatrix} 0.1\cos\left(\dot{s}_{j1}(t)\right)\sin(2\pi t) \\ 0.1\cos\left(\dot{s}_{j2}(t)\right)\sin(2\pi t) \\ 0.1\cos\left(\dot{s}_{j3}(t)\right)\sin(2\pi t) \end{pmatrix} \right) \right\| \leq \left| \dot{x}_j(t) - \dot{s}_j(t) \right|. \tag{49}$$

We choose $\dot{s}(t) = f_6(s(t))$, and the parameters are selected as follows:

$$\begin{aligned} &N = 6, \quad T = 0.5, \quad \gamma = 1, \quad H = 5, \\ &\phi_1(t) = 0.2\sin 8\pi t + 2, \quad \phi_2(t) = 2\cos 4\pi t + 2, \\ &\phi_3(t) = -\sin 8\pi t + 2, \quad \phi_4(t) = \cos 8\pi t + 2, \\ &\phi_5(t) = -2\sin 8\pi t + 2, \quad \phi_6(t) = 2\sin 4\pi t + 2, \\ &\theta = (1, 2, 3, 1.1, 1.5, 1.3)^T. \end{aligned} \tag{50}$$

In the following simulations, we choose

$$\begin{aligned} &q_1 = 1, \quad q_2 = 3, \quad q_3 = 2, \quad q_4 = 5, \\ &q_5 = 1, \quad q_6 = 2, \quad q_{10}(t) = 2tq_1, \quad q_{20}(t) = 2tq_2, \\ &q_{30}(t) = 2tq_3, \quad q_{40}(t) = 2tq_4, \\ &q_{50}(t) = 2tq_5, \quad q_{60}(t) = 2tq_6. \end{aligned} \tag{51}$$

The initially estimated values of the unknown parameters are

$$\hat{\phi}(0) = (1 \;\; 1 \;\; 1 \;\; 1 \;\; 1 \;\; 1)^T, \quad \hat{\theta}(0) = (1, 2, 3, 1.1, 1.5, 0)^T, \tag{52}$$

and the initial states are chosen as

$$\begin{aligned} &x_1 = [0.01 \;\; 0.03 \;\; 0.02]^T, \quad x_2 = [0.03 \;\; 0.02 \;\; 0.03]^T, \\ &x_3 = [0.04 \;\; 0.02 \;\; 0]^T, \quad x_4 = [0 \;\; 0.05 \;\; 0.03]^T, \\ &x_5 = [0.1 \;\; 0 \;\; 0.03]^T, \quad x_6 = [0.1 \;\; 0.01 \;\; 0]^T, \\ &s = [0.1 \;\; 0.5 \;\; 0]^T. \end{aligned} \tag{53}$$

According to Theorem 14, the synchronization of the complex dynamical network can be guaranteed by the distributed adaptive controllers in (15) and the distributed adaptive learning laws when (16)–(18). Figure 1 shows the error evolutions under the designed controller. In this example, $k(\cdot, \cdot)$ is bounded function, we clearly see that the states of the network asymptotically synchronizes with the states of the desired orbit. Figure 2 depicts the time evolution of the controller, and Figure 3 shows the evolution of the estimated time-varying parameters. Figures 2 and 3 show that all signals in the network are bounded. Figures 4 and 5 show that the time-varying parameters are periodic and bounded.

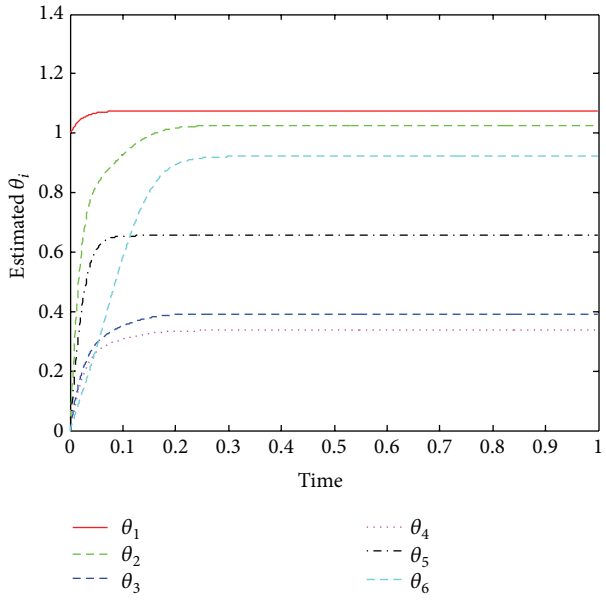

FIGURE 3: The curve of control θ_i with $i = 1, \ldots, 6$.

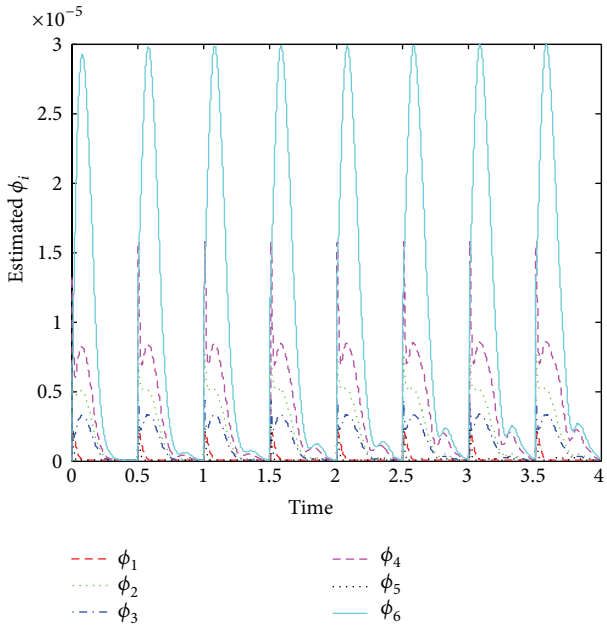

FIGURE 4: The evaluations of parameters ϕ_i with $i = 1, \ldots, 6$.

Remark 15. It is not difficult to draw the evolution of other elements in parameter $M_i(t)$. Here, we only take the first row of $M_{11}(t)$ for example. Compared with existing results [26, 28], the biggest innovation of this paper is the asymptotical synchronization ability for the nonlinear neutral-type coupling complex networks under the designed controller.

5. Conclusion

In this paper, the synchronization problem for a complex dynamical network with nonlinearly derivative couplings is solved via distributed adaptive control method. The adaptive strategies are concerned with the networks topology. By combining inequality techniques and the parameter separation, introducing the composite energy function, the convergence of the tracking error and the boundedness of the system signals are derived. Moreover, the coupling matrix is not assumed to be symmetric or irreducible. Finally, a typical example was simulated to verify the proposed theoretical results.

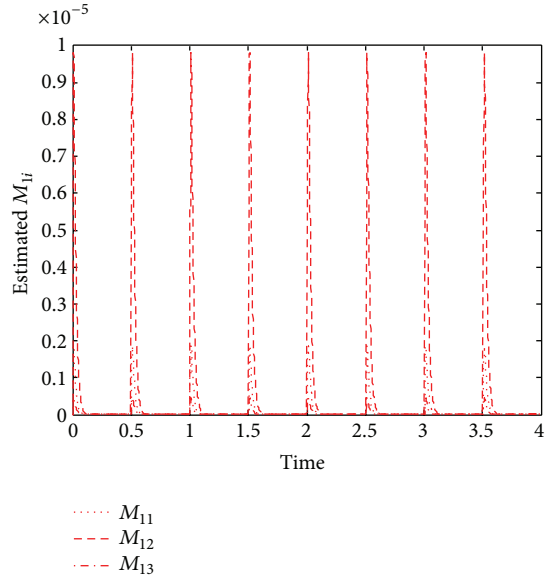

FIGURE 5: The evaluations of parameters $M_{1i}(t)$.

Conflict of Interests

The authors declare that there is no conflict of interests regarding the publication of this paper.

References

[1] J. F. Donges, Y. Zou, N. Marwan, and J. Kurths, "The backbone of the climate network," *EPL*, vol. 87, no. 4, Article ID 48007, 2009.

[2] R. Pastor-Satorras, E. Smith, and R. V. Solé, "Evolving protein interaction networks through gene duplication," *Journal of Theoretical Biology*, vol. 222, no. 2, pp. 199–210, 2003.

[3] M. Chavez, M. Valencia, V. Navarro, V. Latora, and J. Martinerie, "Functional modularity of background activities in normal and epileptic brain networks," *Physical Review Letters*, vol. 104, no. 11, Article ID 118701, 2010.

[4] Z. W. Gao, D. X. Kong, and C. H. Gao, "Modeling and control of complex dynamic systems: applied mathematical aspects," *Journal of Applied Mathematics*, vol. 2012, Article ID 869792, 5 pages, 2012.

[5] G. Chen, X. Wang, X. Li, and J. Lü, "Some recent advances in complex networks synchronization," *Studies in Computational Intelligence*, vol. 254, pp. 3–16, 2009.

[6] B. Song, J. H. Park, Z. G. Wu, and Y. Zhang, "Global synchronization of stochastic delayed complex networks," *Nonlinear Dynamics*, vol. 70, no. 4, pp. 2389–2399, 2012.

[7] Z. G. Wu, J. H. Park, H. Su, B. Song, and J. Chu, "Exponential synchronization for complex dynamical networks with sampled-data," *Journal of the Franklin Institute*, vol. 349, no. 9, pp. 2735–2749, 2012.

[8] K. Yuan, J. D. Cao, and S. M. Fei, "Synchronization of coupled networks with mixed delays by intermittent control," *Journal of Applied Mathematics*, vol. 2012, Article ID 927609, 13 pages, 2012.

[9] T. H. Lee, J. H. Park, D. H. Ji, O. M. Kwon, and S. M. Lee, "Guaranteed cost synchronization of a complex dynamical network via dynamic feedback control," *Applied Mathematics and Computation*, vol. 218, no. 11, pp. 6469–6481, 2012.

[10] T. Chen, X. Liu, and W. Lu, "Pinning complex networks by a single controller," *IEEE Transactions on Circuits and Systems I*, vol. 54, no. 6, pp. 1317–1326, 2007.

[11] J. Zhou, J. A. Lu, and J. Lü, "Pinning adaptive synchronization of a general complex dynamical network," *Automatica*, vol. 44, no. 4, pp. 996–1003, 2008.

[12] M. Porfiri and M. di Bernardo, "Criteria for global pinning-controllability of complex networks," *Automatica*, vol. 44, no. 12, pp. 3100–3106, 2008.

[13] D. H. Ji, S. C. Jeong, J. H. Park, S. M. Lee, and S. C. Won, "Adaptive lag synchronization for uncertain complex dynamical network with delayed coupling," *Applied Mathematics and Computation*, vol. 218, no. 9, pp. 4872–4880, 2012.

[14] X. Y. Guo and J. M. Li, "Stochastic synchronization for time-varying complex dynamical networks," *Chinese Physics B*, vol. 21, no. 2, Article ID 020501, 2012.

[15] Z. G. Wu, J. H. Park, H. Su, and J. Chu, "Non-fragile synchronisation control for complex networks with missing data," *International Journal of Control*, vol. 86, no. 3, pp. 555–566, 2013.

[16] T. H. Lee, J. H. Park, H. Y. Jung, S. M. Lee, and O. M. Kwon, "Synchronization of a delayed complex dynamical network with free coupling matrix," *Nonlinear Dynamics*, vol. 69, no. 3, pp. 1081–1090, 2012.

[17] Z. W. Liu, Z. H. Guan, Y. W. Wang, and R. Q. Liao, "Synchronization of complex dynamical networks via distributed impulsive control," in *Proceedings of the 48th IEEE Conference on Decision and Control held jointly with 2009 28th Chinese Control Conference (CDC/CCC '09)*, pp. 1714–1719, Shanghai, China, December 2009.

[18] W. Yu, P. DeLellis, G. Chen, M. di Bernardo, and J. Kurths, "Distributed adaptive control of synchronization in complex networks," *IEEE Transactions on Automatic Control*, vol. 57, no. 8, pp. 2153–2158, 2012.

[19] J. Xiang and G. Chen, "On the V-stability of complex dynamical networks," *Automatica*, vol. 43, no. 6, pp. 1049–1057, 2007.

[20] Q. Song, J. Cao, and F. Liu, "Synchronization of complex dynamical networks with nonidentical nodes," *Physics Letters A*, vol. 374, no. 4, pp. 544–551, 2010.

[21] J. Zhao, D. J. Hill, and T. Liu, "Global bounded synchronization of general dynamical networks with nonidentical nodes," *IEEE Transactions on Automatic Control*, vol. 57, no. 10, pp. 2656–2662, 2012.

[22] Y. Wang and J. Cao, "Cluster synchronization in nonlinearly coupled delayed networks of non-identical dynamic systems," *Nonlinear Analysis*, vol. 14, no. 1, pp. 842–851, 2013.

[23] J. X. Xu and Y. Tan, "A composite energy function-based learning control approach for nonlinear systems with time-varying parametric uncertainties," *IEEE Transactions on Automatic Control*, vol. 47, no. 11, pp. 1940–1945, 2002.

[24] J. Lü and G. Chen, "A time-varying complex dynamical network model and its controlled synchronization criteria," *IEEE Transactions on Automatic Control*, vol. 50, no. 6, pp. 841–846, 2005.

[25] J. Zhou, J. A. Lu, and J. Lü, "Adaptive synchronization of an uncertain complex dynamical network," *IEEE Transactions on Automatic Control*, vol. 51, no. 4, pp. 652–656, 2006.

[26] T. F. Wang, J. M. Li, and S. Tang, "Adaptive synchronization of nonlinearly parameterized complex dynamical networks with unknown time-varying parameters," *Mathematical Problems in Engineering*, vol. 2012, Article ID 592539, 16 pages, 2012.

[27] Y. Dai, Y. Cai, and X. Xu, "Synchronization criteria for complex dynamical networks with neutral-type coupling delay," *Physica A*, vol. 387, no. 18, pp. 4673–4682, 2008.

[28] Y. Xu, W. Zhou, J. Fang, and W. Sun, "Adaptive synchronization of the complex dynamical network with non-derivative and derivative coupling," *Physics Letters A*, vol. 374, no. 15-16, pp. 1673–1677, 2010.

[29] J. Wang, L. Feng, and S. K. Li, "Adaptive synchronization between two delayed complex networks with derivative coupling and non-identical nodes," in *Proceedings of the International Conference on Information and Automation (ICIA '11)*, pp. 135–140, June 2011.

[30] L. P. Deng, Z. Y. Wu, and Q. C. Wu, "Pinning synchronization of complex network with non-derivative and derivative coupling," *Nonlinear Dynamics*, vol. 73, no. 1-2, pp. 775–782, 2013.

[31] Y. K. Zhu, X. Y. Luo, and S. B. Li, "Exponential synchronization of complex dynamical systems with delay and derivative coupling via impulse," in *Proceedings of the 10th World Congress on Intelligent Control and Automation*, pp. 875–880, July 2012.

[32] Q. Bian and H. Yao, "Adaptive synchronization of bipartite dynamical networks with distributed delays and nonlinear derivative coupling," *Communications in Nonlinear Science and Numerical Simulation*, vol. 16, no. 10, pp. 4089–4098, 2011.

[33] W. Lin and C. Qian, "Adaptive control of nonlinearly parameterized systems: the smooth feedback case," *IEEE Transactions on Automatic Control*, vol. 47, no. 8, pp. 1249–1266, 2002.

[34] G. Tao, "A simple alternative to the Barbălat lemma," *IEEE Transactions on Automatic Control*, vol. 42, no. 5, p. 698, 1997.

Hindawi Publishing Corporation
Journal of Applied Mathematics
Volume 2013, Article ID 123072, 11 pages
http://dx.doi.org/10.1155/2013/123072

Research Article

H_∞ Formation Control and Obstacle Avoidance for Hybrid Multi-Agent Systems

Dong Xue,[1,2] Jing Yao,[1,3] and Jun Wang[1]

[1] *Department of Control Science and Engineering, Tongji University, Shanghai 201804, China*
[2] *Institute for Information-Oriented Control, Technische Universität München, D-80290 München, Germany*
[3] *Department of Electronic and Computer Engineering, The Hong Kong University of Science and Technology, Hong Kong SAR, China*

Correspondence should be addressed to Jing Yao; yaojing@tongji.edu.cn

Received 10 July 2013; Accepted 20 September 2013

Academic Editor: Michael Chen

Copyright © 2013 Dong Xue et al. This is an open access article distributed under the Creative Commons Attribution License, which permits unrestricted use, distribution, and reproduction in any medium, provided the original work is properly cited.

A new concept of H_∞ formation is proposed to handle a group of agents navigating in a free and an obstacle-laden environment while maintaining a desired formation and changing formations when required. With respect to the requirements of changing formation subject to internal or external events, a hybrid multiagent system (HMAS) is formulated in this paper. Based on the fact that obstacles impose the negative effect on the formation of HMAS, the H_∞ formation is introduced to reflect the above disturbed situation and quantify the attenuation level of obstacle avoidance via the H_∞-norm of formation stability. An improved Newtonian potential function and a set of repulsive functions are employed to guarantee the HMAS formation-keeping and collision-avoiding from obstacles in a path planning problem, respectively. Simulation results in this paper show that the proposed formation algorithms can effectively allow the multiagent system to avoid penetration into obstacles while accomplishing prespecified global objective successfully.

1. Introduction

In recent years, there has been a spurt of interest in the area of cooperative control for multiple agents due to its challenging features and many applications, for example, formation control [1, 2], obstacles avoidance [3, 4], rendezvous [5], flocking [6], foraging [7], troop hunting, and payload transport. Referring to the existing literature, it is obvious that multiple agents can perform tasks faster and more efficiently than a single one. The existing approaches for cooperative control of MASs fall into several categories, including behavior-based, artificial potential, virtual structure, leader-follower, graph theory, and decentralized control methods. Other methods and research aspects of the cooperative control for MASs can be found in [8–10].

As one key branch of cooperative control, formation and obstacle avoidance problems of multiagent systems have been received significant attentions [1–4, 8, 11]. In this case, the MAS is usually required to follow a trajectory while maintaining a desired formation and avoiding obstacles. In some practical situations, the group of agents may be necessary to perform certain maneuvers, such as split, reunion and reconfiguration, in order to negotiate the obstacles [2, 12]. Although the formation problem for MASs is attracting increasingly research attention, there are still several open fields deserving further investigation, such as robustness, fragility, and effectiveness of formation. With respect to the most robustness analysis of MASs, such as [13–15], the agents are investigated under uncertain environments with external disturbances. However, in some sense, obstacles in the navigational path can also be regarded as a disturbance from environment, which would impair the performance of formation stability. Furthermore, the influence of obstacles is usually negligible when the distances between agents and obstacles exceed certain range threshold. Inspired by obstacle avoidance issue and H_∞ control theory, we introduce a new concept of H_∞ formation, which treats the effects of obstacles as certain exterior disturbances, to handle the formation problem of MASs in clustered environment. Then a Lyapunov approach is employed to deal with H_∞ analysis.

Artificial potential field (APF) method is widely used in coordination control of MASs due to its simplicity and efficiency [7, 16], which was first introduced by [17] for formation and obstacle avoidance of MASs. Since then, several literatures have attempted to improve the performance of APF method. In [18], bifurcation theory is used to reconfigure the formation through a simple free parameter change to reduce the computational expense. By introducing a new concept of artificial potential trenches in [11], the scalability and flexibility of robot formations are improved. The basic idea of potential field theory is to create a workshop, where the agents are counterbalanced with each other by the interactive potential force between them and suffered a repulsive force from obstacles to steer around them [19]. Despite all the advantages of APFs, the lack of accurate representations of obstacles with arbitrary shapes is regarded as one major limitation to generally extend to practical applications. A potential function based on generalized sigmoid functions, which can be generated from the combinations of implicit primitives or from sampled surface data is proposed in [20]. Using the optical flow, [21] have achieved the automatic detection of obstacles in virtual environment. The formation control with obstacle avoidance is highly related to the flocking problems in [6], where only the obstacles with simple shapes are taken into account. In this paper, we assume that the boundary functions of arbitrary obstacles can be known from the implicit functions which can be constructed from sensor readings or image data. By combining the artificial potential model and the negotiating results with obstacles, a resultant artificial repulsive force is developed to guarantee the obstacles avoidance.

In addition, it may happen that the MASs are desired to perform various formation shapes to achieve specified navigational objective. As a result, it is necessary for the MAS to possess the ability of changing formation shape during the navigation, such as split, rejoin, and reconfiguration. In this case, the MASs consist of both continuous variables and discrete events. In [2], a triple (group element $\mathfrak{g}$, shape variable $\mathfrak{r}$, control graph $\mathfrak{H}$) is employed to model the mobile robots and meet the requirement of changing formations. Furthermore, a Petri-potential-fuzzy hybrid controller is presented for the motion planning of multiple mobile robots with multiple targets in a clustered environment in [22]. In this paper, a hybrid formation controller is proposed where the formation changes as events (tasks) occur. In practice, the correspondence between tasks and formation can be prespecified at the initialization step, and created intelligently by the embedded processors in each agent during the implementation. It is remarkable that the hybrid multiagent systems exhibit continuous-state dynamics and discrete behavior jumping between formations. Then, we formulate the HMAS by a hybrid machine owing to its advantages of illustrating inputs and outputs explicitly [23, 24].

The paper proceeds as follows. The formation control and obstacle avoidance problem are addressed in Section 2. In Section 3, a new concept of H_∞ formation and technical proofs are provided. In Section 4, we discuss the obstacle-avoidance functions. Simulation results to illustrate the results are presented in Section 5. Conclusions and future work are provided in Section 6.

Notation 1. Throughout the paper, let $\overline{\mathbb{Z}}$ be the set of positive integers, and let $\mathbb{J} = [t_0, +\infty)$ $(t_0 \geq 0)$. $\mathbb{R}^n$ represents the real Euclidean n-dimensional vector space. For $x = (x_1, \ldots, x_n)^\intercal \in \mathbb{R}^n$, the norm of x is $\|x\| \triangleq (x^\intercal x)^{1/2}$, where the symbol $(\cdot)^\intercal$ denotes the transpose of a matrix or a vector. I_n denotes the identity matrix of order n (for simplicity I if no confusion arises). $\mathfrak{L}_2[0, \infty)$ is the Lebesgue space of R^n-valued vector-functions $g(\cdot)$, defined on the time interval $[0, \infty)$, with the norm $\|g\|_2 \triangleq \left(\int_0^\infty \|g(t)\|^2\right)^{1/2} dt$.

2. Problem Formulation and Preliminaries

Consider a multiagent system with N nodes and an undirected graph topology $\mathfrak{G} = (\nu, \varepsilon)$; ν and ε are the set of vertices and the set of edges (i.e, $\varepsilon \in \nu \times \nu$), respectively. The notation (i, j) or (j, i) equivalently denotes the edge of the graph between node i and node j. Furthermore, a graph is connected if there exists a path between every pair of distinct nodes; otherwise it is disconnected.

Before proceeding further, the following assumptions are made in this paper.

(1) Each agent is equipped with sensors and computational hardware that allow it to detect the distances to the obstacles within the sensing range. Furthermore, the agent can access its position in the world coordinate system and broadcast to its neighboring agents. The wireless communication has a limited range and is assumed to be imperfect; that is, links may be broken.

(2) The multiagent system has a task set Σ and a formation set $\mathbb{F}$ which meet actual project needs before initiation. And suppose that all agents know the information of Σ and $\mathbb{F}$, as well as the desired formation shape and trajectories in every step.

Referred to hybrid machine presented in [23, 24] and associated with the practical application, we consider a special class of hybrid multiagent system (HMAS) which is modeled by an elementary hybrid machine (EHM) [25] as follows:

$$\text{HMAS} = \left(Q, \Sigma, Dy, E, \left(\Delta^0, x(0)\right)\right). \tag{1}$$

The elements of HMAS are denoted as follows. $Q = \{q_0, q_1, \ldots, q_{m-1}\}$ is a set of vertices (discrete states); in formation control, each discrete state $q_i \in Q$ corresponds to a desired formation shape Δ^i, and we denote a set of formation shape by $\mathbb{F} := \{\Delta^0, \Delta^1, \ldots, \Delta^{m-1}\}$. $\Sigma = \{\mathscr{H}_{q_i q_j}, q_i, q_j \in Q\}$ $(i, j = 0, \ldots, m-1)$ is a finite (task) set of event labels; $(q_0, x(0))$ is the initial desired formation and state of HMAS, respectively. $E = \{(q_i, \mathscr{H}_{q_i q_j}, q_j, x^0_{q_0}) : q_i, q_j \in Q\}$ is a set of edges (transition-paths), where q_i is the exited vertex and q_j is the entered one. If the event $\mathscr{H}_{q_i q_j}$ is triggered, consequently the formation of HMAS transits from Δ^i to Δ^j.

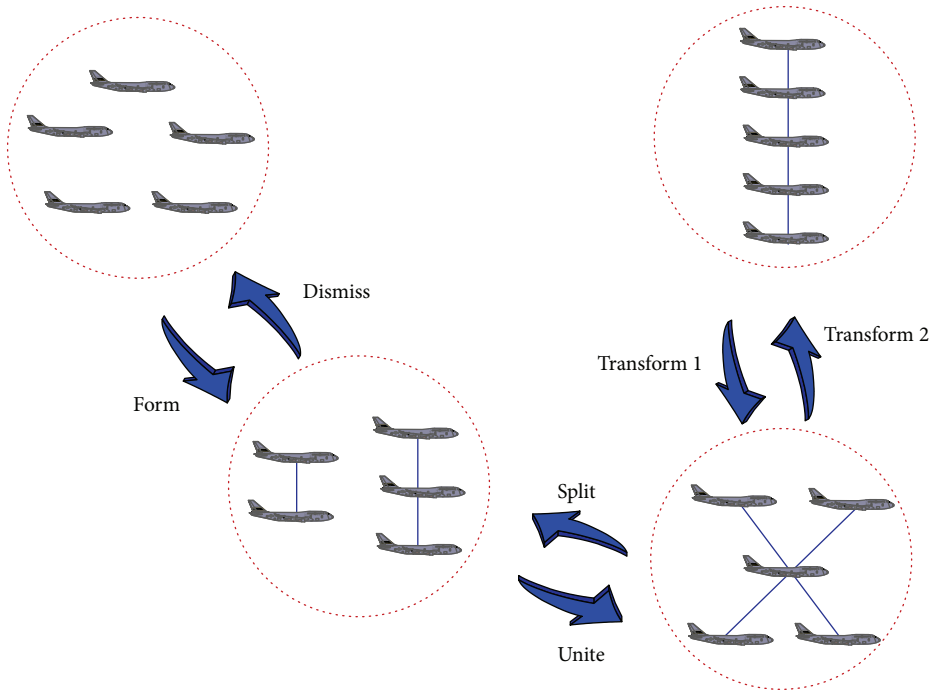

Figure 1: Example of a hybrid multiagent system performing under different events.

For example, Figure 1 shows a sequence of admissible collective behaviors of a HMAS triggered by event set $\Sigma = \{\text{form, dismiss, split, unite, transform 1, transform 2}\}$.

Remark 1. In practical application, the multiagent system is always assigned multiple tasks in the navigation, and each task may correspond to multiple formation shapes. Similarly to the deterministic automaton described in [26], we suppose that the HMAS is deterministic; namely, there cannot be two transitions with the same event label. It is worth mentioning that the following theoretical analysis is available for nondeterministic HMAS; that is, there can be multiple transitions triggered by the same event.

Dy is the dynamics of HMAS and for each agent i and $q \in Q$, which is described by

$$\dot{x}_i(t) = f(t,x) + \sum_{j=1}^{N} J_{ij}(t)\, x_j(t) + u_i^q(t) + C_i w_i(t), \quad (2)$$

where $i \in \{1,2,\ldots,N\}$, $t \in \mathbb{J}$, $x_i(t) \in \mathbb{R}^{n\times 1}$, $x = [x_1^\intercal, x_2^\intercal, \ldots, x_N^\intercal]^\intercal$, and C_i are real constant matrices with appropriate dimensions. $f(t,x) : \mathbb{J} \times \mathbb{R}^{N\times n} \to \mathbb{R}^{n\times 1}$ is continuously differentiable, representing the group motion (i.e., path of the HMAS). $J(t) = (J_{ij}(t))_{N\times N}$ is the time-varying coupling configuration matrix representing the communication strength and communicational topology of the HMAS. If there is an interconnection between agent i and agent j $(j \neq i)$, then $J_{ij}(t) = J_{ji}(t) > 0$; otherwise, $J_{ij}(t) = J_{ji}(t) = 0$, and the diagonal elements of matrix $J(t)$ are defined by

$$J_{ii}(t) = -\sum_{j=1, j\neq i}^{N} J_{ij}(t) = -\sum_{j=1, j\neq i}^{N} J_{ji}(t). \quad (3)$$

$w_i(t)$ here denotes the obstacle-avoiding function, which will be derived from potential function in Section 6.

Moreover, the formation controller in this paper is derived by extending the one in [1] into multiformation case $(q \in Q)$:

$$\begin{aligned} u_i^q(t) = \sum_{\substack{j=1\\ j\neq i}}^{N} 2\left(x_j(t) - x_i(t) - \Delta_{ij}^q\right) \\ \times \left[\frac{S_a}{L_a^2} e^{-\|x_j(t)-x_i(t)-\Delta_{ij}^q\|^2/L_a^2}\right. \\ - \frac{S_r}{L_r^2} e^{-\|x_j(t)-x_i(t)-\Delta_{ij}^q\|^2/L_r^2} \\ + S_r\left(\frac{1}{L_r^2} + \frac{1}{L_a^2}\right) \\ \left. \times e^{-(1/L_r^2+1/L_a^2)\|x_j(t)-x_i(t)-\Delta_{ij}^q\|^2}\right], \end{aligned} \quad (4)$$

where $\Delta_{ij}^q \in \mathbb{R}^{n\times 1}$ and $\Delta^q = (\Delta_{ij}^q)_{N\times N} \in \mathbb{F}$ is the formation-shape matrix of the multiagent system with $\Delta_{ij}^q = -\Delta_{ji}^q$ and $\Delta_{ii}^q = 0$. Parameters S_a, S_r, L_a, and L_r are positive constants representing the strengths and effect ranges of the attractive and repulsive forces, respectively; and with the following constraint we have

$$\begin{aligned} \frac{S_a}{S_r} > \frac{L_a^2}{L_r^2} e^{(-1/L_r^2-1/L_a^2)\|x_j(t)-x_i(t)-\Delta_{ij}^q\|^2} \\ - \left(1 + \frac{L_a^2}{L_r^2}\right) e^{-(\|x_j(t)-x_i(t)-\Delta_{ij}^q\|^2/L_r^2)}, \end{aligned} \quad (5)$$

where $L_a > L_r$.

Remark 2. Compared to the formation controller given in [1], the formation controller in this paper is designed to achieve more complicated control objects, such as formation switching in clustered environment. Furthermore, it is worth mentioning that the obstacle-avoiding function $w_i(t)$ $(i = 1, \ldots, N)$ as a part of the controller is an important contribution for this paper.

In order to simplify (4), define

$$\begin{aligned}\varphi_{ij}^{q}(t) = 2\Bigg[& \frac{S_a}{L_a^2} e^{-(\|x_j(t)-x_i(t)-\Delta_{ij}^{q}\|^2/L_a^2)} \\ & - \frac{S_r}{L_r^2} e^{-(\|x_j(t)-x_i(t)-\Delta_{ij}^{q}\|^2/L_r^2)} \\ & + \left(\frac{S_r}{L_r^2} + \frac{S_r}{L_a^2}\right) \\ & \times e^{(-1/L_r^2+1/L_a^2)(\|x_j(t)-x_i(t)-\Delta_{ij}^{q}\|^2)}\Bigg].\end{aligned} \tag{6}$$

According to (5), one can verify $\varphi_{ij}^{q}(t) > 0$, and the necessity of this constraint can be addressed by referring to that the force vector and position vector are unidirectional.

Then rewrite the formation controller (4) as follows:

$$u_i^{q}(t) = \sum_{\substack{j=1 \\ j\neq 1}}^{N} \varphi_{ij}^{q}(t)\left(x_j(t) - x_i(t) - \Delta_{ij}^{q}\right), \quad q \in Q. \tag{7}$$

Remark 3. Let $\varphi_{ij}^{q}(t)$ be a continuous function with respect to $\|x_j(t) - x_i(t) - \Delta_{ij}^{q}\|$, and it is easy to prove that if the bounds of $\|x_j(t) - x_i(t) - \Delta_{ij}^{q}\|$ exist, then $\varphi_{ij}^{q}(t)$ is bounded on all sets of $\|x_j(t) - x_i(t) - \Delta_{ij}^{q}\|$ $(i, j = 1, \ldots, N$ and $q \in Q)$. Furthermore, regard the fact that most multiagent systems are implemented in finite horizon which means the limitation of interagent distances exists. Throughout the paper, we assume that the lower bound of $\varphi_{ij}^{q}(t)$ exists, and we denote it by

$$0 < \overline{\varphi} \leq \min_{\substack{i,j=1,\ldots,N \\ q=0,\ldots,m-1}} \varphi_{ij}^{q}(t), \tag{8}$$

where $\overline{\varphi} > 0$ can be guaranteed by choosing appropriate values of L_a, L_r, S_a, and S_r in the constraint (5).

3. Analysis of H_∞ Formation Stability

Now, this section will analyze H_∞ formation stability of the above-developed framework of HMAS in a free and an obstacle-laden environment, respectively.

Since we have property (3), the HMAS (1) is equivalent to

$$\begin{aligned}\dot{x}_i(t) = & f(t,x) + \sum_{j=1}^{N} J_{ij}(t)\left(x_j(t) - x_i(t)\right) \\ & + u_i^{q}(t) + C_i w_i(t).\end{aligned} \tag{9}$$

Before moving on, we need to note that the formation switching in the controller will introduce discontinuities to the right hand side of (9). With respect to the dwell-time theory in [27], if the switching of a family of individually stable systems is sufficiently slow, then overall systems remain stable. As a result, we assume that the intervals between consecutive switching signals, that is, dwell time, are large enough. Due to the introduction of average dwell-time, this assumption does not represent a restriction because this concept allows the formation switching mechanism to be more flexible provided that the average interval between consecutive switching is no less than certain fixed positive constant.

To investigate the formation control of MAS, we introduce a measurement error $X_{ij}(t)$ given as

$$X_{ij}(t) = x_j(t) - x_i(t). \tag{10}$$

It follows from (5), (9), and (10) that the time derivative of $X_{ij}(t)$ is as follows:

$$\begin{aligned}\dot{X}_{ij}(t) = & \sum_{k=1}^{N}\left(J_{jk}(t)X_{jk}(t) - J_{ik}(t)X_{ik}(t)\right) \\ & + C_j w_j(t) - C_i w_i(t) \\ & + \sum_{k=1}^{N}\Big(\varphi_{jk}^{q}(t)\left(X_{jk}(t) - \Delta_{jk}^{q}\right) \\ & - \varphi_{ik}^{q}(t)\left(X_{ik}(t) - \Delta_{ik}^{q}\right)\Big).\end{aligned} \tag{11}$$

For a formation of multiple agents moving in a clustered environment, it is inevitable to encounter various obstacles which affect the performance of formation or even break the whole system down. Naturally, the multiagent system is desirable to be able to adapt to the environment. In general, the agents are only affected by the obstacles when they enter a certain region. At other times, the influence being exerted from obstacles can be negligible. With the above analysis, the obstacles can be treated as exogenous disturbances deriving from the environment, and H_∞ analysis can be employed to investigate the formation stability of HMAS.

Associating the system (2) with the formation controller (7), we define a disagreement function similar to [28] as follows:

$$\Phi\left(X_{ij}(t)\right) = \frac{1}{N}\sum_{i=1}^{N-1}\sum_{j>i}^{N}\left\|X_{ij}(t) - \Delta_{ij}^{q}\right\|^2, \tag{12}$$

which demonstrates the formation performance of HMAS for $q \in Q$.

For the HMAS given in (2), H_∞ formation stability means to find a formation controller (7) such that the following conditions in (**DF1**) and (**DF2**) hold.

(***DF1***). The formation of HMAS (1) is asymptotically stable when $w(t) = 0$, where $w(t) = [w_1^{\mathrm{T}}, w_2^{\mathrm{T}}, \ldots, w_N^{\mathrm{T}}]^{\mathrm{T}}$, which is equivalent to the asymptotical formation stability of the

HMAS (1) in the absence of obstacles. That is to say that, all agents asymptotically converge to the desired formation positions; that is, $\|X_{ij}(t)-\Delta_{ij}^{q}\| \to 0$ as $t \to \infty$, where $q \in Q$.

(DF2). The formation controller ensures a certain level of H_∞ formation performance as follows:

$$\sup_{\substack{X_{ij}(0)\\ \omega_i \neq 0}} \frac{\int_0^\infty \Phi\left(X_{ij}(t)\right) dt}{(1/4N)\sum_{i=1}^{N}\sum_{j=1}^{N}\left\|X_{ij}(0)-\Delta_{ij}^{q}\right\|^2 + (1/N)\sum_{i=1}^{N}\left\|w_i(t)\right\|_2^2} < \gamma \tag{13}$$

for initial states $x_i(0) \in \mathbb{R}^{n\times 1}$ and $q \in Q$, where $\gamma \geq 1$ is a constant, $X_{ij}(0) = x_j(0) - x_i(0)$, and $\Phi(X_{ij}(t))$ is given by (12). If the conditions (**DF1**) and (**DF2**) hold, then the formation of HMAS (1) is said to achieve the H_∞ formation stability.

Remark 4. It is worthwhile noting that (**DF2**) is a standard condition arising from the H_∞ control theory, which implies that X_{ij}, $(i, j = 1, \ldots, N)$, converges to Δ_{ij}^{q} in the sense of $\mathfrak{L}_2$.

Remark 5. According to (**DF2**), the attenuation level $\gamma \geq 1$ shows the sensitivity of obstacle avoidance in HMAS (1). Giving a smaller $\gamma \geq 1$ means that the intensity and range of reaction of HMAS towards obstacles are smaller.

Theorem 6. *Given a positive scalar $\gamma \geq 1$, the H_∞ formation problem of the HMAS* (1) *under the conditions* (**DF1**) *and* (**DF2**) *is solved at initial positions $x_i(0) \in \mathbb{R}^n$, if*

$$\begin{bmatrix} -\pi_{ij} + \dfrac{I}{N} & 0 & 0 & -\dfrac{C_i}{N} \\ 0 & -\pi_{ij} & \dfrac{\pi_{ij}+\chi_{ij}}{2} & 0 \\ 0 & \dfrac{\pi_{ij}^{\mathsf{T}}+\chi_{ij}^{\mathsf{T}}}{2} & -\chi_{ij} & 0 \\ -\dfrac{C_i^{\mathsf{T}}}{N} & 0 & 0 & -\dfrac{2\gamma}{N^2} \end{bmatrix} < 0 \tag{14}$$

holds for all $i, j = 1, 2, \ldots, N$, where

$$\pi_{ij} = \frac{\left(\overline{\varphi} + J_{ij}\right) I}{2}, \qquad \chi_{ij} = \frac{\left(\overline{\varphi} - J_{ij}\right) I}{2}, \tag{15}$$

and $\overline{\varphi}$ is defined in (8).

Proof. Without the loss of generality, construct a common Lyapunov function in the form of

$$V = \frac{1}{4N}\sum_{i=1}^{N}\sum_{j=1}^{N}\left\|X_{ij}(t)-\Delta_{ij}^{q}\right\|^2, \tag{16}$$

where $q \in Q$. If the derivative of V with respective to (9) is constantly negative for all subsystems, then the formation of HMAS (1) is stable. For the sake of convenience, $X_{ij}(t)$ is implicitly rewritten as X_{ij}, as well as $J_{ij}(t)$, $\varphi_{ij}^{q}(t)$, and $w_i(t)$ in the proof.

From the above discussion, one has

$$\begin{aligned} \dot{V} &= \frac{1}{2N}\sum_{i=1}^{N}\sum_{j=1}^{N}\left(X_{ij}-\Delta_{ij}^{q}\right)^{\mathsf{T}}\dot{X}_{ij} \\ &= \underbrace{\frac{1}{2N}\sum_{i=1}^{N}\sum_{j=1}^{N}\sum_{k=1}^{N}\left[\left(X_{ij}-\Delta_{ij}^{q}\right)^{\mathsf{T}}\left(J_{jk}X_{jk}-J_{ik}X_{ik}\right)\right]}_{v_1} \\ &\quad + \underbrace{\frac{1}{N}\sum_{i=1}^{N}\sum_{j=1}^{N}\sum_{k=1}^{N}\varphi_{jk}^{q}\left(X_{ij}-\Delta_{ij}^{q}\right)^{\mathsf{T}}\left(X_{jk}-\Delta_{jk}^{q}\right)}_{v_2} \\ &\quad + \underbrace{\frac{1}{2N}\sum_{i=1}^{N}\sum_{j=1}^{N}\left(X_{ij}-\Delta_{ij}^{q}\right)^{\mathsf{T}}\left(C_jw_j-C_iw_i\right)}_{v_3}. \end{aligned} \tag{17}$$

In respect that the coupling configuration matrix $J(t)$ is symmetric, and $X_{ij} = -X_{ji}$, $\Delta_{ij}^{q} = -\Delta_{ji}^{q}$, $X_{ii} = 0$, and $\Delta_{jj}^{q} = 0$, one has

$$\begin{aligned} v_1 &= -\frac{1}{N}\sum_{i=1}^{N}\sum_{j=1}^{N}\sum_{k=1}^{N}\left(X_{ji}-\Delta_{ji}^{q}\right)^{\mathsf{T}}J_{jk}X_{jk} \\ &= -\frac{1}{N}\sum_{i=1}^{N}\sum_{k=1}^{N}\sum_{k<j}^{N}\left(X_{ji}-\Delta_{ji}^{q}\right)^{\mathsf{T}}J_{jk}X_{jk} \\ &\quad \underbrace{-\frac{1}{N}\sum_{i=1}^{N}\sum_{k=1}^{N}\sum_{k>j}^{N}\left(X_{ji}-\Delta_{ji}^{q}\right)^{\mathsf{T}}J_{jk}X_{jk}}_{v_{11}}. \end{aligned} \tag{18}$$

Renaming j in the v_{11} as k, thus one has

$$v_1 = -\frac{1}{N}\sum_{i=1}^{N}\sum_{k=1}^{N}\sum_{k<j}^{N}\left[\left(X_{ji}-\Delta_{ji}^{q}\right)^{\mathsf{T}} - \left(X_{ki}-\Delta_{ki}^{q}\right)^{\mathsf{T}}\right]J_{jk}X_{jk}. \tag{19}$$

One can find the fact that $X_{ji}^{\mathsf{T}} - X_{ki}^{\mathsf{T}} = X_{jk}^{\mathsf{T}}$ and $\Delta_{ji}^{q} - \Delta_{ki}^{q} = \Delta_{jk}^{q}$; then

$$\begin{aligned} v_1 &= -\frac{1}{N}\sum_{i=1}^{N}\sum_{k=1}^{N}\sum_{k<j}^{N}\left(X_{jk}-\Delta_{jk}^{q}\right)^{\mathsf{T}}J_{jk}X_{jk} \\ &= -\sum_{i=1}^{N}\sum_{j>i}^{N}\left(X_{ij}-\Delta_{ij}^{q}\right)^{\mathsf{T}}J_{ij}X_{ij}. \end{aligned} \tag{20}$$

Using the standard completing the square argument, it follows from (20) that

$$\begin{aligned} v_1 = &-\frac{1}{2}\sum_{i=1}^{N-1}\sum_{j>i}^{N} J_{ij}\left\|X_{ij}-\Delta_{ij}^{q}\right\|^2 \\ &-\frac{1}{2}\sum_{i=1}^{N-1}\sum_{j>i}^{N} J_{ij}\left\|X_{ij}\right\|^2 \\ &+\frac{1}{2}\sum_{i=1}^{N-1}\sum_{j>i}^{N} J_{ij}\left\|\Delta_{ij}^{q}\right\|^2. \end{aligned} \tag{21}$$

Furthermore, the v_2 is similarly analyzed as follows:

$$v_2 = -\sum_{i=1}^{N}\sum_{j>i}^{N}\varphi_{ij}^{q}\left(X_{ij}-\Delta_{ij}^{q}\right)^{\mathsf{T}}\left(X_{ij}-\Delta_{ij}^{q}\right). \tag{22}$$

With respect to (8), one can easily obtain

$$\begin{aligned} v_2 &\le -\overline{\varphi}\sum_{i=1}^{N-1}\sum_{j>i}^{N}\left(X_{ij}-\Delta_{ij}^{q}\right)^{\mathsf{T}}\left(X_{ij}-\Delta_{ij}^{q}\right) \\ &= \frac{\overline{\varphi}}{2}\sum_{i=1}^{N-1}\sum_{j>i}^{N}\Big(2X_{ij}^{\mathsf{T}}\Delta_{ij}^{q}-\left\|X_{ij}-\Delta_{ij}^{q}\right\|^2 \\ &\qquad -\left\|X_{ij}\right\|^2-\left\|\Delta_{ij}^{q}\right\|^2\Big). \end{aligned} \tag{23}$$

Then, for v_3, one has

$$v_3 = -\frac{2}{N}\sum_{i=1}^{N-1}\sum_{j>i}^{N}\left(X_{ij}-\Delta_{ij}^{q}\right)^{\mathsf{T}}C_i w_i. \tag{24}$$

Now, we consider the formation stability of HMAS (1) with $w(t) = 0$. From the inequalities (21) and (23), $\dot{V}$ becomes

$$\dot{V} \le \sum_{i=1}^{N-1}\sum_{j>i}^{N}\Omega_{ij}^{\mathsf{T}}\begin{bmatrix} -\pi_{ij} & 0 & 0 \\ 0 & -\pi_{ij} & \dfrac{\pi_{ij}+\chi_{ij}}{2} \\ 0 & \dfrac{\pi_{ij}^{\mathsf{T}}+\chi_{ij}^{\mathsf{T}}}{2} & -\chi_{ij} \end{bmatrix}\Omega_{ij}, \tag{25}$$

where $\Omega_{ij} = [(X_{ij}-\Delta_{ij}^{q})^{\mathsf{T}}, X_{ij}^{\mathsf{T}}, (\Delta_{ij}^{q})^{\mathsf{T}}]^{\mathsf{T}}$, π_{ij}, and χ_{ij} are given in (15). By the Schur complement formula, the achievement of inequality (14) is equivalent to the following inequalities satisfied as follows:

$$\begin{bmatrix} -\pi_{ij}+\dfrac{I}{N} & 0 & 0 \\ 0 & -\pi_{ij} & \dfrac{\pi_{ij}+\chi_{ij}}{2} \\ 0 & \dfrac{\pi_{ij}^{\mathsf{T}}+\chi_{ij}^{\mathsf{T}}}{2} & -\chi_{ij} \end{bmatrix} < 0,$$

$$\begin{bmatrix} \dfrac{C_i}{N} \\ 0 \\ 0 \end{bmatrix}^{\mathsf{T}}\begin{bmatrix} \pi_{ij}-\dfrac{I}{N} & 0 & 0 \\ 0 & \pi_{ij} & -\dfrac{\pi_{ij}+\chi_{ij}}{2} \\ 0 & -\dfrac{\pi_{ij}^{\mathsf{T}}+\chi_{ij}^{\mathsf{T}}}{2} & \chi_{ij} \end{bmatrix}^{-1}\begin{bmatrix} \dfrac{C_i}{N} \\ 0 \\ 0 \end{bmatrix} < \frac{2\gamma}{N^2}. \tag{26}$$

By nonnegative matrix theory, one can easily find that

$$\begin{aligned} &\begin{bmatrix} -\pi_{ij} & 0 & 0 \\ 0 & -\pi_{ij} & \dfrac{\pi_{ij}+\chi_{ij}}{2} \\ 0 & \dfrac{\pi_{ij}^{\mathsf{T}}+\chi_{ij}^{\mathsf{T}}}{2} & -\chi_{ij} \end{bmatrix} \\ &\le \begin{bmatrix} -\pi_{ij}+\dfrac{I}{N} & 0 & 0 \\ 0 & -\pi_{ij} & \dfrac{\pi_{ij}+\chi_{ij}}{2} \\ 0 & \dfrac{\pi_{ij}^{\mathsf{T}}+\chi_{ij}^{\mathsf{T}}}{2} & -\chi_{ij} \end{bmatrix} < 0, \end{aligned} \tag{27}$$

which implies $\dot{V} < 0$. This proves that condition (**DF1**) holds for the HMAS (1) with $w(t) = 0$.

Next, we prove the H_∞ performance constraint (**DF2**) for all nonzero $w_i(t) \in \mathfrak{L}_2[0,\infty)$ and a prescribed $\gamma \ge 1$. Define

$$\begin{aligned} \widetilde{V} = &\int_0^\infty\left(\Phi\left(X_{ij}(t)\right)-\gamma\frac{1}{N}\sum_{i=1}^{N}w_i^{\mathsf{T}}(t)\,w_i(t)\right)dt \\ &-\frac{\gamma}{2N}\sum_{i=1}^{N-1}\sum_{j>i}^{N}\left\|x_j(0)-x_i(0)-\Delta_{ij}^{q}\right\|^2, \end{aligned} \tag{28}$$

and one has

$$\begin{aligned} \widetilde{V} &= \int_0^\infty\left(\Phi\left(X_{ij}(t)\right)-\frac{\gamma}{N}\sum_{i=1}^{N}w_i^{\mathsf{T}}(t)\,w_i(t)+\dot{V}(x(t))\right)dt \\ &\quad -V(x(\infty))+\frac{1-\gamma}{2N}\sum_{i=1}^{N-1}\sum_{j>i}^{N}\left\|x_j(0)-x_i(0)-\Delta_{ij}^{q}\right\|^2 \\ &\le \int_0^\infty\underbrace{\left(\Phi\left(X_{ij}(t)\right)-\frac{\gamma}{N}\sum_{i=1}^{N}\left\|w_i(t)\right\|^2+\dot{V}(x(t))\right)}_{\Xi}dt. \end{aligned} \tag{29}$$

Combining (21), (23), and (24), one obtains

$$\begin{aligned} \Xi = \sum_{i=1}^{N}\sum_{j=1}^{N}\Bigg\{ &\frac{1}{2N}\left\|X_{ij}-\Delta_{ij}^{q}\right\|^2-\frac{\gamma}{N^2}w_i^{\mathsf{T}}w_i \\ &-\frac{1}{N}\left(X_{ij}-\Delta_{ij}^{q}\right)^{\mathsf{T}}C_i w_i \\ &+\Omega_{ij}^{\mathsf{T}}\begin{bmatrix} -\dfrac{\pi_{ij}}{2} & 0 & 0 \\ 0 & -\dfrac{\pi_{ij}}{2} & \dfrac{\pi_{ij}+\chi_{ij}}{4} \\ 0 & \dfrac{\pi_{ij}^{\mathsf{T}}+\chi_{ij}^{\mathsf{T}}}{4} & -\dfrac{\chi_{ij}}{2} \end{bmatrix}\Omega_{ij}\Bigg\} \end{aligned}$$

$$= \sum_{i=1}^{N}\sum_{j=1}^{N}\xi_{ij}^{\mathrm{T}} \times \begin{bmatrix} -\frac{\pi_{ij}}{2}+\frac{I}{2N} & 0 & 0 & -\frac{C_i}{2N} \\ 0 & -\frac{\pi_{ij}}{2} & \frac{\pi_{ij}+\chi_{ij}}{4} & 0 \\ 0 & \frac{\pi_{ij}^{\mathrm{T}}+\chi_{ij}^{\mathrm{T}}}{4} & -\frac{\chi_{ij}}{2} & 0 \\ -\frac{C_i^{\mathrm{T}}}{2N} & 0 & 0 & -\frac{\gamma}{N^2} \end{bmatrix} \xi_{ij}, \tag{30}$$

where $\xi_{ij} = [\Omega_{ij}^{\mathrm{T}}, w_i^{\mathrm{T}}(t)]^{\mathrm{T}}$. From the LMI (14), it is easy to prove $\Xi < 0$ which implies $\widetilde{V} < 0$ and immediately leads to the inequality (13).

Therefore, the formation of HMAS (1) has the property of H_∞ criteria (**DF1**) and (**DF2**). This completes the proof. □

Remark 7. By studying the LMIs (14), the variables $\chi_{ij} > 0$ in (15) indicate the connectivity strength among agents. In particular, due to the monotone decreasing property of φ_{ij} with respect to norm $\|x_j(t)-x_i(t)-\Delta_{ij}\|$ and the discussion in Remark 3, this connectivity strength is inversely proportional to the relatively active scope of MASs.

4. Design Obstacle-Avoiding Functions

In this section, collision avoidance in trajectory tracking is achieved using mutual repulsion between agents and obstacles, which is resulted from the Newtonian potential-based model. By regarding the agents and obstacles as conductors with uniform charges, the repulsive force inversely proportional to the distance of them can be derived in closed form.

Based on practical applications in robotics and haptic rendering, an ideal potential field should possess all of the following attributes.

(i) With respect to the property of obstacle avoidance, the magnitude of potential and corresponding repulsion should be infinite at the boundary of obstacles and drop off with distance. And the range of potential is bounded, which is accordant with the limited detective scope of agent's built-in explorer in this paper.

(ii) The shapes of equipotential surface should be similar with the obstacle surface and spherical symmetrical at the boundary of potential field.

(iii) The first and second derivatives of potential function should exist and be continuous, so that the resulting force field is smooth.

Before moving on, for making this paper self-contained, we revisit the general definition of external disturbance in the H_∞ problem. H_∞ techniques are usually used to evaluate the incremental gain of external input signal in any direction and at any frequency. In the context of H_∞ theory, the external signals with finite energy are often investigated; that is, $\|w(t)\| \le \infty$. More explicitly, the finite energy signal $w(t)$ is said to belong to $L_2[0,\infty)$, which implies

$$\left[\int_0^\infty \|w(t)\|^2 dt\right]^{1/2} = \left[\int_0^\infty \sum_{i=1}^{N} w_i^{\mathrm{T}}(t) w_i(t) dt\right]^{1/2} < \infty. \tag{31}$$

In order to utilize H_∞ theory to design obstacle-avoidance controller, we assume that multiagent systems ultimately get far from the obstacles as time evolves. Incorporated with attributes (ii) this assumption leads to $\lim_{t\to\infty} w(t) = 0$. That is, the obstacle-avoidance functions $w_i(t)$ are available in finite time intervals. In addition, for avoiding obstacles, the agent-obstacle distances are intuitively greater than zero, and consequently the supremum of function $w_i(t)$ $(i = 1,\ldots,N)$ exists. Based on above analysis on obstacle-avoidance function, one can easily derive the conclusion that $w(t)$ belongs to $L_2[0,\infty)$.

Now, we will discuss the obstacle-avoiding function beginning with the instance of mass points (when the bulks of agents and obstacles are close to each other) and then extending to bulky obstacles (over 10 times bigger than agent) with arbitrary shapes.

Consider that an agent i navigates in an obstacle-laden environment with $M \in \overline{\mathbb{Z}}_+$ obstacles, and assume that $s_l \in \mathbb{R}^n$ is the position of obstacle l ($l \in \{1,2,\ldots,M\}$). The potential at agent i due to obstacle l is

$$P_{il}^{o}(t) = \frac{\rho_{il}}{\|x_i(t) - s_l\|}, \tag{32}$$

where ρ_{il} is the repulsion coefficient for obstacles avoidance and is defined as follows:

$$\rho_{il} = \begin{cases} \rho, & \|x_i(t) - s_l\| < \delta \\ 0, & \|x_i(t) - s_l\| \ge \delta, \end{cases} \tag{33}$$

where ρ is a positive scalar and δ is the maximal sensing range of agent. When the relative distance of agent i and obstacle l is shorter than that of the detective scope δ, agent i will receive a signal of possible collision and the obstacle-avoiding function will work. In other words, the repulsive potentials between agents and obstacles act only when they get close to certain range. Now, the obstacle-avoiding function for agent i is introduced based on the negative gradient of the potential (32) in the following form:

$$w_i(t) = -\nabla_{x_i} P_{il}^{o}(x_i, s_l) = \sum_{l=1}^{M} \rho_{il} \frac{x_i(t) - s_l}{\|x_i(t) - s_l\|^3}. \tag{34}$$

Then we extend the obstacle-avoiding function for the bulky objects with arbitrary shapes. In practical situations, particularly in many exploration applications, the implicit functions of obstacles to be modeled are not available. But by samples of boundary surfaces obtained from camera, laser range finder and sonar, and with the help of some techniques such as signal sampling and image processing, the implicit functions can be obtained, and then they construct

the APFs [20]. For convenience, in this paper, assume that the boundary function of obstacle l is known as $\mathbf{B}_l$, and β_l here is the position of arbitrary point on the boundary of obstacle. In fact, most of obstacles can be mathematically approximated with polyhedron. In this paper we focus on the convex polyhedra obstacles. Moreover, the results can be easily extended to obstacles with arbitrary shapes. The repulsion between agent i and an arbitrary point of the obstacle's boundary is

$$F_{il}^{o}(t) = \rho_{il} \frac{x_i(t) - \beta_l}{\left\| x_i(t) - \beta_l \right\|^3}, \tag{35}$$

where ρ_{il} are defined in (33). Then for the agent i the obstacle-avoiding function is defined as

$$w_i(t) = \sum_{l=1}^{M} \oint_{\mathbf{B}_l} dF_{il}^{o}, \tag{36}$$

where $\oint_{\mathbf{B}_l}$ represents the surface integrals on boundary of obstacles.

In view of above analysis, the obstacles laden in the terrain are static. However, it is worth mentioning that all the obstacle-avoidance functions are available for moving obstacles except for those with high-speed. In this case, the position vector $\beta_l(t)$ is a vector-valued function over time $t \in \mathbb{J}$.

5. Numerical Examples

In this section, some simulation results illustrate the performance of the proposed control laws to achieve formation and obstacles avoidance. To avoid triviality, the advantage of formation controllers (4) compared with others is omitted in this paper, and the reader is referred to [1].

Firstly, drive 4 agents with the initialization positions $(-1.2, -1.1)^\intercal$, $(-2.0, 3.8)^\intercal$, $(5.3, 2.0)^\intercal$, and $(4.2, 2.0)^\intercal$ to form a shape of square and realize obstacle avoidance in the navigation. The formation-shape matrix Δ^q is set as

$$\begin{aligned} \Delta_{12}^{1} &= \left[\frac{\sqrt{2}}{2}, \frac{\sqrt{2}}{2}\right]^\intercal, \qquad \Delta_{23}^{1} = \left[\frac{\sqrt{2}}{2}, -\frac{\sqrt{2}}{2}\right]^\intercal, \\ \Delta_{34}^{1} &= \left[-\frac{\sqrt{2}}{2}, -\frac{\sqrt{2}}{2}\right]^\intercal, \qquad \Delta_{41}^{1} = \left[-\frac{\sqrt{2}}{2}, \frac{\sqrt{2}}{2}\right]^\intercal, \\ \Delta_{13}^{1} &= \left[\sqrt{2}, 0\right]^\intercal, \qquad \Delta_{24}^{1} = \left[0, -\sqrt{2}\right]^\intercal, \end{aligned} \tag{37}$$

and two obstacles locate at $[2.50, 5.00]^\intercal$ and $[-0.82, 15.90]^\intercal$. The target trajectory of $f(t, x)$ in HMAS (1) is given by

$$f(t, x) = \begin{bmatrix} -0.1 & 0 \\ 0 & 0.1 \end{bmatrix} x_i + \begin{bmatrix} \cos(0.4 * t) \\ \sin(0.25 * t) \end{bmatrix}, \tag{38}$$

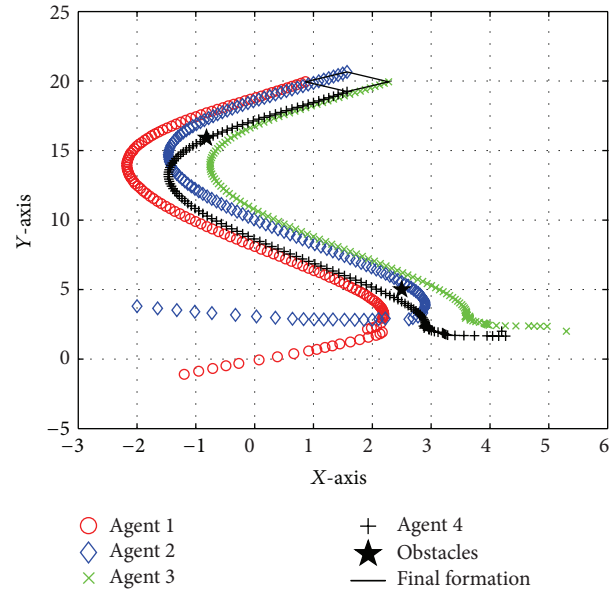

Figure 2: Formation of MAS without obstacle-avoidance functions case.

and the time-varying configuration matrix switches from one mode to another. They are as follows:

$$\begin{aligned} J^1 &= \begin{bmatrix} -0.6 & 0.3 & 0 & 0.3 \\ 0.3 & -0.6 & 0.3 & 0 \\ 0 & 0.3 & -0.6 & 0.3 \\ 0.3 & 0 & 0.3 & -0.6 \end{bmatrix}, \\ J^2 &= \begin{bmatrix} -0.9 & 0.3 & 0.3 & 0.3 \\ 0.3 & -0.9 & 0.3 & 0.3 \\ 0.3 & 0.3 & -0.9 & 0.3 \\ 0.3 & 0.3 & 0.3 & -0.9 \end{bmatrix}. \end{aligned} \tag{39}$$

For the formation controller (5), let $S_a = 8.1$, $L_a = 0.31$, $S_r = 0.69$, $L_R = 0.3$, and $\delta = 3$, $\rho = 0.5$ in obstacle-avoiding function (34).

According to Figures 2 and 3, one can demonstrate the control laws presented in this paper realize the formation keeping while avoiding collision with obstacles (marked by black stars in the figures) in complex environment. For the sake of measuring and visualising the formation effectiveness, we introduce the following formation error:

$$e(t) = \sum_{i=1}^{N-1} \sum_{j>i}^{N} \left(\left\| x_j(t) - x_i(t) \right\| - \left\| \Delta_{ij}^{q} \right\| \right), \tag{40}$$

which is shown in Figure 4. Then, the sensitivity of obstacle-avoiding function is investigated in Figure 5, which depicts the curves of left term in inequality (13) under different repulsion coefficient ρ and repulsion rang δ. From Figure 5, one can verify the fact that the performance index γ in inequality (13) reflects the sensitivity of HMAS towards obstacles; that is, smaller γ requires HMAS to be less active (smaller ρ and δ) towards obstacle.

Next, in an attempt to demonstrate the effectiveness of obstacle-avoidance function (36), a rectangular obstacle

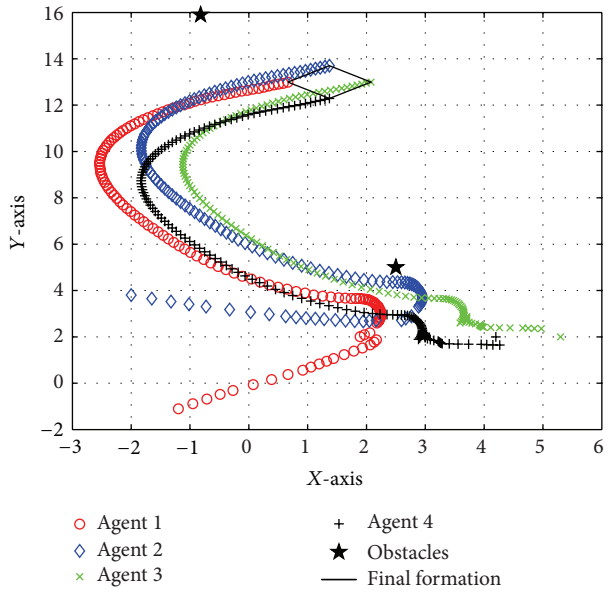

Figure 3: Formation of MAS with obstacle-avoidance functions case.

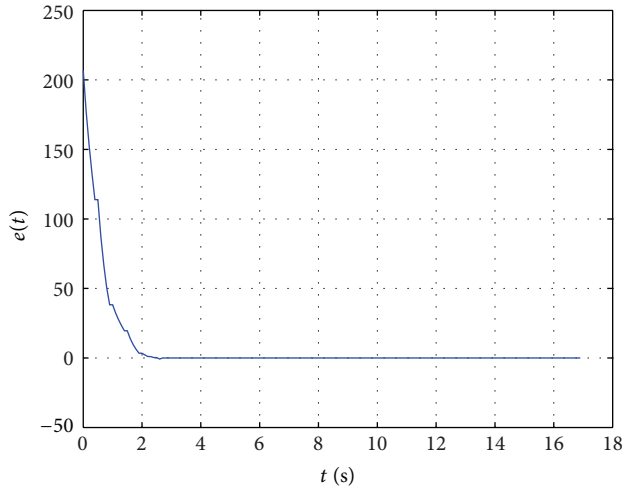

Figure 4: Formation error of MAS controlled by obstacle-avoidance functions.

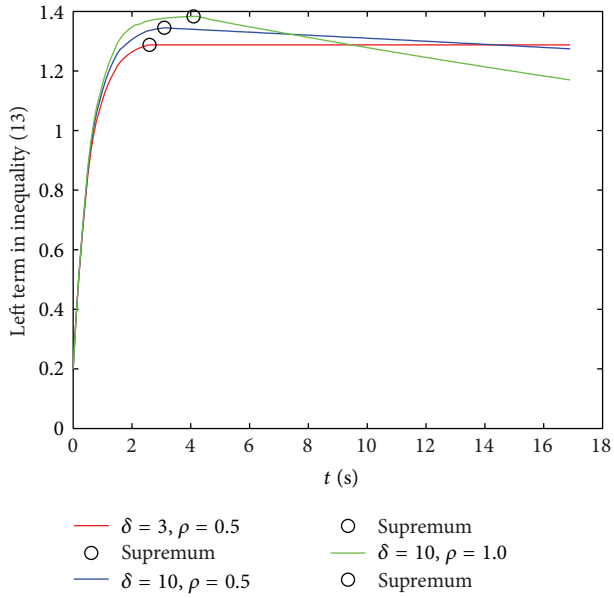

Figure 5: Investigation of parameters γ, ρ, and δ.

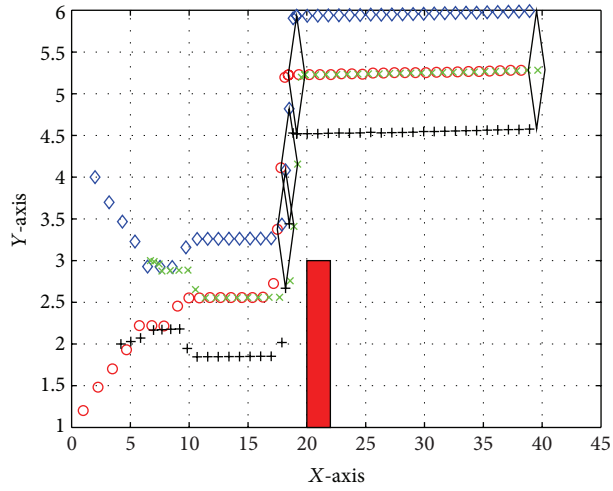

Figure 6: Obstacle avoidance of MAS in 2D.

stands in the way of the HMAS path. Figures 6 and 7 show that the HMAS steers around the obstacle smoothly with the help of obstacle-avoidance functions and keeps a predefined formation in the whole process, as well as the corresponding formation error.

In many practical situations, the HMAS occasionally encounters the trench-shape obstacles which are impossible for the whole system keeping original shape to pass through. In such case, the HMAS has to transform formation to a feasible one. In this example, the task is to transition from a square formation to a straight line to pass the trench safely. When the HMAS detects the trench existed in the tracking path, specified task is triggered and corresponding formation is determined according to the predetermined task-formation scheme. As shown in Figure 8, the HMAS breaks formation, goes in a straight line when it meets the trench, and transforms back into the original formation after passing the trench.

6. Conclusion

In this paper, new formation and obstacle-avoidance protocols of multiagent systems are presented. A notion of H_∞ formation has been first defined to characterize the performance of obstacle-avoiding, and the H_∞ performance index is concreted as a sensitivity of obstacle-avoidance in this paper. Then a hybrid formation controller with a task set and a formation set is introduced to handle distinct obstacles. By designing diverse task-formation mapping, the HMAS

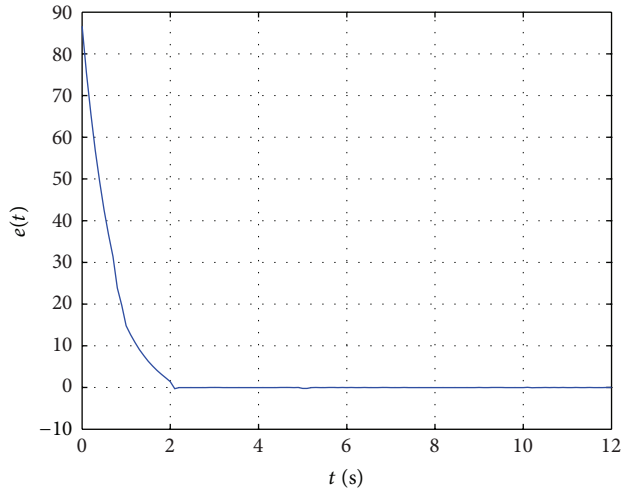

Figure 7: Formation error for obstacle avoidance of MAS in 2D.

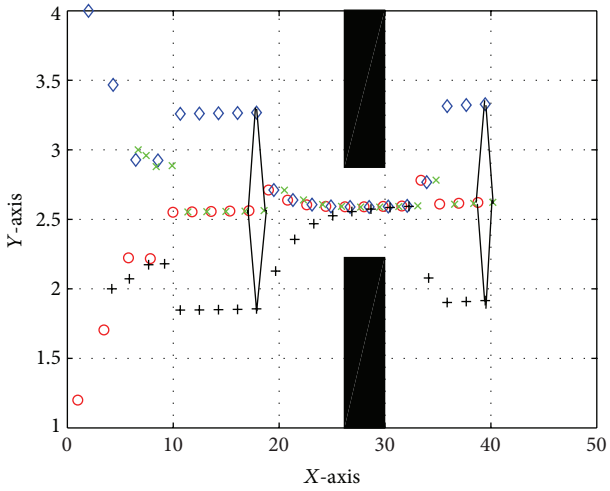

Figure 8: Formation change for HMAS in the presence of trench-shaped obstacle.

can accomplish various complex missions. Then obstacle-avoidance functions using potential field model are specified to realize multiagent systems avoiding arbitrarily-shaped obstacles on the path. According to the simulation results, not only the HMAS can steer around the obstacles with proposed approach, but also the reconfiguration of formation can be achieved in the complex environment.

Acknowledgments

This work was supported by the National Natural Science Foundation of China under Grants 61174158, 61034004, 51075306, and 61272271, Special Financial Grant from the China Postdoctoral Science Foundation (no. 201104286), China Postdoctoral Science Foundation funded project 2012M510117, Natural Science Foundation Program of Shanghai (no. 12ZR1434000), and the Fundamental Research Funds for the Central Universities.

References

[1] D. Xue, J. Yao, G. Chen, and Y.-L. Yu, "Formation control of networked multi-agent systems," *IET Control Theory & Applications*, vol. 4, no. 10, pp. 2168–2176, 2010.

[2] J. P. Desai, J. P. Ostrowski, and V. Kumar, "Modeling and control of formations of nonholonomic mobile robots," *IEEE Transactions on Robotics and Automation*, vol. 17, no. 6, pp. 905–908, 2001.

[3] S. Cristaldi, A. Ferro, R. Giugno, G. Pigola, and A. Pulvirenti, "Obstacles constrained group mobility models in event-driven wireless networks with movable base stations," *Ad Hoc Networks*, vol. 9, no. 3, pp. 400–417, 2011.

[4] X. Wang, V. Yadav, and S. N. Balakrishnan, "Cooperative UAV formation flying with obstacle/collision avoidance," *IEEE Transactions on Control Systems Technology*, vol. 15, no. 4, pp. 672–679, 2007.

[5] Q. Hui, "Finite-time rendezvous algorithms for mobile autonomous agents," *IEEE Transactions on Automatic Control*, vol. 56, no. 1, pp. 207–211, 2011.

[6] R. Olfati-Saber, "Flocking for multi-agent dynamic systems: algorithms and theory," *IEEE Transactions on Automatic Control*, vol. 51, no. 3, pp. 401–420, 2006.

[7] V. Gazi and K. M. Passino, "Stability analysis of Social foraging swarms," *IEEE Transactions on Systems, Man, and Cybernetics B*, vol. 34, no. 1, pp. 539–557, 2004.

[8] F. Zhang, "Geometric cooperative control of particle formations," *IEEE Transactions on Automatic Control*, vol. 55, no. 3, pp. 800–803, 2010.

[9] M. Defoort, T. Floquet, A. Kökösy, and W. Perruquetti, "Sliding-mode formation control for cooperative autonomous mobile robots," *IEEE Transactions on Industrial Electronics*, vol. 55, no. 11, pp. 3944–3953, 2008.

[10] T.-H. Kim and T. Sugie, "Cooperative control for target-capturing task based on a cyclic pursuit strategy," *Automatica*, vol. 43, no. 8, pp. 1426–1431, 2007.

[11] S. S. Ge and C.-H. Fua, "Queues and artificial potential trenches for multirobot formations," *IEEE Transactions on Robotics*, vol. 21, no. 4, pp. 646–656, 2005.

[12] R. Olfati-Saber and R. M. Murray, "Graph rigidity and distributed formation stabilization of multi-vehicle systems," in *Proceedings of the 41st IEEE Conference on Decision and Control*, vol. 3, pp. 2965–2971, Pasadena, Calif, USA, December 2002.

[13] M. Karasalo and X. Hu, "Robust formation control and servoing using switching range sensors," *Robotics and Autonomous Systems*, vol. 58, no. 8, pp. 1003–1016, 2010.

[14] B. Shen, Z. Wang, and X. Liu, "Bounded H_∞ synchronization and state estimation for discrete time-varying stochastic complex networks over a finite horizon," *IEEE Transactions on Neural Networks*, vol. 22, no. 1, pp. 145–157, 2011.

[15] J. A. Guerrero, G. Romero, and R. Lozano, "Robust consensus tracking of leader-based multi-agent systems," in *Proceedings of the American Control Conference (ACC '10)*, pp. 6299–6305, Baltimore, Md, USA, July 2010.

[16] V. Gazi, "Swarm aggregations using artificial potentials and sliding-mode control," *IEEE Transactions on Robotics*, vol. 21, no. 6, pp. 1208–1214, 2005.

[17] O. Khatib, "Real time obstacle avoidance for manipulators and mobile robots," *International Journal of Robotics Research*, vol. 5, no. 1, pp. 90–98, 1986.

[18] D. J. Bennet and C. R. McInnes, "Distributed control of multi-robot systems using bifurcating potential fields," *Robotics and Autonomous Systems*, vol. 58, no. 3, pp. 256–264, 2010.

[19] J.-H. Chuang and N. Ahuja, "An analytically tractable potential field model of free space and its application in obstacle avoidance," *IEEE Transactions on Systems, Man, and Cybernetics B*, vol. 28, no. 5, pp. 729–736, 1998.

[20] J. Ren, K. A. McIsaac, R. V. Patel, and T. M. Peters, "A potential field model using generalized sigmoid functions," *IEEE Transactions on Systems, Man, and Cybernetics B*, vol. 37, no. 2, pp. 477–484, 2007.

[21] A. Eresen, N. Imamoğlu, and M. Ö. Efe, "Autonomous quadrotor flight with vision-based obstacle avoidance in virtual environment," *Expert Systems with Applications*, vol. 39, no. 1, pp. 894–905, 2012.

[22] D. R. Parhi and J. C. Mohanta, "Navigational control of several mobile robotic agents using Petri-potential-fuzzy hybrid controller," *Applied Soft Computing Journal*, vol. 11, no. 4, pp. 3546–3557, 2011.

[23] M. Heymann, F. Lin, and G. Meyer, "Control synthesis for a class of hybrid systems subject to configuration based on safety constraints," NASA Technical Memorandum 112196, 1997.

[24] M. Heymann, F. Lin, and G. Meyer, "Synthesis and viability of minimally interventive legal controllers for hybrid systems," *Discrete Event Dynamic Systems*, vol. 8, no. 2, pp. 105–135, 1998.

[25] J. Yao, F. Lin, and B. Liu, "H_∞ control for stochastic stability and disturbance attenuation in a class of networked hybrid systems," *IET Control Theory & Applications*, vol. 5, no. 15, article 1698, 2011.

[26] C. G. Cassandras and S. Lafortune, *Introduction to Discrete Event Systems*, Springer, New York, NY, USA, 2nd edition, 2008.

[27] R. Shorten, F. Wirth, O. Mason, K. Wulff, and C. King, "Stability criteria for switched and hybrid systems," *SIAM Review*, vol. 49, no. 4, pp. 545–592, 2007.

[28] R. Olfati-Saber and R. M. Murray, "Consensus problems in networks of agents with switching topology and time-delays," *IEEE Transactions on Automatic Control*, vol. 49, no. 9, pp. 1520–1533, 2004.

Hindawi Publishing Corporation
Journal of Applied Mathematics
Volume 2013, Article ID 603063, 11 pages
http://dx.doi.org/10.1155/2013/603063

Research Article

Dynamic Modeling and Control of Electromechanical Coupling for Mechanical Elastic Energy Storage System

Yang Yu and Zengqiang Mi

State Key Laboratory of Alternate Electrical Power System with Renewable Energy Sources, North China Electric Power University, Baoding 071003, China

Correspondence should be addressed to Yang Yu; ncepu_yy@163.com

Received 12 July 2013; Accepted 4 September 2013

Academic Editor: Michael Chen

Copyright © 2013 Y. Yu and Z. Mi. This is an open access article distributed under the Creative Commons Attribution License, which permits unrestricted use, distribution, and reproduction in any medium, provided the original work is properly cited.

The structural scheme of mechanical elastic energy storage (MEES) system served by permanent magnet synchronous motor (PMSM) and bidirectional converters is designed. The aim of the research is to model and control the complex electromechanical system. The mechanical device of the complex system is considered as a node in generalized coordinate system, the terse nonlinear dynamic model of electromechanical coupling for the electromechanical system is constructed through Lagrange-Maxwell energy method, and the detailed deduction of the mathematical model is presented in the paper. The theory of direct feedback linearization (DFL) is applied to decouple the nonlinear dynamic model and convert the developed model from nonlinear to linear. The optimal control theory is utilized to accomplish speed tracking control for the linearized system. The simulation results in three different cases show that the proposed nonlinear dynamic model of MEES system is correct; the designed algorithm has a better control performance in contrast with the conventional PI control.

1. Introduction

Power balance is a basis for stable operation of power system [1, 2], which is frequently disturbed by some factors such as faults and intermittent power generations. These threatening behaviors may lead to oscillation between the generating units and the interconnected systems, and even worse, which probably cause serious large-scale blackout in power system [3]. Currently, one of the principal methods solving the power imbalance is to reserve adequate spare capacity for the system, which not only increases the investment, but also reduces the utilization of electrical equipments. With the development of energy storage (ES) technologies, a new way of utilizing energy storage technology to solve the power imbalance has been paid more and more attentions [4, 5]. From state-of-the-art technologies of ES, a great variety of the technologies have been developed [6–11]. However, from a viewpoint of power system operation, the technologies of ES at least need to have the following features: large capacity, fast power response speed, high efficiency, long service life, low operation cost and environmental friendship, and so forth. In terms of these requests, most of ES technologies are still immature except pumped-storage. A new method utilizing spiral springs as ES medium is proposed in reference [12], which is called mechanical elastic energy storage (MEES); some of the basic characteristics for the technology are discussed in [13]. Due to the benefits of small size, low loss, and high efficiency [14], permanent magnet synchronous motor (PMSM) is chosen as the servomotor for the MEES system. Thus, the MEES system, which is integrated by the mechanical device (spiral springs and the correspondingly coating shell), the electrical installation (PMSM), and relevant control information elements, is a typically complex nonlinear system of electromechanical coupling. Parameter coupling, which is induced between electromagnetic parameters of PMSM and mechanical parameters of spiral springs, may affect the dynamic performance of the system. The preexisting studies have shown that revealing the law of electromechanical interaction from the point of view of energy is an effective solution to research dynamic characteristics of complex electromechanical system. Lagrange-Maxwell equation of flywheel energy storage is deduced in reference [15] by

calculation of integral of magnetic density in the area of magnetic field.

The modeling and control of complex dynamic systems are the rapidly emerging researching topics [16], especially for the nonlinearities in the systems [17]. The paper concentrates on modeling and decoupling control of complex PMSM based MEES system in detail. The mechanical device is taken into account in the analysis of electromechanical coupling, which can make the research become closer to the reality. Especially for the mechanical spiral springs with a big quality and large inertia, neglecting their influence will make the results inaccurate, even unavailable. The overall aim of the paper is to model and control the complex electromechanical system based on the characteristics of mechanical spiral springs in order to improve the operating stability of the system; in particular, the main innovative points of the research are represented as follows:

(a) previous researches mainly focus on the motor ontology for the electromechanical issue; the difference in the research is to consider the mechanical device as a node in generalized coordinate system; the terse nonlinear dynamic model for a complex electromechanical system is deduced and constructed through Lagrange-Maxwell energy method by the principle of electromechanical coupling.

(b) the generalized coordinates of MEES system are determined. The functions of the kinetic energy, magnetic energy, the potential energy, and the energy dissipation of the whole system are obtained, and the differential equations with electromechanical parameters of MEES system are established by applying the extended Lagrange-Maxwell equation.

(c) the theory of direct feedback linearization (DFL) is applied to decouple the nonlinear model and convert the developed model for MEES system from nonlinear to linear. An optimal linear controller is designed to accomplish the speed tracking control for the linearized model.

The paper is organized as the following: it starts with introductions to the ES technologies and the electromechanical characteristics of MEES system in Section 1. The constitution and operating principles of the MEES system are described in Section 2. Mathematical modeling of electromechanical coupling for the complex MEES system is deduced in Section 3. In Section 4, DFL based decoupling control of the dynamic model is proposed, and an optimal linear controller is designed to accomplish the speed tracking control for the linearized model. Section 5 gives the results of numerical simulation. Finally, the conclusions are summarized in Section 6.

2. Preliminaries and Problem Description

2.1. Constitution of MEES System. In order to give the readers a better understanding of the operating principle of the research object, the composition scheme of MEES system served by PMSM and bidirectional converters is described in Figure 1.

PMSM based MEES system consists of several elements: ES box (multiple spiral springs wrapped up in it), gear box, PMSM, bidirectional converters, breaker, and controller. Therefore, the electromechanical coupling is caused by the interaction between electromagnetic parameters of PMSM and mechanical parameters of spiral springs. A MEES power station can be built by getting tens or even more units together. Through a central controller, the units in the power station can be controlled orderly to realize the goal of large-scale energy storage and power generation. It is important to note that a linkage form structure for ES box is proposed in order to increase the energy storage capacity; for details see [13].

2.2. Operating Principle of MEES System. The basic operation principle of the MEES system is concerned with two processes: energy storage and power generation. The load or drive source of MEES system in energy storage or power generation is spiral springs in ES box. In the process of energy storage, PMSM, which is driven by power grid, tightens the springs through gear box. Then, the electric energy is stored in the form of elastic deformation energy. Once the unit receives a signal of releasing energy, the tightened springs start to release energy and drive the motor to generate electricity.

3. Modeling of Electromechanical Coupling for Complex MEES System

3.1. Physical Analysis. The operating rotation speed of the spindle in elastic ES box in the process of energy storage or power generation is required to run basically stable owing to the large size and the big inertia of ES box. As mentioned above, the elastic ES box can be considered as an output load of PMSM in ES. Hence, supposing that the rotation speed of the shaft in ES box is a constant, the torque calculation formula of ES box in ES process can be given by

$$T = \frac{EBH^3\pi}{6L}\omega t + T_0, \tag{1}$$

where T and T_0 denote the operating torque and initial torque, E, B, H, and L are the modulus of elasticity, width, thickness, and length of spring material, and t denotes the time. It should be noted that T must be ensured between the maximum torque and minimum torque. Additionally, it should be compatible with the electromagnetic torque of PMSM. In terms of formula (1), the characteristic curve for ES box in ES can be shown in Figure 2.

The servomotor of PMSM consists of two parts, stator and rotor. When three-phase alternating current (AC) with mutual phase difference of 120° is flowed into the stator windings of the motor, a rotating magnetic field with a uniform motion in space is induced. The rotation speed of the magnetic field is related to the frequency of sinusoidal wave in stator windings. The driven torque, which is produced by the interaction between the rotating magnetic field of stator and permanent magnetic field of rotor, makes the rotor rotate and achieves the conversion of electric energy to elastic energy.

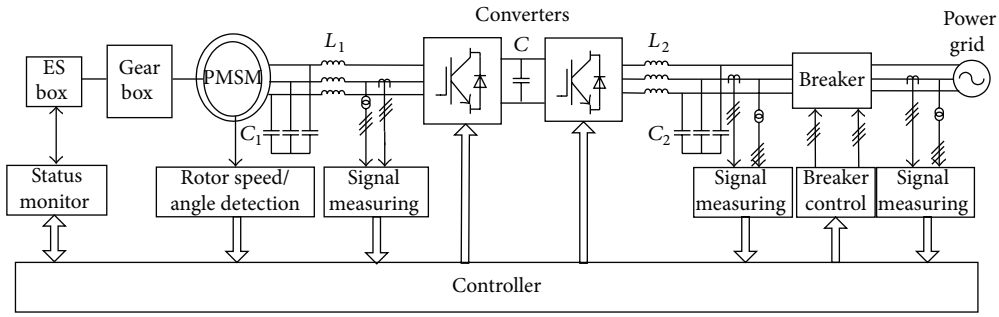

Figure 1: The composition scheme of MEES system served by PMSM and bidirectional converters.

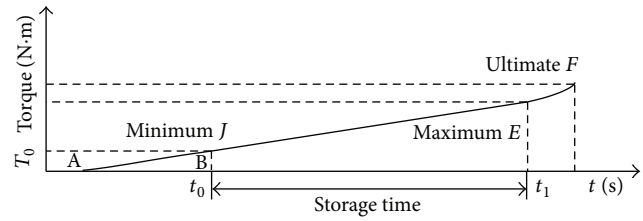

Figure 2: Characteristics curve for ES box in ES.

In the process of ES, the torque of the springs raises with the operation of the system. The power angle between the axis of stator and rotor becomes larger, which augments the magnetic torque to balance the increasing torque of springs. With the rising of energy stored in ES box, the input power and the stator current increase accordingly. Simultaneously, the armature reaction causes the growth of flux linkage of air gap and back electromotive force (e.m.f) of stator and compels the stator voltage to rise. In other words, the interaction between the electromagnetic parameters of electrical system and the mechanical parameters of mechanical system composes the electromechanical coupling in complex MEES system.

3.2. Mathematical Modeling. Before modeling the system of electromechanical coupling, six assumptions are described as follows:

(a) the saturation of the core is neglected,

(b) the losses of eddy and hysteresis are ignored,

(c) the distribution of air gap is uniform,

(d) the self-inductance and mutual inductance among the windings are independent of the position of the rotor,

(e) the damping winding in the rotor and the damping effect of permanent magnet are both neglected,

(f) back e.m.f. maintains the sinusoidal variation.

Based on the principle of electromechanical coupling dynamics, Lagrange-Maxwell energy method is applied to construct the dynamic mathematical model of MEES system as follows.

(1) Determining Generalized Coordinates of the System. Owing to the large size, big quality, and high inertia of the mechanical spiral springs, neglecting their influence will make the results inaccurate, even unavailable. Hence, the mechanical device is taken into account and considered as a node in generalized coordinate system. Six generalized coordinates shown in Table 1 are constructed for the MEES system, four of which belong to electromagnetic system ($k = 1, 2, 3, 4$), and the remaining two are mechanical system ($j = 1, 2$). The parametric descriptions of six generalized coordinates shown in Table 1 are as follows: i_a, i_b, and i_c are three-phase AC flowed in stator, u_a, u_b, and u_c indicate three-phase voltage applied in stator, ψ_f represents the magnetic flux of permanent magnet in rotor, ϑ_1 and ϑ_2 are the angular displacement of rotor and the spindle of ES box, respectively, Ω_1 and Ω_2 are the mechanical angular velocity of rotor and spindle of ES box, respectively, and T_g and T_L represent the torque of gear and load. T_L is equal to the torque T of the springs in the ES box in energy storage.

(2) Finding Out the Energy Relationship for the MEES System. The kinetic energy of the MEES system W_k can be given as

$$\begin{aligned} W_k &= \frac{1}{2}J_1\Omega_1^2 + \frac{1}{2}J_e\Omega_1^2 + \frac{1}{2}J_{\text{sp}}\Omega_2^2 \\ &= \frac{1}{2}J_1\Omega_1^2 + \frac{1}{2}J_e\Omega_1^2 + \frac{1}{2}J_{\text{sp}}\left(\frac{\Omega_1}{i}\right)^2, \end{aligned} \tag{2}$$

where J_1 is the moment of inertia of PMSM, J_e and J_{sp} are the equivalent moment of inertia of the gear and ES box with respect to input shaft, and i is the transformation ratio of gear.

For the MEES system, the magnetic energy W_m, which is jointly produced by the stator current, permanent magnet of rotor, and interaction with each other, consists of three parts.

Table 1: Six generalized coordinates for MEES system.

Generalized coordinates	Electromagnetic system				Mechanical system	
	Stator			Rotor	Gear	ES box
	$k = 1$	$k = 2$	$k = 3$	$k = 4$	$j = 1$	$j = 2$
$e_k(q_j)$	—	—	—	ψ_f	θ_1	θ_2
$\dot{e}_k(\dot{q}_j)$	i_a	i_b	i_c	—	Ω_1	Ω_2
$U_k(Q_j)$	u_a	u_b	u_c	—	$-T_g$	$-T_L$

The calculation of the magnetic energy W_{m1} produced by the current of stator is given as

$$W_{m1} = \frac{1}{2}L_a i_a^2 + \frac{1}{2}L_b i_b^2 + \frac{1}{2}L_c i_c^2 + M i_a i_b + M i_b i_c + M i_c i_a, \tag{3}$$

where L and M indicate the self-inductance and mutual inductance of three-phase windings in stator, for an exterior-gibbose PMSM, $M_{aa} = M_{bb} = M_{cc} = M_{ab} = M_{bc} = M_{ca} = M$, $L_a = L_b = L_c$.

For the distributed winding with a phase belt of 60°, due to the number q of the slots for per pole per phase is often more than two, the magnetic energy of air gap W_{m2} can be considered not changed with the rotation of rotor, namely, the magnetic energy produced by permanent magnet of rotor is a constant, $W_{m2} = C_1$ (C_1 is a constant).

W_{m12} is the magnetic energy produced by the interaction between the stator current and stator flux generated by the rotor; the calculation formula of W_{m12} can be written as

$$\begin{aligned} W_{m12} &= i_a \psi_f \cos\theta_1 + i_b \psi_f \cos\left(\theta_1 - \frac{2}{3}\pi\right) \\ &\quad + i_c \psi_f \cos\left(\theta_1 + \frac{2}{3}\pi\right). \end{aligned} \tag{4}$$

The potential energy of the system V is given by

$$V = \frac{1}{2}\alpha_{\text{sp}}\theta_2^2, \tag{5}$$

where α_{sp} is a torsion constant of the springs.

The Lagrange function can be written as

$$\begin{aligned} L = W_k + W_m - V &= \frac{1}{2}J_1\Omega_1^2 + \frac{1}{2}J_e\Omega_1^2 + \frac{1}{2}J_{\text{sp}}\Omega_2^2 \\ &\quad + \frac{1}{2}L_a i_a^2 + \frac{1}{2}L_b i_b^2 + \frac{1}{2}L_c i_c^2 \\ &\quad + M i_a i_b + M i_b i_c + M i_c i_a + C_1 \\ &\quad + i_a \psi_f \cos\theta_1 + i_b \psi_f \cos\left(\theta_1 - \frac{2}{3}\pi\right) \\ &\quad + i_b \psi_f \cos\left(\theta_1 + \frac{2}{3}\pi\right) - \frac{1}{2}\alpha_{\text{sp}}\theta_2^2. \end{aligned} \tag{6}$$

The dissipation function of magnetic system F_e can be expressed as

$$F_e = \frac{1}{2}R_a i_a^2 + \frac{1}{2}R_b i_b^2 + \frac{1}{2}R_c i_c^2, \tag{7}$$

where R_a, R_b, and R_c indicate three-phase resistance of the stator.

The dissipation function of mechanical system F_m can be written as

$$F_m = \frac{1}{2}\left(B_1 + B_e\right)\Omega_1^2 + \frac{1}{2}B_{\text{sp}}\left(\frac{\Omega_1}{i}\right)^2, \tag{8}$$

where B_1, B_e, and B_{sp} are the equivalent viscous damping coefficients of the motor, the gear, and the spring, respectively.

Then, the dissipation function of the whole system F can be given as

$$\begin{aligned} F = F_e + F_m &= \frac{1}{2}R_a i_a^2 + \frac{1}{2}R_b i_b^2 + \frac{1}{2}R_c i_c^2 \\ &\quad + \frac{1}{2}\left(B_1 + B_e\right)\Omega_1^2 + \frac{1}{2}B_{\text{sp}}\left(\frac{\Omega_1}{i}\right)^2. \end{aligned} \tag{9}$$

Nonconservative generalized force of mechanical system ($j = 1, 2$) can be expressed as

$$\begin{aligned} Q_1 &= -T_g, \quad j = 1, \\ Q_2 &= -T_L, \quad j = 2. \end{aligned} \tag{10}$$

External e.m.f. of electromagnetic system is given by

$$U_k = -u_k. \tag{11}$$

The Lagrange-Maxwell equation of MEES system can be expressed as

$$\begin{aligned} \frac{d}{dt}\left(\frac{\partial L}{\partial \dot{e}_k}\right) - \frac{\partial L}{\partial e_k} + \frac{\partial F}{\partial \dot{e}_k} &= U_k, \\ \frac{d}{dt}\left(\frac{\partial L}{\partial \dot{q}_j}\right) - \frac{\partial L}{\partial q_j} + \frac{\partial F}{\partial \dot{q}_j} &= Q_j. \end{aligned} \tag{12}$$

For electromagnetic system, firstly, the stator winding of A-phase ($k = 1$) is considered as

$$\frac{\partial L}{\partial e_1} = 0,$$

$$\frac{\partial L}{\partial \dot{e}_1} = \frac{\partial L}{\partial i_a} = L i_a + M i_b + M i_c + \psi_f \cos\theta_1,$$

$$\frac{d}{dt}\left(\frac{\partial L}{\partial \dot{e}_1}\right) \longrightarrow \frac{d}{dt}\left(\frac{\partial L}{\partial i_a}\right) = L\frac{di_a}{dt} + M\frac{di_b}{dt} + M\frac{di_c}{dt} + \frac{d\left(\psi_f \cos\theta_1\right)}{dt},$$
$$\frac{\partial F}{\partial \dot{e}_1} \longrightarrow \frac{\partial F}{\partial i_a} = R_a i_a, \tag{13}$$
$$U_1 = \frac{d}{dt}\left(\frac{\partial L}{\partial \dot{e}_1}\right) - \frac{\partial L}{\partial e_1} + \frac{\partial F}{\partial \dot{e}_1},$$
$$u_a = U_1;$$

the voltage equation of stator winding of A-phase can be written as

$$u_a = U_1 = \frac{d}{dt}\left(\frac{\partial L}{\partial \dot{e}_1}\right) - \frac{\partial L}{\partial e_1} + \frac{\partial F}{\partial \dot{e}_1} = L\frac{di_a}{dt} + M\frac{di_b}{dt} + M\frac{di_c}{dt} + \frac{d\left(\psi_f \cos\theta_1\right)}{dt} + R_a i_a. \tag{14}$$

Similarly, the voltage equation of stator winding of B-phase ($k = 2$) can be written as

$$u_b = U_2 = \frac{d}{dt}\left(\frac{\partial L}{\partial \dot{e}_2}\right) - \frac{\partial L}{\partial e_2} + \frac{\partial F}{\partial \dot{e}_2} = L\frac{di_b}{dt} + M\frac{di_c}{dt} + M\frac{di_a}{dt} + \frac{d\left(\psi_f \cos\left(\theta_1 - (2/3)\,\pi\right)\right)}{dt} + R_b i_b; \tag{15}$$

the voltage equation of stator winding of C-phase ($k = 3$) can be written as

$$u_c = U_3 = \frac{d}{dt}\left(\frac{\partial L}{\partial \dot{e}_3}\right) - \frac{\partial L}{\partial e_3} + \frac{\partial F}{\partial \dot{e}_3} = L\frac{di_c}{dt} + M\frac{di_a}{dt} + M\frac{di_b}{dt} + \frac{d\left(\psi_f \cos\left(\theta_1 + (2/3)\,\pi\right)\right)}{dt} + R_c i_c. \tag{16}$$

For permanent magnet of rotor, the effective flux ψ_f of permanent magnet is generally considered to be a constant, namely, $\psi_f = C_2$ (C_2 is a constant). Thus

$$\frac{\partial L}{\partial \psi_f} = 0, \qquad \frac{\partial L}{\partial \dot{\psi}_f} = 0. \tag{17}$$

For mechanical system, when $j = 1$ has

$$\frac{\partial L}{\partial q_1} \longrightarrow \frac{\partial L}{\partial \theta_1} = -i_a\psi_f \sin\theta_1 - i_b\psi_f \sin\left(\theta_1 - \frac{2}{3}\pi\right) - i_c\psi_f \sin\left(\theta_1 + \frac{2}{3}\pi\right) - \alpha_{\mathrm{sp}}\frac{\theta_1}{i^2},$$
$$\frac{\partial L}{\partial \dot{q}_1} \longrightarrow \frac{\partial L}{\partial \Omega_1} = \left(J_1 + J_e\right)\Omega_1 + J_{\mathrm{sp}}\frac{\Omega_1}{i^2},$$
$$\frac{d}{dt}\left(\frac{\partial L}{\partial \dot{q}_1}\right) \longrightarrow \frac{d}{dt}\left(\frac{\partial L}{\partial \Omega_1}\right) = \left(J_1 + J_e + \frac{J_{\mathrm{sp}}}{i^2}\right)\frac{d\Omega_1}{dt},$$
$$\frac{\partial F}{\partial \dot{q}_1} \longrightarrow \frac{\partial F}{\partial \Omega_1} = \left(B_1 + B_e + \frac{B_{\mathrm{sp}}}{i^2}\right)\Omega_1, \tag{18}$$
$$Q_1 = \frac{d}{dt}\left(\frac{\partial L}{\partial \dot{q}_1}\right) - \frac{\partial L}{\partial q_1} + \frac{\partial F}{\partial \dot{q}_1},$$
$$Q_1 = -T_g,$$

the motion equation of mechanical system $j = 1$ can be expressed as

$$\left(J_1 + J_e + \frac{J_{\mathrm{sp}}}{i^2}\right)\frac{d\Omega_1}{dt} = -i_a\psi_f \sin\theta_1 - i_b\psi_f \sin\left(\theta_1 - \frac{2}{3}\pi\right) - i_c\psi_f \sin\left(\theta_1 + \frac{2}{3}\pi\right) - \alpha_{\mathrm{sp}}\frac{\theta_1}{i^2} - \left(B_1 + B_e + \frac{B_{\mathrm{sp}}}{i^2}\right)\Omega_1 - T_g. \tag{19}$$

Let $J = J_1 + J_e + (J_{\mathrm{sp}}/i^2)$ and $B = B_1 + B_e + (B_{\mathrm{sp}}/i^2)$; the motion equation of mechanical system $j = 1$ can be rewritten as

$$J\frac{d\Omega_1}{dt} = -i_a\psi_f \sin\theta_1 - i_b\psi_f \sin\left(\theta_1 - \frac{2}{3}\pi\right) - i_c\psi_f \sin\left(\theta_1 + \frac{2}{3}\pi\right) - \alpha_{\mathrm{sp}}\frac{\theta_1}{i^2} - B\Omega_1 - T_g. \tag{20}$$

For mechanical system, when $j = 2$ has

$$\frac{\partial L}{\partial q_2} \longrightarrow \frac{\partial L}{\partial \theta_2} = -ii_a\psi_f \sin\theta_2 - ii_b\psi_f \sin\left(\theta_2 - \frac{2}{3}\pi\right) - ii_c\psi_f \sin\left(\theta_1 + \frac{2}{3}\pi\right) - \alpha_{\mathrm{sp}}\theta_2,$$
$$\frac{\partial L}{\partial \dot{q}_2} \longrightarrow \frac{\partial L}{\partial \Omega_2} = i^2\left(J_1 + J_e\right)\Omega_2 + J_{\mathrm{sp}}\Omega_2,$$
$$\frac{d}{dt}\left(\frac{\partial L}{\partial \dot{q}_2}\right) \longrightarrow \frac{d}{dt}\left(\frac{\partial L}{\partial \Omega_2}\right) = \left[i^2\left(J_1 + J_e\right) + J_{\mathrm{sp}}\right]\frac{d\Omega_2}{dt}, \tag{21}$$
$$\frac{\partial F}{\partial \dot{q}_2} \longrightarrow \frac{\partial F}{\partial \Omega_2} = \left[i^2\left(B_1 + B_e\right) + B_{\mathrm{sp}}\right]\Omega_2,$$
$$Q_2 = \frac{d}{dt}\left(\frac{\partial L}{\partial \dot{q}_2}\right) - \frac{\partial L}{\partial q_2} + \frac{\partial F}{\partial \dot{q}_2},$$
$$Q_2 = -T_L,$$

the motion equation of mechanical system $j = 2$ can be written as

$$i^2\left(J_1 + J_e + \frac{J_{sp}}{i^2}\right)\frac{d\Omega_2}{dt} = -ii_a\psi_f \sin\theta_2 - ii_b\psi_f \sin\left(\theta_2 - \frac{2}{3}\pi\right) - ii_c\psi_f \sin\left(\theta_2 + \frac{2}{3}\pi\right) - \alpha_{sp}\theta_2 - i^2\left(B_1 + B_e + \frac{B_{sp}}{i^2}\right)\Omega_2 - T_L. \tag{22}$$

In terms of $J = J_1 + J_e + (J_{sp}/i^2)$, $B = B_1 + B_e + (B_{sp}/i^2)$, that is, (22) can be rewritten as

$$i^2 J\frac{d\Omega_2}{dt} = -ii_a\psi_f \sin\theta_2 - ii_b\psi_f \sin\left(\theta_2 - \frac{2}{3}\pi\right) - ii_c\psi_f \sin\left(\theta_2 + \frac{2}{3}\pi\right) - \alpha_{sp}\theta_2 - i^2 B\Omega_2 - T_L. \tag{23}$$

The electromechanical dynamic model of MEES system in static ABC coordinates can be obtained through simultaneous equations of (14), (15), (16), (20), and (23).

Define $C_{abc/dq0}$ as the transformation matrix from static coordinates of ABC to rotating frame of dq0 as follows:

$$C_{abc/dq0} = \frac{2}{3}\begin{bmatrix} \cos\theta & \cos\left(\theta - \frac{2}{3}\pi\right) & \cos\left(\theta + \frac{2}{3}\pi\right) \\ -\sin\theta & -\sin\left(\theta - \frac{2}{3}\pi\right) & -\sin\left(\theta + \frac{2}{3}\pi\right) \\ \frac{1}{2} & \frac{1}{2} & \frac{1}{2} \end{bmatrix}; \tag{24}$$

in terms of the transformation matrix $C_{abc/dq0}$, the relationship between current and voltage in ABC frame and dq0 frame can be written as

$$\begin{bmatrix} i_d \\ i_q \\ i_0 \end{bmatrix} = C_{abc/dq0}\begin{bmatrix} i_a \\ i_b \\ i_c \end{bmatrix}, \qquad \begin{bmatrix} u_d \\ u_q \\ u_0 \end{bmatrix} = C_{abc/dq0}\begin{bmatrix} u_a \\ u_b \\ u_c \end{bmatrix}. \tag{25}$$

Substituting (25) into equations (14), (15), and (16), respectively, the voltage equations of the electromagnetic system in dq0 frame can be obtained as

$$\begin{bmatrix} u_d \\ u_q \end{bmatrix} = \begin{bmatrix} L_d & 0 \\ 0 & L_q \end{bmatrix}\begin{bmatrix} \frac{di_d}{dt} \\ \frac{di_q}{dt} \end{bmatrix} + \begin{bmatrix} R_s i_d - L_q\omega_e i_q \\ R_s i_q + L_d\omega_e i_d + \omega_e\psi_f \end{bmatrix}, \tag{26}$$

where $\omega_e = p_n\Omega_1 = p_n\dot{\theta}_1$ is the electric angular speed, p_n is the number of pole-pairs, R_s is the resistance of the stator, $R_s = R_a = R_b = R_c$, L_d, L_q are the equivalent inductance of direct axis and quadrature axis, and $L_d = L_q = L_s = 3(L - M)/2$.

Similarly, the motion equations of mechanical system in rotating frame of dq0 are given as

$$\begin{bmatrix} J & 0 \\ 0 & i^2 J \end{bmatrix}\begin{bmatrix} \ddot{\theta}_1 \\ \ddot{\theta}_2 \end{bmatrix} + \begin{bmatrix} B & 0 \\ 0 & i^2 B \end{bmatrix}\begin{bmatrix} \dot{\theta}_1 \\ \dot{\theta}_2 \end{bmatrix} + \begin{bmatrix} \frac{\alpha_{sp}}{i^2} & 0 \\ 0 & \alpha_{sp} \end{bmatrix}\begin{bmatrix} \theta_1 \\ \theta_2 \end{bmatrix} + \begin{bmatrix} -\frac{3}{2}\left[i_q\psi_f + \left(L_d - L_q\right)i_d i_q\right] \\ -\frac{3}{2}i\left[i_q\psi_f + \left(L_d - L_q\right)i_d i_q\right] \end{bmatrix} = \begin{bmatrix} -T_g \\ -T_L \end{bmatrix}. \tag{27}$$

Due to $\theta_2 = \theta_1/i$ and $T_g = T_L/i$, two formulas in (27) express the same meaning essentially. Considering $\omega_e = p_n\Omega_1 = p_n\dot{\theta}_1$, namely, $\ddot{\theta}_1 = \dot{\omega}_e/p_n$, (27) can be transformed into a new form:

$$\frac{J}{p_n}\dot{\omega}_e + \frac{B}{p_n}\omega_e - \frac{3}{2}\left[i_q\psi_f + \left(L_d - L_q\right)i_d i_q\right] + \frac{\alpha_{sp}}{i^2}\theta_1 = -T_g, \tag{28}$$

The electromechanical dynamic model of MEES system in rotating frame of dq0 can be obtained through simultaneous equations of (26) and (28).

4. Decoupling Control of the Dynamic Model

4.1. Fundamental Principle of Direct Feedback Linearization. For an affine nonlinear system in the standard form,

$$x = f(x) + \sum_{i=1}^{p} g_i(x)u_i, \quad y_i = h_i(x), \quad i = 1, 2, \ldots, p, \tag{29}$$

where $x \in R^n$ are state variables, $u \in R^p$ are input variables, $y \in R^p$ are output variables, f, g are smooth vectors fields defined on R^n, and h are smooth scalar functions defined on R^n. The nonlinearity of MEES dynamic model in rotating frame of dq0 is caused by product terms of $\omega_e i_d$ and $\omega_e i_q$, which will weaken the performance of conventional PI controller. Linearization and decoupling control of the system are effective solutions to improve the servo capability. The theory of direct feedback linearization (DFL) is known intimately up to now and is applied widespread to the varieties of nonlinear domains [18, 19]. The basic principle of DFL is to differentiate the output function repeatedly, until the rth derivatives $y^{(r)}$ of output variable explicitly contain control variable u, where r is the relatively degree of the system.

4.2. DFL for MEES System. The state variables $x \in R^3$, output variables $y \in R^2$, and control variables $u \in R^2$ are chosen as i_d, i_q, ω_e, i_d, ω_e, and u_d, u_q, respectively. The output variables are differentiated with respect to time until at least an input variable explicitly appears by DFL theory.

Taking the derivative of i_d, we can obtain

$$\dot{i}_d = -\frac{R_s}{L_d} i_d + \omega_e i_q + \frac{1}{L_d} u_d; \tag{30}$$

(30) contains the input u_d and the relatively degree $r_1 = 1$. Introducing a new variable v_1 makes $\dot{i}_d = v_1$.

Taking the derivative of ω_e, we can obtain

$$\dot{\omega}_e = -\frac{B}{J}\omega_e + \frac{3p_n}{2J} i_q \psi_f - \frac{p_n \alpha_{sp}}{Ji^2}\theta_1 + \frac{p_n}{J} T_g; \tag{31}$$

as (31) does not contain any input variable, second derivation calculus to ω_e can be obtained as follows:

$$\begin{aligned}
\ddot{\omega}_e &= \frac{B}{J}\dot{\omega}_e + \frac{3p_n}{2J}\dot{i}_q \psi_f - \frac{p_n \alpha_{sp}}{Ji^2}\dot{\theta}_1 + \frac{p_n}{J}\dot{T}_g \\
&= \frac{B}{J}\left(-\frac{B}{J}\omega_e + \frac{3p_n}{2J} i_q \psi_f - \frac{p_n \alpha_{sp}}{Ji^2}\theta_1 + \frac{p_n}{J} T_g\right) \\
&\quad + \frac{3p_n \psi_f}{2J}\left[-\frac{1}{L_q}\left(R_s i_q + L_d \omega_e i_d + \omega_e \psi_f\right) + \frac{1}{L_q} u_q\right] \\
&\quad - \frac{p_n \alpha_{sp}}{Ji^2}\frac{\omega_e}{p_n} + \frac{p_n}{J}\dot{T}_g;
\end{aligned} \tag{32}$$

(32) contains the input u_q and the relatively degree $r_2 = 2$. Introducing another new variable v_2 makes $\dot{\omega}_e = v_2$.

The comprehensive order of the system equals $r_1 + r_2 = 3$, which is exactly equal to the degree of the original system. Hence, a nonlinear state feedback control law is devised as follows:

$$u = E(x) + D(x)\, v, \tag{33}$$

where $u = [u_d, u_q]^T$, $v = [v_1, v_2]^T$, $D(x) = \begin{bmatrix} L_d & 0 \\ 0 & 2JL_q/3p_n\psi_f \end{bmatrix}$,

$$E(x) = \begin{bmatrix} R_s i_d - L_d \omega_e i_q \\ \dfrac{2L_q B}{3p_n\psi_f}\left(-\dfrac{B}{J}\omega_e + \dfrac{3p_n}{2J} i_q \psi_f - \dfrac{p_n \alpha_{sp}}{Ji^2}\theta_1 + \dfrac{p_n}{J} T_g\right) \\ + \left(R_s i_q + L_d \omega_e i_d + \omega_e \psi_f\right) + \dfrac{\alpha_{sp}}{Ji^2}\omega_e - \dfrac{p_n}{J}\dot{T}_g \end{bmatrix}. \tag{34}$$

Table 2: Operation parameters of a 0.16 kWh/0.8 kW MEES system.

Rated work voltage U_n	380 V
Rated work torque	2.1 N·m
Rated rotating speed of ES box	15 r/min
Number of pole pairs for rotor p_n	4
Rated rotating speed of rotor	600 r/min
Transformation ratio of the gear i	40 : 1
Moment of inertia for rotor J_1	0.8×10^{-3} kg m^2
Equivalent moment of inertia for the gear J_e	0.0013 kg m^2
Equivalent moment of inertia for the ES box J_{sp}	4.3264 kg m^2
Torsion constant of spring α_{sp}	5.0178
Effective flux of permanent magnet ψ_f	0.1442 Wb
Resistance of stator R_s	1.95 Ω
Equivalent inductance of direct axis L_d	0.2541 H
Equivalent inductance of quadrature axis L_q	0.2541 H
Viscous damping coefficient of the motor B_1	0.015 N/rad/s
Viscous damping coefficient of the gear B_e	0.013 N/rad/s
Viscous damping coefficient of the spring B_{sp}	0.005 N/rad/s

Substituting (33) into the electromechanical dynamic model in rotating frame of dq0, the ultimate linearization equation of the MEES system can be obtained as follows:

$$\begin{aligned}
\begin{bmatrix} \dot{i}_d \\ \dot{i}_q \\ \dot{\omega}_e \end{bmatrix} &= \begin{bmatrix} 0 & 0 & 0 \\ 0 & \dfrac{B}{p_n J} & -\left(\dfrac{2B^2}{3p_n\psi_f J} + \dfrac{2\alpha_{sp}}{3\psi_f i^2}\right) \\ 0 & \dfrac{3p_n\psi_f}{2J} & -\dfrac{B}{J} \end{bmatrix} \begin{bmatrix} i_d \\ i_q \\ \omega_e \end{bmatrix} \\
&\quad + \begin{bmatrix} 1 & 0 \\ 0 & \dfrac{2J}{3p_n\psi_f} \\ 0 & 0 \end{bmatrix} \begin{bmatrix} v_1 \\ v_2 \end{bmatrix} \\
&\quad + \begin{bmatrix} 0 \\ \dfrac{2B}{3\psi_f J} T_g + \dfrac{2}{3\psi_f}\dot{T}_g - \dfrac{2Bp_n\alpha_{sp}}{3\psi_f Ji^2}\theta_1 \\ \dfrac{p_n}{J} T_g - \dfrac{p_n \alpha_{sp}}{Ji^2}\theta_1 \end{bmatrix} \\
&= Ax + Ev + C,
\end{aligned} \tag{35}$$

where A, E, and C are three matrices.

4.3. Design of Optimal Linear Control. Optimal linear control block diagram of speed tracking for linearized system (35) is designed in Figure 3.

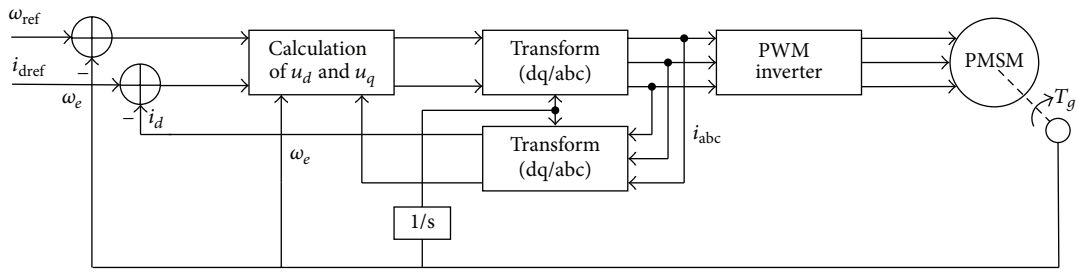

Figure 3: Control block diagram of speed tracking for linearized system.

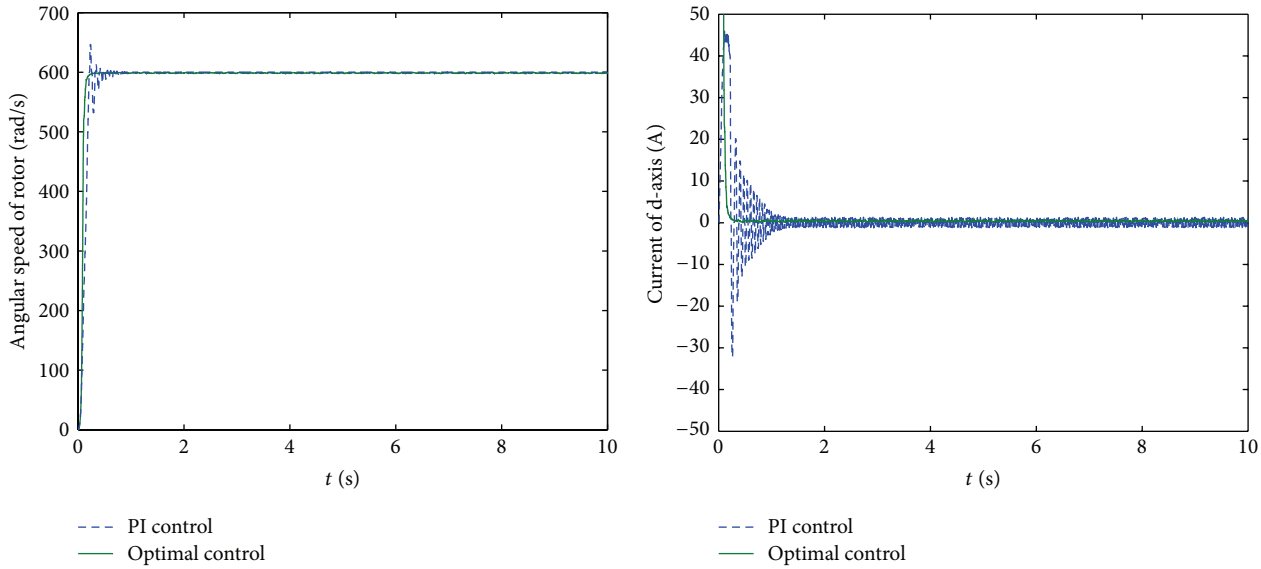

(a) Electric angular speed of rotor

(b) Current of d-axis

Figure 4: The simulation results of case I (always cutting off the energy storage device).

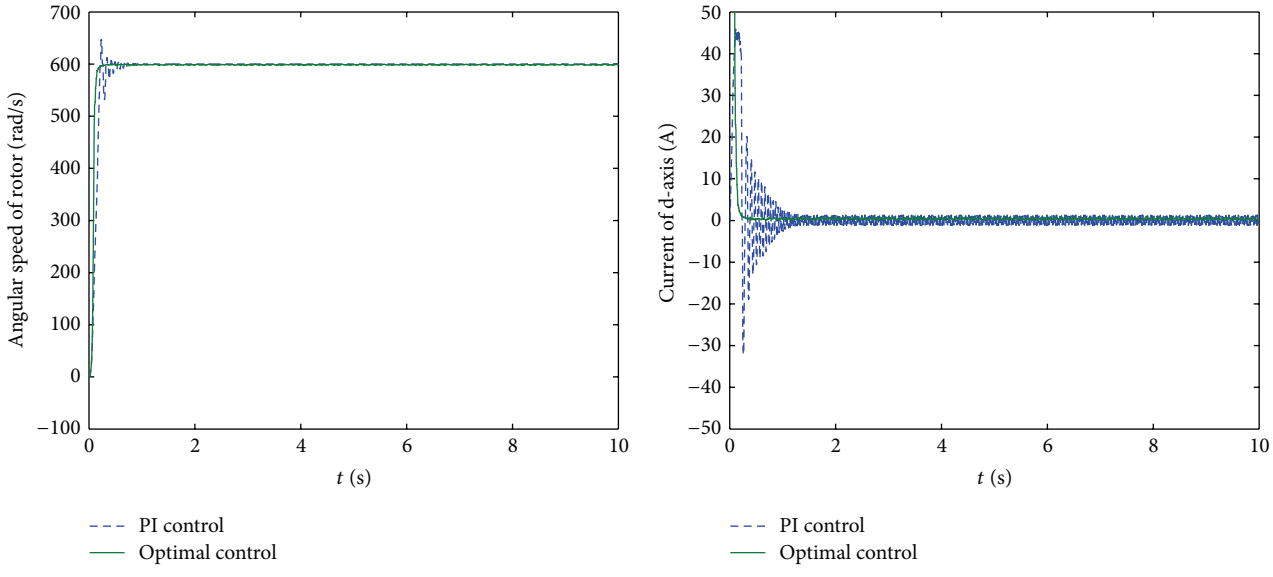

(a) Electric angular speed of rotor

(b) Current of d-axis

Figure 5: The simulation results of case II (from the initial state of storing no energy to the final state of storing full of energy).

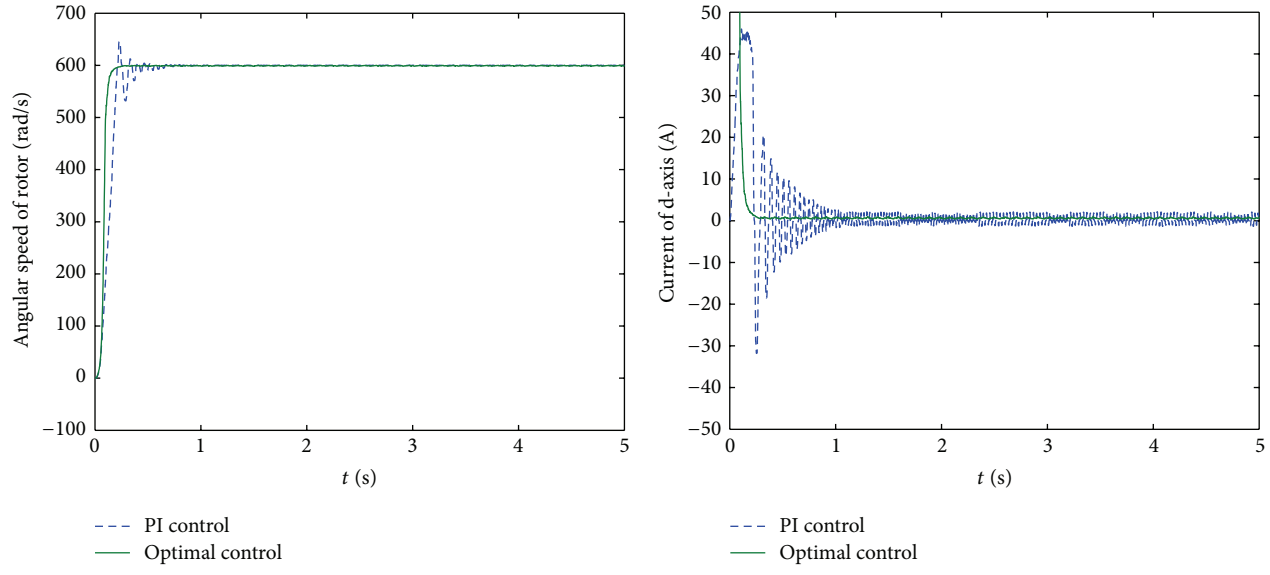

(a) Electric angular speed of rotor

(b) Current of d-axis

FIGURE 6: The simulation results of case III (from the initial state of storing half of full of energy to the final state of storing full of energy).

For the linearized system (35), the theory of linear control can be applied to determine v. In order to improve the control performance, in terms of optimal control theory of linear system, optimal control inputs are chosen as

$$v = -K^* \cdot x, \tag{36}$$

where $K^* = R^{-1}E^TP^*$, $R = R^T$ is the matrix of weight coefficient.

P^* is the solution of Riccati equation as follows:

$$A^TP + PA - PER^{-1}E^TP + Q = 0, \tag{37}$$

where Q is a positive definite matrix.

5. Simulation and Results

Based on a 0.16 kWh/0.8 kW MEES system being developed, the operation parameters of the system are given in Table 2. In terms of the description above, the control objectives in the paper are determined as the speed of rotor and the current of d-axis, namely, the speed of rotor tracking the reference speed and the current of d-axis being zero. The reference speed of the motor is set at 600 r/min. The work of modeling and control is implemented in Matlab environment.

In terms of the operation parameters in Table 2, the matrix parameters A and E in (35) are obtained as follows:

$$A = \begin{bmatrix} 0 & 0 & 0 \\ 0 & \dfrac{B}{p_nJ} & \left(\dfrac{2B^2}{3p_n\psi_fJ} + \dfrac{2\alpha_{sp}}{3\psi_fi^2}\right) \\ 0 & \dfrac{3p_n\psi_f}{2J} & -\dfrac{B}{J} \end{bmatrix} = \begin{bmatrix} 0 & 0 & 0 \\ 0 & 0.0019 & -0.2321 \\ 0 & 0.1999 & 0.0076 \end{bmatrix} \tag{38}$$

$$E = \begin{bmatrix} 1 & 0 \\ 0 & \dfrac{2J}{3p_n\psi_f} \\ 0 & 0 \end{bmatrix} = \begin{bmatrix} 1 & 0 \\ 0 & 5.0029 \\ 0 & 0 \end{bmatrix}. \tag{39}$$

In the paper, the matrices of weight coefficient R and positive definite Q are taken as 1 and a 3×3 identity matrix, respectively. Then, the matrix of P^* can be calculated as

$$P^* = \begin{bmatrix} 1 & 0 & 0 \\ 0 & -0.000228 & -0.017318 \\ 0 & -4.985561 & -0.000265 \end{bmatrix}. \tag{40}$$

Considering (36), the inputs of the optimal control can be expressed as

$$v = -K^* \cdot x = -R^{-1}E^TP^* \cdot x = \begin{bmatrix} -i_d \\ 0.001141i_q + 0.086640\omega_e \end{bmatrix}. \tag{41}$$

Substituting (41) into (33), the nonlinear state feedback controller is given as

$$u = \begin{bmatrix} 1.6969 i_d - 0.2541 i_q \omega_e \\ 1.953387 i_q + 0.265858 \omega_e + 0.2541 i_d \omega_e \end{bmatrix} + \begin{bmatrix} 0 \\ 0.008956 T_g - 0.924108 \dot{T}_g - 0.000449 \theta_1 \end{bmatrix}. \quad (42)$$

In order to evaluate the effectiveness of the proposed algorithm properly and adequately, the simulation schemes are selected as three different cases, which are case I (always cutting off the energy storage device), case II (from the initial state of storing no energy to the final state of storing full of energy), and case III (from the initial state of storing half of full of energy to the final state of storing full of energy). The simulation results are shown in Figures 4, 5, and 6, respectively. In order to better display the control performances, the proposed algorithm is in contrast with the conventional PI control. The proportional and integral coefficients for d-axis PI current controller are set as 2.6 and 50, respectively, and the proportional and integral coefficients for PI speed tracking controller are set as 0.24 and 10, respectively. Case I simulates PMSM operating in no load state, which is to test the no-load performance of the servomotor. The results in Figure 4 show that the proposed algorithm makes the controlled objective become stable more quickly and almost has no oscillation in stabilization process in comparison with the conventional PI control. Figure 5 shows the results of case II, which essentially represents the process from point J to point E in Figure 2. Figure 6 displays the results of case III, and it should be noted that the running time in the condition will be half of the whole time of energy storage, which is 5 s. The simulation results in case II and case III are similar to case I. Therefore, the simulation results reveal that in contrast with conventional PI control, the presented algorithm not only has a preferable ability of speed tracking in all of the three cases, but also makes the electromechanical system have a better dynamic performance in energy storage process.

6. Conclusions

In terms of the characteristics of electromechanical coupling for PMSM based MEES system presented in the paper, dynamic modeling and control of the system are proposed from an electromechanical point of view. The conclusions were made as follows:

(a) dynamic model for PMSM based MEES system is nonlinear with significant electromechanical coupling. The nonlinear model constructed by Lagrange-Maxwell energy method can reflect the characteristics of electromechanical coupling for the system;

(b) DFL can perform the dynamic decoupling for the complex electromechanical system completely;

(c) the speed tracking controller proposed in the paper in terms of optimal linear control theory for linearized system has a better performance in contrast with conventional PI control algorithm, and the simulation results in three different cases prove the validity and feasibility of the designed method.

Conflict of Interests

The authors declare that there is no conflict of interests regarding the publication of this paper.

Acknowledgments

This research is supported by the Specialized Research Fund for the Doctoral Program of Higher Education of China under Grant no. 20120036130001, the Fundamental Research Funds for the Central Universities of China under Grant no. 11MG40, and the Independent Research Funds of State Key Laboratory of Alternate Electrical Power System with Renewable Energy Sources of China under Grant no. 201209.

References

[1] K. T. Tan, P. L. So, Y. C. Chu, and M. Z. Q. Chen, "Coordinated control and energy management of distributed generation inverters in a microgrid," *IEEE Transactions on Power Delivery*, vol. 28, no. 2, pp. 704–713, 2013.

[2] K. T. Tan, X. Y. Peng, P. L. So, Y. C. Chu, and M. Z. Q. Chen, "Centralized control for parallel operation of distributed generation inverters in microgrids," *IEEE Transaction on Smart Grid*, vol. 3, no. 4, pp. 1977–1987, 2012.

[3] A. Bernstein, D. Bienstock, D. Hay, U. Meric, and Z. Gil, "Sensitivity analysis of the power grid vulnerability to large-scale cascading failures," *ACM Sigmtrics Performance Evaluation Review*, vol. 40, no. 3, pp. 33–37, 2012.

[4] M. Black and G. Strbac, "Value of bulk energy storage for managing wind power fluctuations," *IEEE Transactions on Energy Conversion*, vol. 22, no. 1, pp. 197–205, 2007.

[5] K. C. Divya and J. Østergaard, "Battery energy storage technology for power systems—an overview," *Electric Power Systems Research*, vol. 79, no. 4, pp. 511–520, 2009.

[6] A. I. Cohen and S. H. Wan, "An algorithm for scheduling a large pumped storage plant," *IEEE Transactions on Power Apparatus System*, vol. 104, no. 8, pp. 2099–2104, 1985.

[7] A. J. Pimm, S. D. Garvey, and R. J. Drew, "Shape and cost analysis of pressurized fabric structures for subsea compressed air energy storage," *Proceedings of the Institution of Mechanical Engineers C*, vol. 225, no. 5, pp. 1027–1043, 2011.

[8] R. Hebner, J. Beno, and A. Walls, "Flywheel batteries come around again," *IEEE Spectrum Magazine*, vol. 39, no. 4, pp. 46–51, 2002.

[9] M. H. Ali, B. Wu, and R. A. Dougal, "An overview of SMES applications in power and energy systems," *IEEE Transactions on Sustainable Energy*, vol. 1, no. 1, pp. 38–47, 2010.

[10] A. Rufer, D. Hotellier, and P. Barrade, "A supercapacitor-based energy storage substation for voltage compensation in weak transportation networks," *IEEE Transactions on Power Delivery*, vol. 19, no. 2, pp. 629–636, 2004.

[11] K. Senthil, S. Mitra, A. Roy, A. Sharma, and D. P. Chakravarthy, "Compact inductive energy storage pulse power system," *Review of Scientific Instruments*, vol. 83, no. 5, Article ID 054703, 4 pages, 2012.

[12] Y. Yu and Z. Q. Mi, "Nonlinear dynamic model and chaotic characteristics of mechanical elastic energy storage unit in energy storage process," *Acta Physica Sinica*, vol. 62, no. 3, Article ID 038403, 8 pages, 2013.

[13] Z. Q. Mi, Y. Yu, Z. Q. Wang, and J. Q. Tang, "Preliminary exploration on permanent magnet motor based mechanical elastic energy storage unit and key technical issues," *Automation of Electric Power Systems*, vol. 37, no. 1, pp. 26–30, 2013.

[14] Y. A. I. Mohamed and T. K. Lee, "Adaptive self-tuning MTPA vector controller for IPMSM drive system," *IEEE Transactions on Energy Conversion*, vol. 21, no. 3, pp. 636–644, 2006.

[15] S. Jiang and L. Ju, "Study on electromechanical coupling nonlinear vibration of flywheel energy storage system," *Science in China, Series E*, vol. 49, no. 1, pp. 61–77, 2006.

[16] Z. W. Gao, D. X. Kong, and C. H. Gao, "Modeling and control of complex dynamic systems: applied mathematical aspects," *Journal of Applied Mathematics*, vol. 2012, Article ID 869792, 5 pages, 2012.

[17] M. J. Mahmoodabadi, A. Bagheri, N. Nariman-Zadeh, A. Jamali, and R. A. Maafi, "Pareto design of decoupled sliding-mode controllers for nonlinear systems based on a multiobjective genetic algorithm," *Journal of Applied Mathematics*, vol. 2012, Article ID 639014, 22 pages, 2012.

[18] G. Kenné, R. Goma, H. Kwawo, F. Lamnabhi-Lagarrigue, A. Arzandé, and J. C. Vannier, "An improved direct feedback linearization technique for transient stability enhancement and voltage regulation of power generators," *International Journal of Electrical Power and Energy Systems*, vol. 32, no. 7, pp. 809–816, 2010.

[19] Z. H. Abootorabi, G. R. A. Markadeh, and J. Soltani, "Direct torque and flux regulation of synchronous reluctance motor drives based on input-output feedback linearization," *Energy Conversion and Management*, vol. 51, no. 1, pp. 71–80, 2010.

Hindawi Publishing Corporation
Journal of Applied Mathematics
Volume 2013, Article ID 767853, 12 pages
http://dx.doi.org/10.1155/2013/767853

Research Article

PDE Modeling of a Microfluidic Thermal Process for Genetic Analysis Application

Reza Banaei Khosroushahi,[1] Horacio J. Marquez,[1] Jose Martinez-Quijada,[1] and Christopher J. Backhouse[2]

[1] *Electrical and Computer Engineering, University of Alberta, Edmonton, AB, Canada T6G 2V4*
[2] *Electrical and Computer Engineering, University of Waterloo, Waterloo, ON, Canada N2L 3G1*

Correspondence should be addressed to Reza Banaei Khosroushahi; banaeikh@ualberta.ca

Received 12 July 2013; Accepted 29 August 2013

Academic Editor: Zhiwei Gao

Copyright © 2013 Reza Banaei Khosroushahi et al. This is an open access article distributed under the Creative Commons Attribution License, which permits unrestricted use, distribution, and reproduction in any medium, provided the original work is properly cited.

This paper details the infinite dimensional dynamics of a prototype microfluidic thermal process that is used for genetic analysis purposes. Highly effective infinite dimensional dynamics, in addition to collocated sensor and actuator architecture, require the development of a precise control framework to meet the very tight performance requirements of this system, which are not fully attainable through conventional lumped modeling and controller design approaches. The general partial differential equations describing the dynamics of the system are separated into steady-state and transient parts which are derived for a carefully chosen three-dimensional axisymmetric model. These equations are solved analytically, and the results are verified using an experimentally verified precise finite element method (FEM) model. The final combined result is a framework for designing a precise tracking controller applicable to the selected lab-on-a-chip device.

1. Introduction

Biomedical microdevices usually require the very tight performance specification to be satisfied so that they become properly functional. Carefully designed controllers can guarantee certain performance specifications such as robustness and stability. Successful controller design process requires a precise mathematical model. A perfect mathematical model is the one that captures the highest amount of the dynamics of the system. Likewise, numerical tools can provide precise insights into a system's dynamics. Finite element method (FEM) is a common numerical tool that can provide precise simulation of the steady-state and transient behaviour of a microdevice. However, FEM models are not suitable for controller design because they are not in a compact mathematical form. In this work, we present a mathematical model that captures infinite dimensional dynamics of the heat distribution inside a prototype system. The selected system is a lab-on-a-chip (LOC) device that is designed and built to perform the Polymerase Chain Reaction (PCR) and capillary electrophoresis (CE) processes. The three-dimensional complete FEM model of the system is used as the reference to derive the mathematical model. The FEM model is experimentally verified with the actual setup.

Lab-on-a-chip (LOC) devices are finding growing attention in various applications ranging from chemical analysis and water contamination sensors to genetic analysis [1]. A LOC device can be thought of as a miniaturized instrument capable of performing single or multiple laboratory processes that integrate various functionalities such as sample pretreatment, sample transportation, genetic amplification, mixing, reaction, separation, and detection. LOC devices offer advantages beyond conventional biochemical and clinical laboratory settings. Dramatic reduction of sample volume and reduced consumption of costly reagents are two distinct benefits of miniaturized laboratory processes. Most significantly, miniaturization improves analysis characteristics, such as shorter analysis time and higher separation performance, and can even enable innovative applications that are not otherwise attainable.

Genetic and molecular analyses are among the major applications of LOC devices and have become feasible by the adoption of the Polymerase Chain Reaction (PCR) technique. Using PCR, specific regions of even a single DNA molecule can be replicated up to about 10^7 to 10^8 times. This process is also called selective amplification of DNA. The amplified DNA segments can be later analyzed and compared to a standard pattern to find out if they correspond to some disease condition. PCR has been traditionally a lengthy molecular biology operation, but the LOC concept, proposed in the early 1990s [2, 3], has pushed this technology to attain ever shorter reaction times. DNA amplification using PCR involves repeatedly cycling the temperature of the reaction chamber in three predefined temperatures. Optimum reaction temperature and exposure times of the sample to each temperature are key factors for successful DNA amplification [4]. The PCR-LOC research community emphasizes the importance of ±1°C temperature precision and rapid transition time for high amplification efficiency. At the same time, overshoots and undershoots, which are likely to happen at higher speeds, have a detrimental impact on the amplification yield. For example, overshoots at denaturation temperature will reduce the lifetime of replicating enzyme (Taq polymerase). Undershoots at annealing temperature may cause the amplification of unspecified products. Nevertheless, rapid thermal cycling of reaction chamber in DNA amplification not only reduces the amplification time, but it is also important to ensure the stability of biological reagents during amplification as the Taq polymerase has a half lifetime that decreases rapidly at temperatures close to 100°C [5]. It is important to note that about half of the time in a standard PCR process is spent in transitions which are undesirable. As a result, researchers have focused their attention to reduce transition time between temperature steps in PCR process. To achieve this goal, both structural design of the device and thermal control of the process need to be optimized. Consequently, various platforms for PCR-LOC devices have been reported in the literature [6] which can be roughly divided into two major categories: continuous-flow PCR and static PCR [7]. Furthermore, different heating techniques have been chosen, where thermoelectric modules (TEMs) and thin-film resistive heaters [8–11] are the most commonly used techniques. Other techniques, such as infrared radiation [12] and microwaves [13, 14], have also been reported. These different structural designs are discussed in detail in the excellent review papers by Zhang et al. [7], Roper and coworkers [6], Verpoorte [15], and DeMello [16]. The latest achievements in PCR-LOC devices design can be found in the recently published survey paper by Zhang and Ozdemir [1].

Most of the published work on PCR-LOC devices has been devoted to the structural design aspects, and less attention has been paid to optimize the thermal control of the process. As a result, there is very little work in the literature on the dynamics and control of these microsystems. Although neural network based controllers [17] and hybrid controllers [18] are used for thermal control of PCR-LOC devices, PI/PID controllers are still the most commonly preferred controllers to deal with the thermal control problem of PCR-LOCs [5, 19, 20]. What makes the thermal control of most of the PCR-LOC devices a challenging task is the fact that the temperature inside the PCR-LOC chips not only depends on time but is also spatially distributed. Thus lumped modeling and controller design cannot exactly address the problem, fundamentally because in this approach the distributed parameter nature of the system is neglected. We observed this critical problem to some extent in the formerly designed PCR-LOC chip [21] where switching controllers were employed [8]. The PCR-LOC system studied in this paper is the next generation of the one described in our previous work [22]. The new design has undergone significant improvement in structural design with respect to its predecessor.

While lumped modeling can precisely describe the dynamics of lumped systems, it usually cannot provide a fair description of the dynamics of the distributed parameter systems. Those systems that can be described by partial differential equations are often referred to as distributed parameter systems or PDE systems which feature distributed dynamics and are categorized under a general set of the systems known as complex dynamical systems [23]. Distributed parameter systems are subsets of a more general set called infinite dimensional systems because they can be mathematically formulated as differential equations on an abstract linear vector space of infinite dimension [24]. In contrast, lumped systems can be formulated mathematically as ordinary differential equations on a finite dimensional linear vector space. Designing controllers for distributed parameter systems is called infinite dimensional controller design or PDE controller design [24–26].

This paper characterizes the heat distribution dynamics of a microfluidic thermal process. The work begins with a description of the process and experimental setup. Then results of FEM simulations on the system were analyzed to choose a suitable structure for the model. Next the PDE equations describing the model in steady-state and transient parts were derived. These equations were solved analytically from which the dynamic temperature distribution in the whole domain can be expressed by an infinite dimensional model. Next, we optimize the calculated model to minimize the error due to the simplification of the actual multidomain system to an abstract single-domain system. FEM simulation and laboratory experiments are used to verify the model. The result of this work is a framework for boundary control design for thermal control of the aforementioned PCR-LOC device.

2. Materials and Methods

2.1. Chip Configuration. Genetic analysis usually consists of three steps: sample preparation, amplification, and detection. In the first step the DNA is extracted from a raw sample such as blood. Then, a selected fragment of this DNA is amplified through the PCR process to obtain sufficient DNA copies to perform detection. Next, the amplified region of DNA is labelled with a fluorescent dye, and finally it is detected through various analysis techniques [27].

The integrated genetic analysis platform that has been developed in the Applied Miniaturization Laboratory (AML) at the University of Alberta is capable of performing complete genetic analysis on a single microfluidic chip [28]. This system

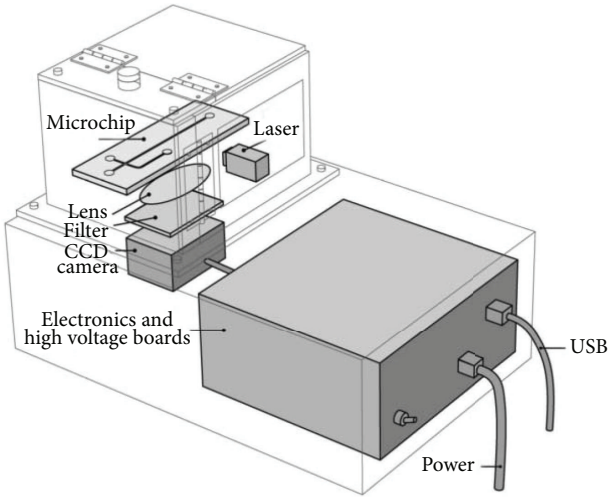

Figure 1: Integrated genetic analysis platform comprising the PCR-LOC device and the control electronics. The platform is operated through a graphical user interface [29].

is depicted in Figure 1. The microchip is composed of two layers of Borofloat glass with a polydimethylsiloxane (PDMS) layer in the middle. Reaction chamber and fluid channels are carved on one of the glass layers, and a Pt heater/sensor is patterned on the bottom glass plate using standard microfabrication techniques. A close-up view of the microfluidic chip, depicted in Figure 2, clearly shows the configuration of the platinum heater-sensor ring. A schematic representation of the components within the chip is shown in Figure 2(a). Perspective view of the glass/PDMS/glass chip with horizontal laser beam is shown in Figure 2(b) and the chip atop a heatsink and light detector is depicted in Figure 2(c). To improve the cooling rate during thermal cycling, the microchip is mounted on a copper heat sink. The heat sink has a circular opening aligned to the center of the PCR chamber and heater/sensor, ring axis. The radius of this opening is optimized to increase the cooling rate without having negative effect on the heating rate [21]. We are mostly interested in heat transfer dynamics around the reaction chamber and heater-sensor ring. The chamber, heater/sensor and heat-sink opening are circular and share the same axis. This suggests that we should look for an axisymmetric cylindrical structure for our model. The half cross-section view of the chip along a vertical plane parallel to the smaller side and passing through the center of the chip is shown in Figure 3. The irregular and multilayer multimaterial structure of the PCR-LOC system is not suitable to form a set of solvable analytic equations; additional simplifications are needed. To find a valid simplified model describing the dynamics of the chip where the heater and chamber are located, we first have to analyze the temperature profile around the heater and chamber area. Figure 4 depicts the temperature profile along the chip thickness for some selected distances from the center of the chip, ranging from 2.5 mm to 5.0 mm. Referring to Figure 4, the temperature profile along the thickness of the chip at the upper glass layer (1.354 mm to 2.454 mm from the bottom of the chip) shows a semilinear trend. By choosing the radius of 3.5 mm from the center of the chip, the slope is negligible, as the temperature varies for less than 0.8°C, which is even less than the acceptable error for the chamber temperature. Therefore, with reasonable approximation, we can consider a constant temperature wall as the boundary, where this boundary is positioned at a distance of 3.5 mm from center of the chip. These calculations, in addition to several other FEM simulations, have been performed using *COMSOL Multiphysics 3.5a* on a comprehensive FEM model of the chip that describes its layered geometry, material properties, and boundary conditions with a high degree of accuracy. More FEM simulations disclosed some other important facts about this chip which can be summarized as follows.

(1) The amount of heat going to the upper portion of the chip through the PDMS and top glass layer has an approximately constant ratio to the total heat being dissipated by the heater.

(2) If we consider a disk-shape bounded volume at the center of the chip, the amount of heat lost by natural convection in air through the upper surface of the disk is negligible compared to the amount of heat lost by conduction through the wall.

(3) If the PDMS layer was replaced by a glass layer, only a small percentage of the dynamic temperature distribution would be affected, due to the alteration of thermal properties (thermal conductivity and specific heat capacity). This small effect on the dynamics can be compensated later by using a correction factor.

(4) The vertical temperature profile in the top glass layer at a distance of 3.5 mm from the center is approximately constant.

2.2. Model Structure. Using these observations we can conclude that, by picking a single layer glass disk, we can model the temperature distribution at a closed disk in the upper side of the chip with a good level of approximation relative to the temperature accuracy of ±1°C demanded by PCR-LOC systems. This model structure is shown in Figure 5 where the heater is defined by the circular strip at the bottom surface with k_2 width and k_1 distance to the vertical axis. It is worth noting that we only modelled the area of interest in the chip, and we have put aside the rest of the chip. Furthermore, we defined a comparison aperture that can be characterized by a fixed size rectangular area in cross-section view of the actual PCR-LOC microchip and our model. The comparison aperture contains the reaction chamber, and it is discussed in detail in the simulation results section. We chose this scenario to arrive at a model structure which is simple enough to find its analytical solution meanwhile it is accurate enough to characterize the actual thermal process. A simple estimate of the thermal capacity and radial thermal resistance of the PDMS layer shows that they are small compared to those of the glass layers. It is expected that treating the PDMS layer as if it has the same thermal properties of glass will make

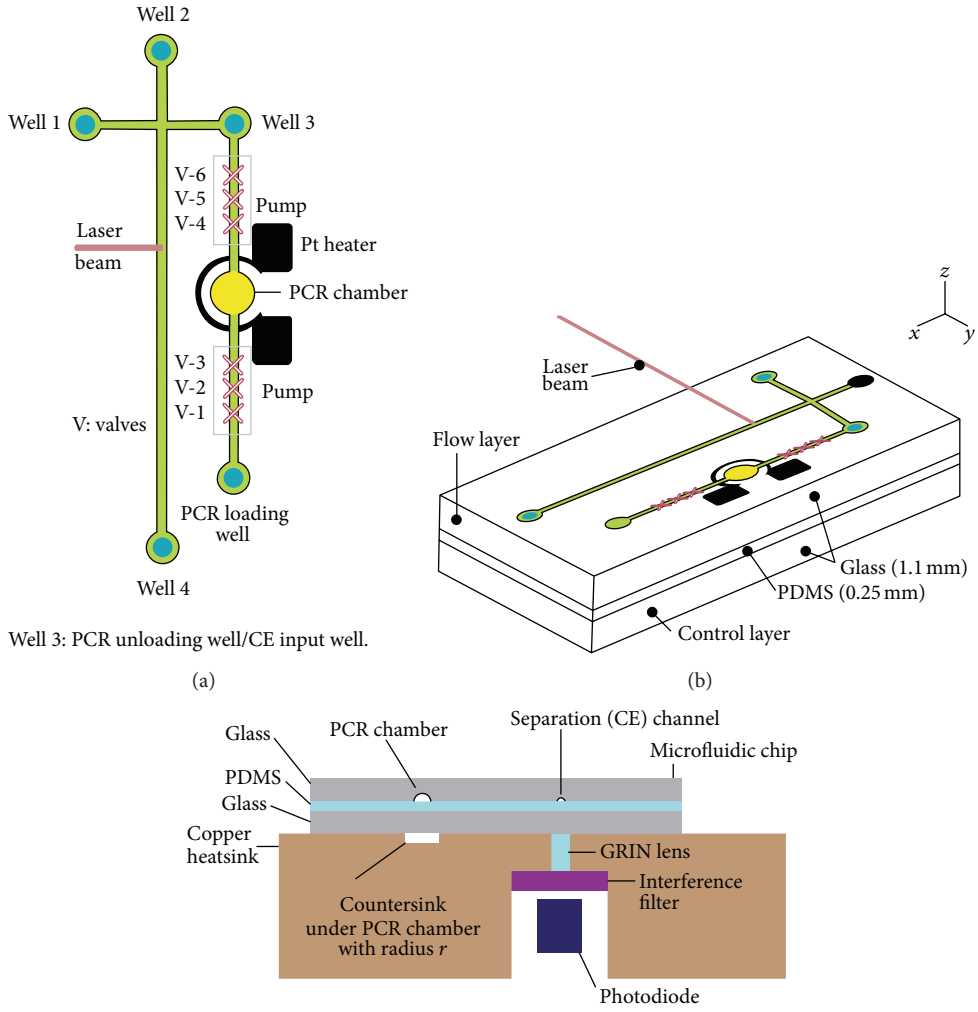

Figure 2: The modelled PCR-LOC device. On (a) a schematic of the chip, showing the PCR chamber as a yellow circle. The chamber is surrounded by the heater ring. The squares in the middle are the heater contact pads. The crossing channels form the CE section. On (b) a 3D view of the chip showing the three layers that comprise the device. On (c) a cross-section view of the chip showing the chip placed on the heatsink that provides passive cooling [28].

the systems dynamic behavior 9% too fast (because the radial resistance is predicted to be 10% too low and the thermal capacity is estimated to be about 1% too high). It is possible to correct for this by scaling the thermal parameters of the glass. The assumptions made will result in underestimating the vertical gradient, but that gradient cannot be controlled by control mechanism and must instead be dealt with at the design and simulation level (i.e., dynamic simulations of the present design ensured that the PCR chamber radius and height were sufficiently small that the vertical gradient could not lead to temperature variations greater than ±1°C). The FEM model by itself was verified by extensive experiments, wherein thermochromic liquid crystal (TLC) sensitive to different temperatures was deposited in the chamber to read the temperature within its volume in steady-state conditions.

3. Heat Distribution Model

3.1. Problem Formulation. The partial differential equation describing temperature distribution in the chosen domain at any time is given by the heat conduction equation as follows [30]:

$$K\nabla^2 u = \overline{\rho}\mathscr{C}\frac{\partial u}{\partial t}, \tag{1}$$

where $u(\rho, \varphi, z, t)$ is the temperature of every point of the domain at any given time. K is thermal conductivity, $\overline{\rho}$ is density, and $\mathscr{C}$ is heat capacity. Since the chosen model features axial symmetry, the temperature in the cylinder does not depend on φ. This means that $\partial u/\partial\varphi = 0 = \partial^2 u/\partial\varphi^2$.

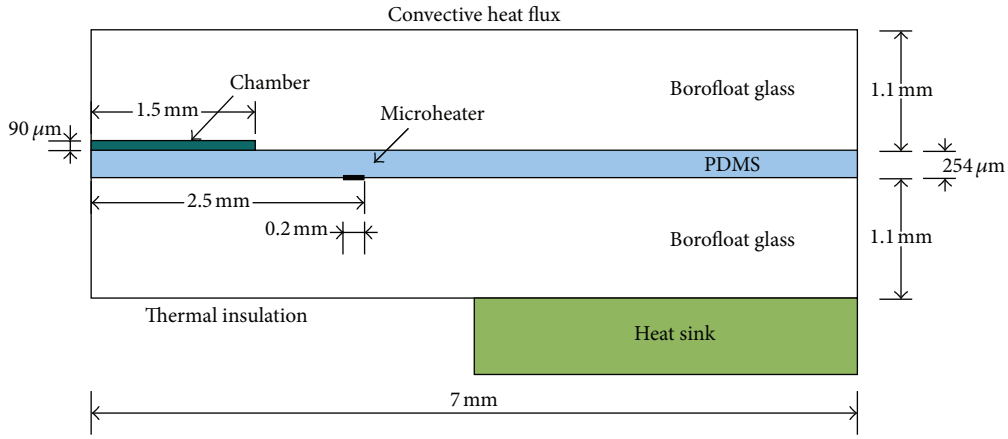

Figure 3: Cross-section view and dimensions of PCR LOC microchip. Due to the axisymmetric geometry of the chip, only half the chip is shown. The axis of symmetry is along the left vertical side. A circular hole is cut in the middle of the heatsink to provide thermal insulation under the heater and chamber. Heat is lost by free convection on the top and by conduction through the heatsink [21].

Therefore φ can be dropped and the Laplace operator can be written in a 2D cross-section domain using ρ and z as follows:

$$\nabla^2 u = \frac{\partial^2 u}{\partial \rho^2} + \frac{1}{\rho}\frac{\partial u}{\partial \rho} + \frac{\partial u^2}{\partial z^2}. \tag{2}$$

To avoid any confusion between ρ and the notation used for density, we introduce here notation κ as follows:

$$\kappa = \frac{K}{\rho \mathscr{C}} \tag{3}$$

which is thermal diffusivity of the material in m^2/s. Finally the partial differential equation giving the temperature $u(\rho, z, t)$ at the half part cross-section of our cylindrical domain with ρ and z as its horizontal and vertical axes can be written as

$$\kappa \nabla^2 u = \frac{\partial u}{\partial t}. \tag{4}$$

The definition of our domain implies that ρ and z are limited to $0 \le \rho \le a$ and $0 \le z \le b$. The initial and boundary conditions are given by

$$u(\rho, z, 0) = u_0(\rho, z), \tag{5}$$

$$u(a, z, t) = T_w, \tag{6}$$

$$u_\rho(0, z, t) = 0, \tag{7}$$

$$u_z(\rho, b, t) = 0, \tag{8}$$

$$u_z(\rho, 0, t) = -f(\rho), \tag{9}$$

where $u_0(\rho, z)$ is the initial distribution of temperature. T_w is the temperature of the outside wall of the cylinder. The boundary condition (7) comes from the axisymmetrical cylindrical structure of the model. The boundary condition (8) is based on the assumption that the upper surface of the chip is isolated. $f(\rho)$ describes the geometric distribution of the control action signal at the bottom surface, which is defined by the heater location. A general solution of (4) can be found by adding the solution of homogeneous and nonhomogeneous equations describing the steady-state and a transient temperature distribution, respectively:

$$u(\rho, z, t) = \widehat{u}(\rho, z, t) + \overline{u}(\rho, z). \tag{10}$$

Substituting (10) in (4) we get

$$\begin{aligned} \frac{1}{\kappa}\widehat{u}_t &= \widehat{u}_{\rho\rho} + \overline{u}_{\rho\rho} + \frac{1}{\rho}\widehat{u}_\rho + \frac{1}{\rho}\overline{u}_\rho + \widehat{u}_{zz} + \overline{u}_{zz} \\ &= \left(\widehat{u}_{\rho\rho} + \frac{1}{\rho}\widehat{u}_\rho + \widehat{u}_{zz}\right) + \left(\overline{u}_{\rho\rho} + \frac{1}{\rho}\overline{u}_\rho + \overline{u}_{zz}\right). \end{aligned} \tag{11}$$

Without the loss of generality, we can assume $\overline{u}_{\rho\rho} + (1/\rho)\overline{u}_\rho + \overline{u}_{zz} = 0$ as we defined $\overline{u}(\rho, z)$ to describe the steady-state temperature. By applying (10) to the initial condition (5) and boundary conditions (6), (7), (8), and (9), we arrive at two PDEs:

$$\frac{1}{\kappa}\widehat{u}_t = \widehat{u}_{\rho\rho} + \frac{1}{\rho}\widehat{u}_\rho + \widehat{u}_{zz} \quad \text{with} \begin{cases} \widehat{u}(\rho, z, 0) = \widehat{u}_0(\rho, z) \\ \widehat{u}(a, z, t) = 0 \\ \widehat{u}_\rho(0, z, t) = 0 \\ \widehat{u}_z(\rho, b, t) = 0 \\ \widehat{u}_z(\rho, 0, t) = 0, \end{cases} \tag{12}$$

$$\overline{u}_{\rho\rho} + \frac{1}{\rho}\overline{u}_\rho + \overline{u}_{zz} = 0 \quad \text{with} \begin{cases} \overline{u}(a, z) = T_w \\ \overline{u}_\rho(0, z) = 0 \\ \overline{u}_z(\rho, b) = 0 \\ \overline{u}_z(\rho, 0) = -f(\rho). \end{cases} \tag{13}$$

The first one is an initial value problem with homogeneous boundaries, while the second one is a nonhomogeneous boundary value problem.

3.2. Steady-State Part. To solve (13), we employ the method of separation of variables [31]:

$$\overline{u}(\rho, z) = \overline{P}(\rho)\overline{Z}(z) + T_w, \tag{14}$$

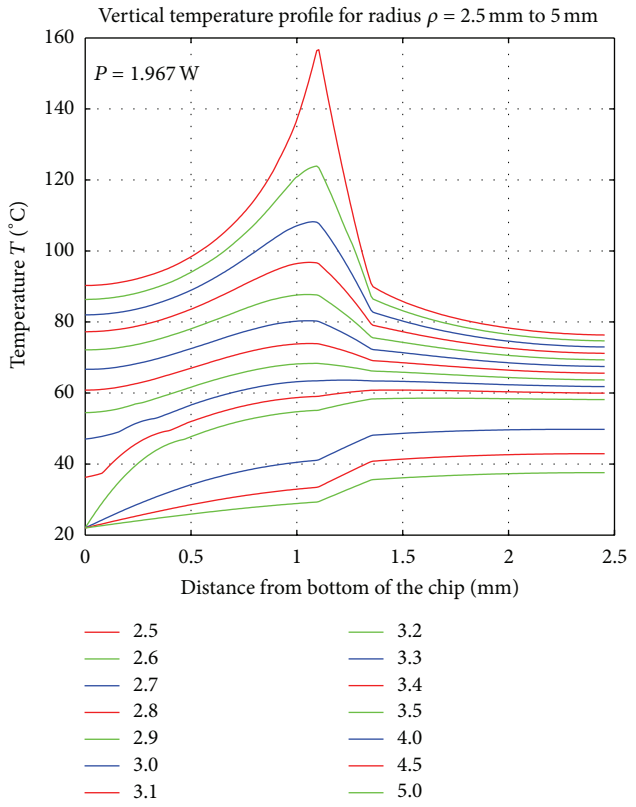

Figure 4: Steady-state vertical temperature profile predicted by FEM. Each curve shows the temperature along a vertical line that crosses through the chip. Such a line is placed at a defined distance from the centre. The legend shows the radial distance in millimetres. The horizontal axis represents the vertical distance from the bottom to the top of the chip, which is 2.454 mm thick. As the distance from the center increases from 2.5 to 5 mm, the curves flattened out towards 22°C. The temperatures in the top glass plate (right side of the curves) are almost constant.

where $\overline{P}$ and $\overline{Z}$ are functions of ρ and z, respectively. The constant part is used to normalize the boundary conditions and to achieve the homogeneous boundary condition. Using (14) in (13) and dividing $\overline{P}\,\overline{Z}$ we arrive to

$$\frac{\overline{P}''(\rho)}{\overline{P}(\rho)} + \frac{1}{\rho}\frac{\overline{P}'(\rho)}{\overline{P}(\rho)} = -\frac{\overline{Z}''(z)}{\overline{Z}(z)}. \tag{15}$$

The left side contains functions of ρ alone, while the right side contains functions of z alone. Since this equality must hold for all ρ and z in the given interval, the common value of the two sides must be a constant; say $-\overline{\lambda}^2$ varying neither with ρ nor with z. The constant here was chosen as a negative value to avoid a trivial solution [31]. Now we have two ODEs for the two factor functions:

$$\begin{aligned} \rho\overline{P}'' + \overline{P}' + \overline{\lambda}^2\rho\overline{P} &= 0, \\ \overline{Z}'' - \overline{\lambda}^2\overline{Z} &= 0. \end{aligned} \tag{16}$$

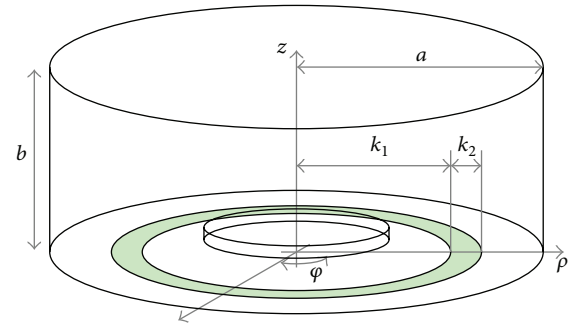

Figure 5: Geometrical representation of the PDE model. Taking advantage of the axial symmetry of the chip, the entire system is represented as a two-dimensional rectangular region. Similarly the heater is represented as a line instead of being a surface. This reduction of one dimension allows the model to be solved for the temperature in a three-dimensional space but at a small fraction of the time and computational resources required by a FEM simulation.

The boundary conditions of (13) can also be stated in the product form (14) which results in the following:

$$\overline{P}(a) = 0, \tag{17}$$

$$\overline{P}'(0) = 0, \tag{18}$$

$$\overline{Z}'(b) = 0, \tag{19}$$

$$\overline{P}(\rho)\,\overline{Z}'(0) = -f(\rho). \tag{20}$$

The solutions of (16) are given by [31]

$$\overline{P} = \overline{c}_1 J_0\left(\overline{\lambda}\rho\right) + \overline{c}_2 Y_0\left(\overline{\lambda}\rho\right), \tag{21}$$

$$\overline{Z} = \overline{c}_3 \cosh\overline{\lambda}(b-z) + \overline{c}_4 \sinh\overline{\lambda}(b-z), \tag{22}$$

where J_0 is the Bessel function of the first kind of order 0 and Y_0 is the Bessel function of the second kind of order 0. From the boundedness condition at $\rho = 0$ stated by (18), we must have $\overline{c}_2 = 0$ because Y_0 is unbounded at zero. Thus the solution (21) becomes

$$\overline{P} = \overline{c}_1 J_0\left(\overline{\lambda}\rho\right). \tag{23}$$

From the boundary condition (19) and the fact that

$$\overline{Z}'(z) = -\overline{\lambda}\left(\overline{c}_3 \sinh\overline{\lambda}(b-z) + \overline{c}_4 \cosh\overline{\lambda}(b-z)\right) \tag{24}$$

we see that

$$\overline{Z}'(b) = -\overline{\lambda}\overline{c}_4 = 0 \tag{25}$$

which implies $\overline{c}_4 = 0$, so the solution (22) becomes

$$\overline{Z}(z) = \overline{c}_3 \cosh\overline{\lambda}(b-z). \tag{26}$$

The boundary condition (17) can be employed to determine $\overline{\lambda}$:

$$\overline{P}(a) = \overline{c}_1 J_0\left(\overline{\lambda}a\right) = 0 \tag{27}$$

which can be satisfied only if $J_0(\overline{\lambda}a) = 0$ so that

$$a\overline{\lambda} = r_1, r_2, r_3, \ldots, r_m, \ldots, \tag{28}$$

where r_m ($m = 1, 2, 3, \ldots$) is the mth positive root of $J_0(x) = 0$. Thus $\overline{\lambda}$'s can be expressed as

$$\overline{\lambda}_m = \frac{r_m}{a}, \quad m = 1, 2, 3, \ldots. \tag{29}$$

So a solution satisfying the boundary conditions is

$$\begin{aligned}\overline{u}(\rho, z) - T_w &= \overline{P}_m(\rho)\,\overline{Z}_m(z) \\ &= \overline{A} J_0\left(\frac{r_m}{a}\rho\right)\cosh\frac{r_m}{a}(b - z),\end{aligned} \tag{30}$$

where $m = 1, 2, 3, \ldots$ and $\overline{A} = \overline{c}_1\overline{c}_3$. The general solution of (13) can be obtained by employing the superposition principle [31]. By replacing $\overline{A}$ with A_m and summing up all eigenfunctions, it follows that

$$\overline{u}(\rho, z) = T_w + \sum_{m=1}^{\infty} A_m J_0\left(\frac{r_m}{a}\rho\right)\cosh\frac{r_m}{a}(b - z). \tag{31}$$

From

$$\frac{\partial\overline{u}}{\partial z} = \sum_{m=1}^{\infty} - A_m\frac{r_m}{a} J_0\left(\frac{r_m}{a}\rho\right)\sinh\frac{r_m}{a}(b - z) \tag{32}$$

and the last boundary condition (20) we can write

$$\sum_{m=1}^{\infty}\left(A_m\frac{r_m}{a}\sinh\frac{r_m b}{a}\right) J_0\left(\frac{r_m}{a}\rho\right) = f(\rho). \tag{33}$$

The right side is the Bessel series expansion of $f(\rho)$ with coefficients equal to $(A_m(r_m/a)\sinh(r_m b/a))$ [31], so we get

$$A_m = \frac{2}{a r_m \sinh(r_m b/a)\, J_1^2(r_m)}\int_0^a \rho J_0\left(\frac{r_m}{a}\rho\right) f(\rho)\, d\rho. \tag{34}$$

3.3. Transient Part. We employ the separation of variables again to solve (12)

$$\widehat{u}(\rho, z, t) = \widehat{P}(\rho)\,\widehat{Z}(z)\,\widehat{T}(t), \tag{35}$$

where $\widehat{P}$, $\widehat{Z}$, and $\widehat{T}$ are functions of ρ, z, and t, respectively. Following the same procedure as the steady-state part and defining μ, ν, and $\widehat{\lambda}$ as eigenvalues for $\widehat{P}$, $\widehat{Z}$, and $\widehat{T}$, respectively, we arrive at the following ODEs:

$$\rho\widehat{P}'' + \widehat{P}' + \mu^2\rho\widehat{P} = 0, \tag{36}$$

$$\widehat{Z}'' - \nu^2\widehat{Z} = 0, \tag{37}$$

$$\widehat{T}' + \kappa\widehat{\lambda}^2\widehat{T} = 0, \tag{38}$$

where $\nu^2 = \mu^2 - \widehat{\lambda}^2$. By applying (35) into (12), the boundary conditions become

$$\widehat{P}(a) = 0, \tag{39}$$

$$\widehat{P}'(0) = 0, \tag{40}$$

$$\widehat{Z}'(b) = 0, \tag{41}$$

$$\widehat{Z}'(0) = 0. \tag{42}$$

The solutions of (36), (37), and (38) are given by

$$\widehat{P} = \widehat{c}_1 J_0(\mu\rho) + \widehat{c}_2 Y_0(\mu\rho), \tag{43}$$

$$\widehat{Z} = \widehat{c}_3\cosh\nu(b - z) + \widehat{c}_4\sinh\nu(b - z), \tag{44}$$

$$\widehat{T} = \widehat{c}_5 e^{-\kappa\widehat{\lambda}^2 t}. \tag{45}$$

From the boundedness condition at $\rho = 0$ expressed by (40), we must have $\widehat{c}_2 = 0$. Thus the solution of (43) becomes

$$\widehat{P}(\rho) = \widehat{c}_1 J_0(\mu\rho). \tag{46}$$

From the boundary condition (41), we have

$$\widehat{Z}'(b) = -\nu\widehat{c}_4 = 0 \tag{47}$$

which implies $\widehat{c}_4 = 0$, so the solution (44) becomes

$$\widehat{Z}(z) = \widehat{c}_3\cosh\nu(b - z). \tag{48}$$

From boundary condition (39) we can determine μ. Consider

$$\widehat{P}(a) = \widehat{c}_1 J_0(\mu a) = 0 \tag{49}$$

so we have

$$\mu_m = \frac{r_m}{a}, \tag{50}$$

where r_m ($m = 1, 2, 3, \ldots$) is the mth positive root of $J_0(x) = 0$. A solution of (36) satisfying the boundary conditions is

$$\widehat{P}_m(\rho) = \widehat{c}_1 J_0\left(\frac{r_m}{a}\rho\right), \tag{51}$$

where $m = 1, 2, 3, \ldots$. From the boundary condition (42) we can determine ν. We have

$$\widehat{Z}'(0) = -\nu\widehat{c}_3\sinh\nu b = 0 \tag{52}$$

which can be satisfied only if $\sinh\nu b = 0$ or

$$\nu = \frac{k\pi i}{b} \quad k = 0, 1, 2, \ldots. \tag{53}$$

Using (53) in (48) and the fact that

$$\cosh ix = \cos x \tag{54}$$

the solution (44) becomes

$$\widehat{Z}_k(z) = \widehat{c}_3\cos\frac{k\pi}{b}(b - z). \tag{55}$$

Now from (53) and (50) it follows that

$$\widehat{\lambda}^2 = \mu^2 - \nu^2 = \left(\frac{r_m}{a}\right)^2 - \left(\frac{k\pi i}{b}\right)^2 = \frac{r_m^2}{a^2} + \frac{k^2\pi^2}{b^2}. \quad (56)$$

So a solution satisfying all boundary conditions is given by

$$\widehat{u}(\rho, z, t) = \widehat{A} e^{-\kappa(r_m^2/a^2 + k^2\pi^2/b^2)t} J_0\left(\frac{r_m}{a}\rho\right) \cos\frac{k\pi}{b}(b - z), \quad (57)$$

where $\widehat{A} = \widehat{c}_1\widehat{c}_3\widehat{c}_5$, $k = 0, 1, 2, 3, \ldots$, and $m = 1, 2, 3, \ldots$. Replacing $\widehat{A}$ with A_{km} and summing up k and m we obtain the solution by the superposition principle

$$\widehat{u}(\rho, z, t) = \sum_{k=0}^{\infty}\sum_{m=1}^{\infty} A_{km} e^{-\kappa(r_m^2/a^2 + k^2\pi^2/b^2)t} \times J_0\left(\frac{r_m}{a}\rho\right)\cos\frac{k\pi}{b}(b - z). \quad (58)$$

From the initial condition $\widehat{u}(\rho, z, 0) = \widehat{u}_0(\rho, z)$ we have

$$\left\{\sum_{k=0}^{\infty}\sum_{m=1}^{\infty} A_{km} J_0\left(\frac{r_m}{a}\rho\right)\cos\frac{k\pi}{b}(b - z)\right\} = u_0(\rho, z) - \overline{u}(\rho, z). \quad (59)$$

This can be written as

$$\sum_{k=0}^{\infty}\sum_{m=1}^{\infty} A_{km} J_0\left(\frac{r_m}{a}\rho\right)\cos\frac{k\pi}{b}(b - z) = (u_0(\rho, z) - T_w) + \sum_{m=1}^{\infty} - A_m J_0\left(\frac{r_m}{a}\rho\right)\cosh\frac{r_m}{a}(b - z), \quad (60)$$

where A_m is defined by (34). To simplify the equation, without the loss of accuracy, we consider that $u_0(\rho, z) = T_w$ which is reasonable because we start the experiment when the system is in a uniform temperature distribution. We can write (60) in this form

$$\sum_{m=1}^{\infty}\left\{\sum_{k=0}^{\infty} A_{km}\cos\frac{k\pi}{b}(b - z)\right\} J_0\left(\frac{r_m}{a}\rho\right) = \sum_{m=1}^{\infty}\left\{-A_m\cosh\frac{r_m}{a}(b - z)\right\} J_0\left(\frac{r_m}{a}\rho\right). \quad (61)$$

Clearly because of orthogonality of the Bessel functions, these coefficients have to be equal; that is,

$$\sum_{k=0}^{\infty} A_{km}\cos\frac{k\pi}{b}(b - z) = -A_m\cosh\frac{r_m}{a}(b - z). \quad (62)$$

Written in standard form, we have

$$A_{0m} + \sum_{k=1}^{\infty} A_{km}\cos\frac{k\pi}{b}(b - z) = -A_m\cosh\frac{r_m}{a}(b - z). \quad (63)$$

Recalling the *Fourier cosine series expansion* [31], the left side of (63) is the Fourier cosine series expansion of the right side with respect to $b - z$. Thus substituting $x = b - z$ and replacing A_{0m} and A_{km} with $a_0/2$ and a_k, respectively, we have

$$\frac{a_0}{2} + \sum_{k=1}^{\infty} a_k\cos\frac{k\pi}{b}x = -A_m\cosh\frac{r_m}{a}x. \quad (64)$$

So a_k for $k = 0, 1, 2, \ldots$ are given by

$$a_k = \frac{2}{b}\int_0^b \left(-A_m\cosh\frac{r_m}{a}x\right)\cos\frac{k\pi}{b}x\,dz. \quad (65)$$

Equation (65) can be written as

$$a_k = -\frac{2}{b}A_m\int_0^b \cosh\frac{r_m}{a}x\cos\frac{k\pi}{b}x\,dz \quad (66)$$

and solving the integral we have

$$a_k = -\frac{2}{b}A_m\frac{ab}{a^2k^2\pi^2 + b^2r_m^2} \times \left(ak\pi\cosh\left(\frac{r_m}{a}b\right)\sin(k\pi) + br_m\cos(k\pi)\sinh\left(\frac{r_m}{a}b\right)\right). \quad (67)$$

Since k takes only positive integers, we can simplify (67) and arrive to

$$a_k = 2A_m\frac{r_m}{ab}\frac{(-1)^{k+1}}{r_m^2/a^2 + k^2\pi^2/b^2}\sinh\left(\frac{r_m}{a}b\right). \quad (68)$$

Thus we have

$$A_{0m} = \frac{a_0}{2} = -A_m\frac{a}{br_m}\sinh\left(\frac{r_m}{a}b\right) \quad (69)$$

and A_{km} is defined by (68) as

$$A_{km} = a_k = 2A_m\frac{r_m}{ab}\frac{(-1)^{k+1}}{r_m^2/a^2 + k^2\pi^2/b^2}\sinh\left(\frac{r_m}{a}b\right), \quad (70)$$

where $k = 1, 2, \ldots$. Hence, it follows that the complete solution to the problem is given by (10), (31), and (58), where their coefficients are defined by (34), (69), and (70).

3.4. Stability Analysis. Stability analysis of the calculated model can be easily performed by studying the transient part of the general solution. A quick visit of transient equation (58) reveals that the infinite poles or eigenvalues of the system are given by the coefficients of the exponential term in infinite series as follows:

$$\text{System Poles: } -\kappa\left(\frac{r_m^2}{a^2} + \frac{k^2\pi^2}{b^2}\right), \quad (71)$$

where $k = 0, 1, 2, \ldots$ and $m = 1, 2, 3, \ldots$. Because thermal diffusivity, κ, takes only positive real values for different materials, all the poles are negative real poles, and therefore the system is stable. Calculating the slowest poles of the system using (71) and the parameters given in Table 1, we arrive to the following results:

$$\text{System Poles} = -0.14, -0.76, -1.5, -1.86, -2.11, \ldots. \quad (72)$$

Table 1: Parameter values of PCR-LOC chip model.

Parameter	Symbol	Value	Unit
Inner radius of heater	k_1	2.3	mm
Heater trace width	k_2	200	μm
Chip radius	a	4.94	mm
Chip height	b	2.10	mm
Heater power	P	0.77	W
Thermal conductivity of Borofloat glass	K	1.11	W/(m·K)
Density of Borofloat glass	$\overline{\rho}$	2200	Kg/m^3
Thermal capacity of Borofloat glass	$\mathscr{C}$	830	J/K

4. Simulation Results

The parameters with the values listed in Table 1 are used in simulation. We assume that $T_w = 22^\circ$C and that an input power of one Watt is being applied to the heater. The input to the system is given by the heat flux transferred from the heater to the system. This heat flux is considered in definition of $f(\rho)$ which by itself determines the A_m coefficients. Definition of $f(\rho)$ is given based on the chosen model configuration by the following equation:

$$f(\rho) = \begin{cases} \dfrac{q}{K} & \text{if } k_1 < \rho < (k_1 + k_2) \\ 0 & \text{otherwise,} \end{cases} \tag{73}$$

where $0 < k_1, k_2 \le a$, $0 < k_1 + k_2 \le a$, q is heat flux from the heater to chip, and K is the thermal conductivity of the chip. For discontinuities we have $f(k_1) = q/2K = f(k_1 + k_2)$. Now for A_m we can write

$$A_m = \frac{2q}{aKr_m \sinh(r_m b/a) J_1^2(r_m)} \times \int_{k_1}^{k_1+k_2} \rho J_0\left(\frac{r_m}{a}\rho\right) d\rho. \tag{74}$$

For heat flux q, we have

$$q = \frac{P}{A}, \tag{75}$$

where P is the amount of the power transferred from the heater to the chip and A is the area of the heater which can be calculated as follows:

$$A = \pi(k_1 + k_2)^2 - \pi k_1^2 = \pi k_2 (2k_1 + k_2). \tag{76}$$

Recalling the recurrence relations for the Bessel function [31], we have

$$\frac{d}{dx}\left[x^n J_n(x)\right] = x^n J_{n-1}(x) \quad (n = 1, 2, \ldots). \tag{77}$$

For $n = 1$, (77) can be written as follows:

$$\int x J_0(x)\, dx = x J_1(x) + c. \tag{78}$$

Using a change of variable, $x = (r_m/a)\rho$, for the integral part of A_m we can write

$$\int_{k_1}^{k_1+k_2} \rho J_0\left(\frac{r_m}{a}\rho\right) d\rho = \left(\frac{a}{r_m}\right)^2 \int_{(r_m/a)k_1}^{(r_m/a)(k_1+k_2)} x J_0(x)\, dx. \tag{79}$$

Using (78) in (79) we get

$$\begin{aligned} &\int_{k_1}^{k_1+k_2} \rho J_0\left(\frac{r_m}{a}\rho\right) d\rho \\ &\quad = \left(\frac{a}{r_m}\right)^2 \left[x J_1(x)\right]\Big|_{(r_m/a)k_1}^{(r_m/a)(k_1+k_2)} \\ &\quad = \frac{a}{r_m}\left((k_1 + k_2) J_1\left(\frac{r_m}{a}(k_1 + k_2)\right) - k_1 J_1\left(\frac{r_m}{a}k_1\right)\right). \end{aligned} \tag{80}$$

Taking into account (75) and (80) in (74), we have

$$\begin{aligned} A_m = 2P &\left((k_1 + k_2) J_1\left(\frac{r_m}{a}(k_1 + k_2)\right)\right. \\ &\left. - k_1 J_1\left(\frac{r_m}{a}k_1\right)\right) \\ &\times \left(\pi k_2 (2k_1 + k_2) K r_m^2 \sinh\left(\frac{r_m b}{a}\right) J_1^2(r_m)\right)^{-1}. \end{aligned} \tag{81}$$

Now we have all the required equations to calculate the temperature distribution using our analytic solution.

The next important step before start running simulations is how to compensate the error caused due to the simplification of the actual system into a single-domain model with Borofloat glass as the only material involved. Substituting the PDMS layer with a glass layer could result in a significant amount of error and mismatch between model and the actual system. To overcome this issue, we constructed an optimization problem to optimize our model parameters arriving to a best fit between single domain analytic model and multidomain actual system. Chip radius, chip thickness, and input power in the mathematical model are selected as the optimization degrees of freedom. We focus our attention on the two regions that have the highest importance. The first region is a rectangular area which starts from the left bottom side of the chamber and continues up to the top of the constant temperature wall and is all made from glass in the analytical model. We called this region comparison aperture. The second region which is a subset of comparison aperture and has higher importance is reaction chamber. To get quantitative measure of the error in both the chamber and the selected aperture, we define the following parameters in both regions: absolute average error, maximum absolute error, and uniformity of the error. The definitions of the first two measures are obvious from their naming, and the last measure is defined as follows:

$$\begin{aligned} U_{\text{ap}} &\doteq \max\left(e_{\text{ap}}(\rho, z)\right) - \min\left(e_{\text{ap}}(\rho, z)\right), \quad \rho, z \in \mathscr{D}_1, \\ U_{\text{ch}} &\doteq \max\left(e_{\text{ch}}(\rho, z)\right) - \min\left(e_{\text{ch}}(\rho, z)\right), \quad \rho, z \in \mathscr{D}_2, \end{aligned} \tag{82}$$

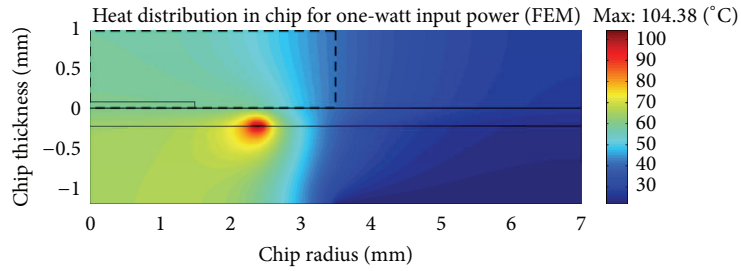

Figure 6: Steady-state temperature distribution of the cross-section of the chip calculated by the FEM. The axis of symmetry is along the left vertical side. The lines bound four domains assigned to the thermals conductivities of glass, PDMS, and water. The glass plates and PDMS layer are 1.1 mm thick and 254 m thick, respectively. The thin rectangle on the left defines the PCR chamber. The heater is located at the point of the highest temperature in red.

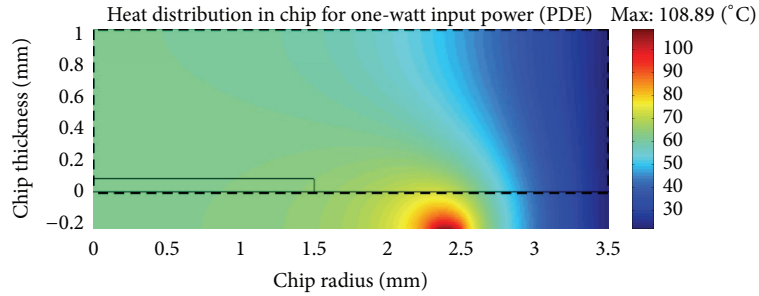

Figure 7: Steady-state temperature distribution calculated by the PDE model. The geometry of the model is a small portion of the geometry of real system and the FEM model. The area shown corresponds to the upper left part of the graph in Figure 6. The PDE model represents the system with a single material. The dashed lines indicate the location of the chamber and PDMS layer but do not define domains of different materials.

where e_{ap} is error at selected aperture indicated by $\mathscr{D}_1$ and e_{ch} is error at chamber region indicated by $\mathscr{D}_2$. Next we define our weighted-sum objective function including $\mathbb{L}_2$ norm of the error at chamber location, uniformity measure at chamber location, and uniformity measure at selected aperture as follows:

$$J = w_1 \frac{1}{A_2} \int_{A_2} {e_{ch}}^2 dA_2 + w_2 U_{ch} + w_3 U_{ap}, \tag{83}$$

where w_1, w_2, and w_3 are weight coefficients and A_2 is area of chamber region. By selecting proper weights, optimization results in a maximum absolute error of 0.14°C in chamber temperature, which is less than 0.03 of the error when compared to the results of a nonoptimized model ($a = 3.5$ mm, $b = 1.354$ mm, and $P = 1$ W), satisfy the acceptable error criteria for reliable PCR operation. Error distribution in whole aperture area is depicted in Figure 8. It is clear that, although the maximum absolute error reaches 3.6°C in the area close to the heater, the error in the chamber area is kept lower than 0.14°C.

The resulted steady-state temperature distributions based on optimized analytical solution and the FEM simulation are shown in Figures 7 and 6, respectively. Comparison aperture is indicated by dash lines. The solutions of the two results show an excellent degree of correlation, verifying accuracy of the steady-state solution.

Dynamic simulation of temperature evolution inside the reaction chamber is the next important result that we would like to study about our analytic model. Precise FEM simulations disclosed that lower center point of the chamber and upper edge of the chamber have the highest and the lowest temperatures inside the chamber, respectively (SW and NE edges of the chamber in Figure 5). The results follow the fact that upper center point of the chamber (NW edge of the chamber in Figure 5) has a temperature close to mean temperature of the chamber. We selected upper center point of the chamber to study the dynamic evolution of temperature in our model and in actual system. An input power which consisted of three predefined values that are required to take the chamber temperature to denaturation, annealing, and extension temperatures is applied to both models. Both systems were powered up after being settled in ambient temperature and kept in each power level for 60 seconds. The experiment ran over a whole PCR cycle in a 240-second interval in open-loop condition. The results are depicted in Figure 9. The optimization was performed for the lowest temperature in PCR cycle. However the error at the highest temperature is still under 1°C. Model dynamics nicely follows the FEM results, and as we expected, the transient response is about 1% faster than that of the actual system, due to the difference between the thermal properties of PDMS and Borofloat glass.

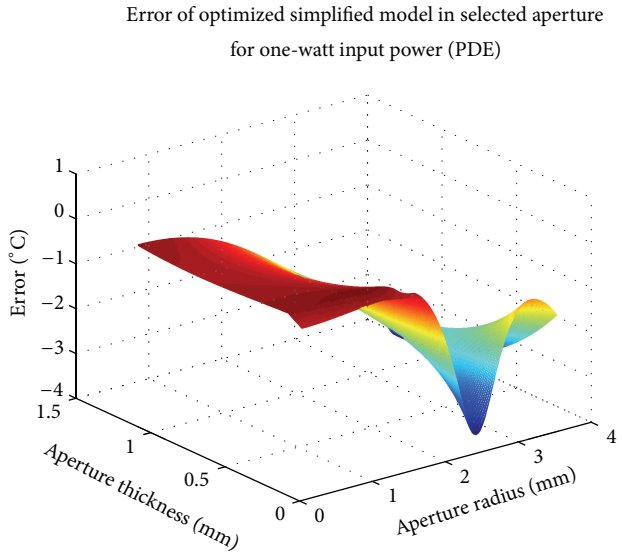

FIGURE 8: Error distribution in selected aperture after optimization. Obviously, the maximum absolute error within the selected aperture is kept under 3.6°C. It reaches to its maximum in the area close to the heater. The error in the chamber area is well kept under 0.14°C. The chamber area is a rectangular area with 0.9 mm thickness and 1.5 mm diameter just on the left bottom corner of the selected aperture.

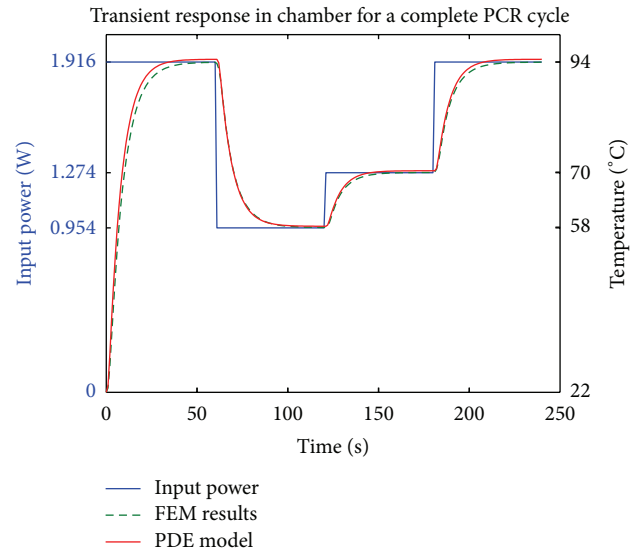

FIGURE 9: Transient response of the PDE model to a predefined input power trajectory in comparison to the FEM results. The input power represents a complete PCR cycle. There is less than 1% error in dynamic response of the derived PDE model and the complete FEM simulation.

5. Conclusion

This paper presents the derivation and the solution of the heat distribution equation of a microfluidic chip designed and manufactured at the Applied Miniaturization Laboratory at the University of Alberta, Canada. The partial differential equation featuring three-dimensional domain was used to describe the heat distribution of the chip during a DNA amplification process. The axisymmetric architecture of the chip helped reduce the domain to two-dimensional cylindrical form. The PDE equation describing the heat distribution of the chip was divided into steady-state and transient equations and then solved explicitly. Precise FEM simulations in addition to laboratory measurements were used to verify the developed model. The modeling approach is considered to be appropriate for similar thermal processes with collocated sensors and actuators. Future work is being carried out toward developing closed-loop tracking control based on boundary control techniques.

A dynamic simulation of the system was made using the developed model to confirm that the scaling of the glass thermal properties could be adjusted to match the temperature predicted by the FEM simulations at all points in the PCR chamber with less than 1°C error at all times during a PCR temperature cycle.

Conflict of Interests

The authors declare that there is no conflict of interests regarding the publication of this paper.

Acknowledgments

This work was supported by the Natural Sciences and Engineering Research Council of Canada (NSERC). The authors would like to thank S. Poshtiban, G. V. Kaigala, and J. Jiang for many helpful technical discussions.

References

[1] Y. Zhang and P. Ozdemir, "Microfluidic DNA amplification—a review," *Analytica Chimica Acta*, vol. 638, no. 2, pp. 115–125, 2009.

[2] M. Northrup, M. Ching, R. White, and R. Watson, "DNA amplification with a microfabricated reaction chamber," *Transducers*, vol. 93, p. 924, 1993.

[3] P. Wilding, M. A. Shoffner, and L. J. Kricka, "PCR in a silicon microstructure," *Clinical Chemistry*, vol. 40, no. 9, pp. 1815–1818, 1994.

[4] D. S. Yoon, Y.-S. Lee, Y. Lee et al., "Precise temperature control and rapid thermal cycling in a micromachined DNA polymerase chain reaction chip," *Journal of Micromechanics and Microengineering*, vol. 12, no. 6, pp. 813–823, 2002.

[5] M. P. Dinca, M. Gheorghe, M. Aherne, and P. Galvin, "Fast and accurate temperature control of a PCR microsystem with a disposable reactor," *Journal of Micromechanics and Microengineering*, vol. 19, no. 6, Article ID 065009, 2009.

[6] M. G. Roper, C. J. Easley, and J. P. Landers, "Advances in polymerase chain reaction on microfluidic chips," *Analytical Chemistry*, vol. 77, no. 12, pp. 3887–3893, 2005.

[7] C. Zhang, J. Xu, W. Ma, and W. Zheng, "PCR microfluidic devices for DNA amplification," *Biotechnology Advances*, vol. 24, no. 3, pp. 243–284, 2006.

[8] G. V. Kaigala, J. Jiang, C. J. Backhouse, and H. J. Marquez, "System design and modeling of a time-varying, nonlinear

temperature controller for microfluidics," *IEEE Transactions on Control Systems Technology*, vol. 18, no. 2, pp. 521–530, 2010.

[9] M. Imran and A. Bhattacharyya, "Thermal response of an on-chip assembly of RTD heaters, sputtered sample and microthermocouples," *Sensors and Actuators A*, vol. 121, no. 2, pp. 306–320, 2005.

[10] R. Pal, M. Yang, R. Lin et al., "An integrated microfluidic device for influenza and other genetic analyses," *Lab on a Chip*, vol. 5, no. 10, pp. 1024–1032, 2005.

[11] T. Yamamoto, T. Nojima, and T. Fujii, "PDMS-glass hybrid microreactor array with embedded temperature control device. Application to cell-free protein synthesis," *Lab on a Chip*, vol. 2, no. 4, pp. 197–202, 2002.

[12] B. C. Giordano, J. Ferrance, S. Swedberg, A. F. R. Hühmer, and J. P. Landers, "Polymerase chain reaction in polymeric microchips: DNA amplification in less than 240 seconds," *Analytical Biochemistry*, vol. 291, no. 1, pp. 124–132, 2001.

[13] J. J. Shah, S. G. Sundaresan, J. Geist et al., "Microwave dielectric heating of fluids in an integrated microfluidic device," *Journal of Micromechanics and Microengineering*, vol. 17, no. 11, pp. 2224–2230, 2007.

[14] S. Sundaresan, B. Polk, D. Reyes, M. Rao, and M. Gaitan, "Temperature control of microfluidic systems by microwave heating," in *Proceedings of Micro Total Analysis Systems*, vol. 1, pp. 657–659, 2005.

[15] E. Verpoorte, "Microfluidic chips for clinical and forensic analysis," *Electrophoresis*, vol. 23, no. 5, pp. 677–712, 2002.

[16] A. J. DeMello, "Control and detection of chemical reactions in microfluidic systems," *Nature*, vol. 442, no. 7101, pp. 394–402, 2006.

[17] C.-S. Liao, G.-B. Lee, H.-S. Liu, T.-M. Hsieh, and C.-H. Luo, "Miniature RT-PCR system for diagnosis of RNA-based viruses," *Nucleic Acids Research*, vol. 33, no. 18, article e156, 2005.

[18] Q. Xianbo and Y. Jingqi, "Hybrid control strategy for thermal cycling of PCR based on a microcomputer," *Instrumentation Science and Technology*, vol. 35, no. 1, pp. 41–52, 2007.

[19] V. P. Iordanov, B. P. Iliev, V. Joseph et al., "Sensorized nanoliter reactor chamber for DNA multiplication," in *Proceedings of IEEE Sensors*, pp. 229–232, October 2004.

[20] I. Erill, S. Campoy, J. Rus et al., "Development of a CMOS-compatible PCR chip: comparison of design and system strategies," *Journal of Micromechanics and Microengineering*, vol. 14, no. 11, pp. 1558–1568, 2004.

[21] V. N. Hoang, *Thermal management strategies for microfluidic devices [M.S. thesis]*, University of Alberta, 2008.

[22] P. M. Pilarski, S. Adamia, and C. J. Backhouse, "An adaptable microvalving system for on-chip polymerase chain reactions," *Journal of Immunological Methods*, vol. 305, no. 1, pp. 48–58, 2005.

[23] Z. Gao, D. Kong, and C. Gao, "Modeling and control of complex dynamic systems: applied mathematical aspects," *Journal of Applied Mathematics*, 2012.

[24] R. F. Curtain and H. Zwart, *An Introduction to Infinite-Dimensional Linear Systems Theory*, vol. 21, Springer, New York, NY, USA, 1995.

[25] P. D. Christofides, *Nonlinear and Robust Control of PDE Systems*, Birkhäuser, Boston, Mass, USA, 2001.

[26] M. Krstić and A. Smyshlyaev, *Boundary Control of PDEs: A Course on Backstepping Designs*, Society for Industrial and Applied Mathematics (SIAM), Philadelphia, Pa, USA, 2008.

[27] G. V. Kaigala, M. Behnam, C. Bliss et al., "Inexpensive, universal serial bus-powered and fully portable lab-on-a-chip-based capillary electrophoresis instrument," *IET Nanobiotechnology*, vol. 3, no. 1, pp. 1–7, 2009.

[28] G. V. Kaigala, M. Behnam, A. C. E. Bidulock et al., "A scalable and modular lab-on-a-chip genetic analysis instrument," *Analyst*, vol. 135, no. 7, pp. 1606–1617, 2010.

[29] G. V. Kaigala, V. N. Hoang, A. Stickel et al., "An inexpensive and portable microchip-based platform for integrated RT-PCR and capillary electrophoresis," *Analyst*, vol. 133, no. 3, pp. 331–338, 2008.

[30] J. H. Lienhard IV and J. H. Lienhard V, *A Heat Transfer Textbook*, Phlogiston Press, 3rd edition, 2008.

[31] R. V. Churchill and J. W. Brown, *Fourier Series and Boundary Value Problems*, McGraw-Hill, New York, NY, USA, 7th edition, 1987.

Hindawi Publishing Corporation
Journal of Applied Mathematics
Volume 2013, Article ID 792196, 10 pages
http://dx.doi.org/10.1155/2013/792196

Research Article

Block Empirical Likelihood for Longitudinal Single-Index Varying-Coefficient Model

Yunquan Song,[1,2] Ling Jian,[2] and Lu Lin[1]

[1] *Shandong University Qilu Securities Institute for Financial Studies and School of Mathematics, Shandong University, Jinan 250100, China*
[2] *College of Science, China University of Petroleum, Qingdao 266580, China*

Correspondence should be addressed to Lu Lin; linlu@sdu.edu.cn

Received 26 May 2013; Revised 15 August 2013; Accepted 15 August 2013

Academic Editor: Zhiwei Gao

Copyright © 2013 Yunquan Song et al. This is an open access article distributed under the Creative Commons Attribution License, which permits unrestricted use, distribution, and reproduction in any medium, provided the original work is properly cited.

In this paper, we consider a single-index varying-coefficient model with application to longitudinal data. In order to accommodate the within-group correlation, we apply the block empirical likelihood procedure to longitudinal single-index varying-coefficient model, and prove a nonparametric version of Wilks' theorem which can be used to construct the block empirical likelihood confidence region with asymptotically correct coverage probability for the parametric component. In comparison with normal approximations, the proposed method does not require a consistent estimator for the asymptotic covariance matrix, making it easier to conduct inference for the model's parametric component. Simulations demonstrate how the proposed method works.

1. Introduction

The single-index varying-coefficient model which was proposed by Huang and Zhensheng [1] is a very important tool to explore the dynamic pattern in many complex dynamic systems, such as economics, finance, politics, epidemiology, medical science, and ecology. As mentioned in Gao et al. [2], the concept of complex dynamic systems arises in many varieties. Such systems are often concurrent and distributed, because they have to react to various kinds of events, signals, and conditions. They may be characterized by a system with uncertainties, time delays, stochastic perturbations, hybrid dynamics, distributed dynamics, chaotic dynamics, and a large number of algebraic loops. Moreover, many related literatures, such as Jian et al. [3] and Hu et al. [4], have been proposed. The single-index varying-coefficient models is one method that can be used to describe the complex dynamic systems. They are natural extensions of classical parametric models with good interpretability and are becoming more and more popular in data analysis.

Longitudinal data arise frequently in many scientific studies. For longitudinal data, we know that the data that are collected from the same subject at different times are correlated and that the observations from different subjects are often independent. Therefore, it is of great interest to estimate the regression function incorporating the within-subject correlation to improve the efficiency of estimation. The single-index varying-coefficient model is a popular nonparametric fitting technique; it is easily interpreted in real applications because it has the features of the single-index model and the varying-coefficient model. In addition, the single-index varying-coefficient model may include cross-product terms of some components of covariates. Hence, it has considerable flexibility to cater for a complex multivariate nonlinear structure.

Without loss of generality, we consider a longitudinal study with N subjects and n_i observations over time for the ith subject ($i = 1, \ldots, N$) with a total of $n = \sum_{i=1}^{N} n_i$ observations. In this article, we apply longitudinal data to a single-index varying-coefficient model, and propose a single-index varying-coefficient longitudinal data model of the form

$$y_{ij} = g^T\left(\beta^T x_{ij}\right) z_{ij} + \varepsilon_{ij}, \quad i = 1, \ldots, N; \; j = 1, \ldots, n_i, \quad (1)$$

where $(x_{ij}, z_{ij}) \in R^p \times R^q$ is a vector of covariates, y_{ij} is the jth measurement on the ith unit, β is an $p \times 1$ vector of unknown

parameters, $g(\cdot)$ is an $q \times 1$ vector of unknown functions, and ε_{ij} is a random error with mean 0 and finite variance σ^2, assuming that ε_{ij} and (x_{ij}, z_{ij}) are independent. For the sake of identifiability, it is often assumed that $\|\beta\| = 1$ and the first nonzero element is positive, where $\|\cdot\|$ denotes the Euclidean metric.

Obviously, model (1) includes a class of important statistical models. For example, if $q = 1$ and $z_{ij} = 1$, model (1) reduces to the single-index longitudinal data model which was proposed by Bai et al. [5] to estimate the index coefficient and unknown link function in a single-index model for longitudinal data by combining penalized splines and quadratic inference functions. If $p = 1$ and $\beta = 1$, (1) is the varying-coefficient longitudinal data model studied by Chiang et al. [6], Huang et al. [7], and Qu and Li [8], among others. So model (1) is easily interpreted in real applications because it has the features of the single-index longitudinal data model and the varying-coefficient longitudinal data model. In addition, model (1) may include cross-product terms of some components of x_{ij} and z_{ij}. Hence, it has considerable flexibility to cater for complex multivariate nonlinear structure.

When $n_i = 1$, model (1) reduces to the nonlongitudinal single-index varying-coefficient model. Some authors have studied the estimation and application of the model. Recently, empirical likelihood methods have been applied to nonlongitudinal single-index varying-coefficient model. For example, Xue and Wang [9] developed statistical techniques for the unknown coefficient functions and single-index parameters in the single-index varying-coefficient models. They first estimate the nonparametric component via the local linear fitting, then construct an estimated empirical likelihood ratio function, and hence obtain a maximum empirical likelihood estimator for the parametric component. The motivation is that empirical likelihood based inference has many desirable statistical properties. For example, this method does not involve any variance estimation which is rather complicated in nonparametric or semiparametric regression settings and hence are robust against the heteroscedasticity; confidence region based on the empirical likelihood method does not have predetermined symmetry so that it can better correspond to the true shape of the underlying distribution, and so on. Owen [10, 11] and many others developed this into a general methodology. For example, Wang and Jing [12], Chen and Qin [13], Shi and Lau [14], and Xue and Zhu [15–17], among others. A recent survey on empirical likelihood can be found in the monograph of Owen [18]. More methods about the single-index varying-coefficient model have been proposed, such as Huang and Zhang [19] and Feng and Xue [20]. When $n_i > 1$, model (1) is the single-index longitudinal data model. The usual empirical likelihood method cannot be applied, however, to the single-index longitudinal data model (1) due to correlation within groups. In this paper, we propose a block empirical likelihood procedure to accommodate this correlation. A nonparametric version of the Wilks' theorem is derived, which can be used to construct confidence regions with asymptotically correct coverage probabilities for the parametric component in the model. Compared with normal approximations, our method has the appealing feature that it does not require one to construct a consistent estimator for the asymptotic covariance matrix. Furthermore, the block empirical likelihood method avoids intensive Monte Carlo simulations usually required by the bootstrap method.

The rest of the paper is organized as follows. Section 2 introduces the estimated block empirical likelihood method. Section 3 derives the nonparametric version of Wilks' theorem. Section 4 provides a data-driven procedure to choose the tuning parameters. A simulation study is given in Section 5. Proof of the main result is relegated to Section 6.

2. Block Empirical Likelihood Method

In this section, we are to extend the results of You et al. [21] and Xue and Wang [9] to the single-index varying-coefficient longitudinal data model.

To apply the block empirical likelihood method to model (1), we introduce an auxiliary random vector

$$\eta_{ij}(\beta) = \left\{y_{ij} - g^T\left(\beta^T x_{ij}\right) z_{ij}\right\} \dot{g}^T\left(\beta^T x_{ij}\right) z_{ij} x_{ij} \omega\left(\beta^T x_{ij}\right), \tag{2}$$

where $\dot{g}(\cdot)$ stands for the derivative of the function vector $g(\cdot)$, and $\omega(\cdot)$ is a bounded weight function with a bounded support $\mathcal{U}_\omega$, which is introduced to control the boundary effect in the estimations of $g(\cdot)$ and $\dot{g}(\cdot)$. For convenience, we pointed that $\omega(\cdot)$ is the indicator function of the set $\mathcal{U}_\omega$. Note that $E\{\eta_{ij}(\beta)\} = 0$ if $\beta = \beta_0$. Hence, the problem of testing whether β is the true parameter is equivalent to testing whether $E\{\eta_{ij}(\beta)\} = 0$, for $i = 1, \ldots, N$; $j = 1, \ldots, n_i$. Because of the unknowns $g(\cdot)$ and $\dot{g}(\cdot)$, we cannot directly use the block empirical likelihood method to make statistical inference on β. A natural way is to replace $g(\cdot)$ and $\dot{g}(\cdot)$ by their estimators. In this paper, we estimate the vector functions $g(\cdot)$ and $\dot{g}(\cdot)$ via the local linear regression technique (see, e.g., Fan and Gijbels [22]). The local linear estimators for $g(u)$ and $\dot{g}(u)$ are defined as $\widehat{g}(u;\beta) = \widehat{a}$ and $\widehat{\dot{g}}(u;\beta) = \widehat{b}$ at the fixed point β_0, where $\widehat{a}$ and $\widehat{b}$ minimize the sum of weighted squares:

$$\sum_{i=1}^{N}\sum_{j=1}^{n_i}\left[y_{ij} - \left\{a + b\left(\beta^T x_{ij} - u\right)\right\}^T z_{ij}\right]^2 K_h\left(\beta^T x_{ij} - u\right), \tag{3}$$

where $K_h(\cdot) = h^{-1}K(\cdot/h)$, $K(\cdot)$ is a kernel function, and $h = h_n$ is a bandwidth sequence that decreases to 0 as n increase to ∞. It follows from the least squares theory that

$$\left(\widehat{g}^T(u;\beta), h\widehat{\dot{g}}^T(u;\beta)\right)^T = S_n^{-1}(u;\beta)\,\xi_n(u;\beta), \tag{4}$$

where

$$S_n(u;\beta) = \begin{pmatrix} S_{n,0}(u;\beta) & S_{n,1}(u;\beta) \\ S_{n,1}(u;\beta) & S_{n,2}(u;\beta) \end{pmatrix},$$
$$\xi_n(u;\beta) = \begin{pmatrix} \xi_{n,0}(u;\beta) & \xi_{n,1}(u;\beta) \\ \xi_{n,1}(u;\beta) & \xi_{n,2}(u;\beta) \end{pmatrix} \tag{5}$$

with

$$S_{n,k}(u;\beta) = \frac{1}{n}\sum_{i=1}^{N}\sum_{j=1}^{n_i} z_{ij} z_{ij}^T \left(\frac{\beta^T x_{ij} - u}{h}\right)^k K_h\left(\beta^T x_{ij} - u\right),$$

$$\xi_{n,k}(u;\beta) = \frac{1}{n}\sum_{i=1}^{N}\sum_{j=1}^{n_i} z_{ij} y_{ij} \left(\frac{\beta^T x_{ij} - u}{h}\right)^k K_h\left(\beta^T x_{ij} - u\right). \tag{6}$$

Remark 1. Since the convergence rate of the estimator of $\dot{g}_0'(u)$ is slower than that of the estimator of $g_0(u)$ if the same bandwidth is used, this leads to a slower convergence rate for the estimator $\widehat{\beta}$ of β than $\sqrt{n}$. To increase the convergence rate of the estimator of $\dot{g}_0'(u)$, we introduce the another bandwidth h_1 to replace h in $\widehat{\dot{g}}(u;\beta)$ and define it as $\widehat{\dot{g}}_{h_1}(u;\beta)$.

Similar to Owen [11] and Shi and Lau [14], $\{\widehat{r}_{ij}(\beta) = y_{ij} - \widehat{g}^T(\beta^T x_{ij}) z_{ij},\ i = 1,\ldots,N;\ j = 1,\ldots,n_i\}$ can be treated as a random sieve approximation of the random error sequence $\{\varepsilon_{ij},\ i = 1,\ldots,N;\ j = 1,\ldots,n_i\}$. In order to deal with the correlation within groups, we use the block empirical likelihood procedure proposed by You et al. [21]. Unlike the usual empirical likelihood method, the block empirical likelihood procedure takes the "data" $\widehat{r}_{ij}(\beta)$ for $j = 1,\ldots,n_i$ into account as a whole. Let $\widehat{\eta}_{ij}(\beta) = \widehat{r}_{ij}(\beta)\widehat{\dot{g}}^T(\beta^T x_{ij}) z_{ij} x_{ij} \omega(\beta^T x_{ij})$ be $\eta_{ij}(\beta)$, with $g(\beta^T x_{ij})$ and $\dot{g}(\beta^T x_{ij})$ replaced by $\widehat{g}(\beta^T x_{ij};\beta)$ and $\widehat{\dot{g}}(\beta^T x_{ij};\beta)$, respectively, for $i = 1,\ldots,N;\ j = 1,\ldots,n_i$. Then an estimated block empirical likelihood function for β is defined as

$$\widehat{L}(\beta) = \max\left\{\prod_{i=1}^{n} p_i \mid p_i \geq 0, \sum_{i=1}^{k} p_i = 1, \sum_{i=1}^{k} p_i \sum_{j=1}^{n_i} \widehat{\eta}_{ij}(\beta) = 0\right\}. \tag{7}$$

For a given β a unique maximum exists, provided that 0 is inside the convex hull of the points $\sum_{j=1}^{n_i} \eta_{ij}(\beta)$ for $i = 1,\ldots,N$. The maximum of (7) may be found via the method of Lagrange multipliers. The optimal value for p_i satisfying (7) may be shown to be

$$p_i = \frac{1}{N} \times \frac{1}{1 + \lambda^T \sum_{j=1}^{n_i} \widehat{\eta}_{ij}(\beta)}, \tag{8}$$

where the Lagrange multiplier $\lambda = (\lambda_1,\ldots,\lambda_p)^T$ is the solution of the following equation:

$$0 = \frac{1}{N}\sum_{i=1}^{N} \frac{\sum_{j=1}^{n_i} \widehat{\eta}_{ij}(\beta)}{1 + \lambda^T \sum_{j=1}^{n_i} \widehat{\eta}_{ij}(\beta)}. \tag{9}$$

Since $p_1 \times \cdots \times p_N$ is maximized for $p_i = 1/N$ in the absence of parametric constraints, we define the corresponding estimated profile block empirical log-likelihood ratio as

$$\widehat{l}(\beta) = -\sum_{i=1}^{N} \log\left[1 + \lambda^T \sum_{j=1}^{n_i} \widehat{\eta}_{ij}(\beta)\right]. \tag{10}$$

We will show in the next section that if β_0 is the true parameter vector, $\widehat{l}(\beta_0)$ is asymptotically chi-square distributed.

3. Theoretical Properties

Throughout this article, we assume that N increases to push up the total sample size $n = n_1 + \cdots + n_N$, while the n_i is fixed. To establish the nonparametric Wilks' theorem for $LR(\beta_0)$, we first make the following assumptions.

(A.1) The density function of $\beta^T x_{ij}$, $f(u)$, is bounded away from zero for $u \in \mathcal{U}_\omega$ and β near β_0 and satisfies the Lipschitz condition of order 1 on $\mathcal{U}_\omega$, where $\mathcal{U}_\omega$ is the support of $\omega(u)$.

(A.2) The function $g_k(u), 1 \leq k \leq q$, have continuous second derivatives on $\mathcal{U}_\omega$, where $g_k(u)$ are the kth components of $g(u)$.

(A.3) $E(\|x_{ij}\|^6) < \infty$, $E(\|z_{ij}\|^6) < \infty$, and $E(|\varepsilon_{ij}|^6) < \infty$.

(A.4) $Nh^2/(\log N)^2 \to \infty$, $Nh^4 \log N \to 0$; $Nhh_1^3/(\log N)^2 \to \infty$, $Nh_1^5 = O(1)$.

(A.5) The kernel $K(\cdot)$ is a symmetric probability density function with a bounded support and satisfies the Lipschitz condition of order 1 and $\int u^2 K(u)du \neq 0$.

(A.6) The matrix $D(u) = E(z_{ij} z_{ij}^T \mid \beta_0^T x_{ij} = u)$ is positive definite, and each entry of $D(u)$ and $C(u) = E(v_{ij} z_{ij}^T \mid \beta_0^T x_{ij} = u)$ satisfies the Lipschitz condition of order 1 on $\mathcal{U}_\omega$, where $v_{ij} = x_{ij}\dot{g}_0^T(\beta_0^T x_{ij}) z_{ij} \omega(\beta_0^T x_{ij})$, and $\mathcal{U}_\omega$ is defined in (A.1).

(A.7) The matrices $B(\beta_0) = E(v_{ij} v_{ij}^T)$ and $B_*(\beta_0) = B(\beta_0) - E\{C(\beta_0^T x_{ij})\dot{g}_0(\beta_0^T x_{ij}) E(x_{ij}^T \mid \beta_0^T x_{ij})\}$ are positive definite, where v_{ij} is defined in (A.6).

Remark 2. Condition (A.1) is used to bound the density function of $\beta^T x_{ij}$ away from zero. This ensures that the denominators of $\widehat{g}(u;\beta)$ and $\widehat{\dot{g}}(u;\beta)$ are, in probability one, bounded away from 0 for $u \in \mathcal{U}_\omega$. The second derivatives in (A.2) are standard smoothness conditions. (A.3)–(A.5) are necessary conditions for the asymptotic normality or the uniform consistency of the estimators. It should be pointed out that the condition can be replaced by $E(\|x_{ij}\|^{6+\delta}) < \infty$, $E(\|z_{ij}\|^{6+\delta}) < \infty$, and $E(|\varepsilon_{ij}|^{6+\delta}) < \infty$ for some $\delta > 0$. In the current work, the exponential index of the norm is set as 6 for it is the minimum value to meet the asymptotic normality or the uniform consistency of the estimators. Conditions (A.6) and (A.7) ensure that the asymptotic variance for the estimator of β_0 exists.

Let $\mathcal{B} = \{\beta \in R^p : \|\beta\| = 1$, and the first nonzero element is positive$\}$. Then β_0 is an inner point of set $\mathcal{B}$. The following theorem shows that $-2\widehat{l}(\beta_0)$ is asymptotically distributed as a weighted sum of independent χ_1^2 variables.

Theorem 3. *Suppose that (A.1)–(A.7) hold, then as* $N \to \infty$,

$$-2\widehat{l}(\beta_0) \xrightarrow{D} \omega_1 \chi^2_{1,1} + \cdots + \omega_p \chi^2_{1,p}, \tag{11}$$

where $\xrightarrow{D}$ *represents convergence in distribution,* $\chi^2_{1,1}, \ldots, \chi^2_{1,p}$ *are independent* χ^2_1 *variables, and the weights* ω_j, *for* $1 \le j \le p$, *are the eigenvalues of* $G(\beta_0) = B^{-1}(\beta_0)A(\beta_0)$. *Here* $B(\beta_0)$ *is defined in condition (A.7),*

$$A(\beta_0) = B(\beta_0) - E\left\{C\left(\beta_0^T x_{ij}\right) D^{-1}\left(\beta_0^T x_{ij}\right) C^T\left(\beta_0^T x_{ij}\right)\right\}, \tag{12}$$

and $C(u)$ *and* $D(u)$ *are defined in condition (A.6).*

To apply Theorem 3 to construct a confidence region or interval for β_0, we need to consistently estimate the unknown weights ω_j. By the plug-in method, $A(\beta_0)$ and $B(\beta_0)$ can be consistently estimated by

$$\widehat{A}\left(\widehat{\beta}\right) = \frac{1}{N}\sum_{i=1}^{N}\sum_{j=1}^{n_i}\left\{\widehat{v}_{ij}\widehat{v}_{ij}^T - \widehat{C}\left(\widehat{\beta}^T x_{ij}\right)\widehat{D}^{-1}\left(\widehat{\beta}^T x_{ij}\right)\widehat{C}^T\left(\widehat{\beta}^T x_{ij}\right)\right\}, \tag{13}$$

$$\widehat{B}\left(\widehat{\beta}\right) = \frac{1}{N}\sum_{i=1}^{N}\sum_{j=1}^{n_i}\widehat{v}_{ij}\widehat{v}_{ij}^T, \tag{14}$$

respectively, where $\widehat{\beta}$ is the maximum empirical likelihood estimator of β_0 defined by (9), $\widehat{v}_{ij} = x_{ij}\widehat{g}^T(\widehat{\beta}^T x_{ij}; \widehat{\beta})z_{ij}\omega(\widehat{\beta}^T x_{ij})$, $\widehat{C}(\cdot) = \sum_{i=1}^{n} W_{ni}(\cdot)\widehat{v}_{ij}z_{ij}^T$, and $\widehat{D}(\cdot) = \sum_{i=1}^{n} W_{ni}(\cdot)z_{ij}z_{ij}^T$ with

$$W_{nij}(\cdot) = \frac{K_1\left(\widehat{\beta}^T x_{ij} - \cdot/b_n\right)}{\sum_{k=1}^{N}\sum_{l=1}^{nk} K_1\left(\widehat{\beta}^T x_{kl} - \cdot/b_n\right)}, \tag{15}$$

where $K_1(\cdot)$ is a kernel function, and b_n is bandwidth with $0 < b_n \to 0$.

This implies that the eigenvalues of $\widehat{G}(\widehat{\beta}) = \widehat{B}^{-1}(\widehat{\beta})\widehat{A}(\widehat{\beta})$, say $\widehat{\omega}_j$, consistently estimate ω_j for $j = 1, \ldots, p$. Let $\widehat{c}_{1-\alpha}$ be the $1-\alpha$ quantile of the conditional distribution of the weighted sum $\widehat{s} = \widehat{\omega}_1\chi^2_{1,1} + \cdots + \widehat{\omega}_p\chi^2_{1,p}$ given the data. Then an approximate $1-\alpha$ confidence region for β_0 can be defined as follows:

$$\mathscr{R}(\alpha) = \left\{\beta \in \mathscr{B} : -2\widehat{l}(\beta) \le \widehat{C}_{1-\alpha}\right\}. \tag{16}$$

In practice, the conditional distribution of the weighted sum $\widehat{s}$, given the sample $\{(y_{ij}, x_{ij}, z_{ij}), 1 \le i \le N; 1 \le j \le n_i\}$, can be calculated using Monte Carlo simulations by repeatedly generating independent samples $\chi^2_{1,1}, \ldots, \chi^2_{1,p}$ from the χ^2_1 distribution.

In addition to the above, direct way of approximating the asymptotic distributions, we can also consider the following alternative. The alternative is motivated by the results of Rao and Scott [24]. Now, we propose another adjusted empirical log-likelihood, whose asymptotic distribution is chi-squared with p degrees of freedom. The adjustment technique is developed by Wang and Rao [25] by using an approximate result in Rao and Scott [24]. Note that $\widehat{\rho}(\beta)$ can be written as

$$\widehat{\rho}(\beta) = \frac{\operatorname{tr}\left\{\widehat{A}^{-}(\beta)\widehat{A}(\beta)\right\}}{\operatorname{tr}\left\{\widehat{B}^{-1}(\beta)\widehat{A}(\beta)\right\}}. \tag{17}$$

By examining the asymptotic expansion of $-2\widehat{l}(\beta)$, which is specified in the proof of Theorem 4 below, we define an adjustment factor

$$\widehat{r}(\beta) = \frac{\operatorname{tr}\left\{\widehat{A}^{-}(\beta)\widehat{\Sigma}(\beta)\right\}}{\operatorname{tr}\left\{\widehat{B}^{-1}(\beta)\widehat{\Sigma}(\beta)\right\}}, \tag{18}$$

by replacing $\widehat{A}(\beta)$ in $\widehat{\rho}(\beta)$ by $\widehat{\Sigma}(\beta)$, where $\widehat{\Sigma}(\beta) = \{\sum_{i=1}^{N}\sum_{j=1}^{n_i}\widehat{\eta}_{ij}(\beta)\}\{\sum_{i=1}^{N}\sum_{j=1}^{n_i}\widehat{\eta}_{ij}(\beta)\}^T$. The adjusted empirical log-likelihood ration is defined by

$$\widehat{l}_a(\beta) = \widehat{r}(\beta)\left\{-2\widehat{l}(\beta)\right\}, \tag{19}$$

where $\widehat{l}(\beta)$ is defined in (10).

Theorem 4. *Suppose that conditions (A.1)–(A.6) hold. Then,* $\widehat{l}_a(\beta) \xrightarrow{D} \chi^2_p$.

According to Theorem 4, $\widehat{l}_a(\beta)$ can be used to construct an approximate confidence region for β_0. Let

$$\mathscr{R}_a(\alpha) = \left\{\beta \in \mathscr{B} : \widehat{l}_a(\beta) \le \chi^2_p(1-\alpha)\right\}. \tag{20}$$

Then, $\mathscr{R}_a(\alpha)$ gives a confidence region for β_0 with asymptotically correct coverage probability $1-\alpha$.

4. Bandwidth Selection

For practical implementation, the tuning parameters need to be decided. We employ a data-driven procedure to choose the tuning parameter h, where h controls the smoothness of $\widehat{g}(\cdot)$ and $\widehat{\widehat{g}}(\cdot)$. We all know that various existing bandwidth selection techniques for nonparametric regression, such as the cross-validation, generalized cross-validation, and the modified multifold cross-validation criterion, can be adapted for the estimation $\widehat{g}(\cdot)$ and $\widehat{\widehat{g}}(\cdot)$. Because the algorithm of the modified multifold cross-validation criterion proposed by Cai et al. [26] to select the optimal bandwidth is simple and quick, throughout the empirical studies in this paper, we consider the modified multifold cross-validation criterion. Specifically, let m and M be two given positive integers and $n > mM$. The basic idea is first to use M subseries of lengths $n - km$ $(k = 1, \ldots, M)$ to estimate the unknown coefficient functions and then to compute the one-step forecasting error of the next section of the sample of length m based on

the estimated models. More precisely, we choose h which minimizes

$$\mathrm{AMS}(h) = \sum_{k=1}^{M} \frac{1}{m} \sum_{i=n-km+1}^{n-km+m} \sum_{j=1}^{n_i} \left\{ y_{ij} - \sum_{l=1}^{q} \widehat{g}_{l,k}\left(\beta^T x_{ij}\right) z_{ij}^{(l)} \right\}^2, \tag{21}$$

where $\widehat{g}_{l,k}(\cdot)$ are computed from the sample $\{(y_{ij}, x_{ij}, z_{ij}), 1 \le i \le n - km; 1 \le j \le n_i\}$ with bandwidth equal to $h(n/(n-km))^{1/5}$. Note that for different sample size, we rescale bandwidth according to its optimal rate, that is, $h \propto n^{-1/5}$. Since the selected bandwidth does not depend critically on the choice of m and M, to computation expediency, we take $m = [0.1n]$ and $M = 5$ in our simulation.

Let h_{opt} be the bandwidth obtained by minimizing (21) with respect to $h > 0$; that is, $h_{\mathrm{opt}} = \inf_{h>0} \mathrm{AMS}(h)$. Then h_{opt} is the optimal bandwidth for estimating $\widehat{g}(\cdot)$. When calculating the block empirical likelihood ratios and estimator of β_0, we use the approximation bandwidth

$$h = h_{\mathrm{opt}} n^{-1/20} (\log n)^{-1/2}, \qquad h_1 = h_{\mathrm{opt}}, \tag{22}$$

because this insures that the required bandwidth has correct order of magnitude for the optimal asymptotic performance (see, e.g., Carroll et al. [27]), and the bandwidth $\widehat{h}$ satisfies condition (A.4).

5. A Simulation Study

In this section, we carry out some simulations to study the finite sample performance of the estimated block empirical likelihood method.

Example 5. The data are generated from

$$Y_{ij} = g_0\left(\beta X_{ij}\right) + g_1\left(\beta X_{ij}\right) Z_{ij} + \varepsilon_{ij}, \quad i = 1, \ldots, N, \quad j = 1, \ldots, n_i, \tag{23}$$

where $X_{ij} \sim N(0,1)$, $Z_{ij} \sim N(0,1)$, $g(t) = \sin(2\pi t)$, $\varepsilon_{ij} = a\varepsilon_{i,j-1} + e_{ij}$, and $e_{ij}'s$ are i.i.d $N(0,1)$. For each combination of N, n_i, and a, 1000 samples are generated from the above model in all simulations. For each sample, a 95% confidence interval for $\beta = 2$ are computed using our estimated block empirical likelihood method. For the smoother, we used a local linear smoother with the Gaussian kernel $K_h(t) = (1/h\sqrt{2\pi}) \exp(-t^2/2h^2)$ with a modified multifold cross-validation criterion bandwidth throughout all smoothing steps. Some representative coverage probabilities and coverage confidence intervals are reported in Table 1. Simulation results show that our estimated block empirical likelihood confidence regions have high coverage probabilities and short average confidence interval lengths.

Example 6. Consider the regression model

$$Y_{ij} = g_0\left(\beta_0^T X_{ij}\right) + g_1\left(\beta_0^T X_{ij}\right) Z_{ij}^{(1)} + g_2\left(\beta_0^T X_{ij}\right) Z_{ij}^{(2)} + \varepsilon_{ij}, \tag{24}$$

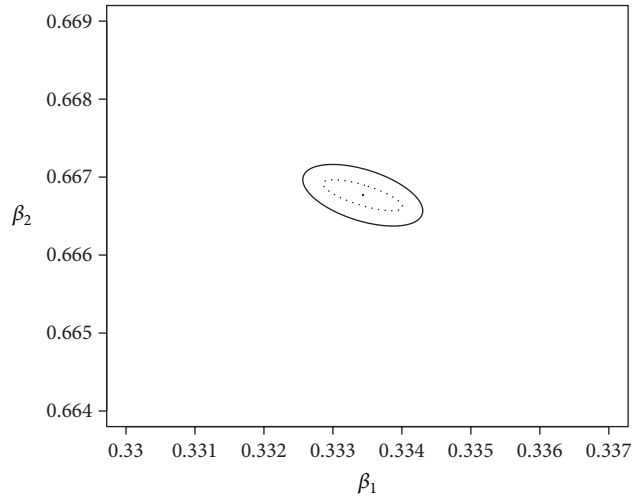

Figure 1: Averages of 95% confidence regions of (β_1, β_2), based on EEL (solid curve) and AEL (dashed curve) when $n = 100$ in the cases of Example 6.

where $\beta_0 = (1/3, 2/3)$ and the $\varepsilon_{ij}s$ are independent $N(0, 1^2)$ random variables. The sample $\{X_{ij} = (X_{ij}^{(1)}, X_{ij}^{(2)})^T; 1 \le i \le N,\ 1 \le j \le n_i\}$ was generated from a bivariate uniform distribution on $[-1, 1]^2$ with independent components, $\{Z_{ij} = (Z_{ij}^{(1)}, Z_{ij}^{(2)})^T; 1 \le i \le N, 1 \le j \le n_i\}$ was generated from a bivariate normal distribution $N(0, \Sigma)$ with $\mathrm{var}(Z_{ij}^{(1)}) = \mathrm{var}(Z_{ij}^{(2)}) = 1$, and correlation coefficient between $Z_{ij}^{(1)}$ and $Z_{ij}^{(2)}$ is $\rho = 0.5$. In model (24), the coefficient functions are $g_0(u) = 8\exp(-2u^2)$, $g_1(u) = 6u^2$ and $g_2(u) = 4\sin(\pi u)$.

For the smoother, we use a local linear smoother with a Gaussian kernel $K_h(u) = (1/h\sqrt{2\pi}) \exp(-u^2/2h^2)$, and use the modified multifold cross-validation criterion proposed by Cai et al. [26] to select the optimal bandwidth throughout all smoothing steps because the algorithm is simple and quick. We take the weight function $\omega(u) = I_{[-1,1]}$. The sample size for the simulated data is 100, and the run is 1000 times in all simulations.

The confidence regions of β_0 and their coverage probabilities, with nominal level $1 - \alpha = 0.95$, were computed from 1000 runs. The estimated block empirical likelihood was used to construct the confidence regions. The simulated results are given in Figure 1. Simulation results show that our block empirical likelihood confidence regions have high coverage probabilities and short average confidence interval lengths.

The histograms of the 1000 estimators of the parameters β_1 and β_2 are in Figures 2(a) and 2(b), respectively. The Q-Q plots of the 1000 estimators of the parameters β_1 and β_2 are in Figures 3(a) and 3(b), respectively. Figures 2 and 3 show empirically that these estimators are asymptotically normal. The means of the estimates of the unknown parameters β_1 and β_2 are 0.33342 and 0.66673, respectively, and their biases (standard deviations) are 0.000128 (0.00308) and 0.000603 (0.00352), respectively.

Table 1: The selection probabilities of adaptive EL shrinkage estimation.

N	Number of replicates	CI	CP
	$a = 0.2$		
50	$n_1 = \cdots = n_{25} = 4, n_{26} = \cdots = n_{50} = 4$	[1.645015, 2.349996]	0.9372
50	$n_1 = \cdots = n_{25} = 4, n_{26} = \cdots = n_{50} = 5$	[1.634619, 2.355068]	0.9270
100	$n_1 = \cdots = n_{25} = 4, n_{26} = \cdots = n_{100} = 4$	[1.634619, 2.355068]	0.9343
100	$n_1 = \cdots = n_{25} = 4, n_{26} = \cdots = n_{100} = 5$	[1.634619, 2.355068]	0.9424
	$a = 0.4$		
50	$n_1 = \cdots = n_{25} = 4, n_{26} = \cdots = n_{50} = 4$	[1.634619, 2.355068]	0.9428
50	$n_1 = \cdots = n_{25} = 4, n_{26} = \cdots = n_{50} = 5$	[1.634619, 2.355068]	0.9334
100	$n_1 = \cdots = n_{25} = 4, n_{26} = \cdots = n_{100} = 4$	[1.634619, 2.355068]	0.9427
100	$n_1 = \cdots = n_{25} = 4, n_{26} = \cdots = n_{100} = 5$	[1.634619, 2.355068]	0.9351

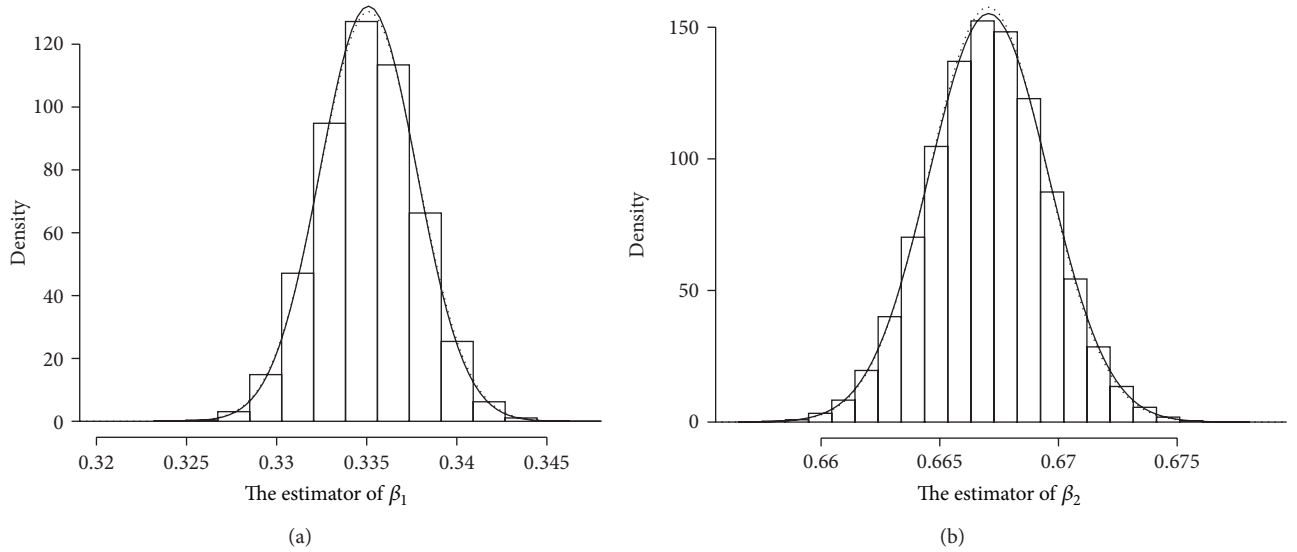

Figure 2: The histograms of the 1000 estimators of every parameter, the estimated curve of density (solid curve) and the curve of normal density (dased curve): (a) for β_1 and (b) for β_2.

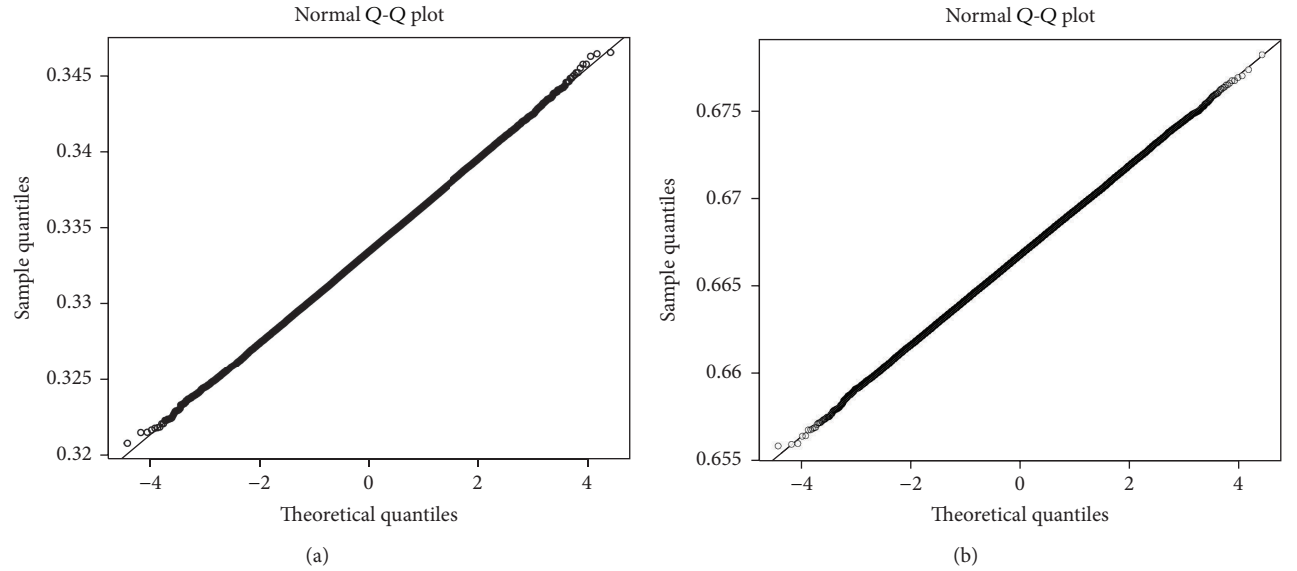

Figure 3: (a) for β_1 and (b) for β_2: the Q-Q plot of the 1000 estimators of every parameter.

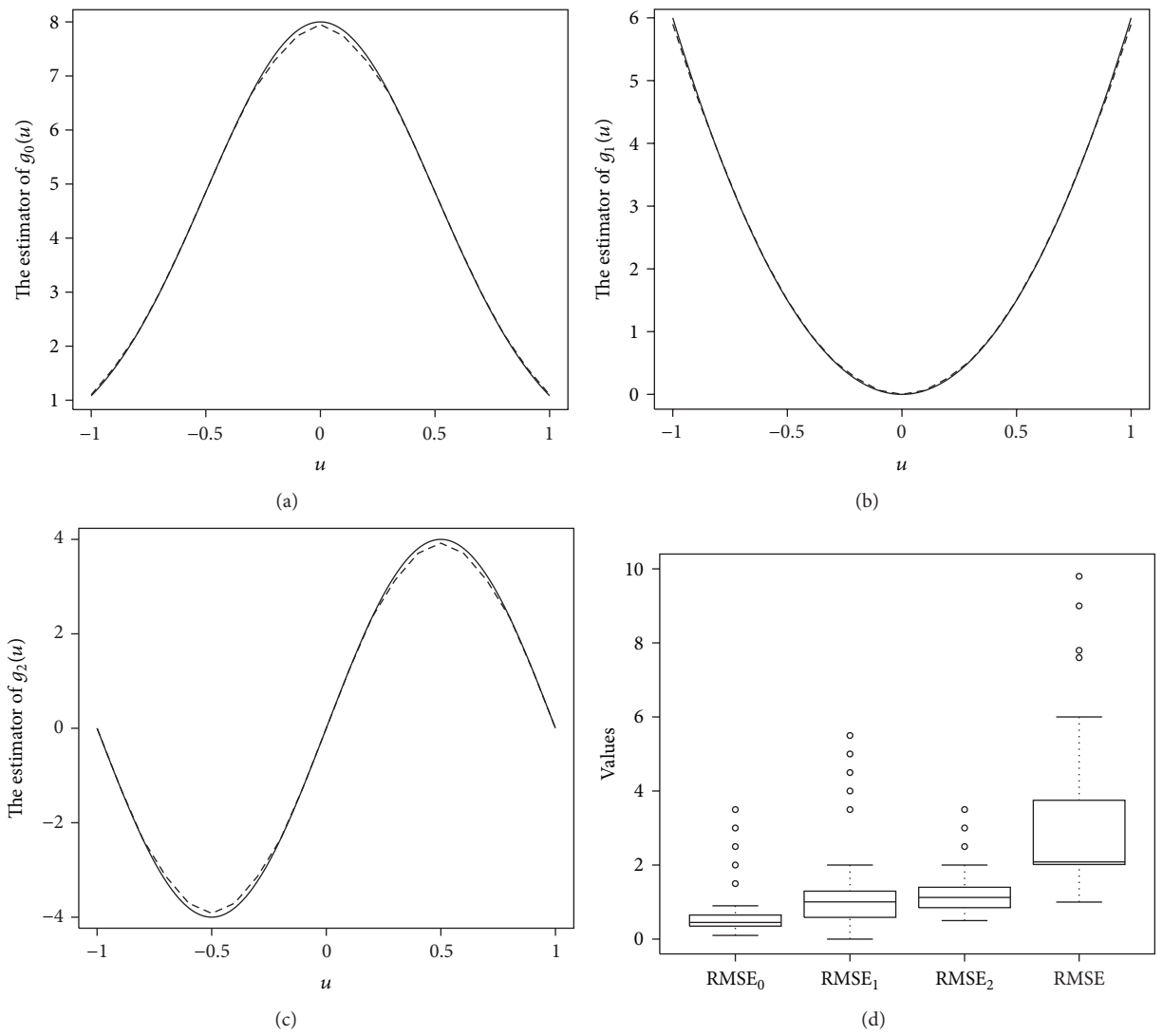

FIGURE 4: The true curve (solid curve) and the estimated curve (dashed curve); (d) the boxplots of the 1000 RMSE values in estimations of $g_0(\cdot)$, $g_1(\cdot)$, and $g_2(\cdot)$ and the sum of the three RMSEs.

We also consider the average estimates of the coefficient functions $g_0(u)$, $g_1(u)$, and $g_2(u)$ over the 1000 replicates. The estimators $\widehat{g}_j(\cdot)$ are assessed via the root mean squared errors (RMSE); that is, RMSE $= \sum_{j=0}^{2} \text{RMSE}_j$, where

$$\text{RMSE}_j = \left[n_{\text{grid}}^{-1} \sum_{k=1}^{n_{\text{grid}}} \left\{ \widehat{g}_j(u_k) - g_j(u_k) \right\}^2 \right]^{1/2}, \quad (25)$$

and $\{u_k, k = 1, \ldots, n_{\text{grid}}\}$ are regular grid points. The boxplot for the 1000 RMSEs is given in Figure 4. From Figures 4(a)–4(c) we see that every estimated curve agrees with the true function curve very closely. Figure 4(d) shows that all RMSEs of estimates for the unknown functions are very small.

Example 7. We now apply the block empirical likelihood method to analyze the data from a longitudinal hormone study [28]. The study involved 34 women whose urine samples were collected in one menstrual cycle and whose urinary progesterone was assayed on alternate days. A total of 492 observations were obtained, with each woman contributing from 11 to 28 observations over time. Each woman's cycle length was standardized uniformly to a reference 28-day cycle since the change of the progesterone level for each woman depends on time during a menstrual cycle. In the following, we consider the following model:

$$\begin{aligned} Y_{ij} = {} & g_0\left(\beta_1 \text{AGE}_{ij} + \beta_2 \text{BMI}_{ij}\right) \\ & + g_1\left(\beta_1 \text{AGE}_{ij} + \beta_2 \text{BMI}_{ij}\right) t_{ij} + \varepsilon_{ij}, \end{aligned} \quad (26)$$

where Y_{ij} is the jth log-transformed progesterone value measured at standardized day t_{ij} since menstruation for ith woman, and AGE_{ij} and BMI_{ij} are age and body mass index for the ith individual at day t_{ij}, respectively.

We apply the block empirical likelihood method to fit the data. Because we focus on the estimators of β_1 and β_2, we only

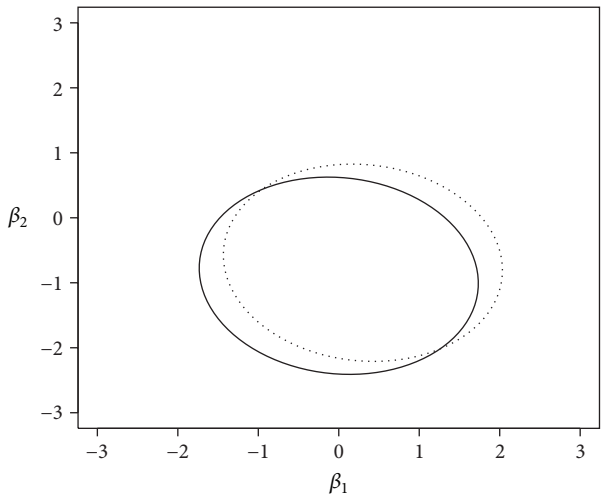

FIGURE 5: The 0.95 confidence regions for the regression coefficients β_1 and β_2 with correlation structures being independence (dotted curve) and first-autoregressive (sold curve).

summarize the estimators of β_1 and β_2 in Figure 5. Next, we denote β_{ind} and β_{AR} as the estimators of $\beta = (\beta_1, \beta_2)$, when the correlation structures are specified as independence and first-order autoregressive, respectively. We see from Figure 5 that both β_{ind} and β_{AR} are significant for neither of confidence regions for the two estimators including (0,0). Therefore, we conclude that the parameters β_1 and β_2 are not significant, which is consistent with the conclusion of Zhang et al. [28].

6. Proof of the Theorem

In order to prove Theorem 3, we introduce the following several lemmas. The following lemma gives uniformly convergent rates of $\widehat{g}(u;\beta)$ and $\widehat{\dot{g}}(u;\beta)$. This lemma is straightforward extension of known results in nonparametric function estimation. Moreover, the proofs of Lemma 9 and Lemma 10 is similar with the corresponding Lemma 9 and Lemma 10 of Xue and Wang [9]. We hence omit these proofs.

Lemma 8. *Let $\mathscr{B}_n = \{\beta \in \mathscr{B} : \|\beta - \beta_0\| \le c_0 n^{-1/2}\}$ for some positive constant c_0. Suppose that conditions (A.1)–(A.3), (A.5), and (A.6) hold. Then*

$$\begin{aligned}
&\sup_{u\in\mathscr{U}_\omega,\beta\in\mathscr{B}_n} \left\|\widehat{g}(u;\beta) - g_0(u)\right\| \\
&= O_p\left(\left\{\frac{\log(1/h)}{nh}\right\}^{1/2} + h^2\right), \\
&\sup_{u\in\mathscr{U}_\omega,\beta\in\mathscr{B}_n} \left\|\widehat{\dot{g}}(u;\beta) - \dot{g}_0(u)\right\| \\
&= O_p\left(\left\{\frac{\log(1/h)}{nh^3}\right\}^{1/2} + h\right).
\end{aligned} \tag{27}$$

In order to describe Lemma 9, we use the following notations. Denote $\mathscr{G} = \{g : \mathscr{U}_\omega \times \mathscr{B} \mapsto R^q\}$, $\|g\|_{\mathscr{G}} = \sup_{u\in\mathscr{U}_\omega,\beta\in\mathscr{B}_n}\|g(u;\beta)\|$. From Lemma 8, we have $||\widehat{g} - g_0||_{\mathscr{G}} = o_p(1)$ and $\|\widehat{\dot{g}} - \dot{g}_0\|_{\mathscr{G}} = o_p(1)$; hence, we can assume that g lies in $\mathscr{G}_\delta$ with $\delta = \delta_n \to 0$ and $\delta > 0$, where

$$\mathscr{G}_\delta = \left\{g \in \mathscr{G} : \|g - g_0\|_g \le \delta, \|\dot{g} - \dot{g}_0\|_g \le \delta\right\}. \tag{28}$$

Let $g_0(\beta^T\mathscr{X};\beta) = E\{g_0(\beta_0^T\mathscr{X})|\beta^T\mathscr{X}\}$ and $\dot{g}_0(\beta^T\mathscr{X};\beta) = E\{\dot{g}_0(\beta_0^T\mathscr{X})|\beta^T\mathscr{X}\}$,

$$\begin{aligned}
&Q(g,\beta) \\
&= E\left[\left\{\mathscr{Y} - g^T\left(\beta^T\mathscr{X};\beta\right)\mathscr{Z}\right\}\dot{g}^T\left(\beta^T\mathscr{X};\beta\right)\mathscr{Z}\mathscr{X}\omega\left(\beta^T\mathscr{X}\right)\right],
\end{aligned} \tag{29}$$

$$\begin{aligned}
&Q_n(g,\beta) \\
&= \frac{1}{n}\sum_{i=1}^{N}\sum_{j=1}^{n_i}\left\{y_{ij} - g^T\left(\beta^T x_{ij};\beta\right)z_{ij}\right\}\dot{g}^T \\
&\qquad \times\left(\beta^T x_{ij};\beta\right)z_{ij}x_{ij}\omega\left(\beta^T x_{ij}\right).
\end{aligned} \tag{30}$$

Lemma 9. *Suppose that conditions (A.1)–(A.6) hold. Let*

$$\begin{aligned}
J_1(g,\beta) &= Q_n(g,\beta) - Q(g,\beta) - Q_n(g_0,\beta_0), \\
J_2(\widehat{g},\beta) &= Q(g,\beta) - Q(g_0,\beta) \\
&\quad - \omega\left(g_0\left(\beta^T\mathscr{X};\beta\right);\beta\right) \\
&\quad \times\left\{g\left(\beta^T\mathscr{X};\beta\right) - g_0\left(\beta^T\mathscr{X}\right)\right\}, \\
J_3(g,\beta) &= \omega\left(g_0\left(\beta^T\mathscr{X}\right),\beta\right)\left\{g\left(\beta^T\mathscr{X};\beta\right) - g_0\left(\beta^T\mathscr{X}\right)\right\} \\
&\quad - \omega\left(g_0\left(\beta^T\mathscr{X};\beta_0\right),\beta_0\right) \\
&\quad \times\left\{g\left(\beta_0^T\mathscr{X};\beta_0\right) - g_0\left(\beta_0^T\mathscr{X};\beta\right)\right\}, \\
J_4(\widehat{g},\beta_0) &= Q_n(g_0,\beta_0) \\
&\quad + \omega\left(g_0\left(\beta^T\mathscr{X}\right),\beta\right)\left\{g\left(\beta^T\mathscr{X};\beta\right) - g_0\left(\beta^T\mathscr{X}\right)\right\}.
\end{aligned} \tag{31}$$

Then

$$\sup_{(g,\beta)\in\mathscr{G}\times\mathscr{B}_n}\|J_1(g,\beta)\| = o_p\left(n^{1/2}\right), \tag{32}$$

$$\sup_{\beta\in\mathscr{B}_n}\|J_2(\widehat{g},\beta)\| = o_p\left(n^{1/2}\right), \tag{33}$$

$$\sup_{(g,\beta)\in\mathscr{G}\times\mathscr{B}_n}\|J_3(g,\beta)\| = o\left(n^{1/2}\right), \tag{34}$$

$$\sqrt{n}J_4(\widehat{g},\beta_0) \xrightarrow{D} N\left(0,\sigma^2 A(\beta_0)\right), \tag{35}$$

where $A(\beta_0)$ is defined in (12).

Lemma 10. *Suppose that conditions (A.1)–(A.6) hold. Then*

$$\sup_{\beta\in\mathscr{B}_n}\left\|Q_n\left(\widehat{g},\beta\right)\right\| = O_p\left(n^{-1/2}\right), \tag{36}$$

$$\sup_{\beta\in\mathscr{B}_n}\left\|R_n\left(\beta\right)-\sigma^2 B\left(\beta_0\right)\right\| = o_p\left(1\right), \tag{37}$$

$$\sup_{\beta\in\mathscr{B}_n}\max_{\substack{1\le i\le N\\ 1\le j\le n_i}}\left\|\widehat{\eta}_{ij}\left(\beta\right)\right\| = o_p\left(n^{1/2}\right), \tag{38}$$

$$\sup_{\beta\in\mathscr{B}_n}\left\|\lambda\left(\beta\right)\right\| = o_p\left(n^{-1/2}\right), \tag{39}$$

where $Q_n(\widehat{g},\beta)$ *is defined in* (30), $R_n(\beta) = n^{-1}\sum_{i=1}^{N}\sum_{j=1}^{n_i}\widehat{\eta}_{ij}(\beta)\widehat{\eta}_{ij}^T(\beta)$, $B(\beta_0)$ *is defined in condition (A.7), and* $\widehat{\eta}_{ij}(\beta)$ *is defined in* (2).

Proof of Theorem 3. Note that, when $\beta = \beta_0$, Lemma 10 also holds. Applying the Taylor expansion to (7) and invoking Lemma 10, we can obtain

$$-2\widehat{l}\left(\beta_0\right) = -\sum_{i=1}^{N}\sum_{j=1}^{n_i}\left[\lambda^T\widehat{\eta}_{ij}\left(\beta_0\right)-\frac{1}{2}\left\{\lambda^T\widehat{\eta}_{ij}\left(\beta_0\right)\right\}^2\right]+o_p\left(1\right). \tag{40}$$

By (9) and Lemma 10, we have

$$\sum_{i=1}^{N}\sum_{j=1}^{n_i}\left\{\lambda^T\widehat{\eta}_{ij}\left(\beta_0\right)\right\}^2 = \sum_{i=1}^{N}\sum_{j=1}^{n_i}\lambda^T\widehat{\eta}_{ij}\left(\beta_0\right)+o_p\left(1\right),$$

$$\lambda = \left\{\sum_{i=1}^{N}\sum_{j=1}^{n_i}\widehat{\eta}_{ij}\left(\beta_0\right)\widehat{\eta}_{ij}^T\left(\beta_0\right)\right\}^{-1}\sum_{i=1}^{N}\sum_{j=1}^{n_i}\widehat{\eta}_{ij}\left(\beta_0\right)+o_p\left(n^{-(1/2)}\right). \tag{41}$$

This together with (40) proves that

$$-2\widehat{l}\left(\beta_0\right) = nQ_n^T\left(\widehat{g},\beta_0\right)R_n^{-1}\left(\beta_0\right)Q_n\left(\widehat{g},\beta_0\right)+o_p\left(1\right), \tag{42}$$

where $Q_n(\widehat{g},\beta_0)$ and $R_n(\beta_0)$ are defined in (30) and (37), respectively. From (37) of Lemma 10 and (42), we obtain

$$\begin{aligned}-2\widehat{l}\left(\beta_0\right) = {}& \left\{\left(\sigma^2 A\right)^{-1/2}\sqrt{n}Q_n\left(\widehat{g},\beta_0\right)\right\}^T G\left(\beta_0\right)\\ &\times\left\{\left(\sigma^2 A\right)^{-1/2}\sqrt{n}Q_n\left(\widehat{g},\beta_0\right)\right\}+o_p\left(1\right),\end{aligned} \tag{43}$$

where $G(\beta_0) = A^{1/2}(\beta_0)B^{-1}(\beta_0)A^{1/2}(\beta_0)$. Let $G_0 = \mathrm{diag}(\omega_1,\ldots,\omega_n)$, where ω_i, $1\le i\le p$, are the eigenvalues of $G(\beta_0)$. Then there exists an orthogonal matrix H such that H^TG_0H. Using the notations of Lemma 9, we have

$$\begin{aligned}Q_n\left(\widehat{g},\beta\right) = {}& J_1\left(\widehat{g},\beta\right)+J_2\left(\widehat{g},\beta\right)+J_3\left(\widehat{g},\beta\right)\\ &+J_4\left(\widehat{g},\beta\right)+Q\left(g_0,\beta\right).\end{aligned} \tag{44}$$

Noting that $Q(g_0,\beta_0)$, from the above equation and Lemma 9, we have

$$Q_n\left(\widehat{g},\beta_0\right) = J_4\left(\widehat{g},\beta_0\right)+o_p\left(n^{-1/2}\right). \tag{45}$$

Hence, by (35) of Lemma 9, we have

$$H\left\{\sigma^{-2}A^-\left(\beta_0\right)\right\}^{1/2}\sqrt{n}Q_n\left(\widehat{g},\beta_0\right)\xrightarrow{D}N\left(0,I_p\right), \tag{46}$$

where I_p is the $p\times p$ identity matrix. This together with (43) proves Theorem 3. □

Proof of Theorem 4. By Lemma 10 and, similarly to the proof of (42), we can obtain

$$\widehat{l}\left(\beta\right) = -\frac{n}{2}Q_n^T\left(\widehat{g},\beta\right)\left\{\sigma^2B\left(\beta\right)\right\}^{-1}Q_n\left(\widehat{g},\beta\right)+O_p\left(1\right), \tag{47}$$

uniformly for $\beta\in\mathscr{B}_n$, where $o_p(1)$ tends to 0 in probability uniformly for $\beta\in\mathscr{B}_n$. Note that $\widehat{A}(\beta_0)\xrightarrow{p}A(\beta_0)$ and $\widehat{B}(\beta_0)\xrightarrow{p}B(\beta_0)$. By the expansion of $\widehat{l}_a(\beta_0)$, defined in (19) and (47), we get

$$\widehat{l}_a\left(\beta_0\right) = Q_n^T\left(\widehat{g},\beta\right)\left\{\sigma^{-2}A^-\left(\beta_0\right)\right\}Q_n\left(\widehat{g},\beta_0\right)+O_p\left(1\right). \tag{48}$$

This together with (44) and (48) proves Theorem 4. Then we complete the proof. □

Acknowledgments

This research was supported by NNSF project (11171188 and 11231005) of China, Mathematical Finance-Backward Stochastic Analysis and Computations in Financial Risk Control of China (11221061), NSF and SRRF projects (ZR2010AZ001 and BS2011SF006) of Shandong Province of China, K C Wong-HKBU Fellowship Programme for Mainland China Scholars 2010-11, and the Fundamental Research Funds for the Central Universities (27R1310008A).

References

[1] Z. Huang, "Empirical likelihood for single-index varying-coefficient models with right-censored data," *Journal of the Korean Statistical Society*, vol. 39, no. 4, pp. 533–544, 2010.

[2] Z. Gao, D. Kong, and C. Gao, "Modeling and control of complex dynamic systems: applied mathematical aspects," *Journal of Applied Mathematics*, vol. 2012, Article ID 869792, 5 pages, 2012.

[3] L. Jian, S. Shen, and Y. Song, "Improving the solution of least squares support vector machines with application to a blast furnace system," *Journal of Applied Mathematics*, vol. 2012, Article ID 949654, 12 pages, 2012.

[4] J. Hu and Z. Gao, "Modules identification in gene positive networks of hepatocellular carcinoma using pearson agglomerative method and pearson cohesion coupling modularity," *Journal of Applied Mathematics*, vol. 2012, Article ID 248658, 21 pages, 2012.

[5] Y. Bai, W. K. Fung, and Z. Y. Zhu, "Penalized quadratic inference functions for single-index models with longitudinal data," *Journal of Multivariate Analysis*, vol. 100, no. 1, pp. 152–161, 2009.

[6] C. T. Chiang, J. A. Rice, and C. O. Wu, "Smoothing spline estimation for varying coefficient models with repeatedly measured dependent variables," *Journal of the American Statistical Association*, vol. 96, no. 454, pp. 605–619, 2001.

[7] J. Z. Huang, C. O. Wu, and L. Zhou, "Varying-coefficient models and basis function approximations for the analysis of repeated measurements," *Biometrika*, vol. 89, no. 1, pp. 111–128, 2002.

[8] A. Qu and R. Li, "Quadratic inference functions for varying-coefficient models with longitudinal data," *Biometrics*, vol. 62, no. 2, pp. 379–391, 2006.

[9] L. Xue and Q. Wang, "Empirical likelihood for single-index varying-coefficient models," *Bernoulli*, vol. 18, no. 3, pp. 836–856, 2012.

[10] A. B. Owen, "Empirical likelihood ratio confidence intervals for a single functional," *Biometrika*, vol. 75, no. 2, pp. 237–249, 1988.

[11] A. Owen, "Empirical likelihood ratio confidence regions," *The Annals of Statistics*, vol. 18, no. 1, pp. 90–120, 1990.

[12] Q. H. Wang and B. Y. Jing, "Empirical likelihood for partial linear models with fixed designs," *Statistics & Probability Letters*, vol. 41, no. 4, pp. 425–433, 1999.

[13] S. X. Chen and Y. S. Qin, "Empirical likelihood confidence intervals for local linear smoothers," *Biometrika*, vol. 87, no. 4, pp. 946–953, 2000.

[14] J. Shi and T. S. Lau, "Empirical likelihood for partially linear models," *Journal of Multivariate Analysis*, vol. 72, no. 1, pp. 132–148, 2000.

[15] L. Xue and L. Zhu, "Empirical likelihood for a varying coefficient model with longitudinal data," *Journal of the American Statistical Association*, vol. 102, no. 478, pp. 642–654, 2007.

[16] L. Xue and L. Zhu, "Empirical likelihood semiparametric regression analysis for longitudinal data," *Biometrika*, vol. 94, no. 4, pp. 921–937, 2007.

[17] L. G. Xue and L. Zhu, "Empirical likelihood for single-index models," *Journal of Multivariate Analysis*, vol. 97, no. 6, pp. 1295–1312, 2006.

[18] A. B. Owen, *Empirical Likelihood*, Chapman & Hall, London, UK, 2001.

[19] Z. Huang and R. Zhang, "Testing for the parametric parts in a single-index varying-coefficient model," *Science China: Mathematics*, vol. 55, no. 5, pp. 1017–1028, 2012.

[20] S. Feng and L. Xue, "Variable selection for single-index varying-coefficient model," *Frontiers of Mathematics in China*, vol. 8, no. 3, pp. 541–565, 2013.

[21] J. H. You, G. M. Chen, and Y. Zhou, "Block empirical likelihood for longitudinal partially linear regression models," *The Canadian Journal of Statistics*, vol. 34, no. 1, pp. 79–96, 2006.

[22] J. Fan and I. Gijbels, *Local Polynomial Modelling and Its Applications*, vol. 66 of *Monographs on Statistics and Applied Probability*, Chapman & Hall, London, UK, 1996.

[23] J. You and Y. Zhou, "Empirical likelihood for semiparametric varying-coefficient partially linear regression models," *Statistics & Probability Letters*, vol. 76, no. 4, pp. 412–422, 2006.

[24] J. N. K. Rao and A. J. Scott, "The analysis of categorical data from complex sample surveys: chi-squared tests for goodness of fit and independence in two-way tables," *Journal of the American Statistical Association*, vol. 76, no. 374, pp. 221–230, 1981.

[25] Q. Wang and J. N. K. Rao, "Empirical likelihood-based inference in linear errors-in-covariables models with validation data," *Biometrika*, vol. 89, no. 2, pp. 345–358, 2002.

[26] Z. Cai, J. Fan, and Q. Yao, "Functional-coefficient regression models for nonlinear time series," *Journal of the American Statistical Association*, vol. 95, no. 451, pp. 941–956, 2000.

[27] R. J. Carroll, J. Fan, I. Gijbels, and M. P. Wand, "Generalized partially linear single-index models," *Journal of the American Statistical Association*, vol. 92, no. 438, pp. 477–489, 1997.

[28] D. Zhang, X. Lin, J. Raz, and M. Sowers, "Semiparametric stochastic mixed models for longitudinal data," *Journal of the American Statistical Association*, vol. 93, no. 442, pp. 710–719, 1998.

Hindawi Publishing Corporation
Journal of Applied Mathematics
Volume 2013, Article ID 394137, 8 pages
http://dx.doi.org/10.1155/2013/394137

Research Article

Adaptive Synchronization of Complex Dynamical Networks with State Predictor

Yuntao Shi,[1] Bo Liu,[2] and Xiao Han[2]

[1] *Key Laboratory of Beijing for Field-Bus Technology & Automation, North China University of Technology, Beijing 100144, China*
[2] *College of Science, North China University of Technology, Beijing 100144, China*

Correspondence should be addressed to Bo Liu; boliu@ncut.edu.cn

Received 12 July 2013; Accepted 27 August 2013

Academic Editor: Michael Chen

Copyright © 2013 Yuntao Shi et al. This is an open access article distributed under the Creative Commons Attribution License, which permits unrestricted use, distribution, and reproduction in any medium, provided the original work is properly cited.

This paper addresses the adaptive synchronization of complex dynamical networks with nonlinear dynamics. Based on the Lyapunov method, it is shown that the network can synchronize to the synchronous state by introducing local adaptive strategy to the coupling strengths. Moreover, it is also proved that the convergence speed of complex dynamical networks can be increased via designing a state predictor. Finally, some numerical simulations are worked out to illustrate the analytical results.

1. Introduction

In recent years, the synchronization problem of complex networks is a hot topic in many areas, including mathematics, physics, biology, computer, and artificial intelligence [1–37]. A complex dynamical network is composed of a large number of nodes to be steered to arrive synchronization. However, it is so hard and impractical to control all nodes to synchronize in the large complex network. In order to solve this problem, the pinning control is introduced, which can decrease the number of controllers for synchronization of the complex networks. Pinning control scheme is an effective way to control dynamical networks to a desired state. The idea of the pinning control is to steer a small fraction nodes, and all nodes of the complex network can achieve control target via localized feedback of those nodes.

A lot of outstanding works about the synchronization problem of complex networks are presented in the recent references [1–37]. In [1], Wang and Chen used specifically and randomly pinning control strategies for scale-free chaotic dynamical networks. De Lellis et al. [19] considered the synchronization of complex networks through local adaptive coupling. The authors [20] proposed a decentralized adaptive pinning control scheme for synchronization of undirected networks using a local adaptive strategy to both coupling strengths and feedback gains. In [4], Yu et al. investigated the synchronization via pinning control on general complex networks. In [5, 6], second-order consensus problem for multiagent systems was investigated by using pinning control method.

The convergence speed of complex dynamical networks is a significant issue. Through limited communication, each agent can forecast the future states of its neighbors and itself; as well as the new control law can be constructed by the predicted states. With this strategy, the complex dynamical network can evolve more quickly to equilibrium. Motivated by it, this paper investigates the synchronization via designing a state predictor. It is proved that all nodes will asymptotically synchronize to the given homogeneous stationary state using the adaptive strategy to the coupling strengths designed, if the complex dynamical network is connected and at least one node is informed. Introducing the state predictor for formation algorithm in multiagent systems, the simulation results show that using the state predictor in multiagent systems can improve the speed of the system to complete the desired task.

The rest of this paper is designed as follows. Section 2 gives a model of the complex dynamical network. Some preliminaries are introduced to solve the adaptive synchronization. Section 3 provides the theoretical analysis of adaptive synchronization of the complex dynamical network. Furthermore, some more detailed analyses are presented in

this section. Section 4 gives some simulations to illustrate our theoretical results. Conclusion is finally summarized in Section 5.

2. Preliminaries and Problem Statement

Consider a complex dynamical network described by

$$\dot{x}_i(t) = f(x_i(t)) - \sum_{j\in\mathcal{N}_i} a_{ij}c_{ij}(t)\left(x_i(t) - x_j(t)\right) + \gamma \sum_{j\in\mathcal{N}_i} a_{ij}c_{ij}(t)\left(\dot{x}_i^p(t) - \dot{x}_j^p(t)\right), \tag{1}$$

where $x_i(t) = (x_{i1}(t), x_{i2}(t), \ldots, x_{in}(t))^T \in R^n$, $(i = 1, 2, \ldots, N)$ represents the state vector of the node i at time t; N_i is the neighbor set of node i; $f(\cdot) \in R^n$ is continuously differentiable; a_{ij} is the coupling weight between any two agents, where $a_{ij} \geq 0$ and $a_{ii} = 0$; $c_{ij}(t)$ denotes the coupling strengths between nodes i and node j; the weighted coupling configuration matrix of the system is defined as

$$U = \left[u_{ij}\right] = \begin{bmatrix} u_{11} & u_{12} & \cdots & u_{1N} \\ u_{21} & u_{22} & \cdots & u_{2N} \\ \vdots & \vdots & \ddots & \vdots \\ u_{N1} & u_{N2} & \cdots & u_{NN} \end{bmatrix} \in R^{N\times N}, \tag{2}$$

with $u_{ii} = a_{ii}c_{ii} = -\sum_{j=1, j\neq i}^{N} a_{ij}c_{ij}$ and $u_{ij} = a_{ij}c_{ij}$ for $i \neq j$. Design the state predictor for the control law as

$$\dot{X}^p = -LX, \tag{3}$$

where $\dot{X}^p = (\dot{x}_1^p, \dot{x}_2^p, \ldots, \dot{x}_N^p)$ and γ is the impact factor of the state predictor.

Under state predictor (3), network (1) can be rewritten as

$$\dot{x}_i(t) = f(x_i(t)) - \sum_{j\in\mathcal{N}_i} a_{ij}c_{ij}(t)\left(x_i(t) - x_j(t)\right) - \gamma\left(\sum_{j\in\mathcal{N}_i}\sum_{k\in\mathcal{N}_i} a_{ij}a_{ik}c_{ij}(t)c_{ik}(t)(x_i - x_k) - \sum_{j\in\mathcal{N}_i}\sum_{p\in\mathcal{N}_j} a_{ij}a_{jp}c_{ij}(t)c_{jp}(t)\left(x_j - x_p\right)\right). \tag{4}$$

Definition 1. Network (4) is said to achieve synchronization if

$$\lim_{t\to\infty}\left\|x_i(t) - \overline{x}(t)\right\| = 0, \quad i = 1, \ldots, N, \tag{5}$$

where the homogeneous state satisfies

$$\dot{\overline{x}}(t) = f(\overline{x}(t), t) = 0. \tag{6}$$

The adaptive control at node i is designed as

$$\dot{c}_{ij}(t) = \sum_{p\in\mathcal{N}_j} a_{ij}a_{jp}c_{jp}(t)\left[x_i(t) - \overline{x}(t)\right]^T\left[x_i(t) - \overline{x}(t)\right] + \sum_{k\in\mathcal{N}_i} a_{ij}a_{ik}c_{ik}(t)\left[x_k(t) - \overline{x}(t)\right]^T\left[x_k(t) - \overline{x}(t)\right], \tag{7}$$

where $c_{ij}(0) \geq 0$.

In the following, some necessary assumptions and lemmas are stated.

Assumption 2. The coupling strengths of the network are bounded:

$$\left\|c_{ij}(t)\right\| \leq c_{ij}. \tag{8}$$

Assumption 3 (see [5]). The vector field $f_i : R^n \to R^n$ $(i = 1, 2, \ldots, N)$ in network (4) satisfies the Lipschitz condition; there exists a positive constant $\rho > 0$, such that

$$\left\|f(x) - f(y)\right\| \leq \rho\left\|x - y\right\|. \tag{9}$$

Assumption 4. The weights satisfy the balance condition:

$$\sum_{j\in N_i} a_{ij}c_{ij}(t) = \sum_{j\in N_i} a_{ji}c_{ji}(t), \quad \forall i. \tag{10}$$

Lemma 5 (see [29]). *For any vectors $x, y \in R^n$ and positive definite matrix $G \in R^{n\times n}$, the following matrix inequality holds:*

$$2x^T y \leq x^T G x + y^T G^{-1} y. \tag{11}$$

Lemma 6 (see [6]). *Supposing that a and b are vectors, then for any positive-definite matrix E, the following inequality holds:*

$$-2a^T b \leq \inf_{E>0}\left\{a^T E a + b^T E^{-1} b\right\}. \tag{12}$$

Lemma 7 (see [38]). *The matrix A of an undirected graph G is irreducible if and only if the undirected graph is connected.*

3. Main Results

In this section, we will give detailed analysis of the adaptive synchronization of the network with the state predictor. By using the Lyapunov function approach, adaptive synchronization conditions of such work are obtained.

Theorem 8. *Considering network* (4) *with N nodes steered by adaptive control* (7)*, under Assumptions 2–4, then all nodes*

will asymptotically synchronize to the given homogeneous stationary state; that is,

$$\lim_{t\to\infty}\left\|x_i(t)-\overline{x}(t)\right\|=0. \tag{13}$$

Proof. Let $\widetilde{x}_i(t) \triangleq x_i(t)-\overline{x}(t)$. Construct the following Lyapunov function:

$$V(t)=V_1(t)+V_2(t), \tag{14}$$

where

$$\begin{aligned} V_1(t)&=\frac{1}{2}\sum_{i=1}^{N}\widetilde{x}_i^T(t)\,\widetilde{x}_i(t),\\ V_2(t)&=\sum_{i=1}^{N}\sum_{j\in\mathcal{N}_i}\frac{\left[(1-m)\,c_{ij}(t)\right]^2}{2}, \end{aligned} \tag{15}$$

where $m>0$ is sufficiently large.

By the definition of the matrix U, it is to see that U is symmetric and irreducible. By Lemmas 5–7, differentiating $V_1(t)$, we can have

$$\begin{aligned} \dot{V}_1(t)&=\sum_{i=1}^{N}\widetilde{x}_i^T(t)\left[f\left(x_i(t)\right)-f\left(\overline{x}(t)\right)\right]\\ &\quad-\sum_{i=1}^{N}\widetilde{x}_i^T(t)\sum_{j\in\mathcal{N}_i}a_{ij}c_{ij}(t)\left(\widetilde{x}_i(t)-\widetilde{x}_j(t)\right)\\ &\quad-\gamma\widetilde{x}_i^T(t)\sum_{j\in\mathcal{N}_i}\sum_{k\in\mathcal{N}_i}a_{ij}c_{ij}(t)\,a_{ik}c_{ik}(t)\left(\widetilde{x}_i(t)-\widetilde{x}_k(t)\right)\\ &\quad+\gamma\widetilde{x}_i^T(t)\sum_{j\in\mathcal{N}_i}\sum_{p\in\mathcal{N}_j}a_{ij}c_{ij}(t)\,a_{jp}c_{jp}(t)\left(\widetilde{x}_j(t)-\widetilde{x}_p(t)\right)\\ &\le\rho\sum_{i=1}^{N}\widetilde{x}_i^T(t)\,\widetilde{x}_i(t)-\sum_{i=1}^{N}\sum_{j\in\mathcal{N}_i}a_{ij}c_{ij}(t)\,\widetilde{x}_i^T(t)\,\widetilde{x}_i(t)\\ &\quad+\sum_{i=1}^{N}\sum_{j\in\mathcal{N}_i}a_{ij}c_{ij}(t)\,\widetilde{x}_i^T(t)\,\widetilde{x}_j(t)\\ &\quad-\gamma\sum_{i=1}^{N}\sum_{j\in\mathcal{N}_i}\sum_{k\in\mathcal{N}_i}a_{ij}c_{ij}(t)\,a_{ik}c_{ik}(t)\,\widetilde{x}_i^T(t)\,\widetilde{x}_i(t)\\ &\quad+\gamma\sum_{i=1}^{N}\sum_{j\in\mathcal{N}_i}\sum_{k\in\mathcal{N}_i}a_{ij}c_{ij}(t)\,a_{ik}c_{ik}(t)\,\widetilde{x}_i^T(t)\,\widetilde{x}_k(t)\\ &\quad+\gamma\sum_{i=1}^{N}\sum_{j\in\mathcal{N}_i}\sum_{p\in\mathcal{N}_j}a_{ij}c_{ij}(t)\,a_{jp}c_{jp}(t)\,\widetilde{x}_i^T(t)\,\widetilde{x}_j(t)\\ &\quad-\gamma\sum_{i=1}^{N}\sum_{j\in\mathcal{N}_i}\sum_{p\in\mathcal{N}_j}a_{ij}c_{ij}(t)\,a_{jp}c_{jp}(t)\,\widetilde{x}_i^T(t)\,\widetilde{x}_p(t)\\ &=\sum_{i=1}^{N}\left[\rho-\sum_{j\in\mathcal{N}_i}a_{ij}c_{ij}(t)\right.\\ &\qquad\left.-\gamma\sum_{j\in\mathcal{N}_i}\sum_{k\in\mathcal{N}_i}a_{ij}c_{ij}(t)\,a_{ik}c_{ik}(t)\right]\widetilde{x}_i^T(t)\,\widetilde{x}_i(t)\\ &\quad+\sum_{i=1}^{N}\sum_{j\in\mathcal{N}_i}\left[a_{ij}c_{ij}(t)\right.\\ &\qquad\left.+\gamma\sum_{p\in\mathcal{N}_j}a_{ij}c_{ij}(t)\,a_{jp}c_{jp}(t)\right]\widetilde{x}_i^T(t)\,\widetilde{x}_j(t)\\ &\quad+\gamma\sum_{i=1}^{N}\sum_{j\in\mathcal{N}_i}\sum_{k\in\mathcal{N}_i}a_{ij}c_{ij}(t)\,a_{ik}c_{ik}(t)\,\widetilde{x}_i^T(t)\,\widetilde{x}_k(t)\\ &\quad-\gamma\sum_{i=1}^{N}\sum_{j\in\mathcal{N}_i}\sum_{p\in\mathcal{N}_j}a_{ij}c_{ij}(t)\,a_{jp}c_{jp}(t)\,\widetilde{x}_i^T(t)\,\widetilde{x}_p(t)\\ &\le\sum_{i=1}^{N}\left[\rho-\sum_{j\in\mathcal{N}_i}a_{ij}c_{ij}(t)-\gamma\sum_{j\in\mathcal{N}_i}\sum_{k\in\mathcal{N}_i}a_{ij}c_{ij}(t)\,a_{ik}c_{ik}(t)\right]\\ &\qquad\times\widetilde{x}_i^T(t)\,\widetilde{x}_i(t)\\ &\quad+\frac{1}{2}\sum_{i=1}^{N}\sum_{j\in\mathcal{N}_i}\left[a_{ij}c_{ij}(t)+\gamma\sum_{p\in\mathcal{N}_j}a_{ij}c_{ij}(t)\,a_{jp}c_{jp}(t)\right]\\ &\qquad\times\widetilde{x}_i^T(t)\,\widetilde{x}_i(t)\\ &\quad+\frac{1}{2}\sum_{i=1}^{N}\sum_{j\in\mathcal{N}_i}\left[a_{ij}c_{ij}(t)+\gamma\sum_{p\in\mathcal{N}_j}a_{ij}c_{ij}(t)\,a_{jp}c_{jp}(t)\right]\\ &\qquad\times\widetilde{x}_j^T(t)\,\widetilde{x}_j(t)\\ &\quad+\frac{1}{2}\gamma\sum_{i=1}^{N}\sum_{j\in\mathcal{N}_i}\sum_{k\in\mathcal{N}_i}a_{ij}c_{ij}(t)\,a_{ik}c_{ik}(t)\,\widetilde{x}_i^T(t)\,\widetilde{x}_i(t)\\ &\quad+\frac{1}{2}\gamma\sum_{i=1}^{N}\sum_{j\in\mathcal{N}_i}\sum_{k\in\mathcal{N}_i}a_{ij}c_{ij}(t)\,a_{ik}c_{ik}(t)\,\widetilde{x}_k^T(t)\,\widetilde{x}_k(t)\\ &\quad+\frac{1}{2}\gamma\sum_{i=1}^{N}\sum_{j\in\mathcal{N}_i}\sum_{p\in\mathcal{N}_j}a_{ij}c_{ij}(t)\,a_{jp}c_{jp}(t)\,\widetilde{x}_i^T(t)\,\widetilde{x}_i(t)\\ &\quad+\frac{1}{2}\gamma\sum_{i=1}^{N}\sum_{j\in\mathcal{N}_i}\sum_{p\in\mathcal{N}_j}a_{ij}c_{ij}(t)\,a_{jp}c_{jp}(t)\,\widetilde{x}_p^T(t)\,\widetilde{x}_p(t) \end{aligned}$$

$$
\begin{aligned}
&= \sum_{i=1}^{N} \left[\rho - \sum_{j\in\mathcal{N}_i} a_{ij}c_{ij}(t) - \gamma \sum_{j\in\mathcal{N}_i} \sum_{k\in\mathcal{N}_i} a_{ij}c_{ij}(t)\, a_{ik}c_{ik}(t) \right] \\
&\quad \times \widetilde{x}_i^T(t)\, \widetilde{x}_i(t) \\
&\quad + \sum_{i=1}^{N} \sum_{j\in\mathcal{N}_i} \left[a_{ij}c_{ij}(t) + \gamma \sum_{p\in\mathcal{N}_j} a_{ij}c_{ij}(t)\, a_{jp}c_{jp}(t) \right] \\
&\quad \times \widetilde{x}_i^T(t)\, \widetilde{x}_j(t) \\
&\quad + \gamma \sum_{i=1}^{N} \sum_{j\in\mathcal{N}_i} \sum_{k\in\mathcal{N}_i} a_{ij}c_{ij}(t)\, a_{ik}c_{ik}(t)\, \widetilde{x}_i^T(t)\, \widetilde{x}_k(t) \\
&\quad - \gamma \sum_{i=1}^{N} \sum_{j\in\mathcal{N}_i} \sum_{p\in\mathcal{N}_j} a_{ij}c_{ij}(t)\, a_{jp}c_{jp}(t)\, \widetilde{x}_i^T(t)\, \widetilde{x}_p(t) \\
&\le \sum_{i=1}^{N} \left[\rho - \sum_{j\in\mathcal{N}_i} a_{ij}c_{ij}(t) - \gamma \sum_{j\in\mathcal{N}_i} \sum_{k\in\mathcal{N}_i} a_{ij}c_{ij}(t)\, a_{ik}c_{ik}(t) \right] \\
&\quad \times \widetilde{x}_i^T(t)\, \widetilde{x}_i(t) \\
&\quad + \frac{1}{2} \sum_{i=1}^{N} \sum_{j\in\mathcal{N}_i} \left[a_{ij}c_{ij}(t) + \gamma \sum_{p\in\mathcal{N}_j} a_{ij}c_{ij}(t)\, a_{jp}c_{jp}(t) \right] \\
&\quad \times \widetilde{x}_i^T(t)\, \widetilde{x}_i(t) \\
&\quad + \frac{1}{2} \sum_{i=1}^{N} \sum_{j\in\mathcal{N}_i} \left[a_{ij}c_{ij}(t) + \gamma \sum_{p\in\mathcal{N}_j} a_{ij}c_{ij}(t)\, a_{jp}c_{jp}(t) \right] \\
&\quad \times \widetilde{x}_j^T(t)\, \widetilde{x}_j(t) \\
&\quad + \frac{1}{2}\gamma \sum_{i=1}^{N} \sum_{j\in\mathcal{N}_i} \sum_{k\in\mathcal{N}_i} a_{ij}c_{ij}(t)\, a_{ik}c_{ik}(t)\, \widetilde{x}_i^T(t)\, \widetilde{x}_i(t) \\
&\quad + \frac{1}{2}\gamma \sum_{i=1}^{N} \sum_{j\in\mathcal{N}_i} \sum_{k\in\mathcal{N}_i} a_{ij}c_{ij}(t)\, a_{ik}c_{ik}(t)\, \widetilde{x}_k^T(t)\, \widetilde{x}_k(t) \\
&\quad + \frac{1}{2}\gamma \sum_{i=1}^{N} \sum_{j\in\mathcal{N}_i} \sum_{p\in\mathcal{N}_j} a_{ij}c_{ij}(t)\, a_{jp}c_{jp}(t)\, \widetilde{x}_i^T(t)\, \widetilde{x}_i(t) \\
&\quad + \frac{1}{2}\gamma \sum_{i=1}^{N} \sum_{j\in\mathcal{N}_i} \sum_{p\in\mathcal{N}_j} a_{ij}c_{ij}(t)\, a_{jp}c_{jp}(t)\, \widetilde{x}_p^T(t)\, \widetilde{x}_p(t) \\
&= \sum_{i=1}^{N} \left[\rho - \sum_{j\in\mathcal{N}_i} a_{ij}c_{ij}(t) - \gamma \sum_{j\in\mathcal{N}_i} \sum_{k\in\mathcal{N}_i} a_{ij}c_{ij}(t)\, a_{ik}c_{ik}(t) \right. \\
&\qquad + \frac{1}{2} \sum_{j\in\mathcal{N}_i} a_{ij}c_{ij}(t) \\
&\qquad + \frac{1}{2}\gamma \sum_{j\in\mathcal{N}_i} \sum_{p\in\mathcal{N}_j} a_{ij}c_{ij}(t)\, a_{jp}c_{jp}(t) \\
&\qquad + \frac{1}{2}\gamma \sum_{j\in\mathcal{N}_i} \sum_{k\in\mathcal{N}_i} a_{ij}c_{ij}(t)\, a_{ik}c_{ik}(t) \\
&\qquad \left. + \frac{1}{2}\gamma \sum_{j\in\mathcal{N}_i} \sum_{p\in\mathcal{N}_j} a_{ij}c_{ij}(t)\, a_{jp}c_{jp}(t) \right] \\
&\quad \times \widetilde{x}_i^T(t)\, \widetilde{x}_i(t) \\
&\quad + \frac{1}{2} \sum_{i=1}^{N} \sum_{j\in\mathcal{N}_i} \left[a_{ij}c_{ij}(t) + \gamma \sum_{p\in\mathcal{N}_j} a_{ij}c_{ij}(t)\, a_{jp}c_{jp}(t) \right] \\
&\quad \times \widetilde{x}_j^T(t)\, \widetilde{x}_j(t) \\
&\quad + \frac{1}{2}\gamma \sum_{i=1}^{N} \sum_{j\in\mathcal{N}_i} \sum_{k\in\mathcal{N}_i} a_{ij}c_{ij}(t)\, a_{ik}c_{ik}(t)\, \widetilde{x}_k^T(t)\, \widetilde{x}_k(t) \\
&\quad + \frac{1}{2}\gamma \sum_{i=1}^{N} \sum_{j\in\mathcal{N}_i} \sum_{p\in\mathcal{N}_j} a_{ij}c_{ij}(t)\, a_{jp}c_{jp}(t)\, \widetilde{x}_p^T(t)\, \widetilde{x}_p(t) \\
&= \sum_{i=1}^{N} \left[\rho - \frac{1}{2} \sum_{j\in\mathcal{N}_i} a_{ij}c_{ij}(t) \right. \\
&\qquad - \frac{1}{2}\gamma \sum_{j\in\mathcal{N}_i} \sum_{k\in\mathcal{N}_i} a_{ij}c_{ij}(t)\, a_{ik}c_{ik}(t) \\
&\qquad \left. + \gamma \sum_{j\in\mathcal{N}_i} \sum_{p\in\mathcal{N}_j} a_{ij}c_{ij}(t)\, a_{jp}c_{jp}(t) \right] \\
&\quad \times \widetilde{x}_i^T(t)\, \widetilde{x}_i(t) \\
&\quad + \frac{1}{2} \sum_{i=1}^{N} \sum_{j\in\mathcal{N}_i} \left[a_{ij}c_{ij}(t) + \gamma \sum_{p\in\mathcal{N}_j} a_{ij}c_{ij}(t)\, a_{jp}c_{jp}(t) \right] \\
&\quad \times \widetilde{x}_j^T(t)\, \widetilde{x}_j(t) \\
&\quad + \frac{1}{2}\gamma \sum_{i=1}^{N} \sum_{j\in\mathcal{N}_i} \sum_{k\in\mathcal{N}_i} a_{ij}c_{ij}(t)\, a_{ik}c_{ik}(t)\, \widetilde{x}_k^T(t)\, \widetilde{x}_k(t) \\
&\quad + \frac{1}{2}\gamma \sum_{i=1}^{N} \sum_{j\in\mathcal{N}_i} \sum_{p\in\mathcal{N}_j} a_{ij}c_{ij}(t)\, a_{jp}c_{jp}(t)\, \widetilde{x}_p^T(t)\, \widetilde{x}_p(t).
\end{aligned}
\tag{16}
$$

Therefore,

$$
\begin{aligned}
&\dot{V}_1(t)\\
&\le \left[\tilde{x}_1^T(t) \ \cdots \ \tilde{x}_N^T(t)\right]
\begin{bmatrix}
\rho - \frac{1}{2}l_{11} - \frac{1}{2}\gamma l_{11}^2 + \gamma\sum_{j=1}^{N} a_{1j}c_{1j}(t)\,l_{jj} & \cdots & 0\\
\vdots & \ddots & \vdots\\
0 & \cdots & \rho - \frac{1}{2}l_{NN} - \frac{1}{2}\gamma l_{NN}^2 + \gamma\sum_{j=1}^{N} a_{Nj}c_{Nj}(t)\,l_{jj}
\end{bmatrix}
\begin{bmatrix}\tilde{x}_1(t)\\ \tilde{x}_2(t)\\ \vdots\\ \tilde{x}_N(t)\end{bmatrix}\\
&\quad + \left[\tilde{x}_1^T(t) \ \cdots \ \tilde{x}_N^T(t)\right]
\begin{bmatrix}
\frac{1}{2}l_{11} + \frac{1}{2}\gamma l_{11}^2 & 0 & \cdots & 0\\
0 & \frac{1}{2}l_{22} + \frac{1}{2}\gamma l_{22}^2 & \cdots & 0\\
\vdots & \vdots & \ddots & \vdots\\
0 & 0 & \cdots & \frac{1}{2}l_{NN} + \frac{1}{2}\gamma l_{NN}^2
\end{bmatrix}
\begin{bmatrix}\tilde{x}_1(t)\\ \tilde{x}_2(t)\\ \vdots\\ \tilde{x}_N(t)\end{bmatrix}\\
&\quad + \left[\tilde{x}_1^T(t) \ \cdots \ \tilde{x}_N^T(t)\right]
\begin{bmatrix}
\frac{1}{2}\gamma\sum_{i=1}^{N} a_{i1}c_{i1}(t)\,l_{ii} & 0 & \cdots & 0\\
0 & \frac{1}{2}\gamma\sum_{i=1}^{N} a_{i2}c_{i2}(t)\,l_{ii} & \cdots & 0\\
\vdots & \vdots & \ddots & \vdots\\
0 & 0 & \cdots & \frac{1}{2}\gamma\sum_{i=1}^{N} a_{iN}c_{iN}(t)\,l_{ii}
\end{bmatrix}
\begin{bmatrix}\tilde{x}_1(t)\\ \tilde{x}_2(t)\\ \vdots\\ \tilde{x}_N(t)\end{bmatrix}\\
&\quad + \left[\tilde{x}_1^T(t) \ \cdots \ \tilde{x}_N^T(t)\right]
\begin{bmatrix}
\frac{1}{2}\gamma\sum_{i=1}^{N} a_{i1}c_{i1}(t)\,l_{ii} & 0 & \cdots & 0\\
0 & \frac{1}{2}\gamma\sum_{i=1}^{N} a_{i2}c_{i2}(t)\,l_{ii} & \cdots & 0\\
\vdots & \vdots & \ddots & \vdots\\
0 & 0 & \cdots & \frac{1}{2}\gamma\sum_{i=1}^{N} a_{iN}c_{iN}(t)\,l_{ii}
\end{bmatrix}
\begin{bmatrix}\tilde{x}_1(t)\\ \tilde{x}_2(t)\\ \vdots\\ \tilde{x}_N(t)\end{bmatrix}\\
&= \left[\tilde{x}_1^T(t) \ \cdots \ \tilde{x}_N^T(t)\right]
\begin{bmatrix}
\rho + \gamma(W_1 + V_1) & \cdots & 0\\
\vdots & \ddots & \vdots\\
0 & \cdots & \rho + \gamma(W_N + V_N)
\end{bmatrix}
\begin{bmatrix}\tilde{x}_1(t)\\ \tilde{x}_2(t)\\ \vdots\\ \tilde{x}_N(t)\end{bmatrix},
\end{aligned}
\tag{17}
$$

where $l_{ii} = -u_{ii} = \sum_{j=1, j\neq i}^{N} a_{ij}c_{ij}(t)$, $W_i = \sum_{j=1}^{N} a_{ij}c_{ij}(t)l_{jj}$, $V_j = \sum_{i=1}^{N} a_{ij}c_{ij}(t)l_{ii}$, $i, j = 1, 2, \ldots, N$.

Differentiating $V_2(t)$, we get

$$
\begin{aligned}
\dot{V}_2(t) &= (1-m)\,c_{ij}(t)\,\dot{c}_{ij}(t)\\
&= \sum_{i=1}^{N}\sum_{j\in\mathcal{N}_i}(1-m)\,c_{ij}(t)\\
&\quad \times \left\{\sum_{p\in\mathcal{N}_j} a_{ij}a_{jp}c_{jp}(t)\left[x_i(t) - \overline{x}(t)\right]^T\right.\\
&\quad \times \left[x_i(t) - \overline{x}(t)\right]\\
&\quad + \sum_{k\in\mathcal{N}_i} a_{ij}a_{ik}c_{ik}(t)\left[x_k(t) - \overline{x}(t)\right]^T
\end{aligned}
$$

$$\times \left[x_k(t) - \overline{x}(t)\right] \Bigg\}$$

$$= (1-m)\sum_{i=1}^{N}\sum_{j\in\mathcal{N}_i}\sum_{p\in\mathcal{N}_j} a_{ij}c_{ij}(t)\,a_{jp}c_{jp}(t)\,\widetilde{x}_i^T(t)\,\widetilde{x}_i(t)$$

$$+ (1-m)\sum_{i=1}^{N}\sum_{j\in\mathcal{N}_i}\sum_{k\in\mathcal{N}_i} a_{ij}c_{ij}(t)\,a_{ik}c_{ik}(t)\,\widetilde{x}_k^T(t)\,\widetilde{x}_k(t)$$

$$= \left[\widetilde{x}_1^T(t) \;\cdots\; \widetilde{x}_N^T(t)\right]$$

$$\times \begin{bmatrix} (1-m)(W_1+V_1) & \cdots & 0 \\ \vdots & \ddots & \vdots \\ 0 & \cdots & (1-m)(W_N+V_N) \end{bmatrix}$$

$$\times \begin{bmatrix} \widetilde{x}_1(t) \\ \widetilde{x}_2(t) \\ \vdots \\ \widetilde{x}_N(t) \end{bmatrix}. \tag{18}$$

Combining $\dot{V}_1(t)$ and $\dot{V}_2(t)$, and since $m > 0$ is sufficiently large, then we can have

$$\dot{V}(t) = \dot{V}_1(t) + \dot{V}_2(t)$$

$$\leq \left[\widetilde{x}_1^T(t) \;\cdots\; \widetilde{x}_N^T(t)\right] \times \begin{bmatrix} \rho + (\gamma + 1 - m)(W_1+V_1) & \cdots & 0 \\ \vdots & \ddots & \vdots \\ 0 & \cdots & \rho + (\gamma + 1 - m)(W_N+V_N) \end{bmatrix}$$

$$\times \begin{bmatrix} \widetilde{x}_1(t) \\ \widetilde{x}_2(t) \\ \vdots \\ \widetilde{x}_N(t) \end{bmatrix} < 0, \tag{19}$$

where l_{ii}, W_i, V_j are defined as before.

So,

$$\lim_{t\to\infty} \left\|x_i(t) - \overline{x}(t)\right\| = 0. \tag{20}$$

These complete the proof. □

Theorem 9. *Network* (4) *solves an agreement problem faster than the same network without the state predictor.*

Proof. The proof is similar to that of Theorem 2 in [33]. □

4. Simulations

In this section, we give the numerical simulations to illustrate the analytical results.

Consider a small network with the undirected topology described as the following symmetric matrix:

$$A = \begin{bmatrix} 0 & 0.0964 & 0.0757 & 0.0570 \\ 0.0964 & 0 & 0.1199 & 0.1396 \\ 0.0757 & 0.1199 & 0 & 0.0581 \\ 0.0570 & 0.1396 & 0.0581 & 0 \end{bmatrix}, \tag{21}$$

where all nodes of the pagebreak network and their synchronous goal will obey the same nonlinear dynamics described as the Lorenz system:

$$f(x(t)) = f\left(x^1, x^2, x^3\right) = \begin{cases} \dot{x}^1 = 10\left(x^2 - x^1\right) \\ \dot{x}^2 = 28x^1 - x^1x^3 - x^2 \\ \dot{x}^3 = x^1x^2 - \dfrac{8}{3}x^3, \end{cases} \tag{22}$$

as shown in Figure 1.

Figure 2 describes the convergence of the state errors on the x-axis, y-axis, and z-axis, respectively. From this figure, we can see that all nodes of the above network can synchronize to the synchronous state gradually. With the same initial state and the same nonlinear dynamics, influenced by the same adaptive strategy, it can be easy to find as in Figure 3 that the network with a state predictor can also synchronize to the synchronous state and be faster than the network without a state predictor.

5. Conclusion

In this paper, we have investigated the adaptive synchronization of complex dynamical networks with nonlinear dynamics. By introducing local decentralized adaptive strategies to the coupling strengths, we have proved that the network with a state predictor can synchronize to the synchronous state.

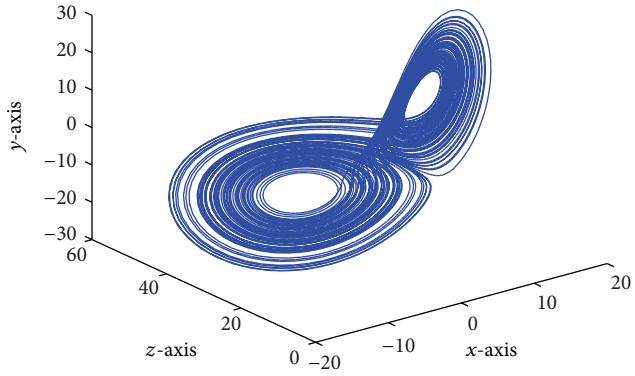

Figure 1: The nonlinear dynamics of the network.

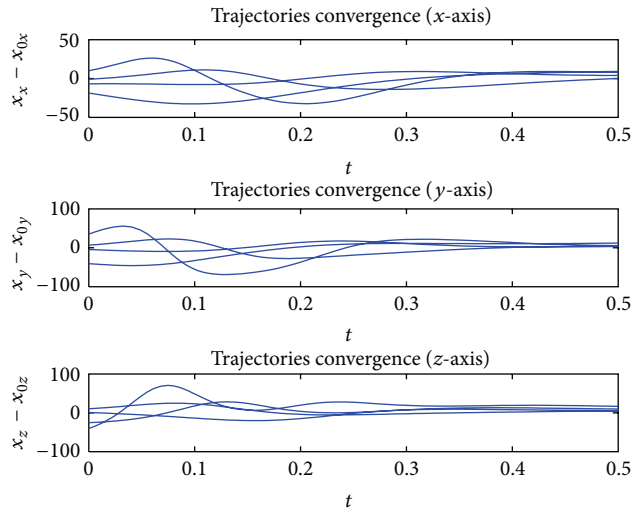

Figure 2: The trajectories of four agents in the dynamical network without a state predictor.

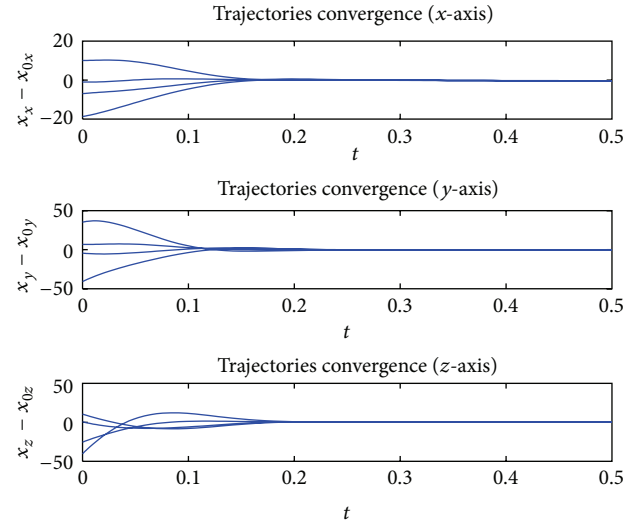

Figure 3: The trajectories of four agents in the dynamical network with a state predictor when $\gamma = 200$.

Acknowledgments

This work was supported in part by the National Natural Science Foundation of China under Grant no. 61304049, no. 61174116, the Beijing Natural Science Foundation Program 4132021, Science and Technology Development Plan Project of Beijing Education Commission (no. KM201310009011), and Funding Project for Academic Human Resources Development in Institutions of Higher Learning Under the Jurisdiction of Beijing Municipality (PHR201108055).

References

[1] X. F. Wang and G. Chen, "Pinning control of scale-free dynamical networks," *Physica A*, vol. 310, no. 3-4, pp. 521–531, 2002.

[2] P. De Lellis, M. di Bernardo, and F. Garofalo, "Synchronization of complex networks through local adaptive coupling," *Chaos*, vol. 18, no. 3, Article ID 037110, p. 8, 2008.

[3] H. Su, Z. Rong, M. Chen, X. Wang, G. Chen, and H. Wang, "Decentralized adaptive pinning control for cluster synchronization of complex dynamical networks," *EEE Transactions on Cybernetics*, vol. 43, pp. 394–399, 2013.

[4] W. Yu, G. Chen, J. Lü, and J. Kurths, "Synchronization via pinning control on general complex networks," *SIAM Journal on Control and Optimization*, vol. 51, no. 2, pp. 1395–1416, 2013.

[5] B. Liu, X. Wang, H. Su, Y. Gao, and L. Wang, "Adaptive second-order consensus of multi-agent systems with heterogeneous nonlinear dynamics and timevarying delays," *Neurocomputing*, vol. 118, pp. 289–300, 2013.

[6] H. Su and W. Zhang, "Second-order consensus of multiple agents with coupling delay," *Communications in Theoretical Physics*, vol. 51, pp. 101–109, 2009.

[7] B. Liu, W. Hu, J. Zhang, and H. Su, "Controllability of discrete-time multi-agent systems with multiple leaders on fixed networks," *Communications in Theoretical Physics*, vol. 58, pp. 856–862, 2012.

[8] H. Su, M. Chen, J. Lam, and Z. Lin, "Semi-global leader-following consensus of linear multi-agent systems with input saturation via low gain feedback," *IEEE Transactions on Circuits and Systems*, vol. 60, pp. 1881–1889, 2013.

[9] G. Wen, Z. Duan, W. Yu, and G. Chen, "Consensus of multi-agent systems with nonlinear dynamics and sampled-data information: a delayed-input approach," *International Journal of Robust and Nonlinear Control*, vol. 23, no. 6, pp. 602–619, 2013.

[10] W. Yu, P. DeLellis, G. Chen, M. di Bernardo, and J. Kurths, "Distributed adaptive control of synchronization in complex networks," *IEEE Transactions on Automatic Control*, vol. 57, no. 8, pp. 2153–2158, 2012.

[11] H. Su, M. Chen, X. Wang, H. Wang, and N. V. Valeyev, "Adaptive cluster synchronization of coupled harmonic oscillators with multiple leaders," *IET Control Theory and Applications*, vol. 7, pp. 765–772, 2013.

[12] M. Wang, H. Su, M. Zhao, M. Chen, and H. Wang, "Flocking of multiple autonomous agents with preserved network connectivity and heterogeneous nonlinear dynamics," *Neurocomputing*, vol. 115, pp. 169–177, 2013.

[13] W. Zhang, H. Su, and J. Wang, "Computation of upper bounds for the solution of continuous algebraic riccati equations," *Circuits, Systems and Signal Processing*, vol. 32, pp. 1477–1488, 2013.

[14] W. Yu, G. Chen, and J. Lü, "On pinning synchronization of complex dynamical networks," *Automatica*, vol. 45, no. 2, pp. 429–435, 2009.

[15] P. Lin and Y. Jia, "Consensus of second-order discrete-time multi-agent systems with nonuniform time-delays and dynamically changing topologies," *Automatica*, vol. 45, no. 9, pp. 2154–2158, 2009.

[16] Z. Tang, T. Huang, J. Shao, and J. Hu, "Consensus of second-order multi-agent systems with nonuniform time-varying delays," *Neurocomputing*, vol. 97, pp. 410–414, 2012.

[17] H. Su, X. Wang, and Z. Lin, "Flocking of multi-agents with a virtual leader," *IEEE Transactions on Automatic Control*, vol. 54, no. 2, pp. 293–307, 2009.

[18] Z. Hou, L. Cheng, and M. Tan, "Decentralized robust adaptive control for the multiagent system consensus problem using neural networks," *IEEE Transactions on Systems, Man, and Cybernetics-Patr B*, vol. 39, pp. 636–647, 2009.

[19] P. De Lellis, M. di Bernardo, and F. Garofalo, "Synchronization of complex networks through local adaptive coupling," *Chaos*, vol. 18, no. 3, Article ID 037110, p. 8, 2008.

[20] H. Su, X. Wang, and G. Chen, "Rendezvous of multiple mobile agents with preserved network connectivity," *Systems & Control Letters*, vol. 59, no. 5, pp. 313–322, 2010.

[21] H. Su, G. Chen, X. Wang, and Z. Lin, "Adaptive second-order consensus of networked mobile agents with nonlinear dynamics," *Automatica*, vol. 47, no. 2, pp. 368–375, 2011.

[22] Y. Hu, H. Su, and J. Lam, "Adaptive consensus with a virtual leader of multiple agents governed by locally Lipschitz nonlinearity," *International Journal of Robust and Nonlinear Control*, vol. 23, no. 9, pp. 978–990, 2013.

[23] W. Zhang, H. Su, H. Wang, and Z. Han, "Full-order and reduced-order observers for one-sided Lipschitz nonlinear systems using Riccati equations," *Communications in Nonlinear Science and Numerical Simulation*, vol. 17, no. 12, pp. 4968–4977, 2012.

[24] O. Faydasicok and S. Arik, "A new robust stability cirterion for dynamical neural networks with multiple time delays," *Neurocomputing*, vol. 99, pp. 290–297, 2013.

[25] H. Su, "Flocking in multi-agent systems with multiple virtual leaders based only on position measurements," *Communications in Theoretical Physics*, vol. 57, pp. 801–807, 2012.

[26] J. Zhang, M. Li, and B. Liu, "Synchronization of a complex network for neighboring agents with time-varying delays," *Communications in Computer and Information Science*, vol. 225, pp. 73–81, 2011.

[27] B. Liu, T. Chu, L. Wang, Z. Zuo, G. Chen, and H. Su, "Controllability of switching networks of multi-agent systems," *International Journal of Robust and Nonlinear Control*, vol. 22, no. 6, pp. 630–644, 2012.

[28] W. Zhang, H. Su, Y. Liang, and Z. Han, "Robust stability test for uncertain discrete-time systems: a descriptor system approach," *Latin American Applied Research*, vol. 41, pp. 359–364, 2011.

[29] W. Yu, "A LMI-based approach to global asymptotic stability of neural networks with time varying delays," *Nonlinear Dynamics*, vol. 48, no. 1-2, pp. 165–174, 2007.

[30] H. Su, X. Wang, and Z. Lin, "Synchronization of coupled harmonic oscillators in a dynamic proximity network," *Automatica*, vol. 45, no. 10, pp. 2286–2291, 2009.

[31] R. Olfati-Saber and R. M. Murray, "Consensus problems in networks of agents with switching topology and time-delays," *IEEE Transactions on Automatic Control*, vol. 49, no. 9, pp. 1520–1533, 2004.

[32] H. Su, X. Wang, and G. Chen, "A connectivity-preserving flocking algorithm for multi-agent systems based only on position measurements," *International Journal of Control*, vol. 82, no. 7, pp. 1334–1343, 2009.

[33] G. Xi, W. Huang, and X. Li, "Consensus of multi-agent system with state predictor," *Control and Decision*, vol. 25, pp. 669–772, 2010.

[34] K. Peng, H. Su, and Y. Yang, "Coordinated control of multi-agent systems with a varying-velocity leader and input saturation," *Communications in Theoretical Physics*, vol. 52, pp. 449–456, 2009.

[35] H. Su, X. Wang, and W. Yang, "Flocking in multi-agent systems with multiple virtual leaders," *Asian Journal of Control*, vol. 10, no. 2, pp. 238–245, 2008.

[36] H. Su, N. Zhang, M. Z. Q. Chen, H. Wang, and X. Wang, "Adaptive flocking with a virtual leader of multiple agents governed by locally Lipschitz nonlinearity," *Nonlinear Analysis: Real World Applications*, vol. 14, no. 1, pp. 798–806, 2013.

[37] B. Liu, T. Chu, and L. Wang, "Stability and oscillation of swarm with interaction time delays," in *Proceedings of the American Control Conference*, pp. 4600–4605, 2007.

[38] C. Godsil and G. Royle, *Algebraic Graph Theory*, vol. 207, Springer, New York, NY, USA, 2001.

Hindawi Publishing Corporation
Journal of Applied Mathematics
Volume 2013, Article ID 361926, 8 pages
http://dx.doi.org/10.1155/2013/361926

Research Article

An Irregular Flight Scheduling Model and Algorithm under the Uncertainty Theory

Deyi Mou and Wanlin Zhao

Institute of Mathematics for Applications, Civil Aviation University of China, Tianjin 300300, China

Correspondence should be addressed to Deyi Mou; deyimou@hotmail.com

Received 20 June 2013; Revised 15 August 2013; Accepted 18 August 2013

Academic Editor: Zhiwei Gao

Copyright © 2013 D. Mou and W. Zhao. This is an open access article distributed under the Creative Commons Attribution License, which permits unrestricted use, distribution, and reproduction in any medium, provided the original work is properly cited.

The flight scheduling is a real-time optimization problem. Whenever the schedule is disrupted, it will not only cause inconvenience to passenger, but also bring about a large amount of operational losses to airlines. Especially in case an irregular flight happens, the event is unanticipated frequently. In order to obtain an optimal policy in airline operations, this paper presents a model in which the total delay minutes of passengers are considered as the optimization objective through reassigning fleets in response to the irregular flights and which takes into account available resources and the estimated cost of airlines. Owing to the uncertainty of the problem and insufficient data in the decision-making procedure, the traditional modeling tool (probability theory) is abandoned, the uncertainty theory is applied to address the issues, and an uncertain programming model is developed with the chance constraint. This paper also constructs a solution method to solve the model based on the classical Hungarian algorithm under uncertain conditions. Numerical example illustrates that the model and its algorithm are feasible to deal with the issue of irregular flight recovery.

1. Introduction

A schedule we have made is frequently complex and dynamic, and uncertainty fittingly characters its intrinsic nature. Various unanticipated events will disrupt the system and make the schedule deviate from its intended course, even make it infeasible; furthermore, they will bring about a large quantity of losses. Then, we apply a method of disruption management to cope with it, to reach our goals while minimizing all the negative impact caused by disruptions and to get back on track in a timely manner while effectively using available resources. The disruption management refers to the real time dynamic revision of an operational plan when a disruption occurs. This is especially important in situations where an operational plan has to be published in advance, and its execution is subject to severe random disruptions. When a published operational plan is revised, there will be some deviation cost associated with the transition from the original plan to the new plan. To reduce such deviation cost, it is essential to take them into account when generating the new plan. Disruption management is a real-time practice and often requires a quick solution when a disruption occurs. The original planning problem usually is regarded as a one-time effort, so it is practically acceptable if generating an optimal operational plan takes a dozen of minutes or hours, or even longer. However, when a disruption occurs, it is critical to immediately provide a resolution to the responsible personnel. Therefore, real-time optimization techniques are very important.

In the area of transportation network, the schedule is not frequently executed according to the original plan; the system is often disturbed because of uncertainties, time delays, stochastic perturbations and so on. It is difficult to deal with the situations. So, the complex dynamic systems are raised by Gao et al. [1] in many varieties, including the areas of transportation networks, energy generation, storage and distribution, ecosystems, gene regulation and health delivery, safety and security systems, and telecommunications. They also present various mathematical methods and techniques to discuss the issues.

Airlines spend a great deal of efforts developing flight schedules for each of their fleets, and the daily operations of an airline are strictly based on a predetermined flight schedule. So, we know how important the fleet assignment is. But there are many uncertain factors having effect on the flights,

such as bad weather, aircraft failure, and airline traffic control. When the flight schedule is disrupted, a deviation from the flight schedule causes not only inconvenience to passenger, but also a large amount of operational cost because the airline has to make a new flight schedule that should satisfy all above constraints. So, the recovery of irregular flights faced by all airlines in the world is important and difficult to solve.

In USA, Delta Airline summed up 95,000 irregular flights, which affected 8,500,000 passengers and caused $500 million of losses (not including satisfaction losses of passengers). Each irregular flight caused losses up to more than $5,200 on average (not including losses to the passengers because of delays). In China, the domestic three major airlines executed 1,492,031 flights, but there were 258,866 irregular flights, and the rate of irregular flight was 17.35% in 2008. In the same year, the domestic airlines of small and medium sized had 176,785 flights, and 39,126 were irregular flights; the rate of irregular flight was up to 22.13%. Hence, the irregular flights brought a large amount of losses to airlines and inconvenience to passenger in actual life.

Due to the complexity of irregular flight scheduling problem, it is impossible for airlines to optimize existing resources relying on experience. The problem of searching fast and efficient algorithm and software has not been solved [2]. Then Teodorović and Guberinić [3] proposed a branch and bound method to minimize total delay minutes of passengers. Teodorobic and Stojkovic [4] raised dynamic programming model based on principle of lexicographic optimization, in order to minimize the cancelled flights and the total delay minutes of passengers. Jarrah et al. [5] introduced two separate models to minimize delay minutes and cancellations, respectively, solved by critical path method (CPD). Thus, the models were not able to consider the trade-off between delay and cancellation. Gang [6] constructed a two-commodities network flow model without solving method. Yan and Yang [7] formulated a model to minimize the duration of time in which the flight scheduling was disrupted. Argüello et al. [8, 9] presented resource allocation path flow model for fleet assignment; the model had clear ideas describing the essence of fleet assignment, but it was difficult to solve it. The period network optimization model about flight operations recovery could be found in Bard et al. [10], and it transformed the aircraft routing problem to a network flow model depending on discrete-time. Bratu and Barnhart [11] introduced a model of flight recovery and algorithm, when irregular flight happened, considering simultaneously aircraft, crew, and passengers, to decide whether to cancel the flight or not; the aim was to minimize the sum of total operation cost of interconnection, cost of passengers, and canceling cost. The objective function wished to search the trade-off point between each cost. The essence of above models was to construct flight leg and cancelled flight or not and select the minimum cost of the program. But how to generate feasible flight routes and calculate the cost of each route were difficult. There was not a paper which found the exact optimal solution by solving model directly for airlines up to now.

During the period of irregular flights, we cannot optimize all situations, and the reasons resulting to irregular flights are frequently uncertainty. For the decision making of uncertain problem, Kouvelis and Yu [12] described robust discrete optimization to deal with decision making in environment of significant data uncertainty. Matsveichuk et al. [13–15] dealt with the flow-shop minimum-length scheduling problem with n jobs processed on two machines when processing time is uncertain. Reference [15] presented minimal (maximal) cardinality of a J-solution generated by Johnson's algorithm to solve the problem above; however, for most generalizations of the two-machine flow-shop problem, the existence of polynomial algorithms is unlikely. For the duration of each irregular flight, we cannot analyze it without enough data, and it is not feasible to be dealt with by using stochastic programming. But we can invite experts to give the approximate duration of delay time and its uncertainty distribution. Then, we can apply uncertainty theory with a great premise. Here we will apply uncertainty theory to component model with uncertain programming and provide a stepwise algorithm for the model. In this paper, we search for minimizing the total delay minutes of passengers under the constraint of estimated cost. Next, this paper gives introduction of uncertainty theory and model, the method of constructing the model, the algorithm of solving model, and numerical example for the model. At last, we provide some future directions.

2. Preliminaries

In this section, some basic definitions are introduced, and the arithmetic operations of uncertain theory which needed throughout this paper are presented.

Definition 1 (Liu [16]). Let Γ be a nonempty set and $\mathscr{L}$ a σ-algebra over Γ. Each element $\Lambda \in \mathscr{L}$ is called an event. The set function $\mathscr{M}$ is called an uncertain measure if it satisfies the following four axioms.

Axiom 1 (normality). $\mathscr{M}\{\Gamma\} = 1$;

Axiom 2 (monotonicity). $\mathscr{M}\{\Lambda_1\} \leq \mathscr{M}\{\Lambda_2\}$ whenever $\Lambda_1 \subset \Lambda_2$;

Axiom 3 (self-duality). $\mathscr{M}\{\Lambda\} + \mathscr{M}\{\Lambda_c\} = 1$ for any event Λ;

Axiom 4 (countable subadditivity). For every countable sequence of events $\{\Lambda_i\}$, we have

$$\mathscr{M}\left\{\bigcup_{i=1}^{\infty}\Lambda_i\right\} \leq \sum_{i=1}^{\infty}\mathscr{M}\left\{\Lambda_i\right\}. \tag{1}$$

Definition 2 (Liu [16]). Let Γ be a nonempty set, $\mathscr{L}$ a σ-algebra over Γ, and $\mathscr{M}$ an uncertain measure. Then the triple $(\Gamma, \mathscr{L}, \mathscr{M})$ is called on uncertainty space.

Definition 3 (Liu [16]). An uncertain variable $\boldsymbol{\xi}$ is a measurable function from the uncertainty space $(\boldsymbol{\Gamma}, \mathscr{L}, \mathscr{M})$ to the set of real numbers; that is, for any Borel set $\mathbf{B}$ of real numbers, the set

$$\{\boldsymbol{\xi} \in \mathbf{B}\} = \{\gamma \in \boldsymbol{\Gamma} \mid \xi(\gamma) \in \mathbf{B}\} \tag{2}$$

is an event.

For a sequence of uncertain variables $\xi_1, \xi_2, \ldots, \xi_n$ and a measurable function f, Liu [17] proved that

$$\boldsymbol{\xi} = f(\xi_1, \xi_2, \ldots, \xi_n) \tag{3}$$

defined as $\xi(\gamma) = f(\xi_1(\gamma), \xi_2(\gamma), \ldots, \xi_n(\gamma))$, for all $\gamma \in \boldsymbol{\Gamma}$ is also an uncertain variable. In order to describe an uncertain variable, a concept of uncertainty distribution is introduced as follows.

Definition 4 (Liu [16]). The uncertainty distribution $\boldsymbol{\Phi}$ of an uncertain variable $\boldsymbol{\xi}$ is defined by

$$\boldsymbol{\Phi}(\mathbf{x}) = \mathscr{M}\{\boldsymbol{\xi} \leq \mathbf{x}\} \tag{4}$$

for any real number $\mathbf{x}$.

Peng and Li [18] proved that a function $\boldsymbol{\Phi} : \Re \to [0, 1]$ is an uncertainty distribution if and only if it is a monotone increasing function unless $\boldsymbol{\Phi}(x) \equiv 0$ or $\boldsymbol{\Phi}(x) \equiv 1$. The inverse function $\boldsymbol{\Phi}^{-1}$ is called the inverse uncertainty distribution of $\boldsymbol{\xi}$. Inverse uncertainty distribution is an important tool in the operation of uncertain variables.

Theorem 5 (Liu [16]). *Let $\xi_1, \xi_2, \ldots, \xi_n$ be independent uncertain variables with regular uncertainty distributions $\boldsymbol{\Phi}_1, \boldsymbol{\Phi}_2, \ldots, \boldsymbol{\Phi}_n$, respectively. If $f(x_1, x_2, \ldots, x_n)$ is an increasing function with respect to $x_1, x_2, \ldots, x_m$ and decreasing with respect to $x_{m+1}, x_{m+2}, \ldots, x_n$, then*

$$\boldsymbol{\xi} = f(\xi_1, \xi_2, \ldots, \xi_n) \tag{5}$$

is an uncertain variable with inverse uncertainty distribution

$$\begin{aligned}\boldsymbol{\Psi}^{-1}(\alpha) = f\Big(&\boldsymbol{\Phi}_1^{-1}(\alpha), \boldsymbol{\Phi}_2^{-1}(\alpha), \ldots, \boldsymbol{\Phi}_m^{-1}(\alpha), \\ &\boldsymbol{\Phi}_{m+1}^{-1}(1-\alpha), \ldots, \boldsymbol{\Phi}_n^{-1}(1-\alpha)\Big).\end{aligned} \tag{6}$$

Expected value is the average of an uncertain variable in the sense of uncertain measure. It is an important index to rank uncertain variables.

Definition 6 (Liu [16]). Let $\boldsymbol{\xi}$ be an uncertain variable. Then the expected value of $\boldsymbol{\xi}$ is defined by

$$E[\boldsymbol{\xi}] = \int_0^\infty \mathscr{M}\{\boldsymbol{\xi} \geq r\}\, dr - \int_{-\infty}^0 \mathscr{M}\{\boldsymbol{\xi} \leq r\}\, dr \tag{7}$$

provided that at least one of the two integrals is finite.

In order to calculate the expected value via inverse uncertainty distribution, Liu [17] proved that

$$\begin{aligned}E[\boldsymbol{\xi}] = \int_0^1 f\Big(&\boldsymbol{\Phi}_1^{-1}(\alpha), \ldots, \boldsymbol{\Phi}_m^{-1}(\alpha), \\ &\boldsymbol{\Phi}_{m+1}^{-1}(1-\alpha), \ldots, \boldsymbol{\Phi}_n^{-1}(1-\alpha)\Big)\, d\alpha\end{aligned} \tag{8}$$

under the condition described in Theorem 5. Generally, the expected value operator E has no linearity property for arbitrary uncertain variables. But, for independent uncertain variables $\boldsymbol{\xi}$ and $\boldsymbol{\eta}$ with finite expected values, we have

$$E[a\boldsymbol{\xi} + b\boldsymbol{\eta}] = aE[\boldsymbol{\xi}] + bE[\boldsymbol{\eta}] \tag{9}$$

for any real numbers a and b.

Theorem 7 (Liu [16]). *Assume the objective function $f(\mathbf{x}, \xi_1, \xi_2, \ldots, \xi_n)$ is strictly increasing with respect to $\xi_1, \xi_2, \ldots, \xi_m$ and strictly decreasing with respect to $\xi_{m+1}, \xi_{m+2}, \ldots, \xi_n$. If $\xi_1, \xi_2, \ldots, \xi_n$ are independent uncertain variables with uncertainty distribution $\Phi_1, \Phi_2, \ldots, \Phi_n$, respectively, then the expected objective function*

$$E[f(\mathbf{x}, \xi_1, \xi_2, \ldots, \xi_n)] \tag{10}$$

is equal to

$$\begin{aligned}\int_0^1 f\Big(&\mathbf{x}, \boldsymbol{\Phi}_1^{-1}(\alpha), \ldots, \boldsymbol{\Phi}_m^{-1}(\alpha), \\ &\boldsymbol{\Phi}_{m+1}^{-1}(1-\alpha), \ldots, \boldsymbol{\Phi}_n^{-1}(1-\alpha)\Big)\, d\alpha.\end{aligned} \tag{11}$$

Theorem 8 (Liu [16]). *Assume $f(\mathbf{x}, \xi_1, \xi_2, \ldots, \xi_n)$ is strictly increasing with respect to $\xi_1, \xi_2, \ldots, \xi_m$ and strictly decreasing with respect to $\xi_{m+1}, \xi_{m+2}, \ldots, \xi_n$, and $g_j(\mathbf{x}, \xi_1, \xi_2, \ldots, \xi_n)$ are strictly increasing with respect to $\xi_1, \xi_2, \ldots, \xi_k$ and strictly decreasing with respect to $\xi_{k+1}, \xi_{k+2}, \ldots, \xi_n$, for $j = 1, 2, \ldots, p$. If $\xi_1, \xi_2, \ldots, \xi_n$ are independent uncertain variables with uncertainty distributions $\Phi_1, \Phi_2, \ldots, \Phi_n$, respectively, then the uncertain programming*

$$\begin{aligned}&\min_x \quad E[f(\mathbf{x}, \xi_1, \xi_2, \ldots, \xi_n)], \\ &\text{s.t.} \quad \mathscr{M}\{g_j(\mathbf{x}, \xi_1, \xi_2, \ldots, \xi_n) \leq C\} \geq \alpha_j, \quad j = 1, 2, \ldots, p,\end{aligned} \tag{12}$$

is equivalent to the crisp mathematical programming

$$\begin{aligned}\min_x \quad &\int_0^1 f\Big(\mathbf{x}, \boldsymbol{\Phi}_1^{-1}(\alpha), \ldots, \boldsymbol{\Phi}_m^{-1}(\alpha), \\ &\qquad \boldsymbol{\Phi}_m + 1^{-1}(1-\alpha), \ldots, \boldsymbol{\Phi}_n^{-1}(1-\alpha)\Big), \\ \text{s.t.} \quad &g_j\Big(\mathbf{x}, \boldsymbol{\Phi}_1^{-1}(\alpha_j), \ldots, \boldsymbol{\Phi}_k^{-1}(\alpha_j), \boldsymbol{\Phi}_{k+1}^{-1}(1-\alpha_j), \ldots, \\ &\qquad \boldsymbol{\Phi}_n^{-1}(1-\alpha_j)\Big) \leq C, \quad j = 1, 2, \ldots, p.\end{aligned} \tag{13}$$

3. Problem Description

For airlines, irregular flights are not expected but they are inevitable frequently owing to objective factors in practice. So, each airline has its own methods to deal with the issue. At present, the irregular flight recovery is a complex and huge project to airlines. Generally speaking, the Airline

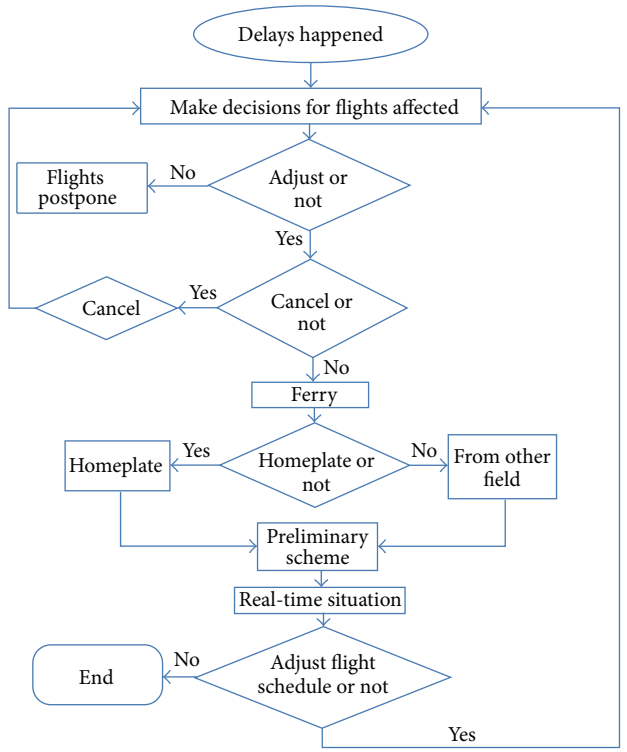

Figure 1: Flow chart of procedure.

Operational Control (AOC) of each airline takes the following procedure for dealing with the irregular flights.

Step 1. Maintenance Control Center (MCC) reports delays to AOC.

Step 2. AOC gets detailed information from relevant departments.

Step 3. AOC gives the expected minutes of flight delay according to the information.

Step 4. AOC makes a decision whether the first delay flight cancels or postpones.

Step 5. Making decisions to the following flights.

Step 6. AOC always pays attention to real-time situations and whether the decision will be to remake or not based on real-time changes.

The flow chart of procedure is shown in Figure 1. From this flow chart, we can get that it is difficult to make a suitable and reasonable schedule. In this paper, we resolve the irregular flight problem about fleet reassignment based on the flow chart. When irregular flights happen, the durations of delay time only are predicted through the data given by experts, in order to help the decision makers to reassign fleets better. During the period of delay time, the airlines can postpone the flights, minimize the delay minutes or delay cost by reassigning and canceling flights, or minimize the total delay minutes under the constraint of estimated cost by reassigning flights; in a word, the aim is to serve the passengers better.

Tobias [19] presented a tabu search and a simulated annealing approach to the flight perturbation problem and used a tree-search algorithm to find new schedules for airlines, and it could be successfully used to solve the flight perturbation problem. Gao et al. [20] put forward a greedy simulated annealing algorithm which integrated the characteristics of GRASP and simulated annealing algorithm, and the algorithm was able to solve large-scale irregular flight schedule recovery. Xiuli [21] introduced a stepwise-delay algorithm to research irregular flight problem. She solved the problem from the delay cost and delay minutes, respectively. In the paper, the delay minutes and delay cost were set down as constant values. From comparing the two methods, Xiuli got the result that to construct the model with delay minutes obtained successful results.

But there are not enough data of irregular flights to analyze; the data is difficult to deal with under the stochastic condition. In actual situations, we cannot obtain enough data to analyze, so, in this paper, we treat the duration of delay time of aircraft as an uncertain variable during the period of irregular flights happening, and its distribution is given by experts. Under the constraints of estimated cost and aircraft assignment model, the objective function is to minimize the total delay minutes of passengers relying on irregular flights. Then we solve the model and get the solution.

4. Model Development

In actual situations, the factors which cause irregular flights are uncontrolled frequently. Especially when the weather is bad and aircraft failure happens, the durations of bad weather and aircraft failure cannot be predicted exactly because of lacking enough data under stochastic condition. In this model, we consider the delay time as an uncertain variable, and its uncertainty distribution is given by experts.

Firstly, we introduce the following notations to present the mathematical formulation throughout the remainder of this paper.

Indices, Sets, and Parameters

f: index for set of flights F

s: index for set of airports S

i: index for set of types of aircrafts I

I: set of types of aircrafts

F: set of flights

S: set of airports

A: set of available aircrafts

t_i: ready time of aircraft i

t_f^d: planning departure time of flight f

t_f^a: planning arrival time of flight f

t_i^f: uncertain delay time of flight f executed by type i of aircraft, $t_i^f \sim \varphi_i(t)$, $i \in A$

p_f^b, p_f^e: reservation number of business and economy class in flight f

q_f^b, q_f^e: fare of a ticket of business and economy class in flight f

n_f: total reservations of flight f

u: disappointment rate of passengers

v: losses value of passengers per minute

p_i^f: delay loss of flight f executed by aircraft i, $p_i^f = wn_f t_i^f$, when $t_i^f > 0$, or = 0

P_f: cost of canceling flight f

β: airport usage charge per minute

γ: cost of depreciation of aircraft per minute

c_i^f: delay cost of flight f executed by aircraft i

c_0^f: estimated cost of flight f

$C^f = (c_i^f), C_0 = (c_0^f)$

α_0: confidence level

k: weight of cost of cancelling flight

x_i^f: binary variable, = 1 if flight f is executed by aircraft i and 0 otherwise

y_f: binary variable, = 1 if flight f is canceled and 0 otherwise.

Xiuli [21] presented two models to deal with the irregular flight. Their objective functions were to minimize delay minutes and total delay cost:

$$\min\left(\sum_{f\in F}\sum_{i\in A} x_i^f p_i^f + \sum_{f\in F} kn_f y_f\right), \qquad \min C^f\left(\mathbf{x}, t^f\right). \tag{14}$$

In our paper, we construct the model under the basis of the two models, and integrate them to one. Next, based on the analysis of the decision making process, we integrate the estimated cost and the total delay minutes of passengers model and propose the following model:

$$\min \quad E\left\{\sum_{f\in F}\sum_{i\in A} x_i^f p_i^f + \sum_{f\in F} kn_f y_f\right\}, \tag{15}$$

$$\text{s.t.} \quad \mathscr{M}\left\{C^f\left(\mathbf{x}, t^f\right) < C_0\right\} \geq \alpha_0, \tag{16}$$

$$\sum_{i\in A} x_i^f + y_f = 1, \quad \forall f \in F, a, d \in S, \tag{17}$$

$$c_i^f = \left\{x_i^f\left(p_f^e \times q_f^e + p_f^b \times q_f^b\right) \times u + (\beta+\gamma) t_i^f + p_f y_f\right\}, \tag{18}$$

$$y_f = 1 - x_i^f,$$

$$\sum_{f\in F} x_i^f \leq 1, \quad \forall i \in A, \tag{19}$$

$$x_i^f \in \{0,1\}, \quad y_f \in \{0,1\}. \tag{20}$$

In the model, (15) is the objective function of minimizing the total delay minutes of passengers, the former is the delay minutes depending on the irregular flights, the latter is the equivalent delay minutes relying on flights cancelled; (16) is the constraint of estimated cost; (17) states a flight is either flown once by an aircraft or canceled; (18) is the delay cost of flight f executed by aircraft i; (19) assigns no more than one aircraft to execute flight f; and (20) is the integer constraint of 0-1.

The model is to minimize the total delay minutes of passengers under the estimated cost. Generally speaking, we need to recur to intelligent algorithm to solve the model; it is a huge project to get its solution [22].

But, it will be much easier under the uncertainty theory to deal with the problem. Note that $C^f(\mathbf{x}, t^f)$ is strictly increasing with respect to t_i^f $(i = 1, 2, \ldots, n)$, and $t_1^f, t_2^f, \ldots, t_n^f$ are independent uncertain variables with uncertainty distributions $t_i^f \sim \varphi_i(t)$ $(i = 1, 2, \ldots, n)$, respectively. According to Theorem 8, the above model will be equivalent to the following deterministic model:

$$\begin{aligned}
\min \quad & \left\{\sum_{f\in F}\sum_{i\in A}\left(x_i^f wn_f \int_0^1 \varphi_i^{-1}\left(t_i^f, \alpha\right) d\alpha\right) + \sum_{f\in F} kn_f y_f\right\}, \\
\text{s.t.} \quad & \boldsymbol{\Phi}^{-1}(\mathbf{x}, \alpha_0) < C_0, \\
& \sum_{i\in A} b_f^{di} b_f^{ai} x_i^f + y_f = 1, \quad \forall f \in F, a, d \in S, \\
& c_i^f = \left\{x_i^f\left(p_f^e \times q_f^e + p_f^b \times q_f^b\right) \times u + \beta t_i^f + p_f y_f\right\}, \quad y_f = 1 - x_i^f, \\
& \sum_{f\in F} x_i^f \leq 1, \quad \forall i \in A, \\
& x_i^f \in \{0,1\}, \quad y_f \in \{0,1\}.
\end{aligned} \tag{21}$$

In this model, the objective function is to minimize the expected total delay minutes of passengers, and the estimated cost is treated as a chance constraint, where

$$\boldsymbol{\Phi}^{-1}(\mathbf{x}, \alpha) = \left(\varphi_i^{-1}\left(t_i^f, \alpha\right)\right). \tag{22}$$

5. Solution Method and Complexity

5.1. Solution Method. In the model, there is an objective function, but it contains two kinds of decision variables x_i^f and y_f. To solve the model, we make use of a stepwise-delay algorithm. The procedure of solution is as follows.

Step 1. Based on the information postponed, getting the timetable of flights as YW.

Table 1: Estimated cost.

f	c_0/RMB
xx1337	55224
xx1338	52452
xx1223	63540
xx1224	88740
xx1209	36546
xx1519	26760
xx1210	34880
	Total: 35,8142

Step 2. Sorting the delay flights depending on original departure time from the timetable of delay flight, and searching the first airport where delay happened. During the delay period, we retrieve the serial number of aircrafts through the airport, and note them down in the table CH.

Step 3. Finding available aircrafts in the delay airport, a time permutation table T is built via the constraints, $\mathbf{\Phi}^{-1}(\mathbf{x}, \alpha) < C_0$. The delay minutes are replaced by $E[t_i^f]$; then we can get the following:

$$T = \left(E\left[t_i^f\right]\right) = \begin{array}{c} \\ f_1 \\ f_2 \\ \vdots \\ f_n \end{array} \begin{array}{c} \begin{array}{cccc} 1* & 2* & \cdots & n* \end{array} \\ \begin{pmatrix} E\left[t_1^1\right] & E\left[t_1^2\right] & \cdots & E\left[t_1^n\right] \\ E\left[t_2^1\right] & E\left[t_2^2\right] & \cdots & E\left[t_2^n\right] \\ \vdots & \vdots & \vdots & \vdots \\ E\left[t_n^1\right] & E\left[t_n^2\right] & \cdots & E\left[t_n^n\right] \end{pmatrix} \end{array}. \quad (23)$$

Step 4. For T, we use Hungarian algorithm to reassign available aircraft and get the new timetable:

$$p = \begin{array}{c} \\ f_1 \\ f_2 \\ \vdots \\ f_n \end{array} \begin{array}{c} \begin{array}{cccc} 1* & 2* & \cdots & n* \end{array} \\ \begin{pmatrix} 1 & 0 & \cdots & 0 \\ 0 & 0 & \cdots & 0 \\ \vdots & \vdots & \vdots & \vdots \\ 0 & 1 & \cdots & 0 \end{pmatrix} \end{array}. \quad (24)$$

Step 5. Renewing the YW, the relevant aircraft assignment is replaced by the consequence from Step 4; then turn to Step 2, and steps are repeated until there are no delay flights or optimal flights. Then the results are put out.

5.2. Complexity. For one delay airport, we use Hungarian algorithm to reassign fleets in that the complexity is $O(n^2)$. When the number of delay airports is m, the algorithm will be iterated in each airport, so that the total complexity is $O(mn^2)$ which is a polynomial. So it is a feasible method in applications.

6. Illustrative Example and Computational Result

In order to test the model and the solution algorithms applied in the actual situation, we perform numerical tests based on the domestic operation department with reasonable assumptions.

We suppose that the airline has the hub airport of s_1; the flights are s_1 to s_2, s_1 to s_3, and s_2 to s_3. Its types of aircrafts are $A310$ and $B737$. Assume that the delay minutes of irregular flights are linear uncertain variables, and their distributions are as follows:

$$\begin{aligned} &t_1 \sim \mathscr{L}(10:40, 11:20), \qquad t_2 \sim \mathscr{L}(15:50, 16:30), \\ &t_3 \sim \mathscr{L}(12:10, 12:50), \qquad t_4 \sim \mathscr{L}(15:10, 15:50), \\ &t_5 \sim \mathscr{L}(16:20, 17:00). \end{aligned} \quad (25)$$

The disappointment rate of passengers $u = 0.07t_i^f/60 + 0.4$. The delay minutes of passengers are as follows:

$$p_i^f = \begin{cases} 0.3n_f \times \dfrac{t_i^f}{60} & t_i^f \in [0, 60), \\ 0.5n_f \times \dfrac{t_i^f}{60} & t_i^f \in [60, 120), \\ 0.7n_f \times \dfrac{t_i^f}{60} & t_i^f \in [120, 240), \\ 0.9n_f \times \dfrac{t_i^f}{60} & t_i^f \in [240, \infty). \end{cases} \quad (26)$$

We assume that the constraint of estimated cost is shown in Table 1.

At last, we assume that the timetable is shown in Table 2.

The predetermined confidence level $\alpha_0 = 0.9$.

Then, we use the algorithm and get the optimal solution shown in Table 3.

Comparing Tables 1, 2 and 3, we can get the optimal solution through the model. From Table 3, we can see that the cost is 196,637 RMB under the constraint of 358,142 RMB, and the flight delay time is ten minutes less than Table 2. Based on Tables 3 and 2, there is a great difference in the total delay minutes of passengers. Table 2 is about 5.5 times as many as Table 3, and there is not a cancelled flight in Table 3. So the reassignment of Table 3 is much better than Table 2. The example shows that the model and algorithm can get a method of flight recovery better.

7. Conclusions and Future Directions

The irregular flights always happen in actual situations; in order to deal with the issue, in this paper, we developed a model for fleet reassignment based on uncertain programming during the period of irregular flights and presented a stepwise optimization method strategy based on Hungarian

Table 2: Timetable postponed.

i	f	t_f^d	t_f^a	t_i	$E(t_i^f)$/minute	p_f^b/q_f^b	p_f^e/q_f^e	b_f^{di}	b_f^{ai}
310/3912	xx3108	8:00	10:30	8:00	0	110/700	8/1400	s_1	s_2
310/3912	xx3109	11:00	13:30	11:00	0	120/700	8/1400	s_2	s_1
737/3010	xx1337	9:50	14:20	t_1	70	144/1800	9/3600	s_1	s_3
737/3010	xx1338	15:00	19:30	t_2	70	135/1800	8/3600	s_3	s_1
737/3023	xx1209	11:00	13:30	t_3	90	157/700	10/1400	s_1	s_2
737/3023	xx1210	14:00	16:30	t_4	90	140/700	10/1400	s_2	s_1
737/3982	xx1223	12:00	16:30	0:00	Canceled	175/1800	10/3600	s_1	s_3
737/3982	xx1224	17:00	21:30	0:00	Canceled	275/1800	10/3600	s_3	s_1
310/8010	xx1518	8:00	12:30	8:00	0	130/1800	10/3600	s_3	s_1
310/8010	xx1519	12:50	14:50	t_5	230	30/1800	0/3600	s_1	s_2

Total delay minutes of flights: 550; canceled: 2; value of objective function: 226,587.

Table 3: Timetable after reassigning.

i	f	t_f^d	t_f^a	t_i	$E(t_i^f)$/minute	b_f^{di}	b_f^{ai}
737/3010	xx1337	9:50	14:20	11:00	70	s_1	s_3
737/3010	xx1338	15:30	19:30	16:10	70	s_3	s_1
737/3023	xx1223	12:00	16:30	12:30	30	s_1	s_3
737/3023	xx1224	17:00	21:30	15:30	30	s_3	s_1
310/8010	xx1518	8:00	12:30	8:00	0	s_3	s_1
310/8010	xx1209	11:00	13:30	13:00	120	s_1	s_2
310/3912	xx3108	8:00	10:30	8:00	0	s_1	s_2
310/3912	xx3109	11:00	13:30	11:00	0	s_2	s_1
310/3912	xx1519	15:50	14:50	14:00	70	s_1	s_2
310/3912	xx1210	14:00	16:30	16:30	150	s_2	s_1

Total delay minutes of flights: 540;, canceled: 0; value of objective function: 41,410.
Total cost of flights delay: 196,637 RMB.

algorithm to solve the problem. Compared with the traditional model, we introduce an uncertain variable into the model and construct it based on uncertain programming. We consider the delay minutes as uncertain variables with their uncertainty distributions given by experts. We construct a stepwise optimization method based on Hungarian algorithm to solve the model. From results of the numerical example, the total delay minutes of passengers are declined extensively, and we can get that the model and algorithm are feasible to deal with the issue of irregular flights.

A major contribution of this paper is that we provide a comprehensive framework for fleet reassignment during the period of irregular flights happen. Much work still needs to be done to improve on the current framework. Partially, we believe future research can be conducted on an integral framework of fleet reassignment and crew schedule recovery. Thus approaching the irregular flights problem is more systematical. Furthermore, considering actual situations, we can also construct an integral uncertain and stochastic model; thus, dealing with the issue of irregular flights is more comprehensive.

Acknowledgments

This work was supported by the Fundamental Research Funds for the Central Universities (Grant ZXH2011C008). The authors would like to thank the anonymous referees for useful suggestions and comments on the earlier draft of this paper.

References

[1] Z. Gao, D. Kong, and C. Gao, "Modeling and control of complex dynamic systems: applied mathematical aspects," *Journal of Applied Mathematics*, vol. 2012, Article ID 869792, 5 pages, 2012.

[2] A. Mathur and J. P. Clarke, *How Healthy Is Your Operation*, AGIFORS, 2005.

[3] D. Teodorović and S. Guberinić, "Optimal dispatching strategy on an airline network after a schedule perturbation," *European Journal of Operational Research*, vol. 15, no. 2, pp. 178–182, 1984.

[4] D. Teodorovic and G. Stojkovic, "Model to reduce airline schedule disturbances," *Journal of Transportation Engineering*, vol. 121, no. 4, pp. 324–331, 1995.

[5] A. I. Z. Jarrah, G. Yu, N. Krishnamurthy, and A. Rakshit, "Decision support framework for airline flight cancellations and delays," *Transportation Science*, vol. 27, no. 3, pp. 266–280, 1993.

[6] Y. Gang, "An optimization model for airlines' irregular operations control," in *Proceedings of the International Symposium on Optimization Applications in Management and Engineering*, 1995.

[7] S. Yan and D. Yang, "A decision support framework for handling schedule perturbation," *Transportation Research B*, vol. 30, no. 6, pp. 405–419, 1996.

[8] M. F. Argüello, J. F. Bard, and G. Yu, "A GRASP for aircraft routing in response to groundings and delays," *Journal of Combinatorial Optimization*, vol. 1, no. 3, pp. 211–228, 1997.

[9] M. F. Argüello, J. F. Bard, and G. Yu, "Models and methods for managing airline irregular operations," *International Series in Operations Research & Management Science*, vol. 9, pp. 1–45, 1998.

[10] J. F. Bard, G. Yu, and M. F. Argüello, "Optimizing aircraft routings in response to groundings and delays," *IIE Transactions*, vol. 33, no. 10, pp. 931–947, 2001.

[11] S. Bratu and C. Barnhart, "Flight operations recovery: new approaches considering passenger recovery," *Journal of Scheduling*, vol. 9, no. 3, pp. 279–298, 2006.

[12] P. Kouvelis and G. Yu, *Robust Discrete Optimization and Its Applications*, vol. 14, Kluwer Academic, Boston, Mass, USA, 1997.

[13] N. Matsveichuk, S. Yuri, and W. Frank, "Pertial job-Oorder for solving the two-machine flow-shop minimum-length problem with uncertain processing times," *Information Control Problems in Manufacturing*, vol. 13, no. 1, pp. 1517–1522, 2009.

[14] N. M. Matsveichuk, Y. N. Sotskov, and F. Werner, "The dominance digraph as a solution to the two-machine flow-shop problem with interval processing times," *Optimization*, vol. 60, no. 12, pp. 1493–1517, 2011.

[15] C. T. Ng, N. M. Matsveichuk, Y. N. Sotskov, and T. C. E. Cheng, "Two-machine flow-shop minimum-length scheduling with interval processing times," *Asia-Pacific Journal of Operational Research*, vol. 26, no. 6, pp. 715–734, 2009.

[16] B. Liu, *Theory and Practice of Uncertain Programming*, Springer, Berlin, Germany, 2nd edition, 2007.

[17] B. Liu, *Uncertainty Theory*, 4th edition, 2012.

[18] J. Peng and S. G. Li, "Spanning tree problem of uncertain network," http://orsc.edu.cn/online/110228.pdf.

[19] T. Andersson, "Solving the flight perturbation problem with meta heuristics," *Journal of Heuristics*, vol. 12, no. 1-2, pp. 37–53, 2006.

[20] Q. Gao, X. Tang, and J. Zhu, "Research on greedy simulated annealing algorithm for irregular flight schedule recovery model," in *Advances in Grey Systems Research*, pp. 503–513, Springer, Berlin, Germany, 2009.

[21] Z. Xiuli, *Research on modeling and algorithm of airline irregular recovery [Ph.D. thesis]*, Nanjing University of Aeronautics and Astronautics, Nanjing, China, 2010.

[22] J. D. Petersen, G. Sölveling, J.-P. Clarke, E. L. Johnson, and S. Shebalov, "An optimization approach to airline integrated recovery," *Transportation Science*, vol. 46, no. 4, pp. 482–500, 2012.

Hindawi Publishing Corporation
Journal of Applied Mathematics
Volume 2013, Article ID 137056, 12 pages
http://dx.doi.org/10.1155/2013/137056

Research Article

Dynamics Control of the Complex Systems via Nondifferentiability

Carmen Nejneru,[1] Anca Nicuță,[2] Boris Constantin,[1] Liliana Rozemarie Manea,[3] Mirela Teodorescu,[4] and Maricel Agop[5,6]

[1] *Faculty of Materials Science and Engineering, "Gheorghe Asachi" Technical University of Iași, 41 D. Mangeron Boulevard, 700050 Iași, Romania*
[2] *Faculty of Civil Engineering and Building Services, "Gheorghe Asachi" Technical University of Iași, 1 D. Mangeron Boulevard, 700050 Iași, Romania*
[3] *Faculty of Textile, Leather Engineering and Industrial Management, "Gheorghe Asachi" Technical University of Iași, Dimitrie Mangeron 29, 700050 Iași, Romania*
[4] *Institute of Macromolecular Chemistry Petru Poni Iași, Aleea Grigore Ghica Voda, No. 41A, 700487 Iași, Romania*
[5] *Physics Department, Faculty of Machine Manufacturing and Industrial Management, "Gheorghe Asachi" Technical University of Iași, Professor Dr. Docent Dimitrie Mangeron Road, No. 59A, 700050 Iași, Romania*
[6] *Lasers, Atoms and Molecules Physics Laboratory, University of Science and Technology, Villeneuve d'Ascq, 59655 Lille, France*

Correspondence should be addressed to Maricel Agop; m.agop@yahoo.com

Received 29 May 2013; Accepted 12 July 2013

Academic Editor: Zhiwei Gao

Copyright © 2013 Carmen Nejneru et al. This is an open access article distributed under the Creative Commons Attribution License, which permits unrestricted use, distribution, and reproduction in any medium, provided the original work is properly cited.

A new topic in the analyses of complex systems dynamics, considering that the movements of complex system entities take place on continuum but nondifferentiable curves, is proposed. In this way, some properties of complex systems (barotropic-type behaviour, self-similarity behaviour, chaoticity through turbulence and stochasticization, etc.) are controlled through nondifferentiability of motion curves. These behaviours can simulate the standard properties of the complex systems (emergence, self-organization, adaptability, etc.).

1. Introduction

Complex systems are very large interdisciplinary research topics that have been intensively studied, particularly since the 1980s, by means of a combination of basic theory, derived especially from physics and computer simulation. Such kind of systems is composed of many interacting elemental units that were called "agents." Examples of complex systems can be found in human societies, the brain, internet, ecosystems, biological evolution, stock markets, economies, and many others [1–4].

The way in which such a system manifests cannot be predicted only by the behaviour of individual elements or by adding their behavior but is determined by the manner in which the elements relate to influence global behaviour. Among the most significant properties of complex systems are emergence, self-organization, adaptability, and so forth [5–9].

The *emergence* of a complex system can be represented by that state of the whole which does not include the sum of its elements.

Self-organization is another characteristic of complex systems. Examples of organization that manifests in nature are found from cells to organisms, ecosystems, and also planets, stars, and galaxies [5–9].

Another characteristic of complex systems is *adaptability*. This occurs when the system changes in response to some information. Continuously oscillating between equilibrium and disorder, complex systems are not "rigid." Any modification induced at microlevel generates a series of fluctuations, exploring new states of self-organization [5–9].

An example of a complex system is represented by polymers. Their forms present a multitude of organizations starting from simple, linear chains of identical structural units to very complex chains consisting of sequences of amino acids that form the building blocks of living things. Probably one of the most intriguing complex systems in nature is DNA, which creates cells by means of a simple but very elegant language. It is responsible for the remarkable way in which individual cells organize into complex systems like organs, and these organs form even more complex systems like organisms. The study of complex systems can offer a glimpse about the realistic dynamics of polymers, solving difficult problems as protein folding [6–10].

Correspondingly, the theoretical models that describe the complex systems dynamics become sophisticated and ambiguous too [6–10]. However the situation can be standardized taking into account that the complexity of interaction process imposes various temporal resolution scales, and the pattern evolution imposes different degrees of freedom.

In order to develop a new theoretical model we must admit that the complex systems that display chaotic behaviour are known to acquire self-similarity (space-time structures seem to appear) in association with strong fluctuations at all possible space-time scales [6–8]. Then, for temporal scales that are large with respect to the inverse of the highest Lyapunov exponent, the deterministic trajectories are replaced by a collection of potential trajectories and the concept of definite positions by that of probability density [11–14]. One of the most interesting examples is the collisions processes in plasma discharge as a complex system, where the dynamics of the particles can be described by Levi-type movements [15]: between two successive collisions, the particle trajectory is a straight line, with the trajectory becoming nondifferentiable in the impact point, which implies that there are left and right derivatives in this point. We note that the Brownian-type motion is a particular case of Levi-type motion [16].

Since the nondifferentiability appears as a universal property of the complex systems, it is necessary to construct a nondifferentiable physics. In such conjecture, by considering that the complexity of the interactions processes is replaced by nondifferentiability, it is no longer necessary to use the whole classical "arsenal" of quantities from the standard physics (differentiable physics) [12–14, 17, 18].

This topic was developed in [12–14, 19–23] using the scale relativity theory (SRT) [12–14]. In the framework of SRT we assume that the movements of complex system entities take place on continuous but nondifferentiable curves (fractal curves) so that all physical phenomena involved in the dynamics depend not only on the space-time coordinates but also on the space-time scales resolution. From such a perspective, the physical quantities that describe the dynamics of complex systems may be considered fractal functions [12–14]. Moreover, the entities of the complex system may be reduced to and identified with their own trajectories, so that the complex system will behave as a special interactionless "fluid" by means of its geodesics in a nondifferentiable (fractal) space.

In the present paper, we propose a new topic to analyse the complex systems dynamics using SRT. Considering that the entities of the complex system are moving on continuous but nondifferentiable curves, we show that the control of different behaviours of these systems implies nondifferentiability.

2. Geodesics Equations

Considering that the dynamics of the complex system entities take place on continuous but nondifferentiable curves, that is, fractal curves (e.g., the Koch curve, the Peano curve, or the Weierstrass curve [11–14, 17, 18]), they are given by the fractal operator $\widehat{d}/dt$ (for details see Appendices A and B):

$$\frac{\widehat{d}}{dt} = \frac{\partial}{\partial t} + \widehat{\mathbf{V}} \cdot \nabla - i\frac{\lambda^2}{\tau}\left(\frac{dt}{\tau}\right)^{(2/D_F)-1}\Delta, \tag{1}$$

where

$$\widehat{\mathbf{V}} = \mathbf{V}_D - i\mathbf{V}_F \tag{2}$$

is the complex velocity, $\mathbf{V}_D$ is the differentiable and resolution scale independent velocity, $\mathbf{V}_F$ is the nondifferentiable and resolution scale dependent velocity, $\widehat{\mathbf{V}} \cdot \nabla$ is the convective term,

$$\left(\frac{\lambda^2}{\tau}\right)\left(\frac{dt}{\tau}\right)^{(2/D_F)-1}\Delta = \left(\frac{\lambda^2}{\tau}\right)\left(\frac{dt}{\tau}\right)^{(2/D_F)-1} \times \left[\left(\frac{\partial^2}{\partial x^2}\right) + \left(\frac{\partial^2}{\partial y^2}\right) + \left(\frac{\partial^2}{\partial z^2}\right)\right] \tag{3}$$

is the dissipative term, $\delta t/\tau$ is the scale resolution identified here with dt/τ by substitution principle [12–14], D_F is the fractal dimension of the movement curves, λ is the reference length scale, τ is the reference time scale, and $\lambda^2/\tau \equiv D$ is the Nottale coefficient specific to fractal-nonfractal transition [12–14]. In the case of fractal dimension D_F, we can use any definition (the Hausdorff-Besicovitch fractal dimension, the Kolmogorov fractal dimension, etc. [11]), but once such definition is accepted, it has to be constant over the entire complex system dynamics analysis.

Applying the fractal operator (1) to the complex velocity (2) and accepting a generalized inertial principle (a generalization of Nottale's principle of scale covariance [12–14]), we obtain the geodesics in the form of the Navier-Stokes-type equations:

$$\frac{\widehat{d}\widehat{\mathbf{V}}}{dt} = \frac{\partial\widehat{\mathbf{V}}}{\partial t} + \left(\widehat{\mathbf{V}}\nabla\right)\widehat{\mathbf{V}} - i\frac{\lambda^2}{\tau}\left(\frac{dt}{\tau}\right)^{(2/D_F)-1}\Delta\widehat{\mathbf{V}} = 0. \tag{4}$$

Equation (4) shows that at any point of a fractal path, local acceleration, $\partial_t\widehat{\mathbf{V}}$, convection, $(\widehat{\mathbf{V}}\nabla)\widehat{\mathbf{V}}$, and dissipation, $(\lambda^2/\tau)(dt/\tau)^{(2/D_F)-1}\Delta\widehat{\mathbf{V}}$, is in equilibrium. According to [2–6], the complex system can be assimilated to a "rheological" fractal fluid. The "rheology" of the fractal fluid gives hysteretic

properties to the complex system (the complex system has a hysteresis cycle, memory, etc.).

Since the movement of the complex system's entities lacks interaction, we practically make use of self-convection and self-dissipation type mechanisms.

3. Fractal Hydrodynamics Model

For irrotational motion

$$\nabla \times \widehat{\mathbf{V}} = 0, \tag{5a}$$

$$\nabla \times \mathbf{V}_D = 0, \tag{5b}$$

$$\nabla \times \mathbf{V}_F = 0 \tag{5c}$$

we can choose $\widehat{\mathbf{V}}$ of the form

$$\widehat{\mathbf{V}} = -2i\frac{\lambda^2}{\tau}\left(\frac{dt}{\tau}\right)^{(2/D_F)-1}\nabla \ln \psi \tag{6}$$

or explicitly, with $\psi = \sqrt{\rho}\exp(iS)$,

$$\widehat{\mathbf{V}} = 2\frac{\lambda^2}{\tau}\left(\frac{dt}{\tau}\right)^{(2/D_F)-1}\nabla S - i\frac{\lambda^2}{\tau}\left(\frac{dt}{\tau}\right)^{(2/D_F)-1}\nabla \ln \rho, \tag{7a}$$

$$\mathbf{V}_D = 2\frac{\lambda^2}{\tau}\left(\frac{dt}{\tau}\right)^{(2/D_F)-1}\nabla S, \tag{7b}$$

$$\mathbf{V}_F = \frac{\lambda^2}{\tau}\left(\frac{dt}{\tau}\right)^{(2/D_F)-1}\nabla \ln \rho, \tag{7c}$$

where ρ is an amplitude and S a phase. The function ψ by means of ln defines the velocity scalar potential

$$\Phi = 2\frac{\lambda^2}{\tau}\left(\frac{dt}{\tau}\right)^{(2/D_F)-1}S - i\frac{\lambda^2}{\tau}\left(\frac{dt}{\tau}\right)^{(2/D_F)-1}\ln \rho. \tag{8}$$

By substituting ((7a)–(7c)) in (4) and separating the real and imaginary parts, up to an arbitrary phase factor which may be at zero by a suitable choice of the phase ψ, we obtain

$$m_0\left[\frac{\partial \mathbf{V}_D}{\partial t} + \left(\mathbf{V}_D \cdot \nabla\right)\mathbf{V}_D\right] = -\nabla Q, \tag{9}$$

$$\frac{\partial \rho}{\partial t} + \nabla\left(\rho \mathbf{V}_D\right) = 0 \tag{10}$$

with Q being the fractal potential

$$\begin{aligned} Q &= -2m_e\frac{\lambda^4}{\tau^2}\left(\frac{dt}{\tau}\right)^{(4/D_F)-2}\frac{\Delta\sqrt{\rho}}{\rho} \\ &= -\frac{m_0\mathbf{V}_F^2}{2} - m_0\frac{\lambda^2}{\tau}\left(\frac{dt}{\tau}\right)^{(2/D_F)-1}\nabla \mathbf{V}_F \end{aligned} \tag{11}$$

and m_0 the rest mass of the complex system's entity. The first equation (9) is the momentum conservation law, the second equation (10) is the density conservation law, and they define together the fractal hydrodynamics (FH) model. We note that, for Peano-type movements in fractal dimension $D_F = 2$ and supposing that fractal potential is assimilated with the pressure, the fractal hydrodynamic model becomes the standard hydrodynamic (for details see [19–23]).

The fractal potential (11) comes from the nondifferentiability and must be considered as a kinetic term and not as a potential one. Moreover, the fractal potential (11) can generate a viscosity stress tensor type [22, 23]

$$\begin{aligned} \widehat{\sigma}_{il} &= m_0\frac{\lambda^4}{\tau^2}\left(\frac{dt}{\tau}\right)^{(4/D_F)-2}\left[\nabla_i\rho\nabla_l\rho - \left(\frac{\nabla_i\rho\nabla_l\rho}{\rho}\right)\right] \\ &= \eta\left(\frac{\partial V_{Fi}}{\partial x_l} + \frac{\partial V_{Fl}}{\partial x_i}\right), \quad \eta = \frac{1}{2}m_0\rho\frac{\lambda^2}{\tau}\left(\frac{dt}{\tau}\right)^{(2/D_F)-1} \end{aligned} \tag{12}$$

of which divergence is equal to the usual force density associated with Q

$$\nabla_i\widehat{\sigma}_{il} = -\rho\nabla_l Q. \tag{13}$$

4. Barotropic-Type Behaviours of the Complex Systems via Nondifferentiability

For a barotropic-type behaviour of the complex system [24],

$$\widehat{\sigma}_{il} = \sigma\delta_{il} = \rho c^2\delta_{il} \tag{14}$$

with c being the critical velocity (for details see [24]); the FH equations become

$$\left[\frac{\partial \mathbf{V}_D}{\partial t} + \left(\mathbf{V}_D \cdot \nabla\right)\mathbf{V}_D\right] = -\frac{c^2}{\rho}\nabla\rho, \tag{15a}$$

$$\frac{\partial \rho}{\partial t} + \nabla\left(\rho \mathbf{V}_D\right) = 0. \tag{15b}$$

In the following, using (15a) and (15b) in a plane symmetry, we analyze the complex fluid dynamics. The presence of an external field is specified by adequate initial and boundary conditions (e.g., spatial-temporal Gaussian). In this situation, let us introduce the normalized coordinates

$$\omega t = \tau_0, \tag{16a}$$

$$kx = \xi, \tag{16b}$$

$$ky = \eta, \tag{16c}$$

$$\frac{V_x k}{\omega} = V_\xi, \tag{16d}$$

$$\frac{V_y k}{\omega} = V_\eta, \tag{16e}$$

$$\frac{\rho}{\rho_0} = N, \tag{16f}$$

where ω, k, and ρ_0 are critical parameters of the complex fluid (in [19, 25–27] the complex fluid is identified with a laser

produced plasma; in such a context ω is the plasma pulsation, ρ_0 is the density of plasma at thermodynamic equilibrium, k is the inverse of the Debye length, and c is the ion acoustic speed).

Then (15a) and (15b) become

$$\frac{\partial}{\partial\tau_0}\left(NV_\xi\right)+\frac{\partial}{\partial\xi}\left(NV_\xi^2\right)+\frac{\partial}{\partial\eta}\left(NV_\xi V_\eta\right)=-N^{-1}\frac{\partial N}{\partial\xi}, \quad (17a)$$

$$\frac{\partial}{\partial\tau_0}\left(NV_\eta\right)+\frac{\partial}{\partial\xi}\left(NV_\xi V_\eta\right)+\frac{\partial}{\partial\eta}\left(NV_\eta^2\right)=-N^{-1}\frac{\partial N}{\partial\eta}, \quad (17b)$$

$$\frac{\partial N}{\partial\tau_0}+\frac{\partial}{\partial\xi}\left(NV_\xi\right)+\frac{\partial}{\partial\eta}\left(NV_\eta\right)=0. \quad (17c)$$

For the numerical integration we will impose the initial conditions

$$V_\xi\left(0,\xi,\eta\right)=0, \quad (18a)$$

$$V_\eta\left(0,\xi,\eta\right)=0, \quad (18b)$$

$$N\left(0,\xi,\eta\right)=\frac{1}{5}, \quad (18c)$$

$$1\le\xi\le 2, \quad (18d)$$

$$0\le\eta\le 1 \quad (18e)$$

as well as the boundary conditions

$$V_\xi\left(\tau_0,1,\eta\right)=V_\xi\left(\tau_0,2,\eta\right)=0, \quad (19a)$$

$$V_\eta\left(\tau_0,1,\eta\right)=V_\eta\left(\tau_0,2,\eta\right)=0, \quad (19b)$$

$$V_\xi\left(\tau_0,\xi,0\right)=V_\xi\left(\tau_0,\xi,1\right)=0, \quad (19c)$$

$$V_\eta\left(\tau_0,\xi,0\right)=V_\eta\left(\tau_0,\xi,1\right)=0, \quad (19d)$$

$$N\left(\tau_0,1,\eta\right)=N\left(\tau_0,2,\eta\right)=\frac{1}{5}, \quad (19e)$$

$$N\left(\tau_0,\xi,0\right)=\frac{1}{10}\exp\left[-\left(\frac{\tau_0-1/5}{1/5}\right)^2\right]\exp\left[-\left(\frac{\xi-3/2}{1/5}\right)^2\right], \quad (19f)$$

$$N\left(\tau_0,\xi,1\right)=\frac{1}{5}. \quad (19g)$$

By using the finite differences method [28], the system ((17a)–(17c)) with the initial conditions ((18a)–(18e)) and the boundary ones ((19a)–(19g)) was numerically resolved.

In Figures 1(a), 1(b), and 1(c), three-dimensional dependences of the normalized density N, normalized velocities, V_ξ and V_η, on the normalized coordinates, ξ and η, are given for the normalized time $\tau_0 = 0.54$. Also in Figures 1(d), 1(e), and 1(f) the two-dimensional contours of the normalized density N, and normalized velocities, V_ξ and V_η, are given for the same normalized time. The followings result in (i) the generation of two complex fluid structures; (ii) the symmetry of the normalized velocity, V_ξ, with respect to symmetry axis of the spatial-temporal Gaussian; and (iii) vertices at the complex fluid periphery for the normalized velocity field, V_η. These results are in agreement with the experimental data on the behaviours of a laser produced aluminium plasma [19, 26, 27, 29–33].

Starting from these numerical solutions we can build the normalized current density

$$j\left(\xi,\eta,\tau_0\right)=N\left(\xi,\eta,\tau_0\right)\left[V_\xi^2\left(\xi,\eta,\tau_0\right)+V_\xi^2\left(\xi,\eta,\tau_0\right)\right]^{1/2}. \quad (20)$$

See Figures 2(a)–2(c).

It results in the splitting of the complex fluid into two structures. By assimilating the complex fluid with a laser produced aluminium plasma, the previous theoretical results are in agreement with the experimental data [32, 33].

5. Self-Similarity Behaviour of the Complex Systems via Nondifferentiability

Neglecting both convection $\widehat{\mathbf{V}}\cdot\nabla\widehat{\mathbf{V}}$ and dispersion $(\lambda^3/\tau)(dt/\tau)^{(3/D_F)-1}\nabla^3\widehat{\mathbf{V}}$, (4) takes the form

$$\frac{d\widehat{\mathbf{V}}}{dt}=\frac{\partial\widehat{\mathbf{V}}}{\partial t}-i\frac{\lambda^2}{\tau}\left(\frac{dt}{\tau}\right)^{(2/D_F)-1}\Delta\widehat{\mathbf{V}}=0 \quad (21)$$

or, by separating the resolution scales,

$$\frac{\partial\mathbf{V}_D}{\partial t}-\frac{\lambda^2}{\tau}\left(\frac{dt}{\tau}\right)^{(2/D_F)-1}\Delta\mathbf{V}_F=0 \quad (22)$$

for the differentiable scale and

$$\frac{\partial\mathbf{V}_F}{\partial t}-\frac{\lambda^2}{\tau}\left(\frac{dt}{\tau}\right)^{(2/D_F)-1}\Delta\mathbf{V}_D=0 \quad (23)$$

for fractal scale. The velocity fields are totally separated, first applying (22) and (23) to the Δ operator, that is,

$$\begin{aligned}\frac{\partial}{\partial t}\left(\Delta\mathbf{V}_D\right)-\frac{\lambda^2}{\tau}\left(\frac{dt}{\tau}\right)^{(2/D_F)-1}\Delta^2\mathbf{V}_F=0,\\ \frac{\partial}{\partial t}\left(\Delta\mathbf{V}_F\right)+\frac{\lambda^2}{\tau}\left(\frac{dt}{\tau}\right)^{(2/D_F)-1}\Delta^2\mathbf{V}_D=0,\end{aligned} \quad (24)$$

then, substituting in the transformed equations the dissipative terms by using (22) and (23). It results in the Kirchhoff-type equations

$$\left(\frac{\partial^2}{\partial t^2}+\frac{\lambda^4}{\tau^2}\left(\frac{dt}{\tau}\right)^{(4/D_F)-2}\Delta^2\right)\begin{pmatrix}\mathbf{V}_D\\ \mathbf{V}_F\end{pmatrix}=\begin{pmatrix}0\\ 0\end{pmatrix}. \quad (25)$$

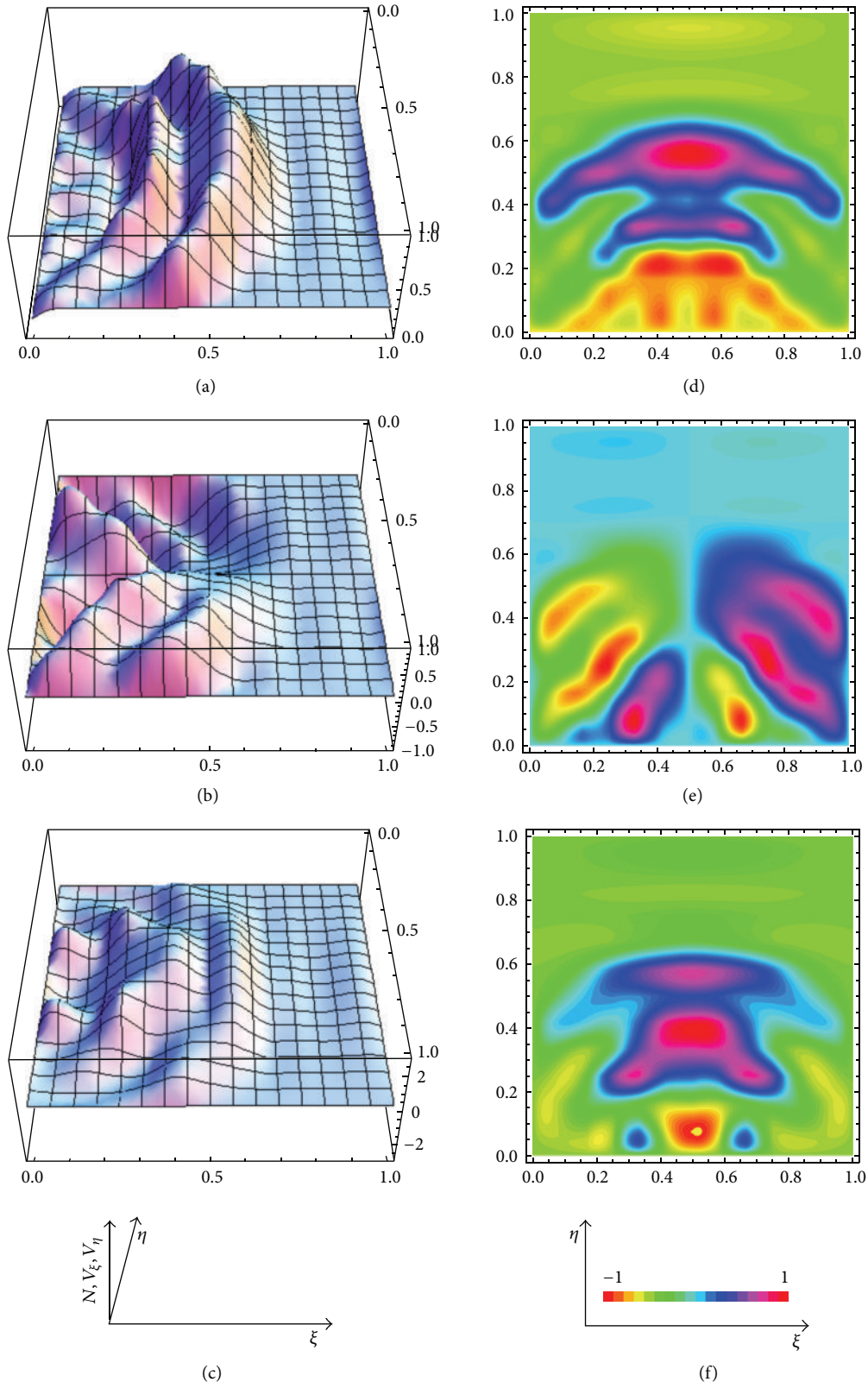

FIGURE 1: Three-dimensional dependences of the normalized density N and normalized velocities, V_ξ and V_η, on the normalized coordinates, ξ and η, for the normalized time $\tau_0 = 0.54$ ((a), (b), and (c)); two-dimensional contour of the normalized density N and normalized velocities, V_ξ and V_η, for the same normalized time ((d), (e), and (f)).

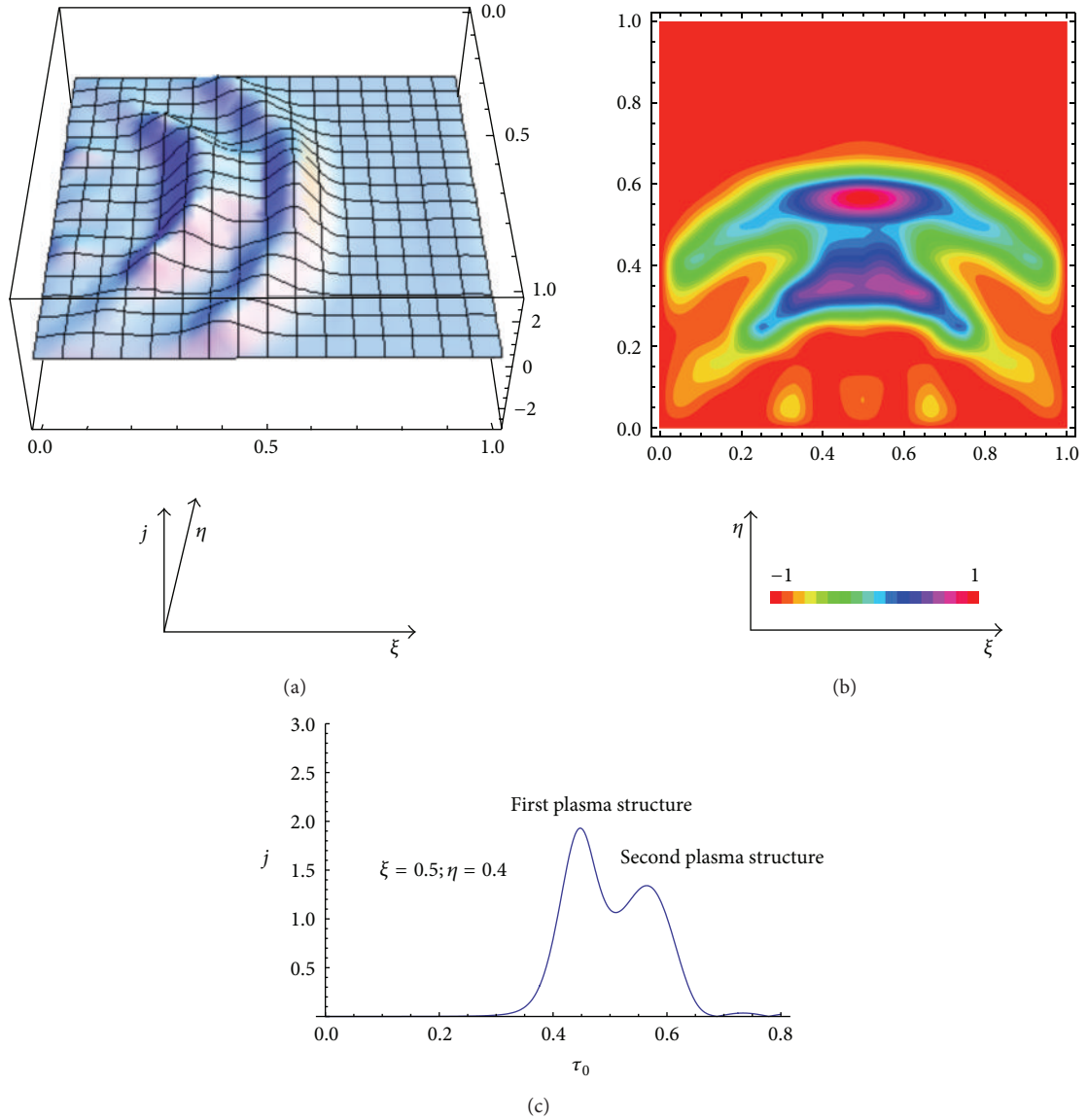

FIGURE 2: Three-dimensional dependences of the normalized density current j, on the normalized coordinates, ξ and η, for the normalized time $\tau_0 = 0.54$ (a); two-dimensional contour of the normalized current density j for the same normalized time (b); time evolution of the normalized density current for $\xi = 0.5$ and $\eta = 0.4$ (c).

For one-dimensional case, the previous equations with the substitutions

$$\frac{x}{L} = \overline{\xi}, \tag{26a}$$

$$\frac{t}{T} = \overline{\tau}, \tag{26b}$$

$$\frac{L^4}{T^2} = \frac{\lambda^4}{\tau^2}\left(\frac{dt}{\tau}\right)^{(4/D_F)-2}, \tag{26c}$$

$$\left(\mathbf{V}_D; \mathbf{V}_F\right) \equiv \overline{K}_i\left(\overline{\xi}, \overline{\tau}\right), \quad i = 1, 2 \tag{26d}$$

take the unitary form

$$L^4 \frac{\partial^4 \overline{K}_i}{\partial \overline{\xi}^4} + T^2 \frac{\partial^2 \overline{K}_i}{\partial \overline{\tau}^2} = 0. \tag{27}$$

On (27), we impose for "clamping" conditions at $\overline{\xi} = 1$

$$\frac{\partial^2 \overline{K}_i(1, \overline{\tau})}{\partial \overline{\xi}^2} = 0, \tag{28a}$$

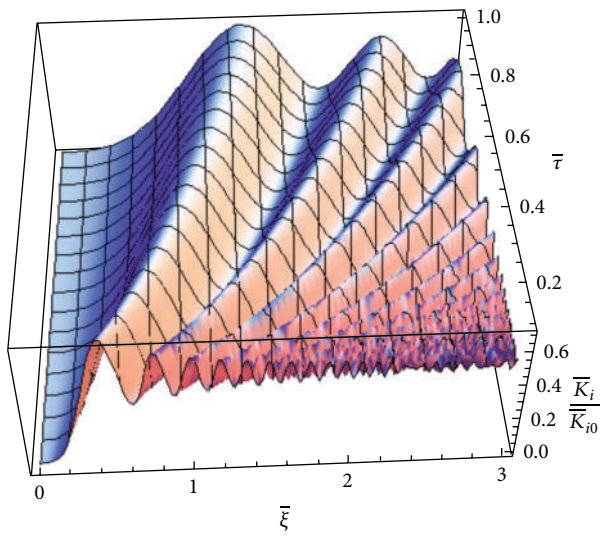

Figure 3: Numerical solution of the Kirchhoff equation (27) with "clamped-free" unitary conditions, for a uniform initial $\overline{K}_{i0}$. $\overline{K}_i(0,\tau)$ relaxes to zero within the first few time steps.

$$\frac{\partial^3 \overline{K}_i(1,\overline{\tau})}{\partial \overline{\xi}^3} = 0 \tag{28b}$$

and for boundary conditions at $\overline{\xi} = 0$

$$\overline{K}_i(0,\overline{\tau}) = 0, \tag{29a}$$

$$\frac{\partial \overline{K}_i(0,\overline{\tau})}{\partial \overline{\xi}} = 0. \tag{29b}$$

These four boundary conditions in $\overline{\xi}$ associated with the two initial conditions

$$\overline{K}_i\left(\overline{\xi},0\right) = \overline{K}_{i0}, \tag{30a}$$

$$\frac{\partial \overline{K}_i\left(\overline{\xi},0\right)}{\partial \overline{\tau}} = 0 \tag{30b}$$

imply a unique solution $\overline{K}_i(\overline{\xi},\overline{\tau})$ to (27); see Figure 3.

Owing to the scaling $x \sim L\sqrt{t/T}$, we seek a solution of (27) in the form

$$\overline{K}_i\left(\overline{\xi},\overline{\tau}\right) = \overline{K}_{i0} u_i\left(\overline{\eta}\right), \tag{31}$$

where the self-similarity variable is

$$\overline{\eta} = \left(\frac{\overline{\xi}}{\sqrt{\overline{\tau}}}\right) = \frac{(x/L)}{\sqrt{t/T}} = \frac{x}{\sqrt{\gamma t}}. \tag{32}$$

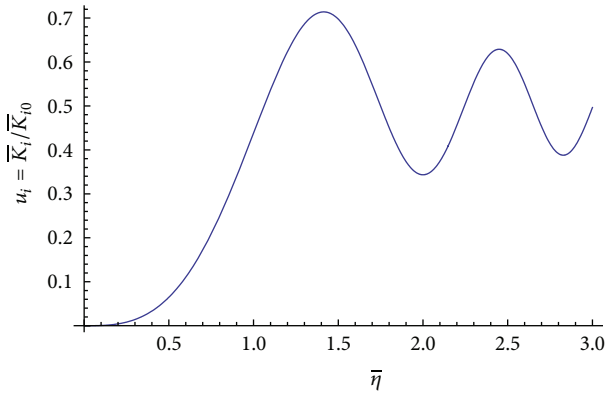

Figure 4: The self-similar solution (36) is a function of $\overline{\eta}$. At later times, $\overline{\tau} \sim 1$, reflections are generated from the "clamped" end $\overline{\xi} = 1$.

The boundary conditions for $u(\overline{\eta})$ are derived from those for $\overline{K}_i$:

$$u_i(0) = 0, \tag{33a}$$

$$u_i'(0) = 0, \tag{33b}$$

$$u_i(+\infty) \longrightarrow 1. \tag{33c}$$

Substituting this self-similar form of $\overline{K}_i(\overline{\xi},\overline{\tau})$ into (27) yields the following equation for the self-similar solution $u_i(\overline{\eta})$:

$$4\frac{d^4 u_i(\overline{\eta})}{d\overline{\eta}^4} + \overline{\eta}^2 \frac{d^2 u_i(\overline{\eta})}{d\overline{\eta}^2} + 3\overline{\eta}\frac{du_i(\overline{\eta})}{d\overline{\eta}} = 0. \tag{34}$$

Imposing that $u_i(\overline{\eta})$ matches the initial condition for large $\overline{\eta}$ implies that

$$\frac{d^2 u_i(0)}{d\overline{\eta}^2} = 0, \tag{35}$$

as shown with the help of an integral of motion. This last condition, combined with the previous ones, yields a unique self-similar solution to (34):

$$2\overline{K}_i\left(\overline{\xi},\overline{\tau}\right) = 2\overline{K}_{i0}\left(\frac{\overline{\eta}}{\sqrt{2\pi}}\right), \tag{36}$$

where we have introduced the Fresnel sine integral, $S(x) = \int_0^x \sin(\pi y^2/2)dy$, also arising in diffraction theory.

Equation (36) describes a self-similar solution. This reflects the dispersive nature of (27), see Figure 4.

In these conditions the phase S associated with the velocity scalar potential is presented in Figure 5.

The states density associated with the same velocity scalar potential has the same behaviour as the one presented in Figure 5. It results in a self-similarity behaviour.

The theoretical oscillations (obtained by means of self-elimination of the dissipative terms between differentiable

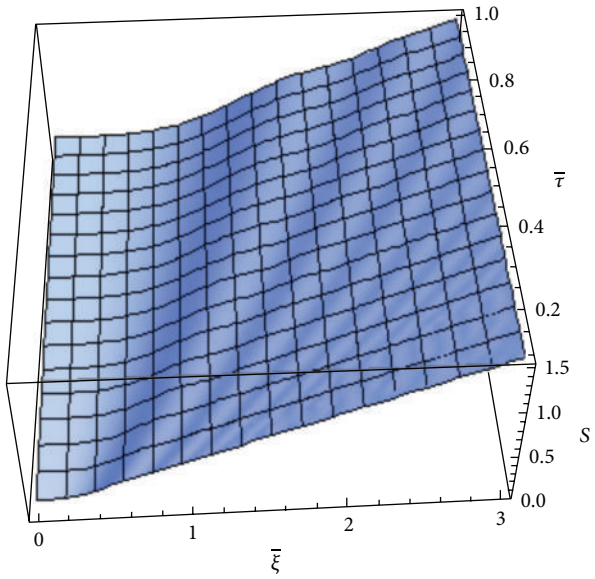

FIGURE 5: The phase dependence versus normalized space-time coordinates.

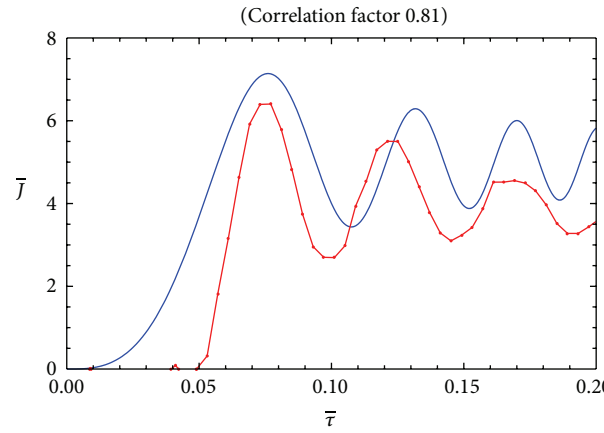

FIGURE 6: The theoretical (blue) and experimental (red) curves of the ionic oscillations of the normalized current density, $\overline{J}$, with normalized time, $\overline{\tau}$, in a laser produced aluminium plasma at a laser power of 40 mJ/pulse.

and fractal scales) can explain the experimental ionic oscillations of the current density that take place in a laser produced aluminium plasma [19, 26, 27, 29]. In Figure 6 we give by comparison the experimental curve (red curve, which reflects the ionic oscillations of the current density with time that take place in a laser produced aluminium plasma at a laser power of 40 mJ/pulse) and the theoretical curve (blue curve). We note that in Figure 6 we used the normalized coordinates.

It results in a good agreement (correlation factor 0.81) between theoretical model and the experimental data.

6. Chaoticity through Turbulence and Stochasticization via Nondifferentiability

Through the fractal velocities field, $\mathbf{V}_F$, the specific fractal potential Q is a measure of nondifferentiability of the complex system particle trajectories, that is, of their chaoticity.

Since the position vector of the particle is assimilated with a stochastic process of Wiener type (for details see [11–13], ψ is not only the scalar potential of a complex speed (through $\ln\psi$) in the frame of fractal hydrodynamics but also density of probability (through $|\psi|^2$) in the frame of a Schrödinger-type theory.

It results in the equivalence between the formalism of the fractal hydrodynamics and the one of the Schrödinger-type equation. Moreover, the chaoticity, either through turbulence in the fractal hydrodynamics approach or through stochasticization in the Schrödinger-type approach, is generated only by the nondifferentiability of the movement trajectories in a fractal space. In this way the nondifferentiability becomes a "control parameter" of the complex system dynamics.

6.1. Full and Fractional Speed Scalar Potential Revivals in the Infinite Square Well: Various Criteria of Evolution to Chaos

6.1.1. Infinite Square Well System. Let us consider that the external perturbation applied to complex system simulates, in our opinion, one-dimension square well system. After solving the time-dependent Schrödinger-type equation according to the method described in [23] we obtain the discrete eigenvalues

$$E_n = 2m_0\mathfrak{D}^2\left(\frac{n\pi}{a}\right)^2, \quad \mathfrak{D} = \frac{\lambda^2}{\tau}\left(\frac{dt}{\tau}\right)^{(2/D_F)-1} \tag{37}$$

and the eigenfunctions

$$\phi_n = \begin{cases} \left(\frac{2}{a}\right)^{1/2}\sin\left(\frac{n\pi x}{a}\right), & n \text{ even } |x| \le \frac{a}{2}, \\ \left(\frac{2}{a}\right)^{1/2}\cos\left(\frac{n\pi x}{a}\right), & n \text{ odd } |x| \le \frac{a}{2}, \end{cases} \tag{38}$$

where a is the well's width and m_0 is the rest mass of the fractal fluid particle.

6.1.2. Time Scales. Some time scales of a speed potential evolution are contained in the coefficients of the Taylor series of the quantized energy levels E_n around the main energy $E_{\overline{n}}$ (see method from [34])

$$E_n = E_{\overline{n}} + 4\pi m_0\mathfrak{D}\left[\frac{n-\overline{n}}{T_\alpha} + \frac{(n-\overline{n})^2}{T_\beta} + \cdots\right], \tag{39}$$

where often the zero of energy is shifted to remove the $E_{\overline{n}}$ term. Regrouping the infinite square well energies (17a)–(17c) in this form gives

$$E_n = E_1 n^2 = E_1\overline{n}^2 + 2E_1\overline{n}(n-\overline{n}) + E_1(n-\overline{n})^2. \tag{40}$$

And comparing (39) and (40) we relate

$$T_\alpha = \frac{2\pi m_0 \mathfrak{D}}{\overline{n} E_1}, \qquad T_\beta = \frac{4\pi m_0 \mathfrak{D}}{E_1}. \tag{41}$$

We note that the time scale T_β does not depend on the mean energy level $\overline{n}$. This will provide us with a "universal" time scale for describing speed potential evolution that does not depend on the particle average energy.

6.1.3. Time Evolution. We write the particle's time $t = 0$ speed scalar potential in the infinite square well as

$$\psi(x, t = 0) = \psi_i(x). \tag{42}$$

We expand this speed scalar potential using the energy eigenstate basis

$$\psi_i(x) = \sum_{n=1}^{\infty} c_n \phi_n(x) \tag{43}$$

with

$$c_n = \int_{-\infty}^{+\infty} \phi_n(x)\, \psi_i(x)\, dx. \tag{44}$$

Using the time scale T_β, the time evolution in the energy eigenstate basis was found from Schrödinger-type equation to be

$$\psi(x, t) = \sum_n \exp\left[-2\pi i \left(\frac{t}{T_\beta}\right) n^2\right] c_n \phi_n(x). \tag{45}$$

6.1.4. Simulation of the Evolution to Chaos Criteria. Now, the full and fractional revivals formalism may be applied. Full and fractional revivals of a speed scalar potential in the infinite square well occur when a speed scalar potential evolves in time to a state that can be described as a collection of spatially distributed subspeed scalar potentials that each closely reproduces the initial speed scalar potential shape; see for details [34]. Therefore, the full and fractional revivals of a speed scalar potential in the infinite square well impliy either

$$\psi\left(x, t = t_0 + 2^k T_\beta\right) = \psi\left(x, t = t_0\right) \tag{46}$$

or

$$\psi\left(x, t_0 + \frac{p}{q} T_\beta\right) = \psi\left(x, t = t_0\right) \tag{47}$$

for any time t_0 and k, p, and q integers. In any of the situations above, either for $t = T_F = 2^k T_\beta$ or for $t = T_{\mathrm{SH}} = (p/q) T_\beta$, we can introduce Reynolds-type criterions

$$\mathrm{Re}_F = \frac{V_F L_F}{\nu_F} = 2^k, \qquad \mathrm{Re}_{\mathrm{SH}} = \frac{V_{\mathrm{SH}} L_{\mathrm{SH}}}{\nu_{\mathrm{SH}}} = \frac{p}{q}, \tag{48}$$

where

$$E_1 \equiv E_{F/\mathrm{SH}} = \frac{1}{2} m_0 V^2{}_{F/\mathrm{SH}}, \tag{49a}$$

$$L_{F/\mathrm{SH}} = V_{F/\mathrm{SH}} T_{F/\mathrm{SH}}, \tag{49b}$$

$$\nu_{F/\mathrm{SH}} = 8\pi \frac{\lambda^2}{\tau} \left(\frac{dt}{\tau}\right)^{(2/D_F)-1} \tag{49c}$$

have the usual signification from fluid mechanics [24]. Up to the values $\mathrm{Re}^c_{F/\mathrm{SH}}$ the fractal fluids become turbulent. Then through $T_F/T_\beta = 2^k$ and $\mathrm{Re}_F = V_F L_F/\nu_F = 2^k$ it is formally simulated through the criterion of evolution to chaos via Feigenbaum scenario (cascade of period doubling bifurcations), while through $T_\beta/T_{\mathrm{SH}} = \omega_{\mathrm{SH}}/\omega_\beta = q/p$ with $p > q$ and $\mathrm{Re}_{\mathrm{SH}} = V_{\mathrm{SH}} L_{\mathrm{SH}}/\nu_{\mathrm{SH}} = p/q$ the criterion of evolution to chaos via a cascade of subharmonic bifurcations.

We admit that in any of these two situations mentioned above the fractal velocity (7c) is null, since $\rho = |\psi|^2 = \mathrm{const}$; meanwhile the differential velocity (7b) is not zero, since the phase S is not constant, with the increase of the systems phase incoherence being associated with the increase in turbulence of fractal fluid.

We note that in the standard model (Landau's scenario [24, 35]) the Fourier spectrum is always discrete and cannot approximate a continuum spectrum than that in case of a large number of frequencies that will generate an unlimited number of spectral components as a result of their beats which appear thanks to the presence of nonlinearities in the system. Yet, considering standard model, the flow can never be truly chaotic, because, in case of multiple periodic functions, correlations tend to be not null but having an oscillating character. Therefore, Landau's scenario can describe transition towards chaotic behaviour only in a system with an infinite number of degrees of freedom, such as a fluid. In our case, because the Reynolds numbers (48) present scale dependencies (49c), when $dt \to 0$ for $D_F \leq 2$, the fractals physical values that describe the dynamics of the system are no longer defined. So, in this approximation, a simulation of a system with an infinite number of degrees of freedom is used.

We note that the results from the present paragraph permit the chaoticity and self-structuring control by means of nondifferentiability. Thus the experimental results on the formation, dynamics, and evolution towards chaos of complex space charge structures that emerge in front of a positively biased electrode immersed in a quiescent plasma from [20] are in agreement with our previous theoretical results.

7. Conclusions

In the present paper, we propose a new topic in the control of complex systems dynamics using the nondifferentiability of complex system movement curves. This topic was developed through the scale relativity approach. Considering the dynamics of complex system entities that take place on fractal curves, we show that the control of different behaviours of these systems implies nondifferentiability. The

main conclusions of the present paper are as follows: (i) the geodesics equations in the form of a Navier-Stokes-type equation are obtained. It results in the rheologic properties of the complex system which implies memory and so forth; (ii) considering that the fractal fluid flows are irrotational, fractal hydrodynamics equations are obtained. These equations are formed from the density and momentum conservations laws, wih the presence of nondifferentiability being induced by the fractal potential; (iii) a barotropic-type behaviour of the complex system is numerically simulated using FH equations. In this way we highlight the self-multiplication mechanism of the substructures that constitute the complex system; (iv) the implications of self-similarity in the dynamics of the complex system are presented; (v) the chaoticity through turbulence and stochaticization via nondifferentiability are obtained; (vi) these previous behaviours can simulate the standard properties of the complex system.

In this way, standard properties of complex systems such as emergence, self-organisation, and adaptability are controlled through nondifferentiability of motion curves of the sub-systems that compose the complex system. We note that general aspects of the dynamics control of the complex system are described in [36], while the concrete cases of this control are presented in [37–39].

Appendices

A. Consequences of Nondifferentiability

The nondifferentiability implies the following [12–14, 19–22].

(i) A continuous and a nondifferentiable curve (or almost nowhere differentiable) is explicitly scale dependent. This means that its length tends to infinity, when the scale interval tends to zero. Therefore, a continuous and nondifferentiable space is fractal, in the general meaning given by Mandelbrot to this concept [11].

(ii) Physical quantities will be expressed through fractal functions, namely, through functions that are dependent both on spatial and temporal coordinates and on resolution scale. The invariance of the physical quantities in relation with the resolution scale generates special types of transformations, called resolution scale transformations. Particularly, the differentiality of the generalized spatial coordinates, $\mathbf{X}$, takes the form

$$d\mathbf{X} = d\mathbf{x} + d\boldsymbol{\xi}, \tag{A.1}$$

where $d\mathbf{x}$ is the classical differential element and $d\boldsymbol{\xi}$ is a differential fractal one.

(iii) There is infinity of fractal curves (geodesics) relating to any couple of points (or starting from any point) and applied for any scale. The phenomenon can be easily understood at the level of fractal surfaces, which, in their turn, can be described in terms of fractal distribution of conic points of positive and negative infinite curvatures. As a consequence, we have replaced velocity on a particular geodesic by fractal velocity field of the whole infinite ensemble of geodesics. This representation is similar to that of fluid mechanics where the motion of the fluid is described in terms of its velocity field, density, and pressure. We will, indeed, recover the fundamental equations of fluid mechanics (Euler and continuity equations), but we will write them in terms of a density of probability (as defined by the set of geodesics) instead of a density of matter and adding an additional term of quantum pressure (the expression of fractal geometry).

(iv) The local differential time invariance is broken, so the time-derivative of the fractal field Q can be written twofold:

$$\begin{aligned} \frac{d_+Q}{dt} &= \lim_{\Delta t \longrightarrow 0_+} \frac{Q(t+\Delta t) - Q(t)}{\Delta t}, \\ \frac{d_-Q}{dt} &= \lim_{\Delta t \longrightarrow 0_-} \frac{Q(t) - Q(t-\Delta t)}{\Delta t}. \end{aligned} \tag{A.2}$$

Both definitions are equivalent in the differentiable case $dt \rightarrow -dt$. In the nondifferentiable situation, these definitions are no longer valid, since limits are not defined anymore. Fractal theory defines physics in relationship with the function behaviour during the "zoom" operation on the time resolution δt, which is here identified with the differential element dt (substitution principle), which is considered an independent variable. The standard field $Q(t)$ is therefore replaced by fractal field $Q(t, dt)$, explicitly dependent on time resolution interval, whose derivative is not defined at the unnoticeable limit $dt \rightarrow 0$. As a consequence, this leads to the two derivatives of the fractal field Q as explicit functions of the two variables t and dt

$$\begin{aligned} \frac{d_+Q}{dt} &= \lim_{\Delta t \longrightarrow 0_+} \frac{Q(t+\Delta t, \Delta t) - Q(t, \Delta t)}{\Delta t}, \\ \frac{d_-Q}{dt} &= \lim_{\Delta t \longrightarrow 0_-} \frac{Q(t, \Delta t) - Q(t-\Delta t, \Delta t)}{\Delta t}. \end{aligned} \tag{A.3}$$

Notation "+" corresponds to the forward process, while "–" to the backward one.

Let us particularize (A.3) for the spatial coordinates. t results in

$$d_\pm \mathbf{X} = d_\pm \mathbf{x} + d_\pm \boldsymbol{\xi}. \tag{A.4}$$

Since, according to [12–14, 19–22], we can write

$$\left\langle d_\pm X^i \right\rangle = d_\pm x^i \tag{A.5}$$

from (A.4) by averaging, it results in

$$\left\langle d\xi_\pm^i \right\rangle = 0. \tag{A.6}$$

(v) The differential fractal part satisfies the fractal equation:

$$d_\pm \xi^i = \lambda_\pm^i \left(\frac{dt}{\tau} \right)^{1/D_F}, \tag{A.7}$$

where $\lambda_\pm^i$ are some constant coefficients, dt is the time differential, τ is the reference time scale, and D_F is a constant fractal dimension. We note that the use of any Kolmogorov or Hausdorff definition [12–14, 19–22] can be accepted for fractal

dimension, but once a certain definition is admitted, it should be used until the end of analyzed dynamics.

(vi) The local differential time reflection invariance is recovered by combining the two derivatives, d_+/dt and d_-/dt, in the complex operator:

$$\frac{\hat{d}}{dt} = \frac{1}{2}\left(\frac{d_+ + d_-}{dt}\right) - \frac{i}{2}\left(\frac{d_+ - d_-}{dt}\right). \tag{A.8}$$

Applying this operator to the "position vector," a complex velocity yields

$$\begin{aligned}\widehat{\mathbf{V}} = \frac{\hat{d}\mathbf{X}}{dt} &= \frac{1}{2}\left(\frac{d_+\mathbf{X} + d_-\mathbf{X}}{dt}\right) - \frac{i}{2}\left(\frac{d_+\mathbf{X} - d_-\mathbf{X}}{dt}\right) \\ &= \frac{\mathbf{V}_+ + \mathbf{V}_-}{2} - i\frac{\mathbf{V}_+ - \mathbf{V}_-}{2} = \mathbf{V}_D - i\mathbf{V}_F\end{aligned} \tag{A.9}$$

with

$$\begin{aligned}\mathbf{V}_D &= \frac{\mathbf{V}_+ + \mathbf{V}_-}{2}, \\ \mathbf{V}_F &= \frac{\mathbf{V}_+ - \mathbf{V}_-}{2}.\end{aligned} \tag{A.10}$$

The real part, $\mathbf{V}_D$, of the complex velocity $\widehat{\mathbf{V}}$ represents the standard classical velocity, which does not depend on resolution, while the imaginary part, $\mathbf{V}_F$, is a new quantity coming from fractality.

B. Covariant Derivative

Let us now assume that curves describing movements of complex systems (continuous but nondifferentiable) are immersed in a 3-dimensional space and that $\mathbf{X}$ of components X^i $(i = \overline{1,3})$ is the position vector of a point on the curve. Let us also consider the fractal field $Q(\mathbf{X}, t)$ and expand its total differential up to the second order:

$$d_\pm Q = \frac{\partial Q}{\partial t}dt + \nabla Q \cdot d_\pm \mathbf{X} + \frac{1}{2}\frac{\partial^2 Q}{\partial X^i \partial X^j} d_\pm X^i d_\pm X^j. \tag{B.1}$$

Relations (B.1) are valid in any point both for the spatial manifold and for the points $\mathbf{X}$ on the fractal curve selected in relations (B.1). Hence, the forward and backward average values of these relations take the form

$$\begin{aligned}\langle d_\pm Q\rangle = \left\langle \frac{\partial Q}{\partial t}dt\right\rangle + \langle \nabla Q \cdot d_\pm \mathbf{X}\rangle \\ + \frac{1}{2}\left\langle \frac{\partial^2 Q}{\partial X^i \partial X^j} d_\pm X^i d_\pm X^j\right\rangle.\end{aligned} \tag{B.2}$$

The following aspects should be mentioned: the mean value of function Q and its derivatives coincide with themselves, and the differentials $d_\pm X^i$ and dt are independent; therefore, the average of their products coincides with the product of averages. Consequently, (B.2) becomes

$$d_\pm Q = \frac{\partial Q}{\partial t}dt + \nabla Q \langle d_\pm \mathbf{X}\rangle + \frac{1}{2}\frac{\partial^2 Q}{\partial X^i \partial X^j}\left\langle d_\pm X^i d_\pm X^j\right\rangle \tag{B.3}$$

or more, using (A.4) and (A.6),

$$\begin{aligned}d_\pm Q = \frac{\partial Q}{\partial t}dt + \nabla Q \cdot d_\pm \mathbf{X} + \frac{1}{2}\frac{\partial^2 Q}{\partial X^i \partial X^j} \\ \times \left(d_\pm X^i d_\pm X^j + \left\langle d_\pm \xi^i d_\pm \xi^j\right\rangle\right).\end{aligned} \tag{B.4}$$

Even if the average value of the fractal coordinate $d_\pm \xi^i$ is null (see (A.6)), for higher order of fractal coordinate average, the situation can still be different. Let us focus on the averages $\langle d_\pm \xi^i d_\pm \xi^j\rangle$. If $i \neq j$, these averages are zero due to the independence of $d_\pm \xi^i$ and $d_\pm \xi^j$. So, using (A.7), we can write

$$\left\langle d_\pm \xi^i d_\pm \xi^j\right\rangle = \lambda_\pm^i \lambda_\pm^j \left(\frac{dt}{\tau}\right)^{(2/D_F)-1}\left(\frac{dt}{\tau}\right). \tag{B.5}$$

Then, (B.4) may be written as follows:

$$\begin{aligned}d_\pm Q = \frac{\partial Q}{\partial t}dt + d_\pm \mathbf{x}\cdot\nabla Q + \frac{1}{2}\frac{\partial^2 Q}{\partial X^i \partial X^j} d_\pm x^i d_\pm x^j \\ + \frac{1}{2}\frac{\partial^2 Q}{\partial X^i \partial X^j}\lambda_+^i \lambda_+^j \left(\frac{dt}{\tau}\right)^{(2/D_F)-1}\left(\frac{dt}{\tau}\right).\end{aligned} \tag{B.6}$$

If we divide by dt and neglect the terms containing differential factors, (B.6) is reduced to

$$\frac{d_\pm Q}{dt} = \frac{\partial Q}{\partial t} + \mathbf{V}_\pm \nabla Q + \frac{1}{2}\frac{\partial^2 Q}{\partial X^i \partial X^j}\frac{\lambda_-^i \lambda_-^j}{\tau}\left(\frac{dt}{\tau}\right)^{(2/D_F)-1}. \tag{B.7}$$

These relations also allow us to define the operators:

$$\frac{d_\pm}{dt} = \frac{\partial}{\partial t} + \mathbf{V}_\pm \cdot \nabla + \frac{\lambda_+^i \lambda_+^j}{2\tau}\left(\frac{dt}{\tau}\right)^{(2/D_F)-1}\frac{\partial^2}{\partial X^i \partial X^j}. \tag{B.8}$$

Under these circumstances, let us calculate $\hat{d}Q/dt$. Taking into account (B.8), (A.8), and (A.9), we will obtain

$$\begin{aligned}\frac{\hat{d}Q}{dt} &= \frac{1}{2}\left[\frac{d_+ Q}{dt} + \frac{d_- Q}{dt} - i\left(\frac{d_+ Q}{dt} - \frac{d_- Q}{dt}\right)\right] \\ &= \frac{\partial Q}{\partial t} + \widehat{\mathbf{V}}\cdot\nabla + \frac{(dt/\tau)^{(2/D_F)-1}}{4\tau} \\ &\quad \cdot \left[\left(\lambda_+^i \lambda_+^j + \lambda_-^i \lambda_-^j\right) - i\left(\lambda_+^i \lambda_+^j - \lambda_-^i \lambda_-^j\right)\right]\frac{\partial^2 Q}{\partial X^i \partial X^j}.\end{aligned} \tag{B.9}$$

This relation also allows us to define the fractal operator:

$$\begin{aligned}\frac{\hat{d}}{dt} &= \frac{\partial}{\partial t} + \widehat{\mathbf{V}}\cdot\nabla + \frac{(dt/\tau)^{(2/D_F)-1}}{4\tau} \\ &\quad \cdot \left[\left(\lambda_+^i \lambda_+^j + \lambda_-^i \lambda_-^j\right) - i\left(\lambda_+^i \lambda_+^j - \lambda_-^i \lambda_-^j\right)\right]\frac{\partial^2 Q}{\partial X^i \partial X^j}.\end{aligned} \tag{B.10}$$

Particularly, by choosing

$$\lambda_+^i \lambda_+^j = -\lambda_-^i \lambda_-^j = 2\lambda^2 \delta^{ij}, \tag{B.11}$$

where λ is the reference length scale, the fractal operator (B.10) (covariant derivative) takes the usual form:

$$\frac{\hat{d}}{dt} = \frac{\partial}{\partial t} + \widehat{\mathbf{V}}\cdot\nabla - i\frac{\lambda^2}{\tau}\left(\frac{dt}{\tau}\right)^{(2/D_F)-1}\Delta. \tag{B.12}$$

References

[1] B.-Y. Yaneer, *Dynamics of Complex Systems, The Advanced Book Program*, Addison-Wesley, Reading, Mass, USA, 1997.

[2] S. V. Buldyrev, R. Parshani, G. Paul, H. E. Stanley, and S. Havlin, "Catastrophic cascade of failures in interdependent networks," *Nature*, vol. 464, no. 7291, pp. 1025–1028, 2010.

[3] K. Kaneko, *Complex Systems: Chaos and Beyond, A Constructive Approach with Applications in Life Sciences*, 2001.

[4] C. Gros, *Complex and Adaptative Dynamical Systems: A Primer*, 2011.

[5] R. Badii and A. Politi, *Complexity: Hierarchical Structure and Scaling in Physics*, Cambridge University Press, Cambridge, UK, 1997.

[6] M. Mitchell, *Complexity: A Guided Tour*, Oxford University Press, Oxford, UK, 2009.

[7] G. W. Flake, *The Computational Beauty of Nature*, The MIT Press, Cambridge, Mass, USA, 1998.

[8] A. T. Winfree, *The Geometry of Biological Time*, Springer, New York, NY, USA, 2nd edition, 2000.

[9] P. Davies, *The New Physics*, Cambridge University Press, 1992.

[10] C. H. Bennett, "How to define complexity in physics, and why," in *Complexity, Entropy, and the Physics of Information*, W. H. Zurek, Ed., pp. 443–454, Addison-Wesley, Reading, Mass, USA, 1990.

[11] Mandelbrot and B. Benoit, *The Fractal Geometry of Nature*, W. H. Freeman, New York, NY, USA, 1983.

[12] L. Nottale, *Fractal Space-Time and Microphysics: Towards a Theory of Scale Relativity*, World Scientific, Singapore, 1993.

[13] L. Nottale, *Scale Relativity and Fractal Space-Time—A New Approach To Unifying Relativity and Quantum Mechanics*, Imperial College Press, London, UK, 2011.

[14] L. Nottale, "Fractals and the quantum theory of spacetime," *International Journal of Modern Physics A*, vol. 4, pp. 5047–5117, 1989.

[15] G. M. Viswanathan, F. Bartumeus, S. V. Buldyrev et al., "Lévy flight random searches in biological phenomena," *Physica A*, vol. 314, no. 1–4, pp. 208–213, 2002.

[16] M. F. Shlesinger, J. Klafter, and G. Zumofen, "Above, below and beyond Brownian motion," *American Journal of Physics*, vol. 67, no. 12, pp. 1253–1259, 1999.

[17] M. S. El Naschie and O. E. Rossler, "Quantum mechanics and chaotic fractals," *Chaos, Solitons and Fractals*, vol. 4, no. 3, pp. 307–309, 1994.

[18] P. Weibel, G. Ord, and O. E. Rosler, *Space Time Physics and Fractility*, Springer, New York, NY, USA, 2005.

[19] S. Gurlui, M. Agop, P. Nica, M. Ziskind, and C. Focşa, "Experimental and theoretical investigations of transitory phenomena in high-fluence laser ablation plasma," *Physical Review E*, vol. 78, Article ID 026405, 2008.

[20] M. Agop, D. G. Dimitriu, O. Niculescu, E. Poll, and V. Radu, "Experimental and theoretical evidence for the chaotic dynamics of complex structures," *Physica Scripta*, vol. 87, no. 4, Article ID 045501, 2013.

[21] M. Agop, N. Forna, I. Casian-Botez, and C. Bejenariu, "New theoretical approach of the physical processes in nanostructures," *Journal of Computational and Theoretical Nanoscience*, vol. 5, no. 4, pp. 483–489, 2008.

[22] I. Casian-Botez, M. Agop, P. Nica, V. Paun, and G. V. Munceleanu, "Conductive and convective types behaviors at nano-time scales," *Journal of Computational and Theoretical Nanoscience*, vol. 7, no. 11, pp. 2271–2280, 2010.

[23] M. Agop, P. E. Nica, S. Gurlui, C. Focşa, V. P. Păun, and M. Colotin, "Implications of an extended fractal hydrodynamic model," *The European Physical Journal D*, vol. 56, no. 3, pp. 405–419, 2010.

[24] E. M. Lifshiëtìs and L. D. Landau, *Fluid Mechanics*, Pergamon Press, 1987.

[25] G. V. Munceleanu, V.-P. Paun, I. Casian-Botez, and M. Agop, "The microscopic-macroscopic scale transformation through a chaos scenario in the fractal space-time theory," *International Journal of Bifurcation and Chaos*, vol. 21, no. 2, pp. 603–618, 2011.

[26] P. Nica, M. Agop, S. Gurlui, C. Bejinariu, and C. Focsa, "Characterization of aluminum laser produced plasma by target current measurements," *Japanese Journal of Applied Physics*, vol. 51, Article ID 106102, 10 pages, 2012.

[27] P. Nica, P. Vizureanu, M. Agop et al., "Experimental and theoretical aspects of aluminum expanding laser plasma," *Japanese Journal of Applied Physics*, vol. 48, no. 6, Article ID 066001, 2009.

[28] O. C. Zienkievicz and R. L. Taylor, *The Finite Element Method*, McGraw-Hill, New York, NY, USA, 1991.

[29] C. Ursu, O. G. Pompilian, S. Gurlui et al., "Al_2O_3 ceramics under high-fluence irradiation: plasma plume dynamics through space- and time-resolved optical emission spectroscopy," *Applied Physics A*, vol. 101, no. 1, pp. 153–159, 2010.

[30] O. G. Pompilian, S. Gurlui, P. Nemec, V. Nazabal, M. Ziskind, and C. Focşa, "Plasma diagnostics in pulsed laser deposition of GaLaS chalcogenides," *Applied Surface Science*, vol. 278, pp. 352–356, 2013.

[31] C. Focsa, P. Nemec, M. Ziskind, C. Ursu, S. Gurlui, and V. Nazabal, "Laser ablation of As_xSe_{100-x} chalcogenide glasses: plume investigations," *Applied Surface Science*, vol. 255, no. 10, pp. 5307–5311, 2009.

[32] C. Ursu, S. Gurlui, C. Focsa, and G. Popa, "Space- and time-resolved optical diagnosis for the study of laser ablation plasma dynamics," *Nuclear Instruments and Methods in Physics Research B*, vol. 267, no. 2, pp. 446–450, 2009.

[33] S. Gurlui and C. Focşa, "Laser ablation transient plasma structures expansion in vacuum," *IEEE Transactions on Plasma Science*, vol. 39, no. 11, pp. 2820–2821, 2011.

[34] D. L. Aronstein and C. R. Stround Jr., "Fractional wave-function revivals in the infinite square well," *Physical Review A*, vol. 55, no. 6, pp. 1050–2947, 1997.

[35] C. P. Cristescu, *Dinamici Neliniare Si Haos, Fundamente Teoretice Si Aplicatii*, Academiei Romane, Bucuresti, Romania, 2008.

[36] J. Zhang and W. Tang, "Optimal control for a class of chaotic systems," *Journal of Applied Mathematics*, vol. 2012, Article ID 859542, 20 pages, 2012.

[37] J. B. Polly and J. M. McDonough, "Application of the poor Man's navier-stokes equations to real-time control of fluid flow," *Journal of Applied Mathematics*, vol. 2012, Article ID 746752, 18 pages, 2012.

[38] E. S. Bacaita, C. Bejinariu, B. Zoltan et al., "Nonlinearities in drug release process from polymeric microparticles: long-time-scale behaviour," *Journal of Applied Mathematics*, vol. 2012, Article ID 653720, 26 pages, 2012.

[39] K. Yuan, J. Cao, and S. Fei, "Synchronization of coupled networks with mixed delays by intermittent control," *Journal of Applied Mathematics*, vol. 2012, Article ID 927609, 13 pages, 2012.

Hindawi Publishing Corporation
Journal of Applied Mathematics
Volume 2013, Article ID 583648, 8 pages
http://dx.doi.org/10.1155/2013/583648

Research Article

Modeling and Analysis of Epidemic Diffusion with Population Migration

Ming Liu and Yihong Xiao

Department of Management Science and Engineering, Nanjing University of Science and Technology, Nanjing 210094, China

Correspondence should be addressed to Ming Liu; liumingseu@126.com

Received 15 June 2013; Revised 24 July 2013; Accepted 30 July 2013

Academic Editor: Zhiwei Gao

Copyright © 2013 M. Liu and Y. Xiao. This is an open access article distributed under the Creative Commons Attribution License, which permits unrestricted use, distribution, and reproduction in any medium, provided the original work is properly cited.

An improved Susceptible-Infected-Susceptible (SIS) epidemic diffusion model with population migration between two cities is modeled. Global stability conditions for both the disease-free equilibrium and the endemic equilibrium are analyzed and proved. The main contribution of this paper is reflected in epidemic modeling and analysis which considers unequal migration rates, and only susceptible individuals can migrate between the two cities. Numerical simulation shows when the epidemic diffusion system is stable, number of infected individuals in one city can reach zero, while the number of infected individuals in the other city is still positive. On the other hand, decreasing population migration in only one city seems not as effective as improving the recovery rate for controlling the epidemic diffusion.

1. Introduction

As mentioned in Rachaniotis et al. [1], a serious epidemic is a problem that tests the ability of a nation to effectively protect its population, to reduce human loss, and to rapidly recover. Sometime such a problem may acquire worldwide dimensions. For example, during the period from November 2002 to August 2003, 8422 people in 29 countries were infected with SARS; 916 of them were dead at last for the effective medical resources appeared late. Other diseases, such as HIV and H1N1, can also cause significant numbers of direct infectious disease deaths. Epidemic diffusion is a typical complex dynamic system problem in Gao et al. [2], for we do not know what kind of epidemic outbreaks, when it outbreaks, and how it diffuses. Generally, after an epidemic outbreaks, public officials are faced with many critical and complex issues, the most important of which is to make certain how the epidemic diffuses so that the rescue operation efficiency is maximized.

Traditionally, analytical works on epidemic diffusion are concentrated on the compartmental epidemic models of ordinary differential equations (Mishra and Saini [3]; Sun and Hsieh [4]; Li et al. [5]; Zhang et al. [6]; Zhang and Ma [7]). In these models, the total population is divided into several independence classes, and each class of individuals is closed into a compartment. The sizes of the compartments are large enough, and the mixing of members is homogeneous. In other words, the models based on the differential equations are always under the assumption of both homogeneous infectivity and homogeneous connectivity of each individual. Recently, Kim et al. [8] described the transmission of avian influenza among birds and humans. The behavior of positive solutions to a reaction diffusion system with homogeneous Neumann boundary conditions was investigated in their work. Liu and Zhang [9] presented an SEIRS epidemic model on the scale-free networks, where the active contact number of each vertex was assumed to be either constant or proportional to its degree in their model. Samsuzzoha et al. [10] used a diffusive epidemic model to describe the transmission of influenza. The equations were solved numerically by using the splitting method under different initial distribution of population density. Further, Samsuzzoha et al. [11] presented a vaccinated diffusive compartmental epidemic model to explore the impact of vaccination as well as diffusion on the transmission dynamics of influenza. A very recent research by Shi and Dong [12] formulates and discusses models for the spread of infectious diseases with variable population sizes and vaccinations on the susceptible individuals.

The other stream of related research to our work is on the epidemic diffusion with population migration. For instance,

Hethcote [13] proposed that deterministic communicable disease models were initial value problems for a system of ordinary differential equations, and thus he considered the asymptotic stability for the equilibrium points for models involving temporary immunity, disease-related fatalities, carriers, migration, dissimilar interacting groups, and transmission by vectors. In his work, both susceptible individuals and infected individuals in each population could migrate (only equal rates were considered), which led to different equilibriums. Another model that considers two interacting populations undergoing SIS dynamics was presented in Kribs-Zaleta and Velasco-Hernández [14]. The authors considered that the two groups may have different values for model parameters especially those dealing with vaccination. Liebovitch and Schwartz [15] proposed that classical disease models always use a mass action term as the interaction between infected and susceptible people in separate patches, and they derived the equations when this interaction is a migration of people between patches. Sani and Kroese [16] formulated various mathematical control problems for HIV spread in mobile heterosexual populations. They applied the cross-entropy method to solve these highly multimodal and nonlinear optimization problems, and demonstrated the effectiveness of the method via a range of experiments and illustrated how the form of the optimal control function depends on the mathematical model used for the HIV spread. Yang et al. [17] considered SIR and SIS epidemic models with bilinear incidence and migration between two patches, where infected individuals cannot migrate from one patch to another due to medical screening. They found the thresholds classifying the global dynamics of the models in terms of the model parameters, and they obtained the global asymptotical stability of the disease free and the disease-endemic equilibrium. Wolkewitz and Schumacher [18] pointed out that the main limitation of the compartmental models is that several parameters are based on uncertain expert guesses (default values) and are not estimated from the study data. Lee et al. [19] extended the SEIR model to incorporate population migration between cities and investigated the effectiveness of travel restrictions as a control against the spread of influenza.

It is worth mentioning that majority of the existing studies relies on different kinds of differential equations. For instance, first-order partial differential equations are used to integrate the age structures; second-order partial differential equations are suitable when a diffusion term exists; integral differential equations or differential equations are often used when time delay or delay factors are considered. These are the typical methods to model and analyze the complex dynamic system of epidemic diffusion. As a continued work of our previous paper in [20], this paper presents an SIS epidemic model with population migration between two cities. We consider unequal migration rates for these two populations, and only susceptible individuals can migrate, which is different from the whole existing works. The remainder of the paper is organized as follows. Section 2 proposes the SIS epidemic diffusion model, which considers susceptible individuals migration between two cities. In Section 3, the dynamic characteristics of the proposed SIS model are analyzed. Numerical simulation and key parameters analysis are presented in Section 4. Finally, Section 5 discusses the conclusions and suggests for the future research.

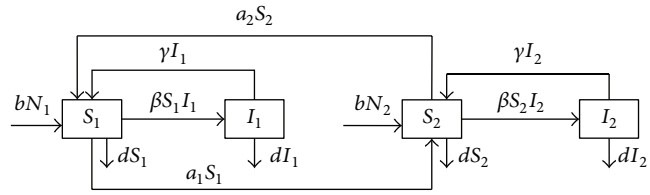

Figure 1: The transfer diagram of SIS model with population migration.

2. Epidemic Diffusion Model (SIS)

Since the compartment model of epidemic diffusion is a mature theory, herein we omit the verbose introduction of the framework process. In this paper, we divide people in epidemic areas into two groups: susceptible individuals (S) and infected individuals (I). The transfer diagram of individuals in the epidemic areas can be illustrated as Figure 1.

To smooth the formulation progress of the SIS epidemic diffusion model in the following subsections, some assumptions and parameters are specified as follows.

(1) The susceptible individuals and the infected individuals in city i at time t are denoted as $S_i(t)$ and $I_i(t)$, respectively. Thus, the total individuals in city i are $N_i(t) = S_i(t) + I_i(t)$, $i = 1, 2$.

(2) b and d are the natural birth rate and the natural death rate, respectively. γ is the recovery rate. β is the propagation coefficient. To facilitate the process in the following sections, we assume that $b = d$. Moreover, disease-related death rate is not considered in this work.

(3) Only the susceptible individuals can migrate in this paper. a_i represents the migrating-out rate of susceptible individuals in city i ($a_i > 0$ for $i = 1, 2$ and $a_1 \neq a_2$).

(4) Using the notation N to represent the total number of the population in these two cities, $N = N_1 + N_2$. Note that N is a constant.

Hence, the ordinary differential equations for the SIS epidemic diffusion model can be formulated as

$$\begin{aligned}
\frac{dS_1}{dt} &= bN_1 - a_1S_1 + a_2S_2 - dS_1 - \beta S_1 I_1 + \gamma I_1,\\
\frac{dI_1}{dt} &= \beta S_1 I_1 - \gamma I_1 - dI_1,\\
\frac{dS_2}{dt} &= bN_2 + a_1S_1 - a_2S_2 - dS_2 - \beta S_2 I_2 + \gamma I_2,\\
\frac{dI_2}{dt} &= \beta S_2 I_2 - \gamma I_2 - dI_2.
\end{aligned} \tag{1}$$

ODE (1) describes the following dynamics of epidemic diffusion among the population groups. (1) The change rate

of the susceptible population in both city 1 and city 2 is determined by the entry population, the exiting population, and the losing population who actually gets exposed to the disease and thus is counted towards the class of infected population. The last one is in proportion to the propagation coefficient β and both of the current mass of the susceptible individuals and the current mass of the infected individuals. (2) The change rate of the infected population is determined by the difference between the entering population, those of the susceptible population who get sick, the exiting population, and the losing population. All parameters β, b, γ, a_1, and a_2 are positive, and initial conditions for the model are demonstrated as follows:

$$\begin{aligned} I_1(0) &= i_1^0 \ll N, \qquad I_2(0) = i_2^0 \ll N, \\ S_1(0) &= s_1^0, \qquad S_2(0) = N - s_1^0 - i_1^0 - i_2^0. \end{aligned} \tag{2}$$

3. Model Analysis

3.1. Condition of the Epidemic Diffusion. As shown above, $I_1(0) = i_1^0 \ll N$, $I_2(0) = i_2^0 \ll N$, $S_1(0) = s_1^0$, and $S_2(0) = N - s_1^0 - i_1^0 - i_2^0$ are initial conditions for the proposed model, which symbolize the initial number of susceptible and infected individuals. Then, it is easy to obtain the initial condition for epidemic diffusion, which should satisfy the following premise:

$$\left.\frac{dI_1}{dt}\right|_{t=0} > 0 \quad \text{or} \quad \left.\frac{dI_2}{dt}\right|_{t=0} > 0. \tag{3}$$

Taking it into (1), we can obtain the initial condition of the susceptible individuals in city 1 and city 2:

$$s_1^0 > \frac{b+\gamma}{\beta} \quad \text{or} \quad s_2^0 < N - i_1^0 - i_2^0 - \frac{b+\gamma}{\beta}. \tag{4}$$

Equation (4) shows that the spread of epidemic happens only when s_1^0 and s_2^0 meet the previous initial conditions.

3.2. Existence of the System Equilibrium Solution. Generally, it is difficult to obtain the analytic solution of (1). To analyze the epidemic diffusion, we consider the stable state of (1). Considering that $b = d$ and expunging S_2, (1) can be rewritten as

$$\begin{aligned} \frac{dS_1}{dt} &= -a_1 S_1 + a_2 (N - S_1 - I_1 - I_2) - \beta S_1 I_1 + (b+\gamma) I_1, \\ \frac{dI_1}{dt} &= \beta S_1 I_1 - (b+\gamma) I_1, \\ \frac{dI_2}{dt} &= \beta (N - S_1 - I_1 - I_2) I_2 - (b+\gamma) I_2. \end{aligned} \tag{5}$$

Letting $dI_1/dt = 0$, we can get $I_1 = 0$ or $S_1 = (b+\gamma)/\beta$. Similarly, letting $dI_2/dt = 0$, we can obtain $I_2 = 0$ or $S_1 + I_1 + I_2 = N - ((b+\gamma)/\beta)$. With the partial derivatives $dS_1/dt = 0$, $dI_1/dt = 0$, and $dI_2/dt = 0$, we can obtain one equilibrium point of the SIS epidemic diffusion system intuitively when $I_1 = 0$ and $I_2 = 0$:

$$P_1 = (S_1, I_1, I_2) = \left(\frac{a_2}{a_1 + a_2} N, 0, 0\right). \tag{6}$$

From (6) we can see that both numbers of infected individuals in city 1 and city 2 are zero, which indicate that epidemic diffusion in these two cities does not happen, and all the individuals in these two cities are susceptible individuals at last. Herein, we call it disease-free equilibrium point.

When $I_1 = 0$ and $S_1 + I_1 + I_2 = N - ((b+\gamma)/\beta)$, we can obtain the second equilibrium point of the SIS epidemic diffusion system:

$$P_2 = (S_1, I_1, I_2) = \left(\frac{a_2}{a_1} \cdot \frac{b+\gamma}{\beta}, 0, N - \frac{a_1 + a_2}{a_1} \cdot \frac{b+\gamma}{\beta}\right). \tag{7}$$

From (7), when the SIS epidemic diffusion system is stable, the number of infected individuals in city 1 is zero, and some infected individuals in city 2 still exist. In this condition, we call it the endemic equilibrium point.

Likewise, when $S_1 = (b+\gamma)/\beta$ and $I_2 = 0$, we can obtain the third equilibrium point of the SIS epidemic diffusion system:

$$P_3 = (S_1, I_1, I_2) = \left(\frac{b+\gamma}{\beta}, N - \frac{a_1 + a_2}{a_2} \cdot \frac{b+\gamma}{\beta}, 0\right). \tag{8}$$

In line with the above work, when the SIS epidemic diffusion system is stable, the number of infected individuals in city 2 is zero, and some infected individuals in city 1 still exist. So it is called endemic equilibrium point as well.

It is worth mentioning that, when $S_1 = (b+\gamma)/\beta$ and $S_1 + I_1 + I_2 = N - ((b+\gamma)/\beta)$, there is $dS_1/dt = (a_2 - a_1) \cdot (b+\gamma)/\beta \neq 0$ for that $a_1 \neq a_2$. That means, under the conditions of $S_1 = (b+\gamma)/\beta$ and $S_1 + I_1 + I_2 = N - ((b+\gamma)/\beta)$, there is no solution for the simultaneous equations $dS_1/dt = 0$, $dI_1/dt = 0$, and $dI_2/dt = 0$.

3.3. Stability of the System Equilibrium Solution

Lemma 1. *Disease-free equilibrium point P_1 in the SIS epidemic diffusion system is stable only when $\beta < \min\{(a_1+a_2)(b+\gamma)/a_1 N, (a_1+a_2)(b+\gamma)/a_2 N\}$.*

Proof. Letting $P = dS_1/dt$, $Q = dI_1/dt$, and $R = dI_2/dt$, the Jacobi matrix of (5) can be obtained as follows:

$$J = \begin{pmatrix} \frac{\partial P}{\partial S_1} & \frac{\partial P}{\partial I_1} & \frac{\partial P}{\partial I_2} \\ \frac{\partial Q}{\partial S_1} & \frac{\partial Q}{\partial I_1} & \frac{\partial Q}{\partial I_2} \\ \frac{\partial R}{\partial S_1} & \frac{\partial R}{\partial I_1} & \frac{\partial R}{\partial I_2} \end{pmatrix} = \begin{pmatrix} -a_1 - a_2 - \beta I_1 & b + \gamma - a_2 - \beta S_1 & -a_2 \\ \beta I_1 & \beta S_1 - (b + \gamma) & 0 \\ -\beta I_2 & -\beta I_2 & \beta (N - S_1 - I_1 - 2I_2) - (b + \gamma) \end{pmatrix}. \tag{9}$$

For $P_1 = (S_1, I_1, I_2) = (a_2/(a_1 + a_2)N, 0, 0)$, the Jacobi matrix J can be rewritten as follows:

$$J_{P_1} = \begin{pmatrix} -a_1 - a_2 & b + \gamma - a_2 - \frac{a_2 N}{a_1 + a_2}\beta & -a_2 \\ 0 & \frac{a_2 N}{a_1 + a_2}\beta - (b + \gamma) & 0 \\ 0 & 0 & \frac{a_1 N}{a_1 + a_2}\beta - (b + \gamma) \end{pmatrix} \tag{10}$$

According to the Jacobi matrix J_{P_1}, it is easy to obtain the secular equation of (5):

$$\left(\lambda + a_1 + a_2\right)\left(\lambda + b + \gamma - \frac{a_2 N}{a_1 + a_2}\beta\right) \times \left(\lambda + b + \gamma - \frac{a_1 N}{a_1 + a_2}\beta\right) = 0. \tag{11}$$

The three latent roots of this secular equation are $-a_1 - a_2$, $a_2 N/(a_1 + a_2)\beta - b - \gamma$, and $a_1 N/(a_1 + a_2)\beta - b - \gamma$. Based on Routh-Hurwitz stability criterion, only when $\beta < (a_1 + a_2)(b + \gamma)/a_1 N$ and $\beta < (a_1 + a_2)(b + \gamma)/a_2 N$, three latent roots of the secular equation would have negative real parts, simultaneously, and then $P_1 = (S_1, I_1, I_2) = (a_2/(a_1 + a_2)N, 0, 0)$ is the stable solution of the differential equations. □

Lemma 2. *Endemic equilibrium point P_2 in the SIS epidemic diffusion system is stable only when $a_2 < a_1$ and $\beta > (a_1 + a_2)(b + \gamma)/a_1 N$.*

Proof. As far as we are concerned, if the endemic equilibrium point $P_2 = (S_1, I_1, I_2) = (a_2/a_1 \cdot (b+\gamma)/\beta, 0, N - (a_1+a_2)/a_1 \cdot (b+\gamma)/\beta)$ exists, it should satisfy condition $I_2 > 0$ firstly. Namely, the propagation coefficient β should satisfy $\beta > (a_1 + a_2)(b + \gamma)/a_1 N$. Then, similar to Lemma 1, we can obtain the Jacobi matrix for P_2 as follows:

$$J_{P_2} = \begin{pmatrix} -a_1 - a_2 & b + \gamma - a_2 - \frac{a_2}{a_1}(b + \gamma) & -a_2 \\ 0 & \frac{a_2}{a_1}(b + \gamma) - (b + \gamma) & 0 \\ \frac{a_1 + a_2}{a_1}(b + \gamma) - \beta N & \frac{a_1 + a_2}{a_1}(b + \gamma) - \beta N & \frac{a_1 + a_2}{a_1}(b + \gamma) - \beta N \end{pmatrix}. \tag{12}$$

According to the Jacobi matrix J_{P_2}, we can obtain the secular equation of (5) again:

$$\left[\lambda + b + \gamma - \frac{a_2}{a_1}(b + \gamma)\right]\left(\lambda^2 + A_1\lambda + A_0\right) = 0, \tag{13}$$

where $A_0 = a_1[\beta N - ((a_1 + a_2)/a_1)(b + \gamma)]$ and $A_1 = a_1 + a_2 + \beta N - ((a_1 + a_2)/a_1)(b + \gamma)$. Obviously, one of the latent roots of (13) is $\lambda_1^* = ((a_2 - a_1)/a_1)(b + \gamma)$. Only when $a_2 < a_1$, the latent root λ_1^* is negative. On the other hand, when $\beta > (a_1 + a_2)(b + \gamma)/a_1 N$, there is $A_0 > 0$ and $A_1 > 0$. Based on Routh-Hurwitz stability criterion, the other two latent roots of (13) will be with negative real parts. Therefore, P_2 is the stable solution of the simultaneous differential equations only when $a_2 < a_1$ and $\beta > (a_1 + a_2)(b + \gamma)/a_1 N$. □

Lemma 3. *Endemic equilibrium point P_3 in the SIS epidemic diffusion system is stable only when $a_1 < a_2$ and $\beta > ((a_1 + a_2)(b + \gamma))/a_2 N$.*

Proof. Similar to Lemma 2, if the endemic equilibrium point $P_3 = (S_1, I_1, I_2) = ((b+\gamma)/\beta, N-(a_1+a_2)/a_2 \cdot (b+\gamma)/\beta, 0)$ exists, it should satisfy condition $I_1 > 0$. That is, the propagation coefficient β should satisfy $\beta > (a_1 + a_2)(b + \gamma)/a_2 N$. Then, we can obtain the Jacobi matrix for P_3 as follows:

$$J_{P_3} = \begin{pmatrix} -a_1 - a_2 - \beta N + \dfrac{a_1 + a_2}{a_2}(b+\gamma) & -a_2 & -a_2 \\ \beta N - \dfrac{a_1 + a_2}{a_2}(b+\gamma) & 0 & 0 \\ 0 & 0 & \dfrac{a_1 - a_2}{a_2}(b+\gamma) \end{pmatrix}. \tag{14}$$

Again, according to the Jacobi matrix J_{P_3}, we can obtain the secular equation of (5):

$$\left[\lambda - \frac{a_1 - a_2}{a_2}(b+\gamma)\right]\left(\lambda^2 + B_1\lambda + B_0\right) = 0, \tag{15}$$

where $B_0 = a_2[\beta N - ((a_1 + a_2)/a_2)(b + \gamma)]$ and $B_1 = a_1 + a_2 + \beta N - ((a_1 + a_2)/a_2)(b + \gamma)$. Obviously, one of the latent roots of (15) is $\lambda_1^* = ((a_1 - a_2)/a_2)(b + \gamma)$. Only when $a_1 < a_2$, the latent root λ_1^* is negative. On the other hand, when $\beta > (a_1 + a_2)(b + \gamma)/a_2 N$, there is $B_0 > 0$ and $B_1 > 0$. Based on Routh-Hurwitz stability criterion, the other two latent roots of (15) will be with negative real parts. Therefore, P_3 is the stable solution of the simultaneous differential equations only when $a_1 < a_2$ and $\beta > (a_1 + a_2)(b + \gamma)/a_2 N$. □

Remark 4. From Lemmas 1, 2, and 3, we can draw a conclusion that the diffusion threshold of the SIS epidemic diffusion model relies on the migrating-out coefficients of susceptible individuals of the two cities a_i $(i = 1, 2)$; it also depends on the three key parameters: the total individuals of the two cities N, the birth rate b, and the recovery rate γ.

4. Numerical Simulation and Key Parameters Discussion

In this section, we take a numerical simulation to test how well the proposed model may be applied in practice. The initial values of parameters in the proposed epidemic diffusion model are acquired from Liu and Zhao [21] and by interviews with public health care administrative personnel, which are given as follows: $\beta = 8 \times 10^{-6}$, $b = 2 \times 10^{-4}$, $\gamma = 0.4$, $a_1 = 0.02$, $a_2 = 0.01$, $N = 10^5$, $S_1(0) = 0.7 \times 10^5$, $I_1(0) = 600$, and $I_2(0) = 400$. We use MATLAB 7.0 mathematical solver together with Runge-Kutta method to simulate the epidemic model. The test is performed on an Intel (R) Core (TM) i3 CPU 2.4 GHz with 2 GB RAM under Microsoft Windows XP. Figure 2 is the evolution trajectories of the epidemic model. The curves, respectively, represent the different groups of people over time in these two cities.

From Figure 2, one can see that the evolution trajectories of the SIS epidemic model with population migration between two cities are complicated. The number of susceptible individuals in city 1 decreases gradually with time increasing, while the number of susceptible individuals in city 2 increases at first and then decreases. On the other hand, the number of infected individuals in city 1 increases at first and then decreases, while the number of infected individuals in city 2 increases gradually with time increasing. However, all the susceptible individuals and infected individuals in city 1 and city 2 tend to the fixed values when time is long enough ($t > 300$). Meanwhile, the limit value of the SIS epidemic diffusion model with population migration between two cities is $Q_1 = (S_1, S_2, I_1, I_2) = (2.5013 \times 10^4, 5.0025 \times 10^4, 0, 2.4961 \times 10^4)$.

In line with the initial values we defined previously, we have $a_2 < a_1$ and $\beta > (a_1 + a_2)(b + \gamma)/a_1 N$. According to Lemma 2 in Section 3, one can get that the number of susceptible and infected individuals will be converged at $Q_2 = (S_1^*, S_2^*, I_1^*, I_2^*) = (2.50125 \times 10^4, 5.00245 \times 10^4, 0, 2.4963 \times 10^4)$. One can see that Q_1 is very close to Q_2, which is not a surprise, as it is consistent with the analytical conclusion in the last section. Once an epidemic outbreak occurs, we are more concerned with the change regularity of the infected individuals in practice. Therefore, in the following subsections, we will discuss the relationship between the key parameters and the number of the infected individuals.

Figure 3 demonstrates the change of the number of the infected individuals in both cities with different propagation coefficients. It is easy to know that the evolution trajectories of infected individuals in city 1 are different from those in city 2 for any certain propagation coefficient β. From Figure 3(a), we can see that, in the first some days, the larger β is, the faster spread of the epidemic in city 1 is. However, from Figure 3(b), we cannot get the similar conclusion. Number of infected individuals in city 2 is not in direct proportion to the propagation coefficient β. It is worth mentioning that, when the number of infected individuals in city 1 reaches zero, the number of infected individuals in the other city is still positive when the epidemic diffusion system is stable. This is consistent with Lemma 2 in Section 3. Similarly, if the initial conditions changed, we can also test and verify the other lemmas.

Figure 4 demonstrates the change of the number of the infected individualss in both cities with different recovery rate γ. As shown in Figure 4(a), when $\gamma = 0.2$, the maximum number of infected individuals in city 1 is about 3.3×10^4.

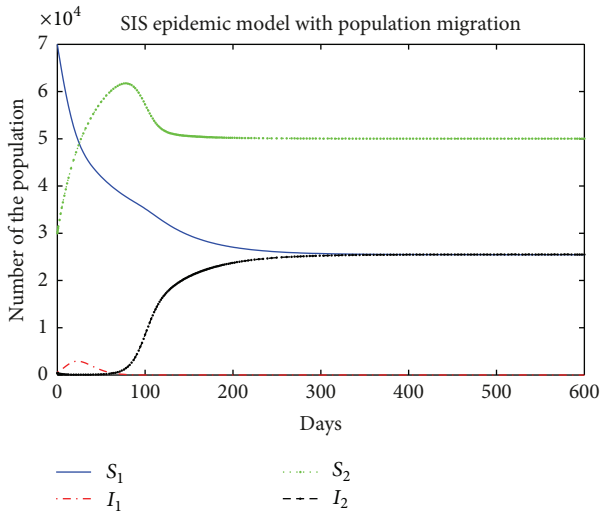

Figure 2: Evolution trajectories of the SIS epidemic model.

When $\gamma = 0.3$, the number is about 1.5×10^4. When $\gamma = 0.4$, the maximum number of infected individual in city 1 is less than 0.5×10^4. It informs us that the larger the recovery rate constant is, the smaller of the maximum number of infected individuals in city 1 is. Similar phenomenon can also be observed from Figure 4(b) in city 2. Such figure informs us that it is important to improve the recovery rate as much as possible when controlling an epidemic spread.

Figure 5 shows the change of the number of infected individuals in both cities with different migrating-out coefficients a_1 and a_2. According to Figure 5, one can observe that no matter in city 1 or in city 2, the evolution trajectories of the infected individuals may generate a serious change when the migrating-out coefficient of susceptible individuals changed. For example, in city 1, when $a_2 < a_1$ ($a_1 = 0.02$, $a_2 = 0.01$ and $a_1 = 0.02$, $a_2 = 0.015$), the number of infected individuals tends to be zero. However, when $a_1 < a_2$ ($a_1 = 0.02$, $a_2 = 0.025$ and $a_1 = 0.02$, $a_2 = 0.03$), the number of infected individuals tends to be a positive constant above 1×10^4. In other words, with the increment of migrating-out coefficient in city 2, the limit number of infected individuals in city 1 may become positive from zero. The larger the migrating-out coefficient in city 2 is, the larger the limit number of infected individuals in city 1 is. Opposite to city 1, when $a_2 < a_1$ ($a_1 = 0.02$, $a_2 = 0.01$ and $a_1 = 0.02$, $a_2 = 0.015$), the number of infected individuals in city 2 tends to be a positive constant above 1×10^4. When $a_1 < a_2$ ($a_1 = 0.02$, $a_2 = 0.025$ and $a_1 = 0.02$, $a_2 = 0.03$), the number of infected individuals is very small and tends to be zero at last. It informs us that with the increment of migrating-out coefficient in city 2, the limit number of infected individuals in city 2 may become zero from a positive value. The larger the migrating-out coefficient in city 2 is, the smaller the limit number of infected individuals in city 2 is. To summarize, decreasing the migration population in only one city is not as effective as improving the recovery rate for controlling the epidemic diffusion. However, we can find a trade-off between the migrating-out coefficients in these two cities and hence can control the infected individuals in both cities at last.

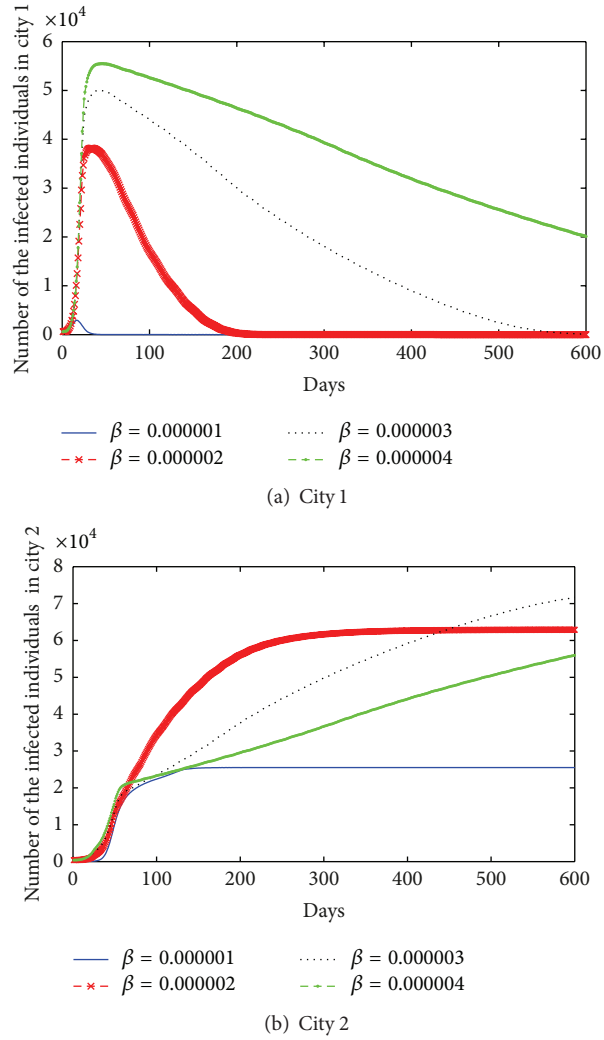

Figure 3: Number of the infected individuals versus different β.

5. Conclusions

In this paper, we considered an SIS epidemic diffusion model with population migration between two cities, and proved that the model has one disease-free equilibrium point and two endemic equilibrium points. To summarize, our model differs from past researches in at least two aspects. Firstly, unequal migration rates between the two cities are considered; secondly, only the susceptible individuals can migrate between the two cities. Numerical simulation shows that number of infected individuals in one city can reach zero, while the number of infected individuals in the other city is still positive when the epidemic diffusion system is stable. One the other hand, decreasing population migration in only one city is not as effective as improving the recovery rate for controlling the epidemic diffusion.

As a limitation of the model, disease-related death rate of infected individuals in both cities was not considered. Actually, some epidemics would cause death, and thus consideration of a disease-related death rate would make it more accurate. On the other hand, epidemic diffusion model with population migration among more than two cities should also be taken into account. A discussion of possible extension to

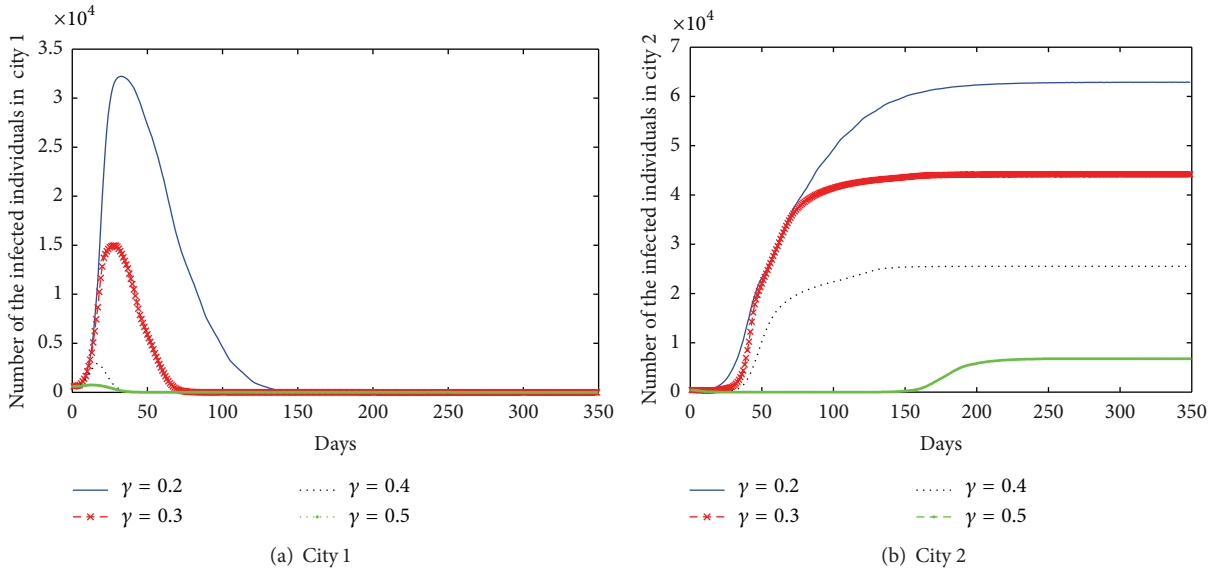

(a) City 1 (b) City 2

Figure 4: Number of the infected individuals versus different γ.

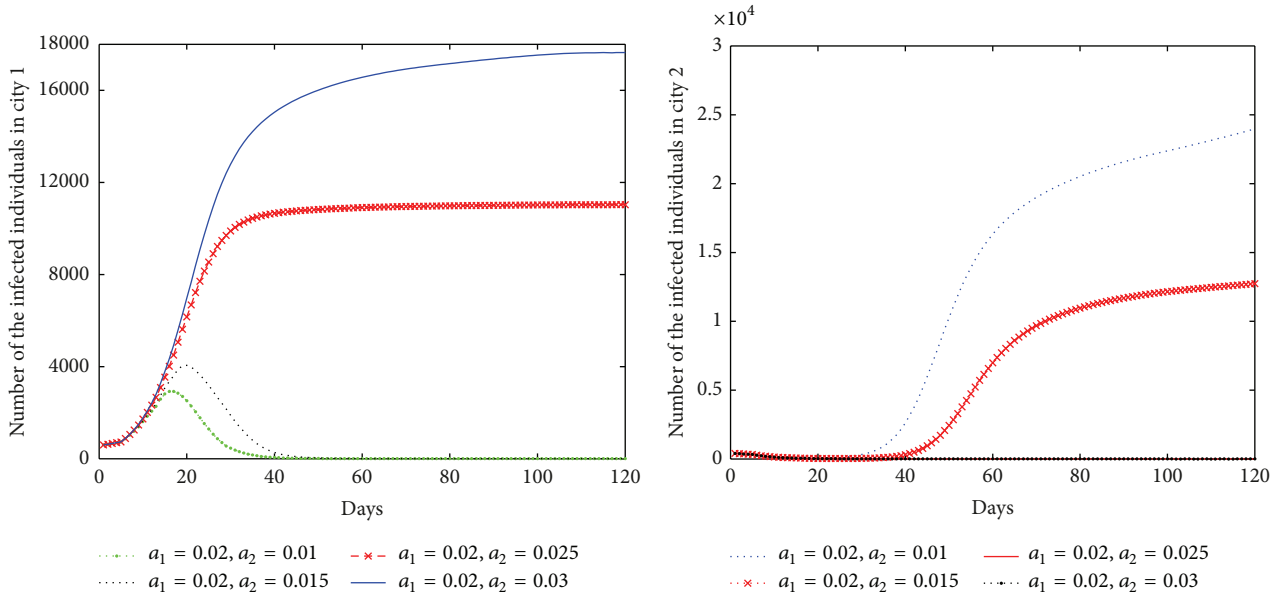

(a) City 1 (b) City 2

Figure 5: Number of the infected individuals versus different a_1 and a_2.

more than two cities would be more realistic and the research would be more practical.

Acknowledgments

This work has been partially supported by the National Natural Science Foundation of China (no. 71301076), the MOE (Ministry of Education in China) Project of Humanities and Social Sciences (no. 11YJCZH109), the Fundamental Research Funds for the Central Universities (nos. 30920130121006, 30920130132011), and the Zijin Intelligent Program in Nanjing University of Science and Technology (no. 2013-ZJ0211).

References

[1] N. P. Rachaniotis, T. K. Dasaklis, and C. P. Pappis, "A deterministic resource scheduling model in epidemic control: a case study," *European Journal of Operational Research*, vol. 216, no. 1, pp. 225–231, 2012.

[2] Z. Gao, D. Kong, and C. Gao, "Modeling and control of complex dynamic systems: applied mathematical aspects," *Journal of Applied Mathematics*, vol. 2012, Article ID 869792, 5 pages, 2012.

[3] B. K. Mishra and D. K. Saini, "SEIRS epidemic model with delay for transmission of malicious objects in computer network,"

Applied Mathematics and Computation, vol. 188, no. 2, pp. 1476–1482, 2007.

[4] C. J. Sun and Y.-H. Hsieh, "Global analysis of an SEIR model with varying population size and vaccination," *Applied Mathematical Modelling*, vol. 34, no. 10, pp. 2685–2697, 2010.

[5] M. Y. Li, J. R. Graef, L. C. Wang, and J. Karsai, "Global dynamics of a SEIR model with varying total population size," *Mathematical Biosciences*, vol. 160, no. 2, pp. 191–213, 1999.

[6] J. Zhang, J. Q. Li, and Z. Ma, "Global dynamics of an SEIR epidemic model with immigration of different compartments," *Acta Mathematica Scientia B*, vol. 26, no. 3, pp. 551–567, 2006.

[7] J. Zhang and Z. Ma, "Global dynamics of an SEIR epidemic model with saturating contact rate," *Mathematical Biosciences*, vol. 185, no. 1, pp. 15–32, 2003.

[8] K. I. Kim, Z. G. Lin, and L. Zhang, "Avian-human influenza epidemic model with diffusion," *Nonlinear Analysis: Real World Applications*, vol. 11, no. 1, pp. 313–322, 2010.

[9] J. L. Liu and T. L. Zhang, "Epidemic spreading of an SEIRS model in scale-free networks," *Communications in Nonlinear Science and Numerical Simulation*, vol. 16, no. 8, pp. 3375–3384, 2011.

[10] M. Samsuzzoha, M. Singh, and D. Lucy, "Numerical study of an influenza epidemic model with diffusion," *Applied Mathematics and Computation*, vol. 217, no. 7, pp. 3461–3479, 2010.

[11] M. Samsuzzoha, M. Singh, and D. Lucy, "A numerical study on an influenza epidemic model with vaccination and diffusion," *Applied Mathematics and Computation*, vol. 219, no. 1, pp. 122–141, 2012.

[12] P. L. Shi and L. Z. Dong, "Dynamical models for infectious diseases with varying population size and vaccinations," *Journal of Applied Mathematics*, vol. 2012, Article ID 824192, 20 pages, 2012.

[13] H. W. Hethcote, "Qualitative analyses of communicable disease models," *Mathematical Biosciences*, vol. 28, no. 3-4, pp. 335–356, 1976.

[14] C. M. Kribs-Zaleta and J. X. Velasco-Hernández, "A simple vaccination model with multiple endemic states," *Mathematical Biosciences*, vol. 164, no. 2, pp. 183–201, 2000.

[15] L. S. Liebovitch and I. B. Schwartz, "Migration induced epidemics: dynamics of flux-based multipatch models," *Physics Letters A*, vol. 332, no. 3-4, pp. 256–267, 2004.

[16] A. Sani and D. P. Kroese, "Controlling the number of HIV infectives in a mobile population," *Mathematical Biosciences*, vol. 213, no. 2, pp. 103–112, 2008.

[17] Y. Yang, J. Wu, J. Li, and Z. Ma, "Global dynamics—convergence to equilibria—of epidemic patch models with immigration," *Mathematical and Computer Modelling*, vol. 51, no. 5-6, pp. 329–337, 2010.

[18] M. Wolkewitz and M. Schumacher, "Simulating and analysing infectious disease data in a heterogeneous population with migration," *Computer Methods and Programs in Biomedicine*, vol. 104, no. 2, pp. 29–36, 2011.

[19] J. M. Lee, D. Choi, G. Cho, and Y. Kim, "The effect of public health interventions on the spread of influenza among cities," *Journal of Theoretical Biology*, vol. 293, pp. 131–142, 2012.

[20] M. Liu and Y. Xiao, "Modeling and analysis of epidemic diffusion within small-world network," *Journal of Applied Mathematics*, vol. 2012, Article ID 841531, 14 pages, 2012.

[21] M. Liu and L. Zhao, "Analysis for epidemic diffusion and emergency demand in an anti-bioterrorism system," *International Journal of Mathematical Modelling and Numerical Optimisation*, vol. 2, no. 1, pp. 51–68, 2011.

Hindawi Publishing Corporation
Journal of Applied Mathematics
Volume 2013, Article ID 454857, 3 pages
http://dx.doi.org/10.1155/2013/454857

Review Article

A New Type of Distributed Parameter Control Systems: Two-Point Boundary Value Problems for Infinite-Dimensional Dynamical Systems

De-Xing Kong and Fa Wu

Department of Mathematics, Zhejiang University, Hangzhou 310027, China

Correspondence should be addressed to De-Xing Kong; dkong@zju.edu.cn

Received 14 June 2013; Accepted 3 July 2013

Academic Editor: Zhiwei Gao

Copyright © 2013 D.-X. Kong and F. Wu. This is an open access article distributed under the Creative Commons Attribution License, which permits unrestricted use, distribution, and reproduction in any medium, provided the original work is properly cited.

This survey note describes a new type of distributed parameter control systems—the two-point boundary value problems for infinite-dimensional dynamical systems, particularly, for hyperbolic systems of partial differential equations of second order, some of the discoveries that have been done about it and some unresolved questions.

1. A New Type of Distributed Parameter Control Systems: Two-Point Boundary Value Problem for Hyperbolic System of Partial Differential Equations of Second Order

The mathematical theory of dynamical systems is based on the famous H. Poincaré's qualitative theory on ordinary differential equations; the works of A. M. Lyapunov and A. A. Andronov also play an essential role in its development. At present, the theory of dynamical systems is an intensively developing branch of modern mathematics, which is closely connected to the theory of ordinary differential equations. Infinite-dimensional dynamical systems generated by nonlinear evolutionary partial differential equations have been rapidly developing in recent years. In this survey note, we will describe a new type of distributed parameter control systems generated by hyperbolic systems of partial differential equations of second order—the two-point boundary value problems. This kind of problems plays an important role in control theory, mathematics, mechanics, physics, and in other areas of sciences and technology.

It is well known that there are many deep and beautiful results on the TBVPs for ordinary differential equations of second order. However, according to the authors' knowledge, only a few of the results on the TBVPs for hyperbolic equations or other nonlinear evolutionary partial differential equations (even for linear or nonlinear wave equations) have been known.

In 2010, the first author introduced the TBVPs for linear wave equations (see page 121 of [1]). For simplicity, we consider the following wave equation:

$$u_{tt} - c^2 \Delta u = 0, \tag{1}$$

where $u = u(t, x)$ is the unknown scalar function, $\Delta = \sum_{i=1}^{n} (\partial^2 / \partial x_i^2)$ denotes the Laplacian, and c is a fixed constant which stands for the propagation speed of the wave. The TBVP for (1) reads as follows:

TBVP for (1). Given two functions $f(x)$ and $g(x) \in C^{[n/2]+2}(\mathbb{R}^n)$ and a positive constant T, can we find a C^2-smooth function $u = u(t, x)$ defined on the strip $[0, T] \times \mathbb{R}^n$ such that the function $u = u(t, x)$ satisfies (1) on the domain $[0, T] \times \mathbb{R}^n$, the initial condition

$$u(0, x) = f(x), \quad \forall x \in \mathbb{R}^n, \tag{2}$$

and the terminal condition

$$u(T, x) = g(x), \quad \forall x \in \mathbb{R}^n? \tag{3}$$

The problem mentioned earlier can be expressed in another way.

Another Statement. Given two functions $f(x)$ and $g(x) \in C^{[n/2]+2}(\mathbb{R}^n)$ and a positive constant T, can we find an initial velocity $v = v(x)$ such that the Cauchy problem for wave equation (1) with the initial data

$$t = 0: \quad u = f(x), \quad u_t = v(x), \tag{4}$$

has a solution $u = (t, x) \in C^2([0, T] \times \mathbb{R}^n)$ which satisfies terminal condition (3)?

Moreover, in [1], the author also introduced the TBVPs for nonlinear wave equations including the nonlinear vibrating string and the semilinear wave equation (see page 122 of [1]). Similarly, we can propose the two-point boundary value problems for infinite-dimensional dynamical systems, particularly, the following general (linear or nonlinear) hyperbolic partial differential equation of second order:

$$\mathscr{P}\left(t, x, u, Du, D^2u\right) = 0, \tag{5}$$

where t is the time variable, $x = (x_1, \ldots, x_n)$ stand for the spacial variables, $u = u(t, x)$ is the unknown function, and $\mathscr{P}$ is a given smooth function of the independent variables $t, x_1, \ldots, x_n$, the unknown function u, the first-order partial derivatives $Du = (u_t, u_{x_1}, \ldots, u_{x_n})$, and the second-order partial derivatives $D^2u = (u_{tt}, u_{tx_1}, \ldots)$ (see [2]).

In fact, the system (1) together with conditions (2)-(3) can be viewed as a *distributed parameter control system* when the initial velocity function $v(x)$ is considered as a control input.

We now introduce the following definition.

Definition 1. For any given $T > 0$, if the TBVP (1), (2)-(3) has a C^2 solution on the strip $[0, T] \times \mathbb{R}^n$, then the system (1), (2)-(3) is called to possess the global exact controllability. If the TBVP (1), (2)-(3) admits a C^2 solution on the strip $[0, T] \times \mathbb{R}^n$ for some given $T > 0$, then one can say that the system (1), (2)-(3) possesses the exact controllability.

Remark 2. For a hyperbolic system of (linear or nonlinear) partial differential equations of second order, we have similar concepts and definitions as mentioned earlier. For hyperbolic partial differential equations of higher order, or more general infinite-dimensional dynamical systems, we also have a similar discussion.

In this survey note, we will describe the two-point boundary value problems for general infinite-dimensional dynamical systems, in particular, hyperbolic system of partial differential equations of second order, some of the discoveries that have been done about it and some unresolved questions.

2. Known Results

Since the two-point boundary value problems for (in particular, nonlinear) hyperbolic partial differential equations of second order are too complex and difficult, they are, in our opinion, challenging problems in the field of nonlinear partial differential equations. Up to now, only a few results on the TBVPs for nonlinear hyperbolic equations or other nonlinear evolutionary partial differential equations (even for nonlinear wave equations) have been known. We now recall some known results on the TBVPs for hyperbolic partial differential equations of second order.

Kong and Sun in [2] proved the following result.

Theorem 3. *The TBVP* (1)–(3) *admits a* C^2*-smooth solution* $u = u(t, x)$ *defined on the strip* $[0, T] \times \mathbb{R}^n$.

This theorem shows that wave equation (1) possesses the global exact controllability. However, the solution of the TBVP of (1)–(3) does not possess the uniqueness (see [2] for the details). On the other hand, by [2], Theorem 3 can be generalized to the case of the following inhomogeneous wave equations: $u_{tt} - c^2\Delta u = G(t, x)$, where $G(t, x)$ is a given function which stands for the source term of the system.

Similar results are also true for some nonlinear wave equations including a wave map equation arising from geometry and the equations for the motion of relativistic strings in the Minkowski space-time $\mathbb{R}^{1+n}$ (see [2]). It is well known that these nonlinear wave equations play an important role in both modern mathematics and theoretical physics.

We now consider the The TBVP of wave equation defined on the unit circle:

$$\begin{aligned} &u_{tt} - u_{\theta\theta} = 0, \quad \forall (t, \theta) \in [0, T] \times \mathbb{S}^1, \\ &u(0, \theta) = f(\theta), \quad \forall \theta \in \mathbb{S}^1, \\ &u(T, \theta) = g(\theta), \quad \forall \theta \in \mathbb{S}^1, \end{aligned} \tag{6}$$

where $\mathbb{S}^1$ stands for the unit circle, $f(\theta)$ and $g(\theta)$ are two given C^2 functions of $\theta \in \mathbb{S}^1$, and their derivative of third order is piecewise smooth. The following result has been proved by [2].

Theorem 4. *The TBVP* (6) *admits a global* C^2 *solution* $u = u(t, \theta)$ *defined on the cylinder* $[0, T] \times \mathbb{S}^1$*, provided that* $T/2\pi$ *is a rational number and* $T/\pi \notin \mathbb{N}$.

Theorem 4 implies that the wave equation defined on a circle possesses the exact controllability. Moreover, for the $(1+n)$-dimensional wave equation (1), we have similar results, provided that the initial/terminal data $f(x)$ and $g(x)$ in (2)-(3) are suitable smooth functions and are periodic in $r = \sqrt{x_1^2 + \cdots + x_n^2}$.

As an application of the results mentioned earlier, Kong and Sun in [2] introduced a hyperbolic curvature flow and obtained a result analogous to the well-known theorem of Gage and Hamilton [3] for the curvature flow of plane curves.

3. Open Problems

Although we have proved the existence of solutions to the TBVPs for linear wave equations or some special nonlinear wave equations, there are quite a number of problems here.

In particular, the following open problems seem to be more interesting and important.

Problem 1. The two-point boundary value problem for a semilinear wave equation

$$u_{tt} - u_{xx} = f(u) \tag{7}$$

with a regular and bounded function $f(y)$. For example, $f(u) = \sin u$ corresponds the famous sine-Gorden equation.

Problem 2. The two-point boundary value problem for a quasilinear wave equation

$$u_{tt} - \left(\mathscr{C}\left(u_x\right)\right)_x = 0 \tag{8}$$

with a smooth and increasing function $\mathscr{C}(v)$, for example, $\mathscr{C}(v) = v/\sqrt{1+v^2}$, which describes the nonlinear vibrating string.

Problem 3. The two-point boundary value problem for the following hyperbolic Monge-Ampère equation (see [4])

$$S_{\tau\tau} = \frac{S_{\theta\tau}^2 - 1}{S_{\theta\theta} + S}, \quad \forall (\theta, \tau) \in \mathbb{S}^1 \times [0, T). \tag{9}$$

This problem plays an important role in geometric analysis, crystal growth, and so forth. Precisely speaking, if does there exist a smooth solution S to (9) such that the following conditions hold

$$S(0,\theta) = S_0(\theta), \qquad S(T,\theta) = S_T(\theta)? \tag{10}$$

where $S_0(\theta)$ and $S_T(\theta)$ are two smooth and positive functions defined on $\mathbb{S}^1$.

Problem 4. Two-point boundary value problems for multidimensional version of the equations mentioned above. Moreover, it is worthy to investigate the two-point boundary value problems for the systems of multidimensional partial differential equations, for example, Einstein's field equations and the system of time-like extremal submanifolds in physical space-times and so forth.

Problem 5. The two-point boundary value problem for hyperbolic geometric flow: Let $\mathscr{M}$ be n-dimensional complete compact Riemannian manifold with the Riemannian metric g_0. Given a positive constant T and another Riemannian metric g_T on $\mathscr{M}$, if does there exist a smooth solution g to the hyperbolic geometric flow equation

$$\frac{\partial^2 g_{ij}}{\partial t^2} = -2R_{ij} \tag{11}$$

such that the following conditions hold

$$g(0) = g_0, \qquad g(T) = g_T? \tag{12}$$

Obviously, (11) is a nonlinear system of second-order partial differential equations for a family of Riemannian metrics $g_{ij}(t)$ on $\mathscr{M}$.

Problem 6. Two-point boundary value problems for infinite-dimensional dynamical systems in the framework of *weak solutions*. For example, we consider the following two-point boundary value problem:

$$\begin{aligned} &\mathbf{r}_{tt} - \mathbf{r}_{\theta\theta} = 0, \quad \forall (t,\theta) \in [0,T] \times \mathbb{S}^1, \\ &\mathbf{r}(0,\theta) = \mathbb{O}(\theta), \quad \forall \theta \in \mathbb{S}^1, \\ &\mathbf{r}(T,\theta) = \mathbb{T}(\theta), \quad \forall \theta \in \mathbb{S}^1, \end{aligned} \tag{13}$$

where $\mathbf{r} = (r_1(t,\theta), r_2(t,\theta))$ is the unknown vector-valued function and $\mathbb{O}(\theta)$ and $\mathbb{T}(\theta)$ stand for a circle and a square, respectively. How about the existence and uniqueness of the *weak solution*? These are interesting problems worthy to study, in particular, for nonlinear partial differential equations.

Acknowledgments

This work was supported in part by the NNSF of China (Grant no. 11271323) and by Zhejiang Provincial Natural Science Foundation of China (Grant no. LZ13A010002).

References

[1] D.-X. Kong, *Partial Differential Equations*, Higher Education Press, Beijing, China, 2010.

[2] D.-X. Kong and Q.-Y. Sun, "Two-point boundary value problems and exact controllability for several kinds of linear and nonlinear wave equations," *Journal of Physics*, vol. 290, article 012008, 26 pages, 2011.

[3] M. Gage and R. S. Hamilton, "The heat equation shrinking convex plane curves," *Journal of Differential Geometry*, vol. 23, no. 1, pp. 69–96, 1986.

[4] D.-X. Kong, K. Liu, and Z. Wang, "Hyperbolic mean curvature flow: evolution of plane curves," *Acta Mathematica Scientia*, vol. 29, no. 3, pp. 493–514, 2009.

Hindawi Publishing Corporation
Journal of Applied Mathematics
Volume 2013, Article ID 248084, 8 pages
http://dx.doi.org/10.1155/2013/248084

Research Article

Multiangle Social Network Recommendation Algorithms and Similarity Network Evaluation

Jinyu Hu,[1] Zhiwei Gao,[2] and Weisen Pan[1]

[1] *Department of Biostatistics and Computational Biology, University of Rochester, Rochester, NY 14642, USA*
[2] *Faculty of Engineering and Environment, Northumbria University, Newcastle upon Tyne, NE1 8ST, UK*

Correspondence should be addressed to Zhiwei Gao; zhiwei.gao@northumbria.ac.uk

Received 14 June 2013; Accepted 22 June 2013

Academic Editor: Dexing Kong

Copyright © 2013 Jinyu Hu et al. This is an open access article distributed under the Creative Commons Attribution License, which permits unrestricted use, distribution, and reproduction in any medium, provided the original work is properly cited.

Multiangle social network recommendation algorithms (MSN) and a new assessment method, called similarity network evaluation (SNE), are both proposed. From the viewpoint of six dimensions, the MSN are classified into six algorithms, including user-based algorithm from resource point (UBR), user-based algorithm from tag point (UBT), resource-based algorithm from tag point (RBT), resource-based algorithm from user point (RBU), tag-based algorithm from resource point (TBR), and tag-based algorithm from user point (TBU). Compared with the traditional recall/precision (RP) method, the SNE is more simple, effective, and visualized. The simulation results show that TBR and UBR are the best algorithms, RBU and TBU are the worst ones, and UBT and RBT are in the medium levels.

1. Introduction

In recent years social tagging systems have become increasingly popular as a means to classify large sets of resources on the web. These systems allow users to add metadata in the form of keywords to share resources [1]. Nevertheless, the rapidly growing data in these systems present new technical challenges involved with recommended resources. Collaborative filtering [2] approach provides a solution to overcome this challenge, which makes recommendations solely base on the preferred database. The Top-N recommendation method [3] tries to recommend the top-n ranked resources that users may be interested in.

Computation of the similarity plays a key role in the collaborative filtering, and there are many different ways to compute the similarities such as the Pearson correlation [4], constrained Pearson correlation [5], cosine-based similarity [6], adjusted cosine similarity [7], and Spearman rank correlation [8]. Currently, the user-based collaborative filtering algorithm mainly considers user similarity from the resource perspective [9]. Some papers did not discuss the resource similarity from the user perspective [10]. Mostly, the tag-based recommendation only takes into account the tag similarity based on the resource tag [11]. Some papers also comprehensively consider the user similarity and resource similarity but do not consider the tag similarity [12]. Based on the pursuit of a recommendation system, the assessment indicators are employed to evaluate an algorithm, for instance, recall/precision, mean absolute error (MAE), mean average precision (MAP), and area under curve (AUC) [13]. For recommended results, there are some auxiliary assessment indicators [14], such as coverage (COV), diversity (DIV), and average popularity (AP).

In this paper, the concepts of the 1-mode network and 2-mode network in social network [15] are addressed for collaborative filtering. For movies, this paper gives recommended explanations of the six algorithms as follows:

UBR: "Users who watched your favorite movies also watch . . ."

UBT: "Users who used your favorite tags also watch . . ."

RBU: "Users who watch this movie also watch . . ."

RBT: "Tags which annotate this movie also annotate . . ."

TBR: "Other Tags of this movie also annotate . . ."

TBU: "Other Tags which you used also annotate . . ."

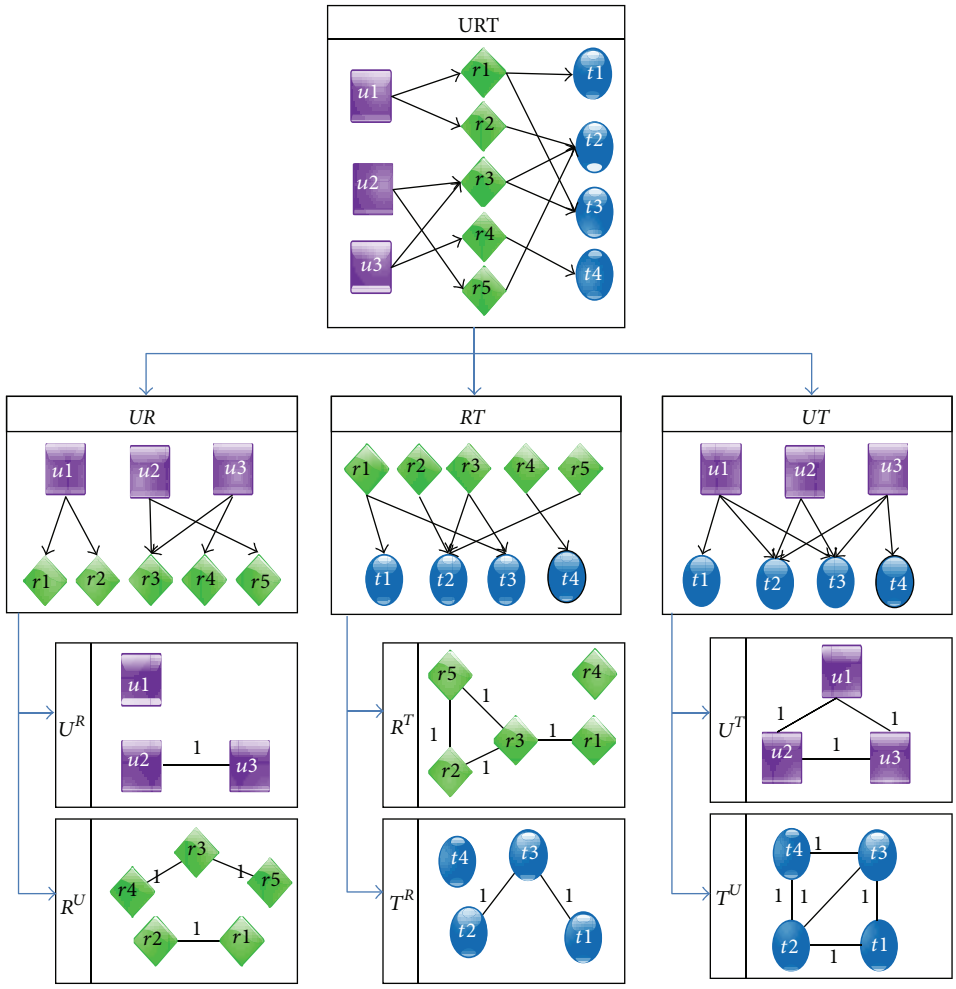

Figure 1: A process to obtain 2-mode networks and 1-mode networks.

On the basis of the similarity network evaluation (SNE), and comparison with the recall/precision, it is indicated that the results from the two assessment methods are consistent, but the SNE is more simple, visualized, and effective with less steps.

2. Multiangle Social Network Recommendation Algorithm (MSN)

2.1. Pretreatment of Social Network. The triple (U, R, T) represents the raw data, which means the user U is given the tag T on the resource R. From this triple, one can deduce three 2-mode networks such as UR, TR, and UT. Each 2-mode network can deduce two 1-mode networks. For instance, UR can infer two 1-mode networks U^R and R^U; RT infers 1-mode networks R^T and T^R; and UT infers 1-mode networks U^T and T^U (see Figure 1). In the present paper, the symbol of A' denotes the transpose of A.

The matrix U^R shows the membership of each pair of users who like the common resources, described by $U^R = UR * UR'$. The matrix R^U represents the membership of each pair of resources which have the common users, described by $R^U = UR' * UR$. The matrix R^T is the membership of each pair of resources which have the same tags, described by $R^T = RT * RT'$. The matrix T^R indicates the membership of each pair of tags which have the common resources, with $T^R = RT' * RT$. The matrix U^T means the membership of each pair of users who annotate the common tags, with $U^T = UT * UT'$. The matrix T^U shows the membership of each pair of tags which have the common users, with $T^U = UT' * UT$.

2.2. User-Based Social Network Algorithm (USN). There are two steps of the USN algorithm: firstly to find other users who are similar to the target user and then recommend the other users' favorite resources to the target user. The algorithm can be divided into the two algorithms UBR and UBT.

(1) *User-Based Algorithm from Resource Perspective (User-Based Resources, UBR).* The user similarity from resource (USR) perspective means that if two users like the same resources, they are similar. The element of the USR, denoted by usr_{ij} is defined as:

$$\mathrm{usr}_{ij} = \frac{u_{ij}}{u_{ii} + u_{jj} - u_{ij}}, \quad u_{ij} \in U^R. \tag{1}$$

Based on the above similarity, the user-resource interest matrix UBR is described by:

$$\mathrm{UBR} = UR' * \mathrm{USR}. \tag{2}$$

(2) *User-Based Algorithm from Tag Perspective (User-Based Tag, UBT)*. The user similarity from tag (UST) perspective indicates two users are similar if they prefer to use the same tags. The element of the UST, denoted by ust_{ij} is computed by

$$\mathrm{ust}_{ij} = \frac{u_{ij}}{u_{ii} + u_{jj} - u_{ij}}, \quad u_{ij} \in U^T. \tag{3}$$

Based on the similarity, the interest matrix UBT is defined as:

$$\mathrm{UBT} = UR' * \mathrm{UST}. \tag{4}$$

2.3. Resource-Based Social Network Algorithm (RSN). The RSN algorithm also has two steps: firstly to find out the resources that the target user likes and then recommend other similar ones to the user. It is divided into two algorithms: RBU and RBT.

(1) *Resource-Based Algorithm from User Perspective (Resources-Based User, RBU).* The resource similarity from user (RSU) perspective means that if two resources are enjoyed by the same user, they are similar, where rsu_{ij} is defined by

$$\mathrm{rsu}_{ij} = \frac{r_{ij}}{r_{ii} + r_{jj} - r_{ij}}, \quad r_{ij} \in R^U. \tag{5}$$

The interest matrix RBU is written as

$$\mathrm{RBU} = \mathrm{RSU} * UR'. \tag{6}$$

(2) *Resource-Based Algorithm from Tag Perspective (Resources-Based Tag, RBT).* The resource similarity from tag (RST) perspective implies that if two resources are enjoyed by the same user, they are similar. The element of the RST is defined as

$$\mathrm{rst}_{ij} = \frac{r_{ij}}{r_{ii} + r_{jj} - r_{ij}}, \quad r_{ij} \in R^T. \tag{7}$$

The interest matrix RBT is described by

$$\mathrm{RBT} = \mathrm{RST} * UR'. \tag{8}$$

2.4. Tag-Based Social Network Algorithm (TSN). The TSN algorithm consists of three parts: the first step is to look for the frequently used tags of the target user, next to find other similar tags and merge both of them into a tag set, finally to recommend these tag-set corresponding resources to the target user.

(1) *Tag-Based Algorithm from Resource Perspective (Tag-Based Resources, TBR).* The tag similarity from resource (TSR) perspective means that if two resources are enjoyed by the same user, they are similar. The element of the TSR is computed as

$$\mathrm{tsr}_{ij} = \frac{t_{ij}}{t_{ii} + t_{jj} - t_{ij}}, \quad t_{ij} \in T^R. \tag{9}$$

The tag similarity matrix TSR, which is viewed from the resources, show that if two tags annotate the same resources, they are similar. One can have

$$\mathrm{TBR} = RT * \mathrm{TSR} * UT'. \tag{10}$$

(2) *Tag-Based Algorithm from User Perspective (Tag-Based User, TBU).* The tag similarity from user perspective (TSU) implies that if two resources are enjoyed by the same user, they are similar. The element of the TSU is defined as

$$\mathrm{tsu}_{ij} = \frac{t_{ij}}{t_{ii} + t_{jj} - t_{ij}}, \quad t_{ij} \in T^U. \tag{11}$$

The interest matrix TBU can be written as:

$$\mathrm{TBU} = RT * \mathrm{TSU} * UT'. \tag{12}$$

3. Similarity Network Evaluation (SNE)

3.1. Basic Concepts

Definition 1 (similarity network (SN)). A connection matrix C is used to store similarity network (SN), whose element is c_{ij}, defined by

$$c_{ij} = \begin{cases} s_{ij}, & i > j,\ s_{ij} \geq T,\ 0 \leq T \leq 1, \\ 0, & i \leq j, \end{cases} \tag{13}$$

where s_{ij} is the similarity between the nodes i and j and $s_{ij} \in [0, 1]$. When $c_{ij} = 0$, there is no edge between nodes i and j; T is a threshold.

The definition of the similarity of the SN is actually borrowed from the definition of the gene community network (GCN) proposed by [16].

Definition 2 (types of the network). The similarity networks can be divided into six categories in terms of the intensity of similarities.

(1) Perfect correlation network (PCN): when $T = 1$, remove the edges whose weights are lower than 1, and the weights of all edges are 1.

(2) Very strong correlation network (VSN): when $T = 0.8$, delete the edges with the weights lower than 0.8.

(3) Strong correlation network (SCN): when $T = 0.6$, remove the edges with the weights lower than 0.6 to form a new network.

(4) Moderate correlation network (MCN): when $T = 0.4$, delete the edges whose weights are lower than 0.4 to form a similarity Network.

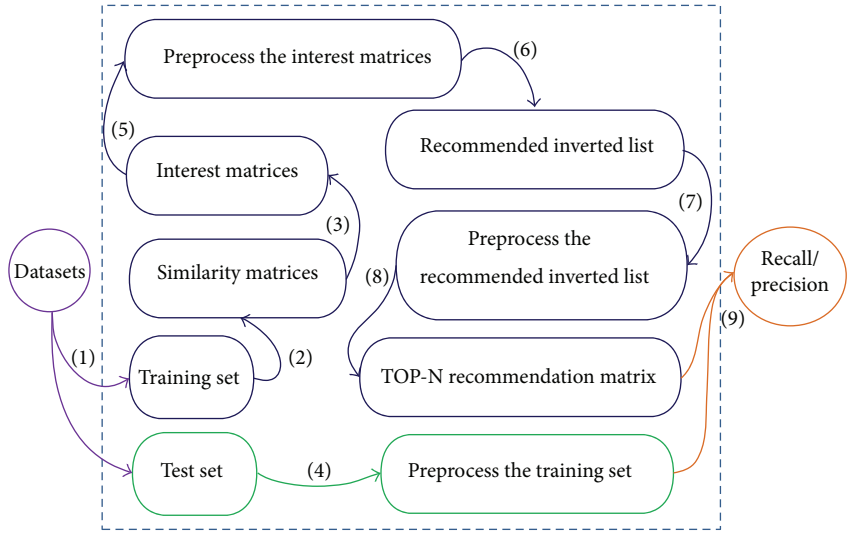

Figure 2: The computing steps of Recall/Precision.

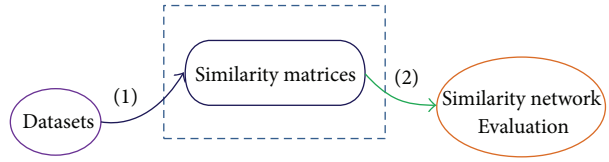

Figure 3: The computing steps of similarity networks evaluation.

(5) Weak correlation network (WCN): when $T = 0.2$, the values of all the edges are lower than 0.2 in the network.

(6) Uncorrelated network (UCN): when $T = 0$, all nodes are isolated nodes.

3.2. Algorithm Principle. The core of the collaborative filtering algorithm is to calculate the similarity. The SNE method can better evaluate the algorithm if under a certain threshold value there are fewer isolated nodes but more small communities in its similarity networks. It includes the following requirements.

(1) *A Certain Threshold Value.* Relative to the entire resource, these recommended resources are quite few. Therefore, when we evaluate an algorithm, the PCN network ($T = 1$) only needs to be considered. However, in order to have a comprehensive analysis, the VSN network ($T = 0.8$) and the SCN network ($T = 0.6$) should be considered together.

(2) *Fewer Isolated Nodes.* Recommendation algorithm is based on the similarity. The isolated node is not similar to any other nodes. In this case, the algorithm can not give a recommendation about these isolated nodes. Therefore, a good algorithm may produce a similarity network with fewer isolated nodes and more nonisolated ones.

(3) *More Communities.* Each community (nodes > 2) represents a different interest of users. The more the communities, the more detailed features can they reflect, which makes the recommended results more in line with the user's taste.

(4) *Fewer Nodes in the Largest Community.* In the largest community, there are too many nodes to reflect the user's taste in detail. The nodes in the largest community should be as few as possible.

Taking into account the previous points, and also considering these different networks with different number of nodes, the score of the similarity network evaluation (SNE) is described by

$$\mathrm{SS}(T) = \frac{\mathrm{NC} * \mathrm{NI}}{\mathrm{NA} * \mathrm{NL}}, \quad \mathrm{NA} \geq 1,\ \mathrm{NL} \geq 1, \tag{14}$$

where SS is the score function of similarity network, T is the threshold, NA is the number of all nodes in the network, NI is the number of nonisolated nodes in the network, NC is the number of communities, and NL is the number of nodes in the largest community.

3.3. Steps of SNE. The recall/precision rate of an algorithm has nine calculation steps (see Figure 2).

The SNE method only needs to calculate similarity matrices; thus one can directly evaluate the algorithms after constructing similarity networks. It is a simple method, which only has one intermediate step (see Figure 3).

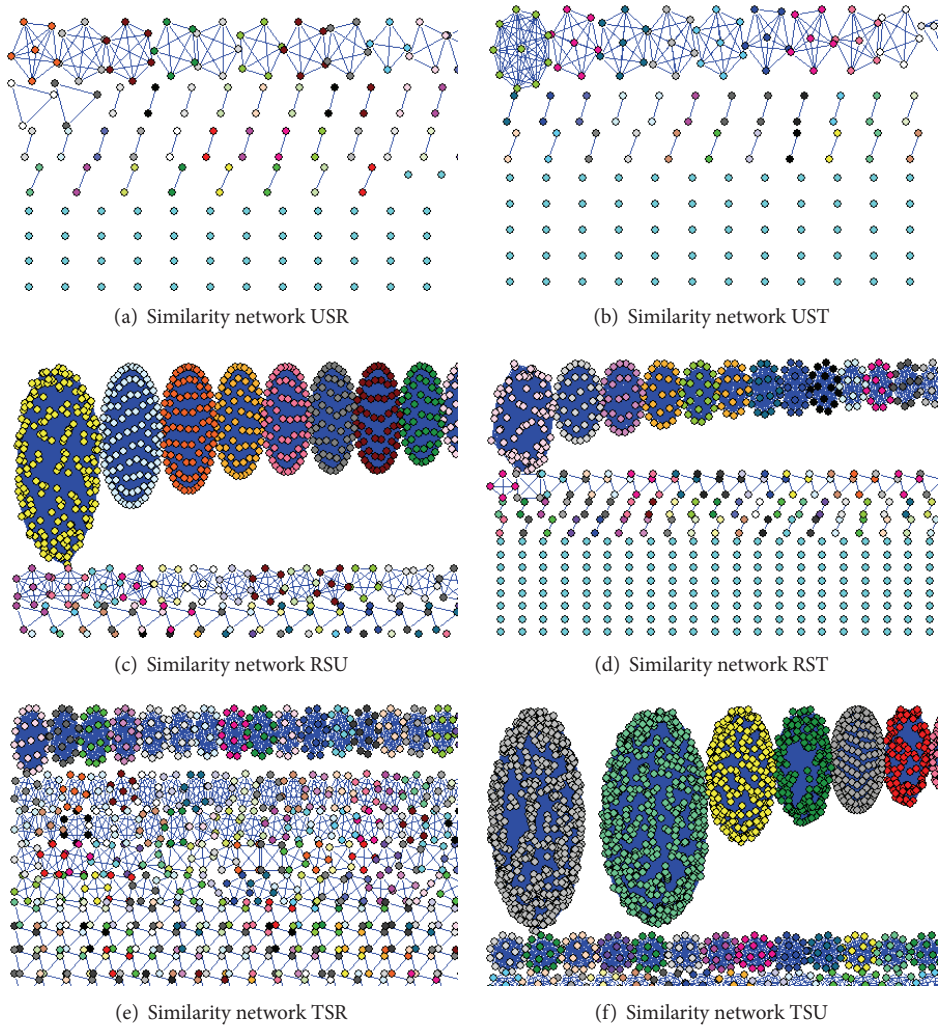

(a) Similarity network USR (b) Similarity network UST

(c) Similarity network RSU (d) Similarity network RST

(e) Similarity network TSR (f) Similarity network TSU

Figure 4: The PCN networks of six algorithms.

Table 1: The score of the PCN.

SN	NA	NC	NL	NI	SS(T)
USR	2007	137	6	343	3.9
UST	2007	115	10	319	1.83
RSU	5640	315	201	2253	0.63
RST	5640	255	74	1081	0.66
TSR	8390	1146	23	4005	23.78
TSU	8390	544	611	5656	0.6

SS: the score function of similarity network; T: the threshold of similarity network; NA: the number of all nodes in the network; NI: the number of nonisolated nodes in the network; NC: the number of communities; NL: the number of nodes in the largest community.

Table 2: The score of the VSN.

SN	NA	NC	NL	NI	SS(T)
USR	2007	137	6	343	3.9
UST	2007	115	10	319	1.83
RSU	5640	321	201	2267	0.64
RST	5640	258	74	1089	0.67
TSR	8390	1150	23	4014	23.92
TSU	8390	546	611	5660	0.6

SS: the score function of similarity network; T: the threshold of similarity network; NA: the number of all nodes in the network; NI: the number of nonisolated nodes in the network; NC: the number of communities; NL: the number of nodes in the largest community.

4. Results and Discussions

The dataset is "hetrec2011-movielens-2k" from HetRec 2011 [17], which is an extension of MovieLens 10M dataset, with 2113 users, 10197 movies, 13222 tags, and 855598 ratings. In this paper, we focus on the users, resources, and tags and ignore the ratings.

4.1. Visual Analysis of the SNE. Visual similarity network analysis can be more intuitive to roughly evaluate various kinds of recommendation algorithms. We use the Pajek [18] to show the six PCN networks. To see more clearly, we just intercept 1/16 of the original screen in the upper-left corner (see Figure 4).

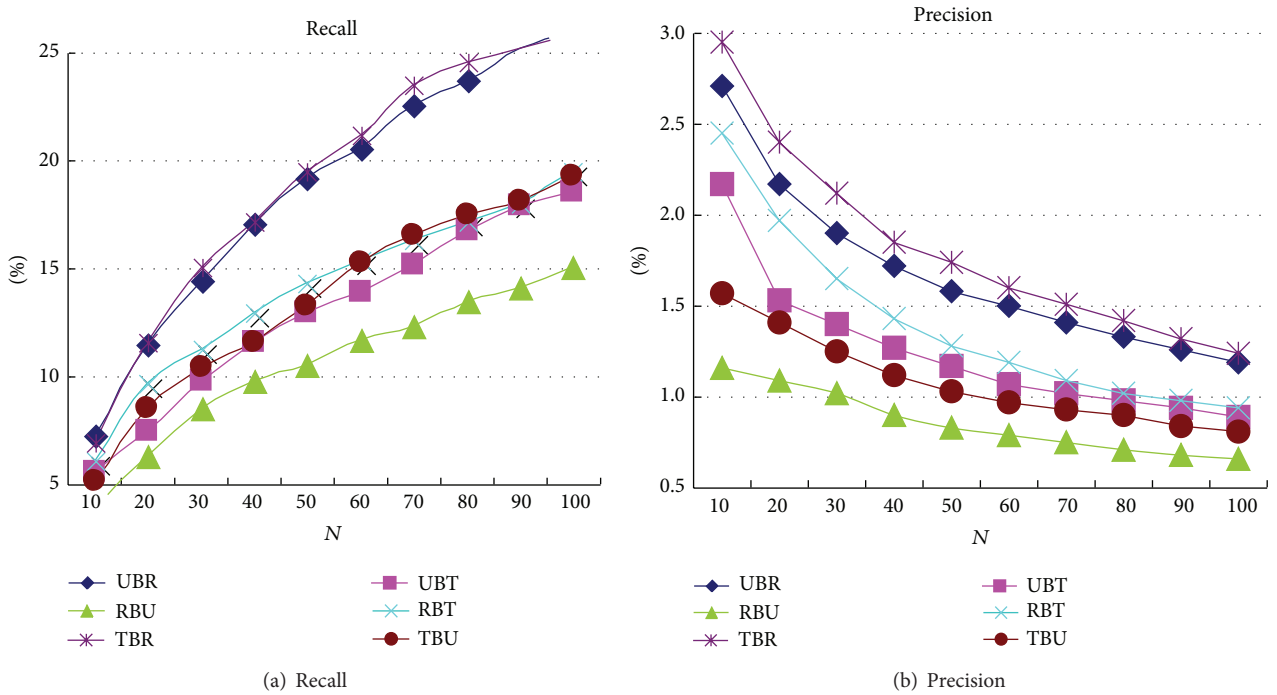

(a) Recall (b) Precision

Figure 5: Recall/precision of the six algorithms.

Table 3: The score of the SCN.

SN	NA	NC	NL	NI	SS(T)
USR	2007	137	6	343	3.9
UST	2007	119	10	328	1.94
RSU	5640	288	799	2944	0.19
RST	5640	299	74	1263	0.9
TSR	8390	851	23	5518	24.33
TSU	8390	540	611	6041	0.64

SS: the score function of similarity network; T: the threshold of similarity network; NA: the number of all nodes in the network; NI: the number of nonisolated nodes in the network; NC: the number of communities; NL: the number of nodes in the largest community.

Table 4: Recall of the six algorithms.

Top-N	UBR	UBT	RBU	RBT	TBR	TBU
10	7.27%	5.65%	3.95%	6.18%	7.05%	5.18%
20	11.49%	7.55%	6.36%	9.71%	11.67%	8.57%
30	14.44%	9.80%	8.63%	11.34%	15.14%	10.44%
40	17.08%	11.61%	9.79%	12.95%	17.23%	11.65%
50	19.24%	12.96%	10.61%	14.39%	19.52%	13.29%
60	20.55%	13.95%	11.76%	15.43%	21.25%	15.35%
70	22.57%	15.20%	12.39%	16.39%	23.48%	16.56%
80	23.70%	16.77%	13.54%	17.21%	24.54%	17.51%
90	25.17%	17.94%	14.11%	18.07%	25.17%	18.21%
100	25.98%	18.54%	15.10%	19.51%	25.85%	19.35%

In the SNE evaluation, an algorithm with more small communities is better than the one with more large communities. In Figure 4, we can see the following:

Table 5: Precision of the six algorithms.

Top-N	UBR	UBT	RBU	RBT	TBR	TBU
10	2.71%	2.17%	1.16%	2.45%	2.95%	1.57%
20	2.17%	1.53%	1.09%	1.97%	2.40%	1.41%
30	1.90%	1.40%	1.02%	1.65%	2.12%	1.25%
40	1.72%	1.27%	0.90%	1.43%	1.85%	1.12%
50	1.58%	1.17%	0.83%	1.28%	1.74%	1.03%
60	1.50%	1.07%	0.79%	1.19%	1.60%	0.97%
70	1.41%	1.02%	0.75%	1.09%	1.51%	0.93%
80	1.33%	0.98%	0.71%	1.02%	1.42%	0.90%
90	1.26%	0.94%	0.68%	0.98%	1.32%	0.84%
100	1.19%	0.89%	0.66%	0.94%	1.24%	0.81%

(1) The UST's big communities are more obvious than the USR's; therefore, UBR is better than UBT, denoted by UBR > UBT.

(2) The RSU has more big communities than the RST; thus RBT > RBU, indicating RBT is better than RBU.

(3) There are very big communities in TSU. Conversely, TSR has fewer ones. Therefore, TBR > TBU, meaning TBR is better than TBU.

(4) Obviously, the TSU and RSU have the largest communities; thus the algorithms TBU and RBU are relatively poor.

(5) In the same way, the better algorithms are UBR and TBR, and the medium ones are UBT and RBT.

4.2. Quantitative Analysis of SNE. Based on score function of SNE, the scores of different algorithms under the threshold

Table 6: Comparison analysis of RP and SNE.

	Recall/precision (RP)	Similarity network evaluation (SNE)
Results of evaluation	Recall: UBR > TBR > RBT > UBT > TBU > RBU Precision: TBR > UBR > RBT > UBT > TBU > RBU Conclude from above: TBR > UBR > RBT > UBT > TBU > RBU	$T = 1$: TBR > UBR > UBT > RBT > RBU > TBU $T = 0.8$: TBR > UBR > UBT > RBT > RBU > TBU $T = 0.6$: TBR > UBR > UBT > RBT > TBU > RBU Conclude from above: TBR > UBR > UBT > RBT > TBU > RBU
Complexity	9 middle steps, high complexity	1 middle step, very simple
Visualization	No	Yes

values of 1, 0.8, and 0.6 are, respectively, displayed in Tables 1–3.

According to the similarity scores shown by Tables 1 and 2, one can give the order of the algorithms from best to worst as follows: TBR > UBR > UBT > RBT > RBU > TBU. And from Table 3, in order of the best algorithm, it goes as follows: TBR > UBR > UBT > RBT > TBU > RBU. Overall, RBU and TBU are the worst algorithms.

4.3. Comparison with Recall/Precision. The recall/precision rates can evaluate the accuracy of algorithms. Based on the training set, we recommend the top-N resources to users by using the six algorithms. Corresponding to the test set, one can obtain the Recall/Precision rates under different N values, respectively (see Tables 4 and 5).

The Recall and Precision rates of different algorithms and different N values are shown in Figure 5.

The comparative analysis of two evaluation indicators is given in Table 6.

From the comparison, one can see that the results of two evaluation algorithms are very agreeable, where the same results are UBR > UBT, RBT > RBU, and TBR > TBU. The similarity network visualization method can roughly evaluate algorithms. From the perspective of the complexity and visualization, the similarity network assessment algorithm is in an advantageous position.

5. Conclusion and Future Work

In the paper, not only the collaborative filtering algorithms are proposed based on social network, but also a new assessment method of similarity network evaluation is addressed. For these six algorithms, TBR and UBR are the best algorithms, RBU and TBU are the worst ones, and UBT and RBT are in the medium levels. From the recommended effects, we can conclude that UBR > UBT, RBT > RBU, and TBR > TBU. It is noted that, in the actual use of algorithms, the accuracy of the algorithm is not the unique factor to be considered; the complexity of the algorithm and the maintenance cost of the algorithm have to be taken into account as well.

Future work is encouraged for the three aspects: (1) recommended algorithm based on the current similarity calculation method is of interest; (2) hybrid algorithms based on two recommendation algorithms are of significance; (3) the SNE assessment would be extended to evaluate other algorithms rather than the collaborative recommended algorithms.

References

[1] A. K. Milicevic, A. Nanopoulos, and M. Ivanovic, "Social tagging in recommender systems: a survey of the state-of-the-art and possible extensions," *Artificial Intelligence Review*, vol. 33, no. 3, pp. 187–209, 2010.

[2] A. K. Menon, K. Chitrapura, S. Garg, D. Agarwal, and N. Kota, "Response prediction using collaborative filtering with hierarchies and side-information," in *Proceedings of the 17th ACM SIGKDD International Conference on Knowledge Discovery and Data Mining (KDD '11)*, pp. 141–149, San Diego, Calif, USA, August 2011.

[3] X. Ning and G. Karypis, "SLIM: sparse linear methods for top-n recommender systems," in *Proceedings of the 11th IEEE International Conference on Data Mining (ICDM '11)*, pp. 497–506, Vancouver, Canada, December 2011.

[4] J. Bobadilla, F. Serradilla, and A. Hernando, "Collaborative filtering adapted to recommender systems of e-learning," *Knowledge-Based Systems*, vol. 22, no. 4, pp. 261–265, 2009.

[5] G. Chen, F. Wang, and C. Zhang, "Collaborative filtering using orthogonal nonnegative matrix tri-factorization," *Information Processing and Management*, vol. 45, no. 3, pp. 368–379, 2009.

[6] L. Candillier, F. Meyer, and M. Boullé, "Comparing state-of-the-art collaborative filtering systems," in *Proceedings of the International Conference on Machine Learning and Data Mining*, pp. 548–562, Leipzig, Germany, July 2007.

[7] K. Choi and Y. Suh, "A new similarity function for selecting neighbors for each target item in collaborative filtering," *Knowledge-Based Systems*, vol. 37, no. 1, pp. 146–153, 2013.

[8] D. Helic, "Managing collaborative learning processes in e-learning applications," in *Proceedings of the 29th IEEE International Conference on Information Technology Interfaces*, pp. 345–350, Dubrovnik, Croatia, June 2007.

[9] C. Cechinela, M. Siciliab, and S. Sánchez-Alonsob, "Evaluating collaborative filtering recommendations inside large learning object repositories," *Information Processing and Management*, vol. 49, no. 1, pp. 34–50, 2013.

[10] A. Rajput, M. Dubey, S. Thakur, and M. Gondgly, "Improved item based collaboration filtering using recommendation system," *Binary Journal of Data Mining and Networking*, vol. 1, no. 1, pp. 6–13, 2011.

[11] R. Jäschke, A. Hotho, F. Mitzlaff, and G. Stumme, "Challenges in tag recommendations for collaborative tagging systems: recommender systems for the social web," *Intelligent Systems Reference Library*, vol. 32, pp. 65–87, 2012.

[12] D. Zhang and C. Xu, "A collaborative filtering recommendation system by unifying user similarity and item similarity," in *Web-Age Information Management*, vol. 7142 of *Lecture Notes in Computer Science*, pp. 175–184, Springer, Berlin, Germany, 2012.

[13] Y. Shi, M. Larson, and A. Hanjalic, "Mining contextual movie similarity with matrix factorization for context-aware recommendation," *ACM Transactions on Intelligent Systems and Technology*, vol. 4, no. 1, article 16, 2013.

[14] L. Lü, M. Medob, C. Yeungb, Y. Zhang, Z. Zhang, and T. Zhou, "Recommender systems," *Physics Report*, vol. 519, no. 1, pp. 1–49, 2012.

[15] A. Mislove, B. Viswanath, K. P. Gummadi, and P. Druschel, "You are who you know: inferring user profiles in online social networks," in *Proceedings of the ACM 3rd International Conference on Web Search and Data Mining (WSDM '10)*, pp. 251–260, New York, NY, USA, February 2010.

[16] J. Hu and Z. Gao, "Modules identification in gene positive networks of hepatocellular carcinoma using Pearson agglomerative method and Pearson cohesion coupling modularity," *Journal of Applied Mathematics*, vol. 2012, Article ID 248658, 21 pages, 2012.

[17] I. Cantador, P. Brusilovsky, and T. Kuflik, "Second Workshop on Information Heterogeneity and Fusion in Recommender Systems," in *Proceedings of the 5th ACM conference on Recommender Systems (RecSys '11)*, pp. 387–388, Chicago, Ill, USA, October 2011.

[18] W. Nooy, A. Mrva, and V. Batagelj, *Exploratory Social Network Analysis with Pajek*, Cambridge University Press, Cambridge, UK, 2005.

Hindawi Publishing Corporation
Journal of Applied Mathematics
Volume 2013, Article ID 347248, 6 pages
http://dx.doi.org/10.1155/2013/347248

Research Article

Optimal Combination of EEFs for the Model Reduction of Nonlinear Partial Differential Equations

Jun Shuai and Xuli Han

School of Mathematics and Statistics, Central South University, Changsha 410083, China

Correspondence should be addressed to Jun Shuai; csu_math01@163.com

Received 16 April 2013; Accepted 22 June 2013

Academic Editor: Dexing Kong

Copyright © 2013 J. Shuai and X. Han. This is an open access article distributed under the Creative Commons Attribution License, which permits unrestricted use, distribution, and reproduction in any medium, provided the original work is properly cited.

Proper orthogonal decomposition is a popular approach for determining the principal spatial structures from the measured data. Generally, model reduction using empirical eigenfunctions (EEFs) can generate a relatively low-dimensional model among all linear expansions. However, the neglectful modes representing only a tiny amount of energy will be crucial in the modeling for certain type of nonlinear partial differential equations (PDEs). In this paper, an optimal combination of EEFs is proposed for model reduction of nonlinear partial differential equations (PDEs), obtained by the basis function transformation from the initial EEFs. The transformation matrix is derived from straightforward optimization techniques. The present new EEFs can keep the dynamical information of neglectful modes and generate a lower-dimensional and more precise dynamical system for the PDEs. The numerical example shows its effectiveness and feasibility for model reduction of the nonlinear PDEs.

1. Introduction

Many problems in science and engineering are reduced to a set of nonlinear partial differential equations (PDEs) [1] through a process of mathematical modeling. In this paper, we focus on the modeling of the dynamics for the following kind of nonlinear PDEs:

$$\frac{\partial u(x,t)}{\partial t} = Qu(x,t) + F\left(u(x,t), \frac{\partial u(x,t)}{\partial x}, \ldots, x, t\right). \tag{1}$$

Equation (1) will satisfy many types of the boundary conditions. It can use the following description to denote boundary conditions containing the Dirichlet boundary condition and Neumann boundary condition of the nonlinear PDEs (1):

$$\begin{aligned} B_1 u(\alpha,t) + C_1 \frac{\partial u(\alpha,t)}{\partial x} &= D_1, \\ B_2 u(\beta,t) + C_2 \frac{\partial u(\beta,t)}{\partial x} &= D_2. \end{aligned} \tag{2}$$

The initial conditions are also given:

$$u(x,0) = u_0(x), \tag{3}$$

where $u(x,t)$ denotes the spatiotemporal state variable, $x \in \Omega = [\alpha, \beta] \subset R$ is the spatial coordinate, and $t \in [0, \infty)$ is the time variable. Q is a linear operator involving linear spatial derivatives on the state variable. $F(u(x,t), \partial u(x,t)/\partial x, \ldots, x, t)$ is a nonlinear function which contains spatial derivatives of the state variable. B_1, C_1, D_1, B_2, C_2, and D_2 are constants and $u_0(x)$ is a function of x.

Generally, two kinds of methods are mainly used to model the dynamics of nonlinear PDEs: conventional discretization approaches and advanced methods based on spatial basis function expansions [2–4]. However, conventional discretization approaches such as finite difference method (FDM) [5] and finite element method (FEM) [6] often lead to high-order dynamical models of nonlinear PDEs. The advanced methods based on spatial basis function expansions such as spectral methods [2, 3] can derive a low-order ODE system to model the dynamics of nonlinear PDEs.

Empirical eigenfunctions (EEFs) [7, 8] which are identified by proper orthogonal decomposition are one of the spatial basis functions used for the time/space separation.

With the help of the traditional identification technique [9], EEFs are widely used for PDE model identification. It is well known that the amount of energy of a system represented by the EEFs is often taken as an indication of the quality of a reduced model using those first several EEFs. However, the linear approximation for the nonlinear system cannot guarantee the assumption that minor components do not contain important information [10]. Modes representing only a tiny amount of energy can also be crucial in the generation of certain types of dynamics. For instance, the EEF-based models can have difficulties in reproducing behavior dominated by irregular transitions between different dynamical states, which have been pointed out in the past studies [11–13]. For the more precise approximation of the PDEs, it is necessary to keep the influence of the neglectful modes representing only a tiny amount of energy on retained dominated modes. Adding the dynamical information by the combination of the initial EEFs will give both qualitatively and quantitatively better results than the common EEFs-based models [8].

In this paper, an optimal combination of EEFs is proposed for model reduction of nonlinear partial differential equations (PDEs), which is obtained by the basis function transformation from the initial EEFs. High-order EEFs are initially obtained by the proper orthogonal decomposition of the measured data. Thus, a new set of basis functions is constructed by the basis function transformation of the initial EEFs. The transformation matrix is derived from straightforward optimization techniques. The present new EEFs can keep the dynamical information of neglectful modes and generate a lower dimensional and more precise dynamical system for the PDEs. The numerical example shows its effectiveness and feasibility for model reduction of the nonlinear PDEs.

2. EEFs for Model Reduction

The proper orthogonal decomposition (POD) [14], also known as the Karhunen-Loeve (K-L) decomposition, principal component analysis (PCA), and empirical orthogonal function analysis (EOF) can facilitate the modal projections of partial differential equations into reduced-order models, via a Galerkin projection [15]. The POD is a mean of extracting spatial structure from a set of time series available on a domain. The most attracting property of the POD is that it can minimize the average squared distance between the original measured signal and its reduced representation. POD allows the identification of a useful set of empirical eigenfunctions and the dimension of the subspace necessary to achieve a satisfactory approximation of nonlinear PDEs.

For simplicity, assume the measured spatial-temporal variable $\{u(x_i,t_j)\}_{i=1,t=1}^{n,K}$ (called snapshots) is uniformly sampled in the space and time coordinates. Define the inner product, norm, and ensemble average as $(f(x),g(x))=\int_\Omega f(x)g(x)dx$, $\|f(x)\|=(f(x),f(x))^{1/2}$, and $\langle f(x,t)\rangle = 1/K\sum_{t=1}^{K} f(x,t)$. Motivated by the Fourier series, the spatiotemporal variable $u(x,t)$ can be expanded onto an infinite number of orthonormal spatial basis functions $\phi_i(x)$ with temporal coefficients $u_i(t)$:

$$u(x,t)=\sum_{i=1}^{\infty} u_i(t)\,\phi_i(x). \tag{4}$$

The spatial basis functions are orthonormal; the following are derived:

$$\left(\phi_i(x),\phi_j(x)\right)=\int_\Omega \phi_i(x)\,\phi_j(x)\,dx=\begin{cases}0, & i\neq j,\\ 1, & i=j.\end{cases} \tag{5}$$

The temporal coefficients can be calculated from

$$u_i(t)=\left(\phi_i(x),u(x,t)\right),\quad i=1,\ldots,\infty. \tag{6}$$

If a large enough M is given (i.e., $M\to\infty$), $u(x,t)$ can be approximated by the following M-order approximation, which is truncated to be a finite dimension:

$$u(x,t)\approx u_M(x,t)=\sum_{i=1}^{M} u_i(t)\,\phi_i(x), \tag{7}$$

where $u_M(x,t)$ denotes the M-order approximation.

The main problem of using proper orthogonal decomposition for time/space separation is to obtain the most characteristic spatial structure $\{\phi_i(x)\}_{i=1}^{N}$ from the spatiotemporal snapshots $\{u(x_i,t_j)\}_{i=1,t=1}^{n,K}$. Finding the typical $\{\phi_i(x)\}_{i=1}^{N}$ can be performed by using the following eigenvalue problems:

$$\int_\Omega R(x,\mu)\,\phi_i(\mu)\,d\mu=\lambda_i\phi_i(x),\quad (\phi_i,\phi_i)=1, \tag{8}$$

where $R(x,\mu)=\langle u(x,t)u(\mu,t)\rangle$ denotes the spatial two-point correlation function.

Since the data are always discrete in space, one must solve numerically the integral equation (8). Discretizing the integral equation gives an $n\times n$ matrix eigenvalue problem. Thus, at most eigenfunctions at n sampled spatial locations can be obtained. Then one can interpolate the eigenfunctions to locations where the data are not available.

Assume that the maximum number of nonzero eigenvalues is $M\le n$. Let $\lambda_1>\lambda_2>\cdots>\lambda_M$ be the eigenvalues with the corresponding eigenfunctions $\{\phi_1(x),\phi_2(x),\ldots,\phi_M(x)\}$. The eigenfunction that corresponds to the first eigenvalue is considered to be the most "energetic." The total "energy" is defined as being the sum of the eigenvalues. To each eigenfunction, assign an "energy" percentage based on the associated eigenvalue:

$$E_i=\frac{\lambda_i}{\sum_{j=1}^{M}\lambda_j}. \tag{9}$$

Usually, the sufficient number of eigenfunctions that capture 99% of the system "energy" is used to determine the value of N. Experiences show that only the first few basis functions can represent the dominant dynamics of many PDE systems.

As to the model reduction for PDE (1), the spatiotemporal variables $u(x,t)$ can be approximated by expanding onto the first N spatial-dependent EEFs $\{\phi_1(x), \phi_2(x), \ldots, \phi_N(x)\}$ with the corresponding temporal coefficients $u_i(t)$:

$$u(x,t) \approx u_N(x,t) = \sum_{i=1}^{N} u_i(t)\,\phi_i(x). \tag{10}$$

For PDE (1), the following can be derived:

$$\begin{aligned}&\sum_{i=1}^{N} \dot{u}_i(t)\,\phi_i(x)\\ &\quad = Q\left(\sum_{i=1}^{N} u_i(t)\,\phi_i(x)\right)\\ &\qquad + F\left(\sum_{i=1}^{N} u_i(t)\,\phi_i(x), \sum_{i=1}^{N} u_i(t)\,\frac{\partial \phi_i(x)}{\partial x}, \ldots, x, t\right).\end{aligned} \tag{11}$$

Via a Galerkin projection, the following N-order dynamical systems are then obtained:

$$\dot{u}_i(t) = \lambda_i u_i(t) + f_i(u(t), t), \tag{12}$$

where λ_i, $i = 1, 2 \ldots, N$ denote the eigenvalues, $f_i(u(t), t)$ denote the nonlinear terms, and $u(t) = [u_1(t)\, u_2(t), \ldots, u_N(t)]^T$. The series of dynamical systems can be rewritten in a general form as follows:

$$\dot{u}(t) = Lu(t) + f(u(t), t), \tag{13}$$

where $L = \mathrm{diag}(\lambda_1, \lambda_2, \ldots, \lambda_N)$; $f(u(t), t) = [f_1(u(t), t), f_2(u(t), t), \ldots, f_N(u(t), t)]^T$ and $f_i(u(t), t) = (\phi_i(x), F(\sum_{i=1}^{N} u_i(t)\phi_i(x), \sum_{i=1}^{N} u_i(t)(\partial\phi_i(x)/\partial x), \ldots, x, t))$.

3. Line Combination of EEFs

Considering the influence of neglectful EEFs with the tiny amount energy, a new kind of EEFs can be derived by line combinations of the initial EEFs. As to obtain the lower-order dynamical systems of nonlinear PDEs, a smaller set of new basis functions can be derived. Each new basis function is the line combination of the M EEFs from POD:

$$\begin{aligned}\varphi_j(x) = a_{1j}\phi_1(x) + a_{2j}\phi_2(x) + \cdots + a_{Mj}\phi_M(x),\\ j = 1, 2, \ldots, N,\end{aligned} \tag{14}$$

where $N < M$. Equation (14) can also be rewritten as follows:

$$[\varphi_1(x), \varphi_2(x), \ldots, \varphi_N(x)] = [\phi_1(x), \phi_2(x), \ldots, \phi_M(x)]\, A, \tag{15}$$

where the transformation matrix $A = \begin{bmatrix} a_{11} & a_{12} & \cdots & a_{1N} \\ a_{21} & a_{22} & \cdots & a_{2N} \\ \vdots & \vdots & \ddots & \vdots \\ a_{M1} & a_{M2} & \cdots & a_{MN} \end{bmatrix}$.

Using spatial basis functions expansion based on the set of new basis functions (14), the approximation of spatiotemporal variables $u(x,t)$ can be expanded as follows:

$$u(x,t) \approx \sum_{i=1}^{N} \overline{u}_i(t)\,\varphi_i(x). \tag{16}$$

Combining (7), (15), and (16), the time coefficients have

$$\overline{u}(t) = A^{+} u(t), \tag{17}$$

where $u(t) = [u_1(t), u_2(t), \ldots, u_M(t)]^T$; $\overline{u}(t) = [\overline{u}_1(t), \overline{u}_2(t), \ldots, \overline{u}_N(t)]^T$, where A^+ denotes the generalized inverse of transformation matrix A.

For PDE (1), the following is derived:

$$\begin{aligned}&\sum_{i=1}^{N} \dot{\overline{u}}_i(t)\,\varphi_i(x)\\ &\quad = Q\left(\sum_{i=1}^{N} \overline{u}_i(t)\,\varphi_i(x)\right)\\ &\qquad + F\left(\sum_{i=1}^{N} \overline{u}_i(t)\,\varphi_i(x), \sum_{i=1}^{N} \overline{u}_i(t)\,\frac{\partial \varphi_i(x)}{\partial x}, \ldots, x, t\right).\end{aligned} \tag{18}$$

Using the Galerkin method, a lower-dimensional dynamical system of nonlinear PDE (1) in a general form can be derived as follows:

$$\dot{\overline{u}}(t) = \overline{L}\,\overline{u}(t) + \overline{f}(\overline{u}(t), t), \tag{19}$$

where $\overline{u}(t) = [\overline{u}_1(t), \overline{u}_2(t), \ldots, \overline{u}_N(t)]^T$;

$$\overline{L} = \left\{\overline{L}_{ij}\right\}, \quad i, j = 1, 2, \ldots, N;\ \overline{L}_{ij} = \left(\varphi_i, L\left(\varphi_j\right)\right);$$

$$\overline{f}(\overline{u}(t), t) = \left[\overline{f}_1(\overline{u}(t), t), \overline{f}_2(\overline{u}(t), t), \ldots, \overline{f}_N(\overline{u}(t), t)\right]^T;$$

$$\begin{aligned}\overline{f}_i(\overline{u}(t), t) = \Bigg(\varphi_i(x),\ F\Bigg(\sum_{i=1}^{N} \overline{u}_i(t)\,\varphi_i(x),\\ \sum_{i=1}^{N} \overline{u}_i(t)\,\frac{\partial \varphi_i(x)}{\partial x}, \ldots, x, t\Bigg)\Bigg).\end{aligned} \tag{20}$$

4. Optimization for the Transformation Matrix

An error function that measures energy error between the ODE system (13) and the lower-dimensional dynamical system (19) is introduced by

$$\text{Error} = \int_0^{\infty} \left(\sum_{i=1}^{M} (u_i(t))^2 - \sum_{i=1}^{N} (\overline{u}_i(t))^2\right)^2 dt. \tag{21}$$

Combining the vector expressions of $u(t)$, $\overline{u}(t)$ with (17), the error (21) can be strictly derived as follows:

$$\begin{aligned}\text{Error} &= \int_0^{\infty} \left(\sum_{i=1}^{M} (u_i(t))^2 - \sum_{i=1}^{N} (\overline{u}_i(t))^2\right)^2 dt\\ &= \int_0^{\infty} \left(u(t)^T u(t) - \overline{u}(t)^T \overline{u}(t)\right)^2 dt\\ &= \int_0^{\infty} \left(u(t)^T u(t) - u(t)^T \left(\left(A^+\right)^T A^+\right) u(t)\right)^2 dt\\ &= \int_0^{\infty} \left(u(t)^T \left(I - \left(A^+\right)^T A^+\right) u(t)\right)^2 dt.\end{aligned} \tag{22}$$

The combination matrix A is determined by minimizing the error function (22). To evaluate the error function, a temporal interval $[0, T_{\max}]$ is considered for (22) and approximated by a finite sum, where the max integral time $T_{\max}$ is selected as free parameter. The temporal integral interval $[0, T_{\max}]$ generally contains the processes from initial state to steady state of the nonlinear PDEs. The restricted condition for the minimizing problem (22) is that the combination matrix should be column orthogonal. Thus, the error functions for combination matrix can be approximated as follows.

Since

$$\begin{aligned}\text{Error}(A) &\approx \int_0^{T_{\max}} \left(u(t)^T \left(I - \left(A^+\right)^T A^+\right) u(t)\right)^2 dt \\ &\approx \left(\sum_i (t_i - t_{i-1}) \left(u(t_i)^T \left(I - \left(A^+\right)^T A^+\right) u(t_i)\right)\right)^2,\end{aligned} \tag{23}$$

we consider approximate error

$$\begin{aligned}&E(A) \\ &= \left(\sum_i (t_i - t_{i-1}) \left(u(t_i)^T \left(I - \left(A^+\right)^T A^+\right) u(t_i)\right)\right)^2, \\ &\text{subject to } A(:,i)^T A(:,j) = k_i \delta_{ij}.\end{aligned} \tag{24}$$

The optimization of $E(A)$ (24) mainly contains several steps. Firstly, the fourth-order Runge-Kutta method is used to calculate the ODE system (13); thus t_i, $u(t_i)$ of Error (24) are known.

Secondly, the particle swarm optimization (PSO) algorithm [16] is used to optimize the restricted error functions (24). PSO is an efficient, robust, and simple optimization algorithm for solving many optimization problems. In nature, PSO is a stochastic optimization approach which maintains a swarm of candidate solutions, referred to as particles. The method is inspired by the movement of particles and their interactions with their neighbors in the group. The principle and details of PSO algorithm are given in [17].

For the optimization of (24) by PSO directly, the obtained combination matrix $\widetilde{A}$ is not orthogonal. To keep the minimization of the error function (24), a satisfied combination matrix A can be derived by singular value decomposition for $\widetilde{A}$. Let the singular value decomposition of $\widetilde{A}$ be $\widetilde{A} = USV^T$, where U, S are orthogonal and diagonal matrices, respectively. Thus combination matrix $A = US$ is orthogonal and it can be derived that $(\widetilde{A}^+)^T \widetilde{A}^+ = US(S^TS)^{-1}(S^TS)^{-1}S^TU^T = (A^+)^T A^+$, which means that the minimum of the error function (24) is retained.

5. Numerical Example

In this section, the optimal combination of EEFs is applied for model reduction of a simple PDE model. Note that this example serves as an illustration of the proposed methodology rather than a demonstration of the reduction of a very large and complex system.

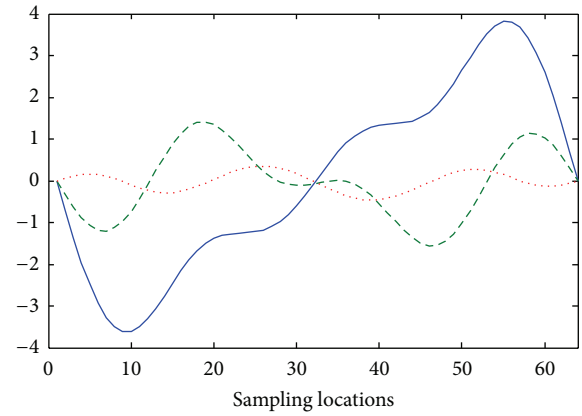

Figure 1: The first 3 initial EEFs.

In order to evaluate the performance of optimal combination of EEFs for model reduction of nonlinear PDEs, the Burgers equation [18, 19] is studied. The Burgers equation is a one-dimensional spatial model of a variety of three-dimensional physical phenomena, greatly simplifying the problems while retaining many of the complex behavior characteristics. This equation contains nonlinear convection and diffusion terms and retains many of the interesting features of the Navier-Stokes equation. The governing equation may be written as follows:

$$\frac{\partial u(x,t)}{\partial t} + u\frac{\partial u(x,t)}{\partial x} = \varepsilon \frac{\partial^2 u(x,t)}{\partial x^2}, \tag{25}$$

where the viscosity ε is 0.2 and (25) subjects to the following boundary conditions:

$$u(0,t) = u(2\pi,t) = 0, \tag{26}$$

and an initial condition:

$$u(x,0) = \sin(x) + \sin(2x) + \sin(3x). \tag{27}$$

Thirty-two sensors uniformly distributed in the space are used for measurement. A noise-free dataset of 300 data is collected from (25). The sampling interval Δt is 0.01 s and the simulation time is 3 s.

5.1. Comparisons with the EEFs. The EEFs are obtained from the singular value decomposition for the sampling data. The energy values of the dynamical systems based on the EEFs are shown in Table 1.

Using spatial basis functions expansion based on the new basis functions and the Galerkin methods, low-dimensional dynamical systems can be derived. Meanwhile, the energy functions of the obtained dynamical systems are calculated. The results in Table 2 show that the low-dimensional dynamical system based on the first several optimal combinations of EEFs can capture the dynamics of the nonlinear PDE (25) perfectly.

Table 1: Energy value of the dynamical systems based on EEFs.

EEFs	1 order	2 order	3 order	4 order	5 order	6 order	7 order	8 order
Energy value	0.0026	0.0074	0.0220	0.0340	0.1176	0.1245	0.1279	0.1281

Table 2: Energy value of the dynamical systems based on new basis functions.

New basis functions	1 order	2 order	3 order
Energy value	0.1277	0.1280	0.1281

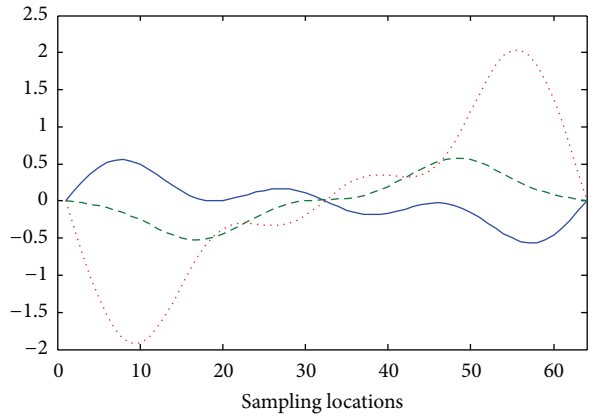

Figure 2: The first 3 optimal combined EEFs.

5.2. Low-Dimensional Approximation Based on 3 Optimal Combined EEFs. Using the line combinations of the EEFs and optimization for the energy error functions of the line combination coefficients, the optimal combination of EEFs for model reduction of nonlinear PDEs is obtained, where the first 3 initial EEFs and 3 optimal combined EEFs are shown in Figures 1 and 2.

A new set of data is collected for testing to demonstrate the spatial-temporal performance of the two kinds of EEFs. For practical industrial control, the low-dimensional model based on optimal combined EEFs is very useful because it cannot only capture the dominant dynamics of the nonlinear PDEs but simplify the control design as well. The spatiotemporal errors of the predicted output of two models combined with two kinds of EEFs are shown in Figures 3 and 4, respectively. As given in Figures 3 and 4, the predicted distributed error of the approximate model based on the optimal combination of EEFs is shown to be significantly smaller than that of the same order approximate model based on initial EEFs.

6. Conclusions

In this note, an optimal combination of EEFs is proposed for model reduction of nonlinear partial differential equations (PDEs), which is obtained by the basis function transformation from the initial EEFs. The transformation matrix is determined by the optimization for the energy error functions of the dynamical systems; the present new EEFs can keep the dynamical information of neglectful modes and generate a lower-dimensional and more precise dynamical system for the PDEs. The numerical example shows its effectiveness and feasibility for model reduction of the nonlinear PDEs.

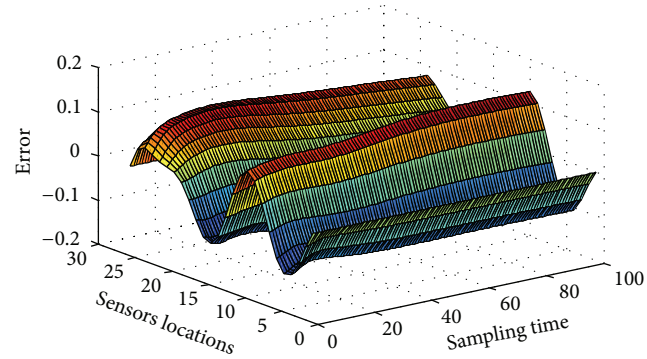

Figure 3: Predicted error based on 3 initial EEFs.

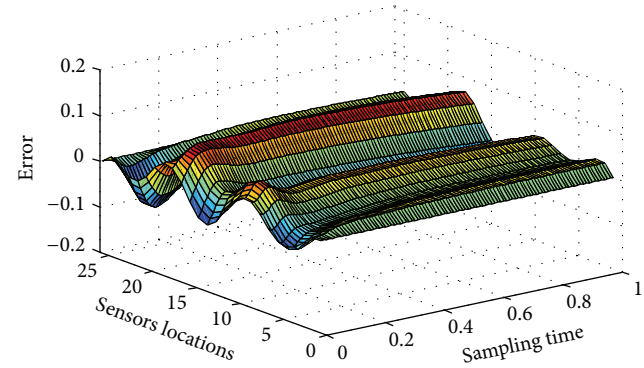

Figure 4: Predicted error based on 3 optimal combined EEFs.

Acknowledgment

Financial support from National Natural Science Foundation of China (11271376) is gratefully acknowledged.

References

[1] P. D. Christofides, *Nonlinear and Robust Control of PDE Systems: Methods and Applications to Transport-Reaction Processes*, Birkhäuser, 2001.

[2] J. P. Boyd, *Chebyshev and Fourier Spectral Methods*, Dover Publications, 2001.

[3] C. Canuto, *Spectral Methods in Fluid Dynamics*, Springer, New York, NY, USA, 1988.

[4] M. Jiang and H. Deng, "Optimal combination of spatial basis functions for the model reduction of nonlinear distributed

parameter systems," *Communications in Nonlinear Science and Numerical Simulation*, vol. 17, no. 12, pp. 5240–5248, 2012.

[5] A. R. Mitchell and D. F. Griffiths, *The Finite Difference Method in Partial Differential Equations*, John Wiley & Sons, Chichester, UK, 1980.

[6] S. C. Brenner and L. R. Scott, *The Mathematical Theory of Finite Element Methods*, Springer, New York, NY, USA, 1994.

[7] L. G. Bleris and M. V. Kothare, "Low-order empirical modeling of distributed parameter systems using temporal and spatial eigenfunctions," *Computers and Chemical Engineering*, vol. 29, no. 4, pp. 817–827, 2005.

[8] M. Jiang and H. Deng, "Improved empirical eigenfunctions based model reduction for nonlinear distributed parameter systems," *Industrial & Engineering Chemistry Research*, vol. 52, no. 2, pp. 934–940, 2013.

[9] E. Aggelogiannaki and H. Sarimveis, "Nonlinear model predictive control for distributed parameter systems using data driven artificial neural network models," *Computers and Chemical Engineering*, vol. 32, no. 6, pp. 1225–1237, 2008.

[10] D. J. H. Wilson, G. W. Irwin, and G. Lightbody, "RBF principal manifolds for process monitoring," *IEEE Transactions on Neural Networks*, vol. 10, no. 6, pp. 1424–1434, 1999.

[11] N. Aubry, W. Y. Lian, and E. S. Titi, "Preserving symmetries in the proper orthogonal decomposition," *SIAM Journal on Scientific Computing*, vol. 14, no. 2, pp. 483–505, 1993.

[12] D. Armbruster, R. Heiland, E. J. Kostelich, and B. Nicolaenko, "Phase-space analysis of bursting behavior in Kolmogorov flow," *Physica D*, vol. 58, no. 1–4, pp. 392–401, 1992.

[13] C. Qi and H.-X. Li, "Nonlinear dimension reduction based neural modeling for distributed parameter processes," *Chemical Engineering Science*, vol. 64, no. 19, pp. 4164–4170, 2009.

[14] J. Baker and P. D. Christofides, "Finite-dimensional approximation and control of non-linear parabolic PDE systems," *International Journal of Control*, vol. 73, no. 5, pp. 439–456, 2000.

[15] V. Lenaerts, G. Kerschen, and J.-C. Golinval, "Identification of a continuous structure with a geometrical non-linearity. Part II: proper orthogonal decomposition," *Journal of Sound and Vibration*, vol. 262, no. 4, pp. 907–919, 2003.

[16] N. Yusup, A. M. Zain, and S. Z. M. Hashim, "Overview of PSO for optimizing process parameters of machining," *Procedia Engineering*, vol. 29, pp. 914–923, 2012.

[17] G. Cui, L. Qin, S. Liu, Y. Wang, X. Zhang, and X. Cao, "Modified PSO algorithm for solving planar graph coloring problem," *Progress in Natural Science*, vol. 18, no. 3, pp. 353–357, 2008.

[18] N. Smaoui, "Boundary and distributed control of the viscous Burgers equation," *Journal of Computational and Applied Mathematics*, vol. 182, no. 1, pp. 91–104, 2005.

[19] J. Baker, A. Armaou, and P. D. Christofides, "Nonlinear control of incompressible fluid flow: application to Burgers' equation and 2D channel flow," *Journal of Mathematical Analysis and Applications*, vol. 252, no. 1, pp. 230–255, 2000.

Hindawi Publishing Corporation
Journal of Applied Mathematics
Volume 2013, Article ID 865643, 5 pages
http://dx.doi.org/10.1155/2013/865643

Research Article

Analysis of Average Shortest-Path Length of Scale-Free Network

Guoyong Mao[1,2] and Ning Zhang[3]

[1] *Department of Electronic Information and Electric Engineering, Changzhou Institute of Technology, Changzhou 213002, China*
[2] *German Research School for Simulation Science, 52062 Aachen, Germany*
[3] *Business School, University of Shanghai for Science and Technology, Shanghai 200093, China*

Correspondence should be addressed to Guoyong Mao; gymao@mail.shu.edu.cn

Received 4 April 2013; Revised 15 June 2013; Accepted 17 June 2013

Academic Editor: Michael Chen

Copyright © 2013 G. Mao and N. Zhang. This is an open access article distributed under the Creative Commons Attribution License, which permits unrestricted use, distribution, and reproduction in any medium, provided the original work is properly cited.

Computing the average shortest-path length of a large scale-free network needs much memory space and computation time. Hence, parallel computing must be applied. In order to solve the load-balancing problem for coarse-grained parallelization, the relationship between the computing time of a single-source shortest-path length of node and the features of node is studied. We present a dynamic programming model using the average outdegree of neighboring nodes of different levels as the variable and the minimum time difference as the target. The coefficients are determined on time measurable networks. A native array and multimap representation of network are presented to reduce the memory consumption of the network such that large networks can still be loaded into the memory of each computing core. The simplified load-balancing model is applied on a network of tens of millions of nodes. Our experiment shows that this model can solve the load-imbalance problem of large scale-free network very well. Also, the characteristic of this model can meet the requirements of networks with ever-increasing complexity and scale.

1. Introduction

The research on complex networks is developing at a brisk pace, and significant achievements have been made in recent years [1–4]. Now it is attracting researchers from various areas, including mathematics, physics, biology, computer science, sociology, epidemiology, and others [5].

A scale-free network is a complex network or a connected graph with the property that the number of links originating from a given node exhibits a power law distribution [6]. Many networks are conjectured to be scale-free, including World Wide Web links, biological networks, and social networks.

Like other networks, specific structural features can characterize a scale-free network, among them are degree distribution, average shortest-path length (ASPL), clustering coefficient, and other aspects yet to be explored. Average shortest-path length is a concept in network topology that is defined as the average number of steps along the shortest paths for all possible pairs of network nodes. It is a measure of the efficiency of information or mass transport on a network. Some examples are the average number of clicks which will lead you from one website to another, or the number of people you will have to communicate through on average, to contact a complete stranger.

The average shortest-path length is defined as follows. Consider a network G with the set of vertices V. Let $\mathrm{dist}(v_1, v_2)$ denote the shortest distance between v_1 and v_2 ($v_1, v_2 \in V$). Assume that $\mathrm{dist}(v_1, v_2) = 0$ if $v_1 = v_2$ or v_2 cannot be reached from v_1, $\mathrm{has_path}(v_1, v_2) = 0$ if $v_1 = v_2$ or if there is no path from v_1 to v_2, and $\mathrm{has_path}(v_1, v_2) = 1$ if there is a path from v_1 to v_2; then the average shortest-path length ASPL_G is

$$\mathrm{ASPL}_G = \frac{\sum_{i,j}^{N} \mathrm{dist}\left(v_i, v_j\right)}{\sum_{i,j}^{N} \mathrm{has_path}\left(v_i, v_j\right)}. \quad (1)$$

Here N denotes the number of nodes in G, $\sum_{i,j}^{N} \mathrm{dist}(v_i, v_j)$ is the value of all-pairs shortest-path length of graph G, and $\sum_{i,j}^{N} \mathrm{has_path}(v_i, v_j)$ is the number of paths that exist in graph G. For a connected undirected graph, $\sum_{i,j}^{N} \mathrm{has_path}(v_i, v_j) = N(N-1)$, because paths exist between any pair of nodes.

For unweighted directed networks, the time complexity is $O(N * (N + E))$ for computing the all-pairs shortest-path

length using breadth-first-search algorithm [7], where E is the number of edges in G. For weighted directed network, the time complexity is $O(N^3)$ using Floyd algorithm [8]. If the network has millions of nodes or edges, the time needed in computing will be unbearable. Hence, parallel algorithm must be used to effectively reduce the computing time.

All-pairs shortest-path length is the sum of single-source shortest-path length (SSSPL) of each node in G. There are two types of parallel methods to compute all-pairs shortest-path length, the fine-grained parallelization method and the coarse-grained parallelization method. In fine-grained parallelization, the computing of the SSSPL for each node is accomplished using multiple cores to reduce the computing time [9–11]. Therefore, the time needed in getting the sum of the SSSPL of every node can be reduced as well. While in coarse-grained parallelization, suppose that there are N nodes in G and P cores available for computing; then one core is responsible for the computing of the SSSPL of N/P nodes. This kind of parallelization will not reduce the time needed in computing the SSSPL of one node, but ideally, the time needed in computing the all-pairs shortest-path length can be reduced to $1/P$ of that of a serial algorithm.

Compared with fine-grained parallelization, coarse-grained parallelization is much easier to implement on most parallel computers, because only a reduction operation is needed after all cores have finished their assignments of computing the SSSPL of their respective N/P nodes. In fine-grained parallelization, apart from a reduction operation in the end, a lot of scheduling and communication operations will be needed in computing the SSSPL of each node. These operations will decrease the performance of parallelization, as there are more and more computing nodes available to us, and the complexity and scale of networks are ever increasing. For any realistic scenario, the number of nodes in large scale-free networks will be significantly larger than the number of cores used by the parallel algorithm. Therefore, the coarse-grained method is also efficient because no computing resources are wasted.

Based on the observation mentioned previously, we will use coarse-grained parallelization to compute the all-pairs shortest-path length of large scale-free networks. It is a typical single-program-single-data (SPSD) parallelization; that is, program and data are the same in different cores; only the range of source nodes are different. Load imbalance might be the only problem, which is caused by the difference of time in computing the SSSPL of different nodes, as different cores are assigned different source nodes. Hence, in coarse-grained parallelization, the problem is how to schedule different source nodes to different cores such that the load is balanced across all cores.

Little work can be found on the load-balancing problem of this coarse-grained parallelization, due mainly to the fact that the research on scale-free networks was not popular until the end of last century. Even in the past decade, due to the large scale of network and restriction in computing power, the computing of the average shortest-path length was mainly achieved through approximation [12–15]. But nowadays, thanks to multicore and manycore technologies, the development in parallel computing has made it possible for accurate computing of such a problem.

We only concentrate on scale-free networks here, as in other networks, for example, the small-world network generated using WS and NW models [16] and the random network generated using the ER model [17], load imbalance is not a big problem for coarse-grained parallelization, because the computing time of the SSSPL for different nodes does not vary significantly.

The remainder of this paper is organized as follows. The influence of outdegree on computing time of the SSSPL is discussed in Section 2. The load-balancing model is discussed in Section 3. The evaluation of this model in large scale-free networks is discussed in Section 4, before discussing conclusion and future work in Section 5.

2. Analysis of the Outdegree on Computing Time

We only study the directed complex networks in this paper because most of the networks that naturally exist are directed. The SSSPL problem is to find the shortest-path length from a source node to all other nodes in the network or graph. It is easy to see that if a node has an outdegree of 0, the SSSPL will be 0 as well, because no path exists from this node to all other nodes in this network. Therefore, these nodes can be safely excluded from the job assignment without affecting the average shortest-path length. But apart from this, we can hardly find other relations between the feature of a node and its SSSPL. For example, if nodes with outdegree of 1 are selected, the corresponding computing time of the SSSPL is illustrated in Table 1. The network in Table 1 is taken from [1], and we name it BA network hereafter. It contains 325,729 nodes and 1,797,134 edges, among them 21,941 nodes have outdegree of 1.

In Table 1, the first column is the ratio of computing time of these nodes to the maximum computing time of the node in the whole network. We can see that the time needed in computing the SSSPL of these nodes varies greatly. If we randomly assign these nodes to different processors, the load balancing will become a problem.

However, we know that if one node has large outdegree, which means that many nodes are connected to this node, the possibility of a long computing time of the SSSPL of this node will be high. For example, there are 1,882 nodes with outdegree larger than 900 in BA network, among them 1,760 nodes have computing time larger than $1e-2$; that is, more than 93.5% of the computing time of these nodes can be regarded as long. To express this more clearly, we give the detailed information about the relation between threshold of outdegree and computing time in BA network in Table 2.

The average outdegree of this network is about 10.85. From Table 2, we can see that bigger outdegree can in some sense reflect longer computing time. A similar situation can be observed for China education network in 2004 [18, 19], as listed in Table 3. We name it edu04 network hereafter, in which the average outdegree is 2.81.

However, there are still many nodes that have a long computing time with small outdegree. In Table 1, there are

Table 1: The relation between time span and number of nodes with outdegree 1.

Time span	Number of nodes	Number percentage
$(1e-1, 1)$	5989	27.29
$(1e-2, 1e-1)$	9667	44.05
$(1e-3, 1e-2)$	924	4.21
$(1e-4, 1e-3)$	791	3.61
$(1e-5, 1e-4)$	2359	10.76
$(1e-6, 1e-5)$	2211	10.08

Table 2: Threshold of outdegree and computing time of BA network.

Threshold of outdegree	Number of nodes	Number of nodes with computing time bigger than 0.01	Percentage
>10	28181	21652	76.83
>27	11720	10096	86.14
>47	5147	4666	90.65
>900	1882	1760	93.52

15,656 nodes having outdegree of 1, but their computing times is also long (the computing time is bigger than $1e-2$). We know that if one node has a small outdegree (e.g., 1), but this node is connected to a node with a large outdegree, then the possibility of a long computing time of the SSSPL of this node will be high. Also, if one node has a big outdegree, but all its neighbors have a small outdegree, then the possibility of a short computing time of the SSSPL of this node will also be high. Therefore, the computing time of the SSSPL of one node is related not only to its outdegree but also to the outdegree of its neighbors of the ith ($i = 1, 2, 3, \ldots$) level. The neighbor of the first level is the direct neighbor of this node and the neighbor of the second level is the neighbor of the direct neighbor of this node, and so on.

The outdegree of the neighbors can be expressed in two terms, the sum of outdegree and the average outdegree Avg(i). Obviously, the latter can better express the connectivity of the neighboring nodes. For unweighted graph, the average outdegree Avg(i) of the neighbor of node i is

$$\text{Avg}(i) = \frac{1}{|N_i|} \sum_{j \in N_i} k_j, \tag{2}$$

where N_i are the neighbors of node i and k_j is the outdegree of a node j that belongs to N_i. We will discuss the overall impact factor of each level of the average outdegree on the computing time of the SSSPL in the next section.

3. The Dynamic Programming Model of the Load-Imbalance Problem

Based on the analysis mentioned previously, we present the dynamic programming model of the load-balancing problem. Suppose that there are N nodes in graph G, D_{ij} is the average outdegree of the jth level neighbor of node i ($i = 1, 2, 3, \ldots, N$, $j = 0, 1, 2, 3, \ldots$), D_{i0} is the outdegree of node i, T_i is the computing time of the SSSPL of node i, P is the number of computing cores, C_j is the coefficients of D_{ij}, and $\sum C_j = 1$. We sort T_i using the value of $\sum C_j D_{ij}$; then the load-balancing problem is changed into computing C_j such that $\sum_k^N T_i$ ($k = 1, 2, 3, \ldots, P$, $i = i+P$) are as equal as possible, where $\sum_k^n T_i$ is the total computing time in core k. The sorted nodes with id starting from k and step size P are assigned to core k, and N/P nodes are assigned to each core.

Table 3: Threshold of outdegree and computing time of edu04 network.

Threshold of outdegree	Number of nodes	Number of nodes with computing time bigger than 0.01	Percentage
>3	20881	8225	39.39
>10	9472	4875	51.47
>50	1068	848	79.41
>100	268	232	86.56

3.1. Implementation of the Load-Balancing Model. The serial computing time of the SSSPL of each node and the average outdegree of different levels of each node are measured using NetworkX [20] and Python [21]. To make the goal of this model more clear, we use Max T to denote the maximum sum of computing time among P cores, Min T to denote the minimum sum of computing time among P cores, and time difference = (Max T − MinT)/ Max T. Then, the goal of this model can be expressed as finding the coefficients such that time difference takes the minimum among all possible values.

We only compute the average outdegree till the second level, as it will take too long if the level goes deeper. Hence, the sum of $C_0 * D_{i0} + C_1 * D_{i1} + C_2 * D_{i2}$ is used as the index value to sort T_i, where $C_0 + C_1 + C_2 = 1$, $0.1 \le C_j \le 0.8$, and the variation of C_j is 0.1; there are 36 combinations for C_j ($j = 0, 1, 2$). We use different numbers of cores and different coefficients to compute the time difference of the BA and edu04 networks. The results show that time difference will be the smallest when $C_0 = 0.6$, $C_1 = 0.3$, and $C_2 = 0.1$. Figure 1 illustrates the relation between time difference and number of cores of these two networks, where the x-axis is the number of cores and y-axis time difference. Different values of time difference of BA network with coefficients 0.6, 0.3, and 0.1 are described using solid circles. The values of edu04 network with the same coefficients are described using up triangles.

3.2. Analysis of the Model. From the analysis of these two networks, we get two results. First, when the average degree of a network (the number of edges divided by the number of nodes) is large, the time difference is relatively small. Second, when the number of cores is small, the difference is also very small. For example, the difference is 0 when 2 cores are used. The difference will be larger when more cores are used. The first characteristic of this model can meet the demands of the ever-increasing complexity of the network, because

Table 4: Time difference for different coefficients and number of cores.

	Coefficients		
Cores	0.6, 0.3, 0.1	0.7, 0.2, 0.1	0.5, 0.3, 0.2
8	1.55%	1.48%	1.65%
16	2.37%	2.49%	4.21%
32	4.12%	4.81%	6.34%

the network is becoming more and more complex, and the average degree is getting bigger and bigger. For example, the average degree of the edu04 network is only about 1.5. But in 2008, it has grown into a network with 2,508,811 nodes and 25,278,346 edges [22], and the average degree reaches nearly 10. For the second characteristic, we did experiments on networks of various sizes and found out that the real cause is the decrease of the number of nodes assigned to each core when more cores are used. In other words, for a fixed number of cores, the difference will become smaller when the network is getting larger. We know that the network is growing very fast. Therefore, this characteristic of the model can meet the requirements of the ever-increasing scale of networks.

We also use this load-balancing model on other scale-free networks of various sizes. These networks are generated using BA model with different parameters [1]. We find out that when the ratio of the number of nodes over the number of cores (N/P) is getting larger, the coefficients are not unique to get the acceptable time difference values, but in every scenario, the difference to the best is very small. For example, when 16 cores are used in a network with 500,000 nodes and 1,500,000 edges, N/P being 31,250, there are 2 combinations of coefficients to get similar minimum time difference values; when 8 cores are used in this network, N/P being 62,500, there will be 3 combinations of coefficients to get similar minimum values. The time difference values related to different numbers of cores and coefficients are listed in Table 4. We can see that the coefficients of 0.6, 0.3, and 0.1 might not be the best, but they can still be safely used when the ratio is getting bigger. Similar situations can be found in other networks with different parameters.

For large-scale complex networks, it will take too long to compute the average neighbor outdegree of the second level. Hence, we simplify this model into just one level; that is, only outdegree and the average outdegree of the neighbor of the first level are considered. That is, the sum of $C_0 * D_{i0} + C_1 * D_{i1}$ is used as the index value to sort T_i, $C_0 + C_1 = 1$, $0.1 \leq C_j \leq 0.9$, the variation of C_j is also 0.1. The results show that the difference will be the least when $C_0 = 0.8$ and $C_1 = 0.2$. Different values of TimeDifference of BA network with these coefficients are described using down triangles in Figure 1, the values of edu04 network with the same coefficients are described using rectangles.

4. Evaluation

There are various algorithms for the computation of the ASPL, for example, NetworkX [21]. However, if the network is large, it will take a large amount of memory to represent the network. The network we used in the experiment has 2,508,811 nodes and 25,278,346 edges, and the memory needed to represent this network would be around 74 G if NetworkX were used, much bigger than the memory capacity of a workstation. It is obviously impossible to parallelize the serial algorithm because each core will get a copy of the whole network during the parallel execution process.

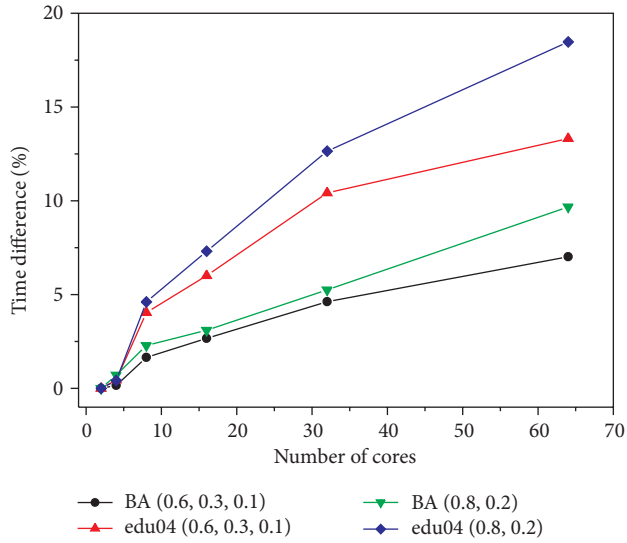

Figure 1: Relation between time difference and number of cores.

To solve this space-complexity problem, we used a native 2-dimensional array to represent the network, where the first row in the array is the start node of an edge and the second row is the target node. Also, as there are many search operations in the Breadth-First-Search algorithm, we transform the array into a C++ multimap using the start node as the key and all nodes connected to this node as the values of this key. With this data structure, the memory needed for loading the same network is reduced to only 1.48 G. Also, these structures can significantly speed up the keywords-based fast index, as all data in this map is sorted.

With the simplified load-balancing model, we compute the average shortest-path length of the network with 2,508,811 nodes on a cluster of 6 Dell PowerEdge workstations that have 72 cores; the operating system is CentOS 5.5 64 bit, and the compiler is Intel C++ 11.1. We use MPI to implement job assignment and to get the time used on each core, and the average computation time is 537,721 seconds or about 6 days and 5.5 hours. The time difference between the maximum time and the minimum time is only about 1.43%.

5. Conclusion and Future Work

The main contribution of this paper is the dynamic programming model that can be used to solve the load-balancing problem in coarse-grained parallel computing of average shortest-path length problem of large scale-free network. Though we only test the model with networks of up to tens of millions of edges, the feature of this model can make it scalable to networks with more complexity and larger scale.

In this paper, we presented our reason of using coarse-grained parallelization to compute the average shortest-path length. We analyzed the relationship between the computing time of the SSSPL of node and the features of nodes and presented a dynamic programming model to reduce the time difference among all computing cores. We used time measurable networks to get the coefficients of this model and applied this model to large scale-free network with satisfactory result.

In the future, we will evaluate this model with various kinds of networks to determine the relation between the features of the network (e.g., the average degree) and the coefficients. With this relation, we can distribute the nodes more evenly among cores to achieve better load balance and make this model more scalable to networks of different types.

Acknowledgments

The authors are grateful to colleagues in German Research School for Simulation Science for their constructive suggestions. The authors are also grateful to the reviewers for their valuable comments and suggestions to improve the presentation of this paper. This work is supported by the National Natural Science Foundation of China under Grant no. 70971089, Shanghai Leading Academic Discipline Project under Grant no. XTKX2012, and Jiangsu Overseas Research and Training Programs for University Prominent Young and Middle-Aged Teachers and Presidents.

References

[1] R. Albert, H. Jeong, and A. Barabási, "Diameter of the world-wide web," *Nature*, vol. 401, no. 6749, pp. 130–131, 1999.

[2] A.-L. Barabási and R. Albert, "Emergence of scaling in random networks," *Science*, vol. 286, no. 5439, pp. 509–512, 1999.

[3] A.-L. Barabási, R. Albert, and H. Jeong, "Mean-field theory for scale-free random networks," *Physica A*, vol. 272, no. 1, pp. 173–187, 1999.

[4] R. Albert and A. Barabási, "Statistical mechanics of complex networks," *Reviews of Modern Physics*, vol. 74, no. 1, pp. 47–97, 2002.

[5] A. E. Motter and R. Albert, "Networks in motion," *Physics Today*, vol. 65, pp. 43–48, 2012.

[6] S. H. Strogatz and D. J. Watts, "Collective dynamics of 'small-world' networks," *Nature*, vol. 393, no. 6684, pp. 440–442, 1998.

[7] E. W. Dijkstra, "A note on two problems in connexion with graphs," *Numerische Mathematik*, vol. 1, no. 1, pp. 269–271, 1959.

[8] Floyd and W. Robert, "Algorithm 97: shortest path," *Communications of the ACM*, no. 5, p. 345, 1962.

[9] A. Crauser, K. Mehlhorn, U. Meyer, and P. Sanders, "A parallelization of Dijkstra's shortest path algorithm volume," in *Mathematical Foundations of Computer Science (MFCS)*, vol. 1450 of *Lecture Notes in Computer Science*, pp. 722–731, 1998.

[10] J. L. Träff and C. D. Zaroliagis, "A simple parallel algorithm for the single-source shortest path problem on planar digraphs," *Journal of Parallel and Distributed Computing*, vol. 60, no. 9, pp. 1103–1124, 2000.

[11] K. Madduri, D. A. Bader, W. B. Jonathan, and J. R. Crobak, "An experimental study of a parallel shortest path algorithm for solving large-scale graph instances," in *Proceedings of the 9th Workshop on Algorithm Engineering and Experiments and the 4th Workshop on Analytic Algorithms and Combinatorics (ALENEX '07)*, pp. 23–35, New Orleans, La, USA, January 2007.

[12] Q. Ye, B. Wu, and B. Wang, "Distance distribution and average shortest path length estimation in real-world networks," in *Proceedings of the 6th International Conference on Advanced Data Mining and Applications*, vol. 6440, pp. 322–333, 2010.

[13] M. Potamias, F. Bonchi, C. Castillo, and A. Gionis, "Fast shortest path distance estimation in large networks," in *Proceedings of the 18th International Conference on Information and Knowledge Management (CIKM '09)*, pp. 867–876, November 2009.

[14] A. Gubichev, S. Bedathur, S. Seufert, and G. Weikum, "Fast and accurate estimation of shortest paths in large graphs," in *Proceedings of the 14th ACM International Conference on Information and Knowledge Management (CIKM '10)*, Toronto, O'ntario, Canada, October 2010.

[15] l. Su, N. Zhang, and L. Ma, "A new approximation algorithm for finding the shortest path in large networks," *Complex System and Complex Science*, vol. 5, no. 2, pp. 51–54, 2008.

[16] X. F. Wang and G. Chen, "Complex networks: small-world, scale-free and beyond," *IEEE Circuits and Systems Magazine*, vol. 3, no. 1, pp. 6–20, 2003.

[17] P. Erdős and A. Rényi, "On the evolution of random graphs," *Mathematical Institute of the Hungarian Academy of Sciences*, no. 5, pp. 17–61, 1960.

[18] N. Zhang, "Demonstration of complex network: CERNET," *Journal of Systems Engineering*, vol. 21, no. 4, pp. 337–340, 2006 (Chinese).

[19] N. Zhang, "Analysis of china education network structure," *Computer Engineering*, vol. 33, no. 17, pp. 140–142, 2007 (Chinese).

[20] "NetWorkX1. 7, Official website for NetWorkX," http://networkx.lanl.gov/index.html.

[21] "Python2. 7, Official website of python," http://www.python.org/index.html.

[22] N. Zhang, L. Su, and L. Ma, "Comparative studies on the topological structure of China Education Network," *Journal of University of Shanghai for Science and Technology*, vol. 30, no. 3, pp. 297–299, 2008 (Chinese).

Hindawi Publishing Corporation
Journal of Applied Mathematics
Volume 2013, Article ID 452391, 9 pages
http://dx.doi.org/10.1155/2013/452391

Research Article

A Data-Based Approach for Modeling and Analysis of Vehicle Collision by LPV-ARMAX Models

Qiugang Lu, Hamid Reza Karimi, and Kjell Gunnar Robbersmyr

Department of Engineering, Faculty of Engineering and Science, University of Agder, P.O. Box 509, 4898 Grimstad, Norway

Correspondence should be addressed to Hamid Reza Karimi; hamid.r.karimi@uia.no

Received 30 March 2013; Revised 21 May 2013; Accepted 21 May 2013

Academic Editor: Zhiwei Gao

Copyright © 2013 Qiugang Lu et al. This is an open access article distributed under the Creative Commons Attribution License, which permits unrestricted use, distribution, and reproduction in any medium, provided the original work is properly cited.

Vehicle crash test is considered to be the most direct and common approach to assess the vehicle crashworthiness. However, it suffers from the drawbacks of high experiment cost and huge time consumption. Therefore, the establishment of a mathematical model of vehicle crash which can simplify the analysis process is significantly attractive. In this paper, we present the application of LPV-ARMAX model to simulate the car-to-pole collision with different initial impact velocities. The parameters of the LPV-ARMAX are assumed to have dependence on the initial impact velocities. Instead of establishing a set of LTI models for vehicle crashes with various impact velocities, the LPV-ARMAX model is comparatively simple and applicable to predict the responses of new collision situations different from the ones used for identification. Finally, the comparison between the predicted response and the real test data is conducted, which shows the high fidelity of the LPV-ARMAX model.

1. Introduction

In the past few decades, as one of the major concerns in the automotive industry, the vehicle crashworthiness has been attracting exceptional attention all over the world. Before appearing on roads, each car must undergo a series of crash tests to be verified whether they satisfy the safety requirements and conform to safety standards set by the road safety organizations or rate programs such as Euro NCAP or National Highway Traffic Safety Administrations (NHTSA). In terms of the crash tests, they are exceptionally costly and complicated due to the need of appropriate facilities, qualified staff, and data-acquisition system. Moreover, the proper arrangement of measuring devices (e.g., accelerometers and cameras used to record the crash event) or precise positioning of the research centers has also added the complexity of such crash tests. Thus it would be highly attractive if the overall car performance can be predicted and assessed without the need to execute numerous full-scale crash experiments, which renders the proposition of a mathematical models with accurate input-output behavior as the real tests to be of great interest.

Recently we can distinguish two main approaches of vehicle crash modeling: finite element method (FEM) simulations and lumped parameter modeling (LPM). FEM is considered as the most thorough computational tool with detailed insight into the vehicle crash modeling and thus has been widely employed; refer to [1–4] and the references therein. It offers high accuracy of results and makes it possible to describe large number of details such as connections and interactions between particular bodies, their deformation rate, or material properties. The major disadvantages of this method include the high computational demand of powerful hardware and the purchase of software used to perform the numerical simulation. The second approach frequently used in vehicle crash is an analytical method of formulating a model called lumped parameter modeling (LPM). It consists of formulating equations of motion of spring-damper-mass systems and solving them so as to precisely determine the model's response. However, the drawback of this method is that it can perform well only when used for a given set of collisions. With respect to this shortcoming, several methodologies such as artificial neural networks and wavelet transforms are utilized to make it possible to simulate various crash scenarios; see [5].

On the other hand, for the modeling of complex systems, the model identification based on the data training or estimation can be an alternative to the traditional modeling by using physical laws [6, 7]. Up to now, the data-based modeling for

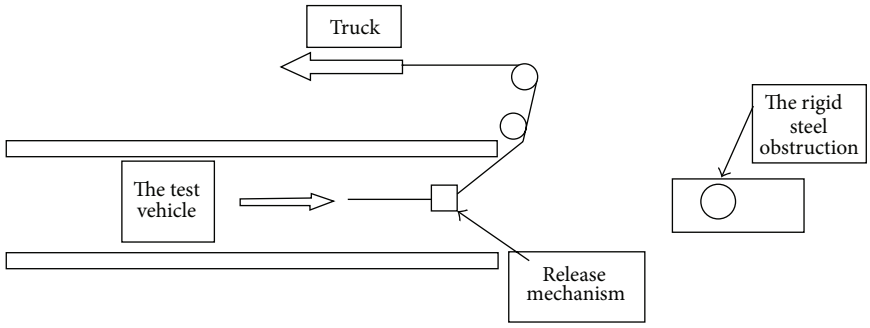

Figure 1: Scheme of crash test.

Figure 2: Obstruction.

the vehicle crashworthiness has been extensively investigated. It has been well proven that the applications of autoregressive models like nonlinear autoregressive (NAR), nonlinear autoregressive with exogenous input (NARX), or nonlinear autoregressive moving average with exogenous input (NARMAX) are capable of predicting the time-series data with high fidelity. Up to now, a wide range of areas in the applications of autoregressive models have been well explored. In [8], the ARMA model of edge-localized modes (ELM) time series has been established, which can decompose the time series into deterministic and noise components. A hybrid of NARX and ARMA models was employed to predict the long-term machine state based on vibration data in [9]. NARX models have been successfully applied to black box modeling of the gas turbine operating in isolated and nonisolated modes in [10]. The prediction performance assessment of recurrent NARX model was investigated in [11], in which the effects of the changing network's architecture on the quality of predictions are verified. Apart from the technical applications, the regressive models have also been widely employed as an advantageous methodology in other areas of research, such as stock market [12], cardiovascular diseases prevention [13], and prediction of freshwater phytoplankton dynamics [14].

A significant contribution to data-based approach in modeling automobile crash was made in [15], where the autoregressive moving average (ARMA) model was used to estimate lumped parameters (i.e., stiffness, damping, and masses) of analytical models (differential equations). Those physical parameters are changeable in time, which thus makes it possible to simulate the vehicle frontal and side impacts with high level of accuracy. What is more, the

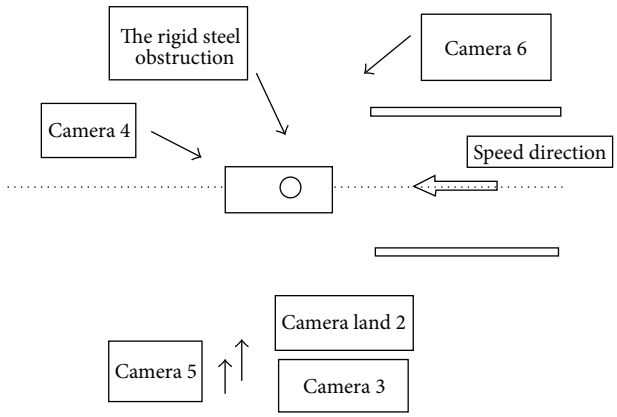

Figure 3: Cameras layout.

neural networks have been successfully used to estimate the parameters of vehicle crash models. Specifically, the values of the spring stiffness and damping coefficients for the LPM were obtained through the radial basis artificial neural network (RBFNN) in [16]. Artificial neural networks (ANNs) were also implemented in [17] to predict the crash severity and occupants injury. Other up-to-date technologies currently utilized in vehicle crashworthiness modeling include wavelets, fuzzy logic, and intelligent approach; refer to [18–20].

Recently, the research scope of crashworthiness has been focused on defining a dynamic vehicle crash with changing parameters according to the changeable input such as initial impact velocity [21, 22]. In particular, in [21], a nonlinear occupant model is established and a scheduling variable is

Figure 4: Car's deformation.

Figure 5: Steps of the experiment recorded by the high-speed camera.

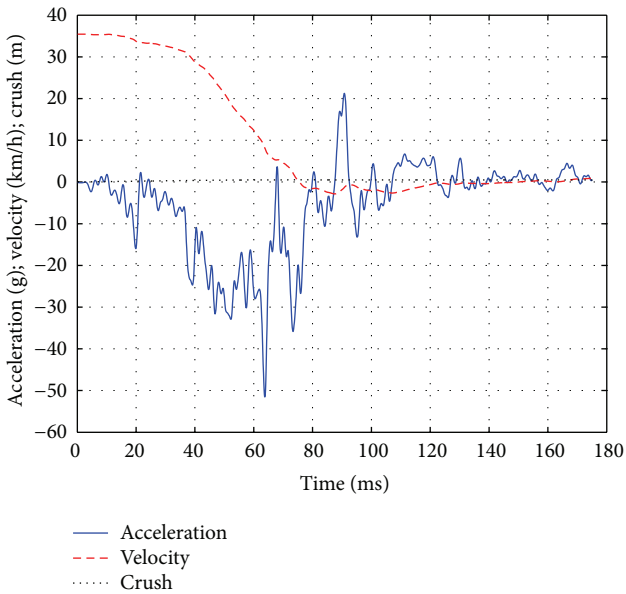

Figure 6: Vehicle kinematics with $\overline{v} = 35$ km/h.

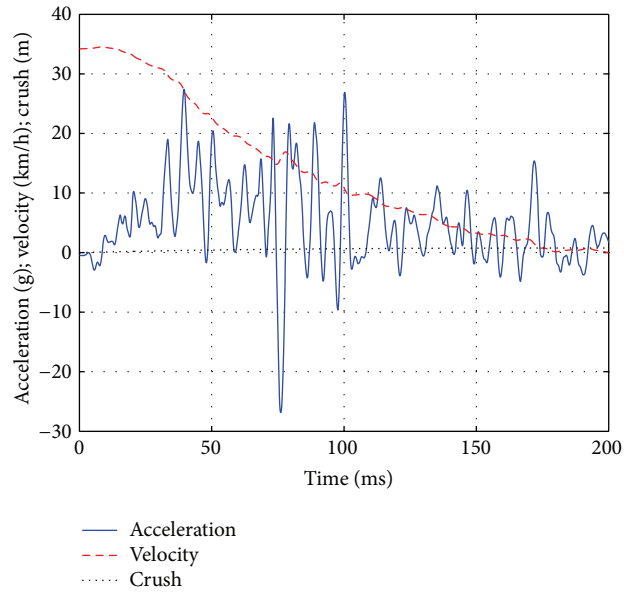

Figure 7: Vehicle kinematics with $\overline{v} = 35.57$ km/h.

defined to formulate the linear parameter-varying (LPV) model. Inspired by this work, in this paper, we aim to establish the LPV-ARMAX models for the vehicle crash, and the scheduling parameter is selected as the initial impact velocity. This LPV model consists of a set of ARMAX models in which the parameters are not constant but are functions of the impact velocity that can be regarded as an input determining the "operating condition" of the model [23]. So instead of generating a large database of ARMAX models for every possible impact velocity, we can calculate a single model that is function of impact velocity, which is far more attractive.

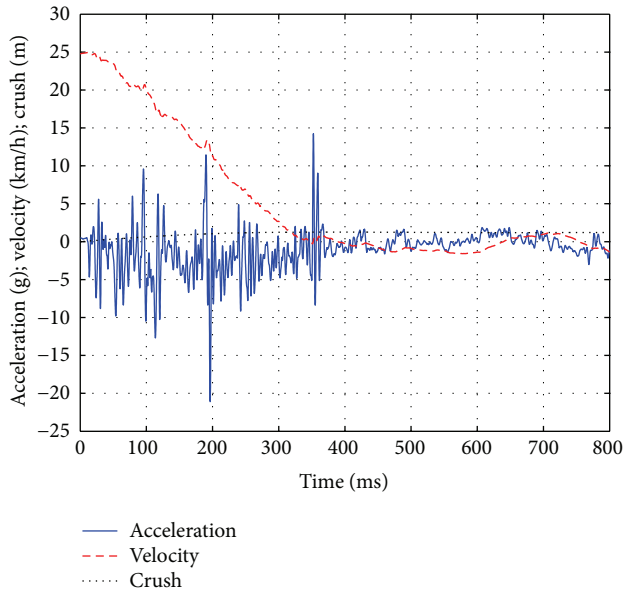

Figure 8: Vehicle kinematics with $\overline{v} = 24.63$ km/h.

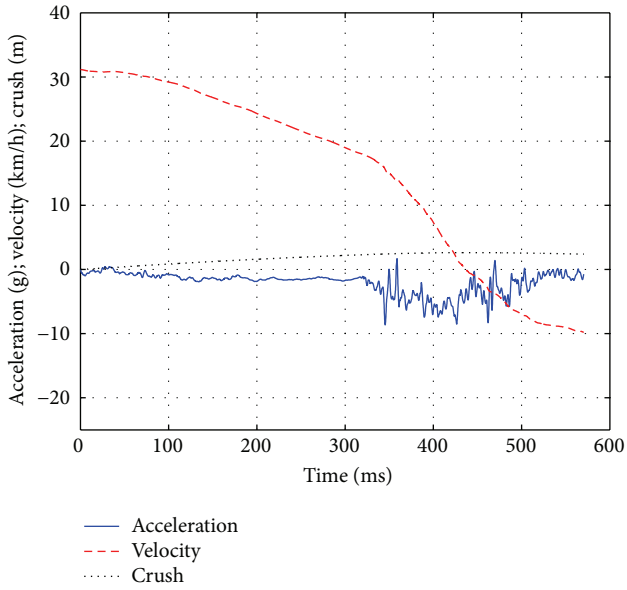

Figure 9: Vehicle kinematics with $\overline{v} = 31.35$ km/h.

The structure of this paper is organized as follows. The detailed introduction about the full-scale vehicle-to-pole collision is presented in Section 2. In Section 3, the notation and main ideas of this approach are developed. Section 4 illustrates the application of LPV-ARMAX-based time series analysis to the modeling of vehicle crash, and simulation results are analyzed and compared. Finally, the conclusion is given in Section 5.

2. Crash Test Description

In this section we present car-to-pole collisions with different initial impact velocities so as to test if the model proposed is capable of representing different crash scenarios.

The car tests were subjected to impact with a vertical and rigid cylinder. During the tests, the acceleration was measured in three directions, that is, longitudinal, lateral, and vertical. The yaw rate from the car's center of gravity was also recorded. The acceleration field was 100 meters long with two anchored parallel pipelines. The pipelines have a clearance of 5 mm to the front wheel tires. The force to accelerate the test car was generated using a truck and a tackle. The release mechanism was placed 2 m before the end of the pipelines, and the distance from there to the test item was 6.5 m. The car was steered using the pipelines that were bolted to the concrete runaway. The experimental scheme is shown in Figure 1.

2.1. Description of the Car and Pole. As illustrated in Figure 2, the pole was constructed with two components: a baseplate and a pipe. The baseplate had dimensions $740 \times 410 \times 25$ mm. The pipe had a length of 1290 mm and overall diameter equal to 275 mm. The pipe was filled with concrete and mounted on a concrete foundation with five bolts. These bolts connected the concrete foundation with the baseplate of the obstruction which was fixed to the shovel of a bulldozer. The initial velocities of the cars are 35 km/s, 35.57 km/h, 24.63 km/h, and 31.35 km/h.

2.2. Instrumentation. During the test, the acceleration at the center of gravity in three dimensions (x-longitudinal, y-lateral, and z-vertical) was recorded. The car speed before the collision was measured. The yaw rate was also measured with a gyrometer. Using normal speed and high-speed video cameras, the behavior of the safety barrier and the test car during the collision was recorded; see Figure 3.

A 3-D accelerometer was mounted on a steel bracket close to the car's center of gravity, and it was fastened by screws to the car's chassis. Data from the sensor was fed to an eight-channel data logger and subsequently sampled with a frequency of 10 kHz. The memory was able to store 6.5 s of data per channel. The velocity of the car was checked by an inductive monitor. It was directed towards a perforated disc mounted on a wheel on the right side of the test car. Figure 4 shows the car before, during, and after the collision. The steps of the experiment recorded by the high-speed camera are illustrated in Figure 5.

2.3. Analysis of Crash Pulse. All the tests are central impact; thus, as already mentioned only the pulse recorded in the longitudinal direction (x-axis) is analyzed. By integrating car's acceleration

$$v(t) = \int_{t_0}^{t} a(\tau)\, d\tau,$$
$$x(t) = \int_{t_0}^{t} v(\tau)\, d\tau, \tag{1}$$

we can obtain plots of velocity $v(t)$ and crush (or displacement) $x(t)$ for different initial impact velocities $\overline{v}$; see Figures 6, 7, 8, and 9. Take the vehicles kinematics with $\overline{v} = 35$ km/h (Figure 6) as an example. At the time when the

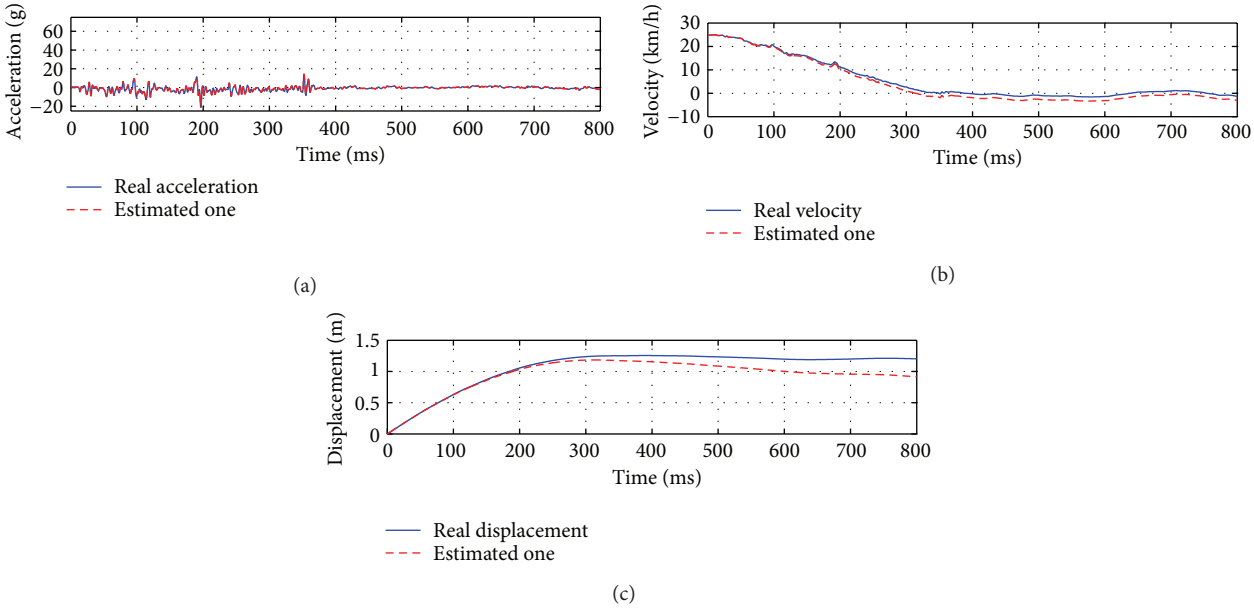

Figure 10: ARMAX simulation results for vehicle with $\bar{v} = 24.63$ km/h.

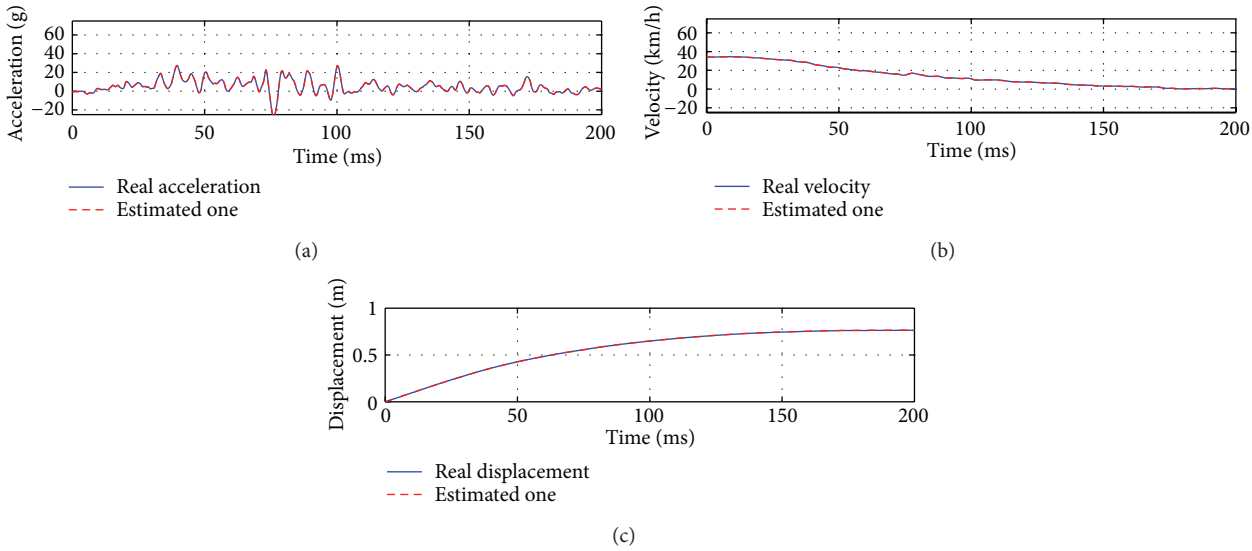

Figure 11: ARMAX simulation results for vehicle with $\bar{v} = 35.57$ km/h.

relative approach velocity is zero, the maximum dynamic crush occurs. The relative velocity in the rebound phase then increases negatively up to the final separation (or rebound) velocity, at which time a vehicle rebounds from an obstacle. The contact duration of the two masses includes both contact time in deformation and restitution phases. When the relative acceleration becomes zero and relative separation velocity reaches its maximum recoverable value, we have the separation of the two masses.

3. Mathematical Modeling

There are two types of mathematical modelings of real world systems that are commonly used [24]. The first is mathematical approach, in which the dynamics of a system is derived from the fundamental law of physics, for example, Newton's Laws or conservation principle. The secondary approach is the system identification. It is a process to select the model's parameters so that the model's behavior can fit the experimental data. In this paper, we adopt the second approach.

3.1. ARMAX Model Description. Analysis of the autoregressive model with moving average exogenous input (ARMAX) was done according to [24]. The ARMAX model can be defined as

$$y(t) + a_1 y(t-1) + \cdots + a_{n_a} y(t-n_a)$$

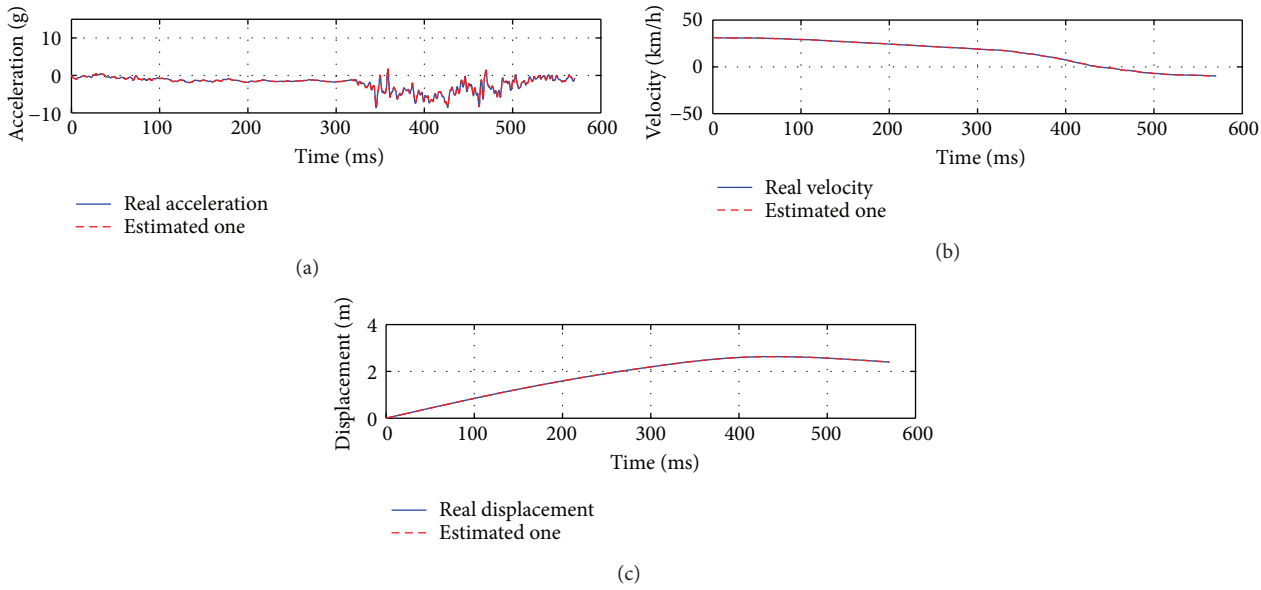

FIGURE 12: ARMAX simulation results for vehicle with $\bar{v} = 31.35$ km/h.

$$= b_1 u(t-n_k) + \cdots + b_{n_b} u(t-n_k-n_b+1) + c_1 e(t-1) + \cdots + c_{n_c} e(t-n_c) + e(t), \quad (2)$$

where t is the time, $y(t)$ is system's output, and $a_1, \ldots, a_{n_a}$, $b_1, \ldots, b_{n_b}$, $c_1, c_2, \ldots, c_{n_c}$ are model's parameters. n_a, n_b, and n_c are, respectively, the number of model's poles, model's zeros + 1, and parameters in c vector. n_k is the order of input delay. $y(t-1), \ldots, y(t-n_a)$ are system's outputs in previous moments and $u(t-1), \ldots, u(t-n_b)$ are system's inputs in previous moments. $e(t-1), \ldots, e(t-n_c)$ are white noise.

The ARMAX model can be simplified as

$$A(q^{-1})\, y(t) = B(q^{-1})\, u(t-n_k) + C(q^{-1})\, e(t), \quad (3)$$

where

$$A(q^{-1}) = 1 + a_1 q^{-1} + a_2 q^{-2} + \cdots + a_{n_a} q^{-n_a},$$
$$B(q^{-1}) = b_1 + b_2 q^{-1} + \cdots + b_{n_b} q^{-n_b}, \quad (4)$$
$$C(q^{-1}) = c_1 + c_2 q^{-1} + \cdots + c_{n_c} q^{-n_c}.$$

3.2. LPV-ARMAX Model Establishment. As stated in Section 1, the ARMAX models of vehicle crash in most literature are assumed to be linear time invariant (LTI). So for collisions under different initial conditions (e.g., initial impact velocities and vehicle masses), we have to extract different ARMAX models accordingly, which suffer from serious limitation especially when the number of LTI-ARMAX models is huge. Thus it is quite attractive if we can establish one LPV-ARMAX model whose parameters are functions of initial condition variables and are applicable to collision under a wide range of initial situations. Consider the parameters in the LPV-ARMAX models of the vehicle crash which are dependent on the initial impact velocity $\bar{v}$. What we are interested in is to find the dependence relationship and predict parameters and then the output of the LPV-ARMAX models for any initial impact velocity.

In the following, we will adopt a LPV-ARMAX model which can be described as

$$A(q^{-1}; \bar{v})\, y(t; v) = B(q^{-1}; \bar{v})\, u(t-n_k) + C(q^{-1}; \bar{v})\, e(k), \quad (5)$$

where

$$A(q^{-1}; \bar{v}) = 1 + a_1(\bar{v}) q^{-1} + a_2(\bar{v}) q^{-2} + \cdots + a_{n_a}(\bar{v}) q^{-n_a},$$
$$B(q^{-1}; \bar{v}) = b_1(\bar{v}) + b_2(\bar{v}) q^{-1} + \cdots + b_{n_b}(\bar{v}) q^{-n_b},$$
$$C(q^{-1}; \bar{v}) = c_1(\bar{v}) + c_2(\bar{v}) q^{-1} + \cdots + c_{n_c}(\bar{v}) q^{-n_c}. \quad (6)$$

Note that the parameters $a_i(\bar{v})$, $i = 1, 2, \ldots, n_a$, $b_j(\bar{v})$, $j = 1, 2, \ldots, n_b$ and $c_j(\bar{v})$, $j = 1, 2, \ldots, n_c$ are continuous functions of the impact velocity $\bar{v}$. The specific dependence form can be selected as polynomials, radical basis functions, splines, or other linear combinations of given functions. We define this model as LPV-ARMAX (n_a, n_b, n_c) for simplicity.

The following instructions specify the steps of such identification.

(1) Suppose that we have a set of groups of vehicle crash data, all of them are in the type of pole collision but under different impact velocities $\{\bar{v}_1, \bar{v}_2, \ldots, \bar{v}_n\}$. For any $\bar{v}_j$, $j = 1, 2, \ldots, n$, a set of time-series data is collected. From this data set, an LTI-ARMAX model with the same structure of the LPV-ARMAX model is identified. Thus, n distinct LTI-ARMAX models are obtained, each for $\bar{v}_j$, $j = 1, 2, \ldots, n$. And we can get the jth ARMAX model parameters $a_i(\bar{v}_j)$, $i = 1, 2, \ldots, n_a$, $b_i(\bar{v}_j)$, $i = 1, 2, \ldots, n_b$ and $c_i(\bar{v}_j)$, $i = 1, 2, \ldots, n_c$.

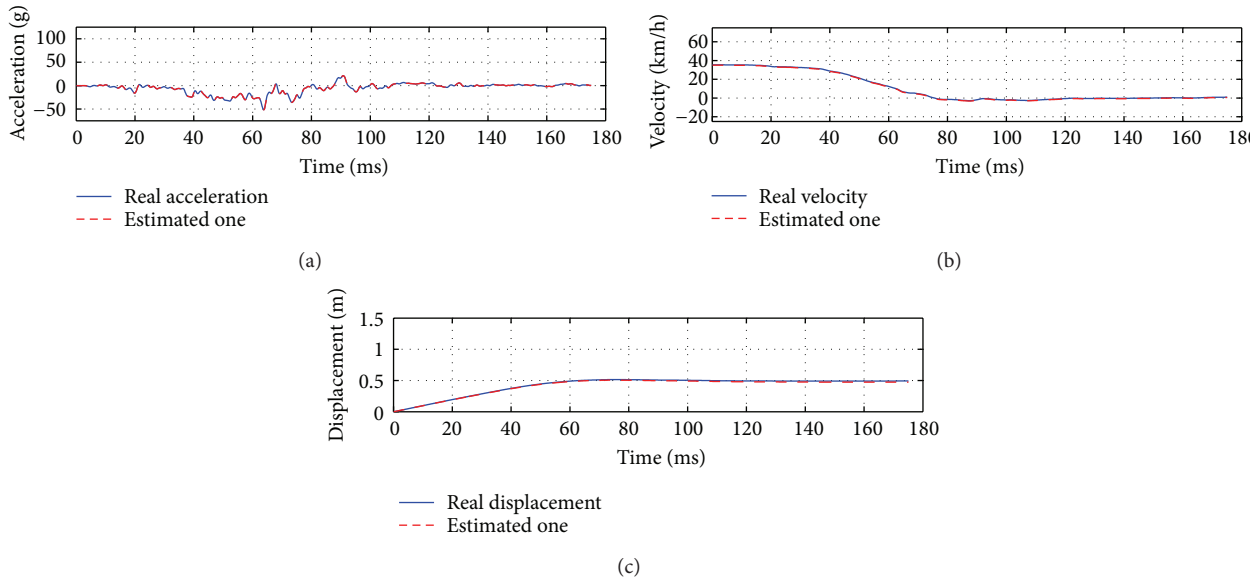

FIGURE 13: LPV-ARMAX perdition for vehicle with $\overline{v} = 35$ km/h.

(2) The n different values of the same parameter $(a_i(\overline{v}_j), b_i(\overline{v}_j), c_i(\overline{v}_j))$ in the n distinct LTI-ARMAX models obtained in step (1) can then be used to identify the dependence functions $(a_i(\overline{v}), b_i(\overline{v}), c_i(\overline{v}_j))$. These dependence functions may be, for instance, polynomials or splines, which can result in the LPV parameters by interpolating the parameters of the n LTI-ARMAX models.

From the resulting LPV model, the output $y(t;\overline{v})$ then can be obtained for any initial impact velocity $\overline{v}$, even different from those utilized in the identification process.

When the functions $a_i(\overline{v})$, $i = 1, 2, \ldots, n_a$, $b_i(\overline{v})$, $i = 1, 2, \ldots, n_b$ and $c_i(\overline{v})$, $i = 1, 2, \ldots, n_c$, are described using generalized polynomials such as B splines, that is,

$$\begin{aligned} a_i(\overline{v}) &= \sum_{j=1}^{n_s} \alpha_{i,j} \varphi_j(\overline{v}), \\ b_i(\overline{v}) &= \sum_{j=1}^{n_s} \beta_{i,j} \varphi_j(\overline{v}), \\ c_i(\overline{v}) &= \sum_{j=1}^{n_s} \gamma_{i,j} \varphi_j(\overline{v}), \end{aligned} \tag{7}$$

where $\varphi_j(\overline{v})$, $j = 1, 2, \ldots, n_s$ are linear independent continuous functions, the parameter-dependent ARX can be written as

$$\begin{aligned} y(t;\overline{v}) = &\sum_{i=1}^{n_a} \sum_{j=1}^{n_s} \alpha_{i,j} \varphi_j(v)\, y(t-i;\overline{v}) \\ &+ \sum_{i=0}^{n_b} \sum_{j=1}^{n_s} \beta_{i,j} \varphi_j(v)\, u(t-i) \\ &+ \sum_{i=0}^{n_c} \sum_{j=1}^{n_s} \gamma_{i,j} \varphi_j(v)\, e(t-i), \end{aligned} \tag{8}$$

where $\alpha_{i,j}$, $i = 1, 2, \ldots, n_a$, $j = 1, 2, \ldots, n_s$, $\beta_{i,j}$, $i = 1, 2, \ldots, n_b$, $j = 1, 2, \ldots, n_s$, and $\gamma_{i,j}$, $i = 1, 2, \ldots, n_c$, $j = 1, 2, \ldots, n_s$ are the parameters to be estimated.

It should be noted that the LPV-ARMAX model is linear with respect to $\alpha_{i,j}$, $\beta_{i,j}$, and $\gamma_{i,j}$. Assuming the error $e(t)$ to be Gaussian, it is possible to estimate the parameters using the techniques in [25].

Remark 1. It should be noted that the recorded acceleration signal in real car crash test is actually time-series data. Thus in the established LPV-ARMAX model (5), $B(q^{-1};\overline{v}) = 0$ for the vehicle crash since there exists no input (as will be shown in the simulation part), and the output $y(t;\overline{v})$ of (5) corresponds to the acceleration signal in the vehicle crash test.

Remark 2. In the previous literature, the most commonly used method is to establish an ARMAX model based on a group of vehicle crash data obtained under one specific impact velocity, which may not be applicable to other situations with different impact velocities. Thus it is desirable to know the models in the whole relevant volume of initial velocity instead of one (or several) specific values. Moreover, since the impact velocity can be arbitrarily valued in practice, the corresponding local model can be obtained easily with aid of the LPV-ARMAX model once we know the specific initial velocity, which is the advantage of our approach.

In the next section, we will present the simulation of vehicle crash to test the efficiency proposed in this paper. In the simulation, the error noise is Gaussian, and the lumped LTI-ARMAX models are identified via the MATLAB Identification Toolbox.

4. Simulation Results

In this section, the parameters of the LPV-ARMAX are estimated. We have four data sets corresponding to four initial impact velocities at our disposal, of which three data sets will be used to obtain the LPV-ARMAX model while

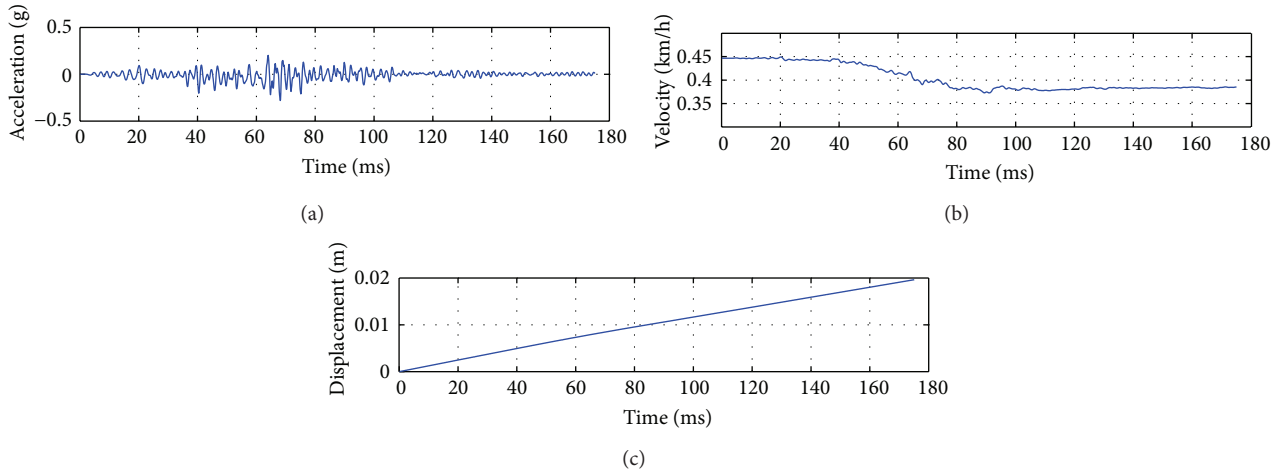

Figure 14: Simulation error by LPV-ARMAX model for vehicle with $\overline{v} = 35$ km/h.

the rest data set will be used for the purpose of verification. If one data set under a specific initial impact velocity $\overline{v} = \overline{v}^*$ is considered, the recorded acceleration signal can be approximated with a time-invariant ARMAX model. The derived LTI model can account well for the initial impact velocity at $\overline{v}^*$. However, the obtained results do not give any information about initial impact velocity in any other section different from $\overline{v}^*$. Therefore, for the sake of prediction, the use of this LTI model is inadequate.

With this in mind, in order to represent with a simplified model of the vehicle crash that can be applicable to the collisions with different initial impact velocity, the LPV-ARMAX model should be well constructed. It is assumed that the time series data of acceleration during the collision can be well represented by a LPV-ARMAX $(2, 0, 2)$ (note that for time series data, $n_b = 0$) model whose parameters $a_1(\overline{v})$, $a_2(\overline{v})$, $c_1(\overline{v})$, and $c_2(\overline{v})$ are functions of the initial impact velocity $\overline{v}$. The functions relating the parameters to impact velocity $\overline{v}$ are assumed to be cubic splines obtained by the interpolation of the parameters of three LTI-ARMAX $(2, 0, 2)$ models at three impact velocities. In this simulation, the four data sets selected to get the LPV-ARMAX model are those with impact velocities $\overline{v} = \{24.63\,\text{km/h}, 31.35\,\text{km/h}, 35.57\,\text{km/h}\}$. The obtained three LTI-ARMAX models and their simulation results are illustrated in Table 1 and Figures 10, 11, and 12, respectively.

From Table 1, we can get the resulting LPV-ARMAX $(2, 0, 2)$ model. Then for the vehicle crash with $\overline{v} = 35$ km/h, its LTI-ARMAX model can be obtained by interpolation as shown below:

$$A(q) = 1 - 1.9840q^{-1} + 0.9879q^{-2},$$
$$C(q) = 1 + 1.1170q^{-1} + 0.6581q^{-2}. \quad (9)$$

With (9), the prediction of acceleration under the other impact velocity $\overline{v} = 35$ km/h that is not used for identification is conducted. Figure 13 shows the simulation of the identified LPV model at impact velocity $\overline{v} = 35$ km/h, together with the integrated velocity and displacement. The acceleration data series obtained in real test are also illustrated in Figure 13.

Table 1: Parameters of ARMAX models for different impact velocities.

Impact velocity $\overline{v}$	Parameters of corresponding ARMAX models
$\overline{v} = 24.63$ km/h	$A(q) = 1 - 1.990q^{-1} + 0.9956q^{-2}$
	$C(q) = 1 + 1.992q^{-1} + 0.992q^{-2}$
$\overline{v} = 31.35$ km/h	$A(q) = 1 - 1.987q^{-1} + 0.9871q^{-2}$
	$C(q) = 1 + 1.993q^{-1} + 0.9938q^{-2}$
$\overline{v} = 35.57$ km/h	$A(q) = 1 - 1.983q^{-1} + 0.9883q^{-2}$
	$C(q) = 1 + 0.9916q^{-1} + 0.5794q^{-2}$

Figure 14 shows the error response between the estimation and origin of the signal. It can be observed that the approximation is quite good, and the errors coming from LPV-ARMAX (2,0,2) are so small that they can be neglected.

The simulation results show that the established LPV-ARMAX (2,0,2) model can not only reproduce the crash pulse signals which were utilized for the identification, but also predict the kinematic responses of crash pulses with new impact velocity which were not presented in the creation stage. Thus, it can be proved that the LPV-ARMAX model allows us to obtain the accurate estimations of vehicle's acceleration signal under different initial conditions and therefore the integration of acceleration which closely resembles the original ones.

5. Conclusion

In this paper, a new method to approximate the modeling of the vehicle's acceleration pulses under different impact velocities is investigated by using LPV approach. The LPV-ARMAX model allowing to approximate the behavior of vehicle crash with various initial conditions is investigated. Specifically, the parameters of the LPV-ARMAX model are assumed to be functions of the initial impact velocity which may produce significant influence on the acceleration pulse during the crash. By interpolating the LTI-ARMAX models obtained from the training data sets, the overall LPV-ARMAX model

can be achieved which can predict accurately the kinematic responses of vehicle crashes with various impact velocities. Simulation results illustrate that the LPV-ARMAX model can exactly reproduce both the new vehicle crash scenarios and those used for training. Future works may include taking the masses of vehicles into account as well since the masses can affect the acceleration pulses during the collision to some extent. But this attempt may increase the complexity since it will result in the coupling of the parameters in the LPV-ARMAX identification process, and thus it remains further investigation.

References

[1] T. Belytschko, "On computational methods for crashworthiness," *Computers and Structures*, vol. 42, no. 2, pp. 271–279, 1992.

[2] Z. Moumni and F. Axisa, "Simplified modelling of vehicle frontal crashworthiness using a modal approach," *International Journal of Crashworthiness*, vol. 9, no. 3, pp. 285–297, 2004.

[3] M. Borovinšek, M. Vesenjak, M. Ulbin, and Z. Ren, "Simulation of crash tests for high containment levels of road safety barriers," *Engineering Failure Analysis*, vol. 14, no. 8, pp. 1711–1718, 2007.

[4] C. A. Soto, "Structural topology optimization for crashworthiness," *International Journal of Crashworthiness*, vol. 9, no. 3, pp. 277–283, 2004.

[5] H. R. Karimi, W. Pawlus, and K. G. Robbersmyr, "Signal reconstruction, modeling and simulation of a vehicle full-scale crash test based on Morlet wavelets," *Neurocomputing*, vol. 93, no. 15, pp. 88–99, 2012.

[6] Z. Gao, D. Kong, and C. Gao, "Modeling and control of complex dynamic systems: applied mathematical aspects," *Journal of Applied Mathematics*, vol. 2012, Article ID 869792, 5 pages, 2012.

[7] Z. Gao, X. Dai, T. Breikin, and H. Wang, "Novel parameter identification by using a high-gain observer with application to a gas turbine engine," *IEEE Transactions on Industrial Informatics*, vol. 4, no. 4, pp. 271–279, 2008.

[8] G. Zvejnieks, V. N. Kuzovkov, O. Dumbrajs et al., "Autoregressive moving average model for analyzing edge localized mode time series on Axially Symmetric Divertor Experiment (ASDEX) Upgrade tokamak," *Physics of Plasmas*, vol. 11, no. 12, article 10, pp. 5658–5667, 2004.

[9] H. T. Pham, V. T. Tran, and B. Yang, "A hybrid of nonlinear autoregressive model with exogenous input and autoregressive moving average model for long-term machine state forecasting," *Expert Systems with Applications*, vol. 37, no. 4, pp. 3310–3317, 2010.

[10] M. Basso, L. Giarré, S. Groppi, and G. Zappa, "NARX models of an industrial power plant gas turbine," *IEEE Transactions on Control Systems Technology*, vol. 13, no. 4, pp. 599–604, 2005.

[11] R. Zemouri, R. Gouriveau, and N. Zerhouni, "Defining and applying prediction performance metrics on a recurrent NARX time series model," *Neurocomputing*, vol. 73, no. 13–15, pp. 2506–2521, 2010.

[12] C. Cheng, T. Chen, and L. Wei, "A hybrid model based on rough sets theory and genetic algorithms for stock price forecasting," *Information Sciences*, vol. 180, no. 9, pp. 1610–1629, 2010.

[13] L. Faes, G. Nollo, and K. H. Chon, "Linear and nonlinear parametric model identification to assess granger causality in short-term cardiovascular interactions," in *Proceedings of the Computers in Cardiology (CAR '08)*, pp. 793–796, Bologna, Italy, September 2008.

[14] K. Jeong, D. Kim, J. Jung, M. Kim, and G. Joo, "Non-linear autoregressive modelling by Temporal Recurrent Neural Networks for the prediction of freshwater phytoplankton dynamics," *Ecological Modelling*, vol. 211, no. 3-4, pp. 292–300, 2008.

[15] U. N. Gandhi and S. J. Hu, "Data-based approach in modeling automobile crash," *International Journal of Impact Engineering*, vol. 16, no. 1, pp. 95–118, 1995.

[16] W. Pawlus, J. E. Nielsen, H. R. Karimi, and K. G. Robbersmyr, "Comparative analysis of vehicle to pole collision models established using analytical methods and neural networks," in *Proceedings of the 5th IET International Conference on System Safety*, Manchester, UK, October 2010.

[17] J. McFadden, W. Yang, and S. R. Durrans, "Application of artificial neural networks to predict speeds on two-lane rural highways," *Transportation Research Record*, no. 1751, pp. 9–17, 2001.

[18] H. R. Karimi and K. G. Robbersmyr, "Signal analysis and performance evaluation of a vehicle crash test with a fixed safety barrier based on Haar wavelets," *International Journal of Wavelets, Multiresolution and Information Processing*, vol. 9, no. 1, pp. 131–149, 2011.

[19] W. Pawlus, H. R. Karimi, and K. G. Robbersmyr, "A fuzzy logic approach to modeling a vehicle crash test," *Central European Journal of Engineering*, vol. 3, no. 1, pp. 67–79, 2013.

[20] A. R. Varkonyi-Koczy, A. Rovid, and P. Varlaki, "Intelligent methods for car deformation modeling and crash speed estimation," in *Proceedings of the 1st Romanian-Hungarian Joint Symposium on Applied Computational Intelligence*, Timisoara, Romania, May 2004.

[21] E. van der Laan, F. Veldpaus, B. de Jager, and M. Steinbuch, "LPV modeling of vehicle occupants," in *Proceedings of the AVEC 9th International Symposium on Advanced Vehicle Control*, Kobe, Japan, 2008.

[22] A. M. Elmarakbi and J. W. Zu, "Crash analysis and modeling of two vehicles in frontal collisions using two types of smart front-end structures: an analytical approach using IHBM," *International Journal of Crashworthiness*, vol. 11, no. 5, pp. 467–483, 2006.

[23] G. Belforte, F. Dabbene, and P. Gay, "LPV approximation of distributed parameter systems in environmental modelling," *Environmental Modelling and Software*, vol. 20, no. 8, pp. 1063–1070, 2005.

[24] T. Soderstrom and P. Stoica, *System Identification*, Prentice Hall, Upper Saddle River, NJ, USA, 1989.

[25] L. Ljung, *System Identification: Theory for the User*, Prentice Hall, Englewood Cliffs, NJ, USA, 1987.